High performance and low-cost permanent magnet devices

Abdullah K. Shanshal

A thesis submitted for the degree of

Doctor of Philosophy

Department of Electronic and Electrical Engineering

October 2018

Abstract

Permanent magnet machines have high efficiency, high power density and ease of control due to the use of high energy density permanent magnets (PMS) as source of excitation which consume less power and allow achieving high airgap flux density and therefore high torque density can be produced comparing with other type of motor of the same rotor volume, employing them for various applications such as automotive and domestic appliance. Accordingly, permanent magnet characteristics have an important effect on the performance of the machine. However, their cost should be taken into consideration, because it can be a significant proportion of the total cost of the machine. Therefore, in this thesis the investigation of the modelling, design and analysis of novel permanent magnet machine for cost sensitive applications is presented. More specifically, a novel technique of arranging Ferrite permanent magnets with low energy density to achieve high airgap flux densities like those encountered in devices equipped with high cost rare-earth permanent magnets, thus, achieving significant cost savings, without substantial change in performance. Consequently, a spoke -type rotor equipped with axially magnetized permanent magnets in addition to the conventional circumferential permanent magnets is proposed, in order to increase the flux focusing and the airgap flux density.

For the electromagnetic design and analysis, a combination of 2D-FEA and 3D-FEA are used for the simulation of the conventional spoke-type rotor and the new proposed rotor machines respectively and the results concerning the fundamental airgap flux densities are compared with simple lumped parameter magnetic circuits considering the investigation of leading parameters, such as stator active length, airgap length, pole arc to pole pitch ratio and ratio of inner to outer diameter of the rotor, which can be employed as initial design stage.

Furthermore, 12 slots and 8 poles machine is designed to meet the specifications of a small personal mobility vehicle and the waveforms of flux linkage, airgap flux density and cogging torque are initially predicted at No-load condition using 3D-FEA. Then the torque / power speed envelopes and efficiency map are predicted on load condition at different operating conditions. The results show that the novel machine can achieve airgap shear stress in excess of 20KPa under natural air-cooling conditions with high efficiencies reaching 97% making it a strong contender for electric vehicle applications.

A new lumped parameter magnetic circuit model is developed to represent and simulate the new proposed rotor machine considering most important details such as stator active axial length, leakage in stator slot, back iron, tooth tips and the (linear, nonlinear) magnetic characteristic of the stator iron material. Simulation results including linkage flux, BEMF voltage waveform at No-load condition and the linkage flux, phase voltage and torque/speed envelope at variety of load condition are compared with 3D-FEA, and relatively good agreement exists. Albeit, room for improvement of the lumped parameter magnetic circuit model still exists.

Finally, a prototype is built, and the most important tests undertaken are investigated and the results are compared with predicted by 3D-FEA.

Publications

1) An accepted paper "High performance Ferrite permanent magnet brushless machines," in the MMM-INTERMAG Conference in January 14-18, 2019. Washington, DC. USA.

2) A paper has been accepted in the IEEE Transactions on Magnetics journal. Shanshal A, Hoang K, Atallah K. "High-Performance Ferrite Permanent Magnet Brushless Machines,". IEEE Transactions on Magnetics. 2019 Mar 28.

Acknowledgment

Firstly, I would like to express my sincere gratitude to my supervisor Prof. Kais Atallah for the continuous support my PhD study and related research, for his patience, motivation, and immense knowledge. His guidance helped me in all of research and writing up this thesis.

I would like to express particular thanks to everyone in the department of Electrical and Electronic engineering and EMD group, who supported and encouraged me over the whole study.

I am grateful to my parents, brother and sisters for the love and support that they have provided me with throughout my life. Last but not least, I would like to thank my wife pharmacist **Thura Al-saleem** for her outstanding character, endless support and for enabling me to endeavor into this PhD.

List of figures

List of tables

List of abbreviations

AC	Alternating current
AFPM	Axial flux permanent magnet
BEMF	Back electromotive force
DC	Direct current
EPS	Electrical power steering
EV	Electric vehicle
FEA	Finite element Analysis
FMM	Flat magnet motor
FSCW	Fractional slot concentrated winding
HEV	Hybrid electric vehicle
IPM	Inner permanent magnet
kPa	kilopascal
LPCM	Lumped parameter circuit model
MCM	Magnetic circuit model

MGOe	Mega gauss-oersted
MMF	Magneto motive force
MTPA	Maximum torque per ampere
NdFeB	Neodymium iron boron
NEDC	New European Driving Cycle
PM	Permanent magnet
RFPM	Radial flux permanent magnet
RIOD	Ratio of inner to outer diameter
SMC	Soft magnetic composite
SmCo	Samarium cobalt
SPM	Surface mounted permanent magnet

List of symbols

A_a	mm^2	Area of axially magnetised PM
A_c	mm^2	Area of circumferentially magnetised PM
A_g	mm^2	Airgap area in which flux is perpendicular
A_m	mm^2	Cross sectional area of the magnet
B_1	Tesla (T)	Fundamental airgap flux density
B_{airgap}	Tesla (T)	Airgap flux density
B_{core}	Tesla (T)	Flux density in the back-iron core
B_r	Tesla (T)	Remanence of the magnet
B_{tooth}	Tesla (T)	Flux density in the stator tooth
C_d		Skin friction coefficient

C_f		friction coefficient,
d	m	Stator lamination thickness
$\mathrm{d_c}$	mm	Back iron width
D_{airgap}	mm	Airgap diameter
$D_{bearing}$	mm	Bearing inner diameter
$D_{bore-stator}$	mm	Stator bore diameter
$D_{inner-rotor}$	mm	Rotor inner diameter
$D_{outer-rotor}$	mm	Rotor outer diameter
$D_{outer-stator}$	mm	Stator outer diameter
D_{stator}	mm	Stator outer diameter
F_a	V	MMF for the axially magnetised PM
$F_{bearing}$	kN	The bearing load
F_c	V	MMF for the circumferentially magnetised PM
H	mm	Pole depth
I_d, I_q	A	Direct axis current and quadrature axis current
K		correction factor
$\mathrm{K_e}$	$(\mathrm{W/(T/s)^{1.5}/m^3})$	Excess losses coefficient
$\mathrm{K_f}$		Stacking factor
$\mathrm{K_h}$	$(\mathrm{Ws/T^2/m^3})$	Hysteresis losses coefficient
k_i		Lamination factor
K_w		Winding factor
L	m	Length of the rotor part
L_{axial}	mm	Axial length of the machine
$L_{axial-rotor}$	mm	Rotor pole piece length
L_a	mm	Thickness of the axially magnetized PM

L_{APM}	mm	Axial PM length
L_{beam}	mm	Length of the beam
L_c	mm	Thickness of CPM
L_{CPM}	mm	Circumferential PM length
L_{d}	mH	Direct axis inductance
L_g	mm	Airgap length
L_m	mm	Thickness of the magnet
L_{q}	mH	Quadrature axis inductance
L_{ring}	mm	Soft magnetic ring axial length
l_s	mm	Stator slot width
L_{shaft}	mm	Length of the shaft
M_{dq}	mH	Mutual inductance (d-q axis)
M_{qd}	mH	Mutual inductance (q-d axis)
N		No. of turns
N_{base}	r/min	Based Speed
N_s		No. of slots
$P_{bearing}$	Watt	Bearing losses
P_{fe}	Watt	Iron losses
P_{rated}	kw	Rated power
$P_{windage}$	Watt	Windage losses
$Q_{r.m.s}$	A/m	Electrical loading
R	mm	Radius of the rotor
R_a		Reluctance associated with the axially magnetized PM
R_e		Reynolds number for the airgap
R_c		Reluctance associated with the circumferentially magnetized PM

R_g R_{airgap}		Reluctance associated with the Airgap
$R_{inner-rotor}$	mm	Rotor inner radius
$R_{outer-rotor}$	mm	Rotor outer radius
r/min		Revolution per minute
S_{lw}	mm	Stator lower width
S_{uw}	mm	Stator upper width
T_e	N.m	Electromagnetic torque
T_{rated}	N.m	Rated torque
T_s	mm	Stator tooth width
T_{sl}	mm	Tooth stalk width
T_{tw}	mm	Tooth tip width
V_{DC}	Volt	DC link voltage
V_{rotor}	m^3	Volume of the rotor
w	mm	Flux tube width
$\mathrm{W_t}$	mm	Width of tooth
W_{CPM}	mm	Circumferential PM width
α		Pole arc to pole pitch ratio
α_c		B exponent for Classical losses
α_e		B exponent for Excess losses
α_h		B exponent for Hysteresis losses
β_h		f exponent for Hysteresis losses
γ	Electrical degree	Gamma (Current angle)
θ	Electrical degree	Rotor rotation angle
λ		Ratio of R_c/R_a

λ_p	mm	Rotor pole pitch
λ_s	mm	Stator slot pitch
μ_0	henry per meter	Permeability of the air
μ_{dyn}	$\mathrm{kg/m.s}$	Dynamic viscosity of air
μ_r	1/henry	Relative recoil permeability of the magnet
ρ	$\mathrm{Kg/m^3}$	Density of air
σ	S/m	Classical losses coefficient
$\sigma_{shear\ stress}$	kN/m^2, kPa	Shear (normal) stress
ϕ_s	Weber	Flux per slot pitch
ϕ_P	Weber	Flux per pole pitch
φ_g	Weber	Per pole flux in the airgap
φ_s	Weber	Per pole flux in the stator
Ψ_d	Turn.weber	d–axis Linkage flux component
Ψ_{md}	Turn.weber	d–axis Linkage flux component (only PM)
Ψ_{mq}	Turn.weber	q–axis Linkage flux component (only PM)
Ψ_q	Turn.weber	q–axis Linkage flux component
Ω	rad/sec	angular frequency of the shaft
ω	rad/sec	Angular velocity

Contents

Chapter 1
Introduction

1.1 Motivation

Permanent magnet (PM) machines were introduced in 1930, when alnico magnet was discovered [1]. At that time, the use of PM machines was limited due to its properties and the lack of frequency converters. However, in recent decades, the performance of PM machines has improved significantly, by the development of high-energy permanent magnet, such as NdFeB rare earth PM and SmCo, Fig. 1.1 [2], power electronic converters, and control techniques. Recently, due to the many restrictions on future supply and fluctuation in price, the motivation to reduce and eliminate the use of rare earth PM in the realization of electrical machines has increased [3]. Therefore, permanent magnet free machines such as induction machines and switched reluctance machines or machines using alternative permanent magnets such as ferrite magnet have been seriously considered in many applications including automotive application (electrical and hybrid vehicles) and direct drive generators used in wind power generation. Table 1.1 shows the average price in ($/K$_g$) for two grades of magnet (Neodymium-iron boron and ferrite) and based on the average maximum energy $(BH)_{max.}$ It can be noticed that the average price of the neodymium magnet is about 10 times that of the ferrite [4].

Material	Average $(BH)_{max}$ (MGOe)	Average price ($/K$_g$)
NdFeB	40	75
Ferrite	3.8	7.1

Table 1.1 Average price comparison between neodymium and ferrite magnets.

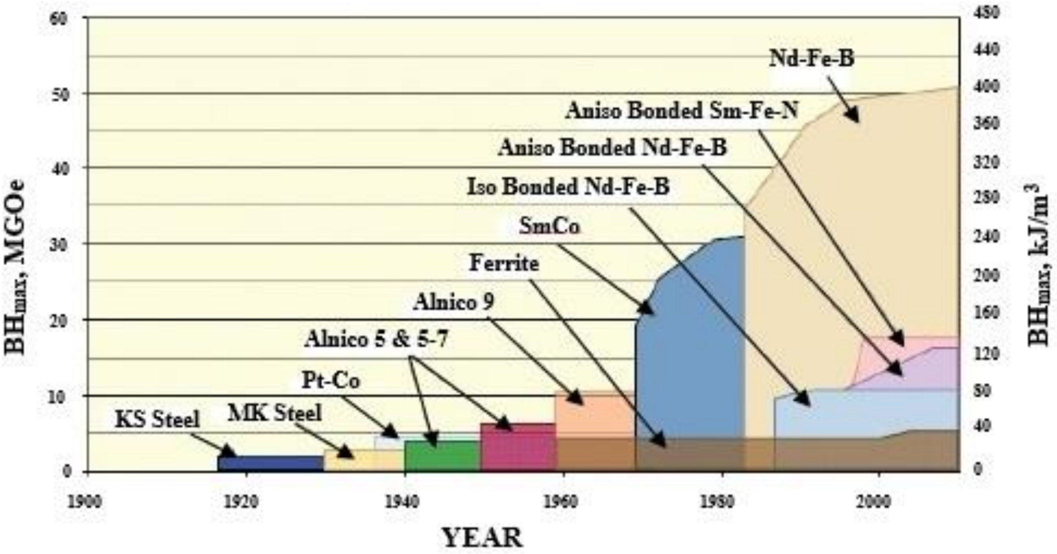

Fig. 1.1 A historical development of PM materials [2]

Nowadays, due to their high torque density and efficiency, permanent magnet (PM) machines are used in many applications such as: air conditioning compressors, hybrid electric vehicle traction, computer fans, washing machines, wind energy generation, domestic appliances and aerospace Fig. 1.2 [5].

(a) Power steering (b) Hybrid Camry PM synchronous

(c) Washing-machine motors (d) Wind Power (Siemens)

Fig. 1.2 Applications of PM machines [5]

According to [6], PM machines can be mainly classified into two types, sinusoidal or trapezoidal BEMF or (AC & DC) PM machines. Depending on the field orientation in the machines, two main types of brushless PM machines, are used in industry: (Axial and Radial) field machines as shown in Fig. 1.3 [7]. In radial flux PM machines, the direction of the magnetic field is perpendicular to the rotation axis while, in the axial flux PM machines, the direction of the magnetic field is parallel to rotation axis.

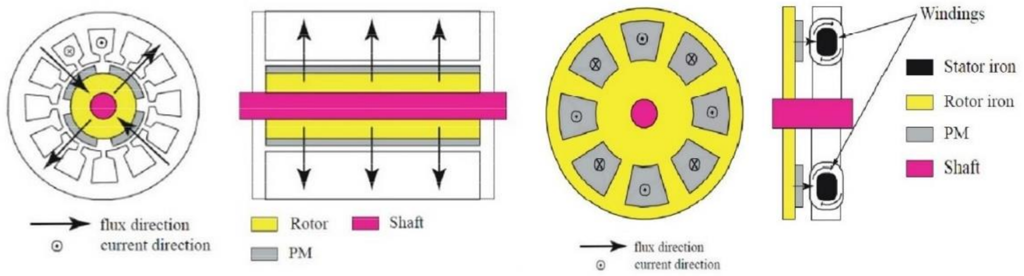

(a) (b)

Fig. 1.3 a) Radial PM machine b) Axial PM machine [7].

Two main types of radial flux PM machines exist: (Internal and external rotor) radial flux PM machines as shown in Fig. 1.4. For internal rotor PM machines, the rotor is surrounded by the stator and the airgap is between the rotor outer diameter and stator inner diameter. For external rotor PM machines, the airgap is located between stator outer diameter and the rotor inner diameter this will affect on the value of the torque. Depending on the configuration of the PM magnet, the rotor of PM machines has many topologies which were developed with special features to make it desirable for specific application requirements, some of these topologies are: 1) surface mounted SPM machines (SPM), 2) Interior permanent magnet machines (IPM). SPM, IPM and axial flux PM machines (AFPM) are shown in Fig. 1.5 & Fig. 1.6. Each type of (SPM and IPM) has different magnet configuration such as [8][9]: inset magnet SPM, surface bread loaf SPM, spoke rotor type IPM, Wing shape IPM, etc.

Axial flux permanent magnet machines have been used in different applications since the mid-70s due to their compact structure and higher toque and efficiency at low speed [10][11].

Depending on the number of rotors and stators, various topologies of (AFPM) exist: single rotor single stator, single stator double rotor (TORUS), single rotor double stator (AFIR) and multi rotor multi stator, each one of these topologies are sub divided into slotted, slotless and air-cored stator as shown in Fig. 1.6 and Fig. 1.7.

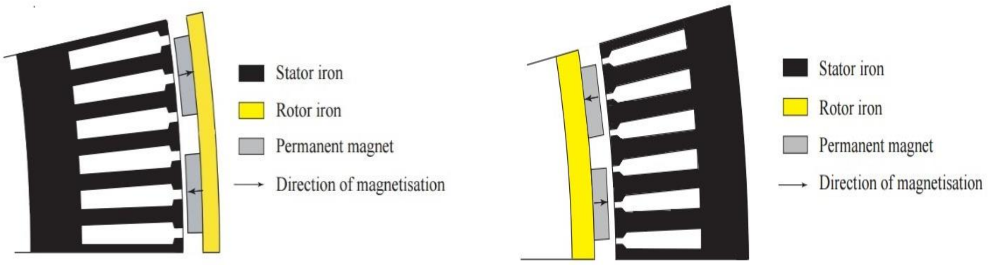

(a) (b)

Fig. 1.4 Radial PM machine a) External Rotor, b) Internal rotor [7]

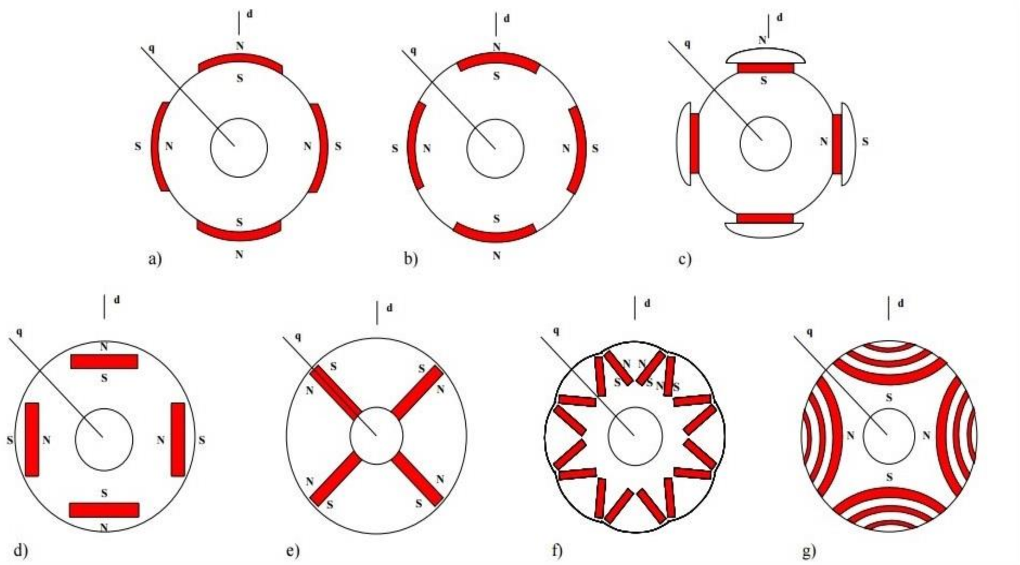

Fig. 1.5 a) Surface mounted magnets, b) inset rotor with surface magnets, c) surface magnets with pole shoes, d) embedded tangential magnets, e) embedded radial magnets, f) embedded inclined V-magnets and g) permanent magnet assisted synchronous reluctance motor [9].

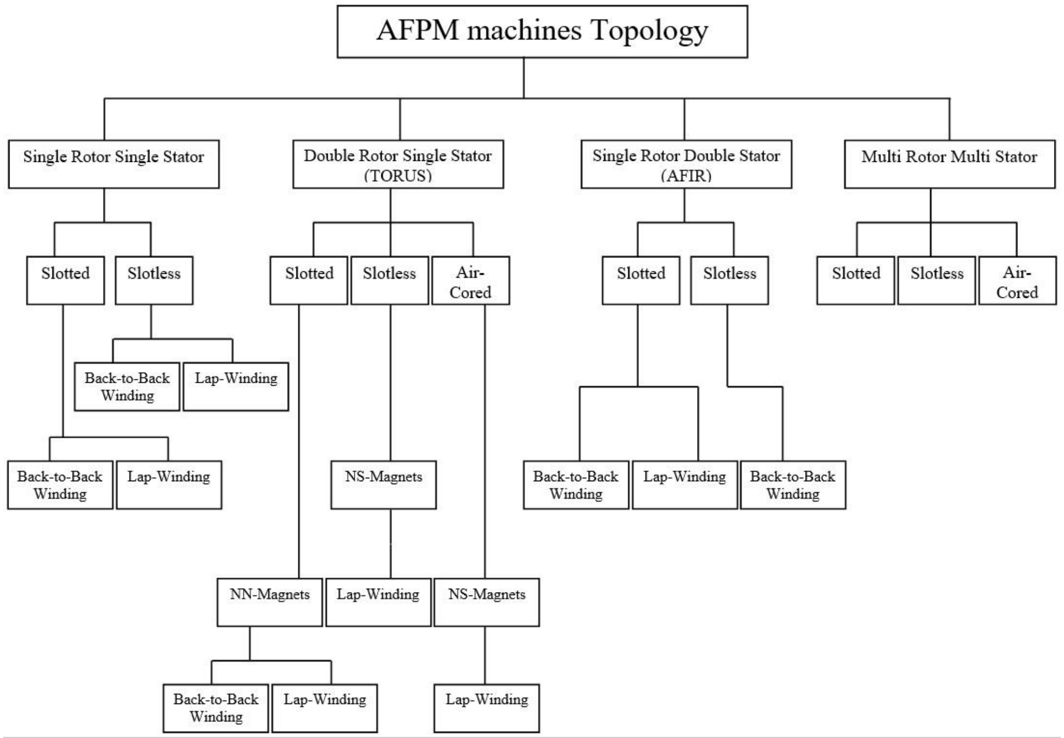

Fig. 1.6 Topologies of AFPM machines [11].

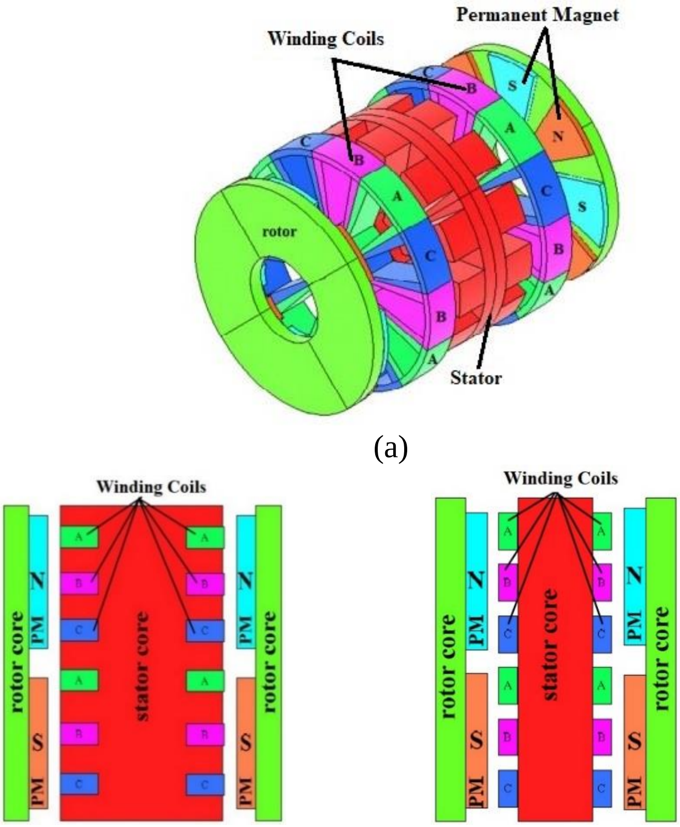

(a)

(b)

(c)

Fig. 1.7 AFPM machines: (a) Single Stator Double Rotor (TORUS), 3D view, (b) Slotted Stator (TORUS), (c) Slotless Stator (TORUS) [11].

In this research, ferrite permanent magnet will be used in the design of the machine. Although, the major disadvantage of ferrite magnet is their low energy, compared with the other type of PMs such as rare earth PM, Ferrite PMs are significantly cheaper and don’t suffer from supply. Therefore, the project would investigate novel techniques of arranging Ferrite permanent magnets to achieve airgap flux densities similar to those encountered in devices equipped with rare-earth permanent magnets, thus, achieving a significant cost savings, without substantially changing in performance [12]. This has been achieved by using axially and circumferentially magnetized ferrite PMs on special rotor designs, as can be seen in Fig. 1.8.

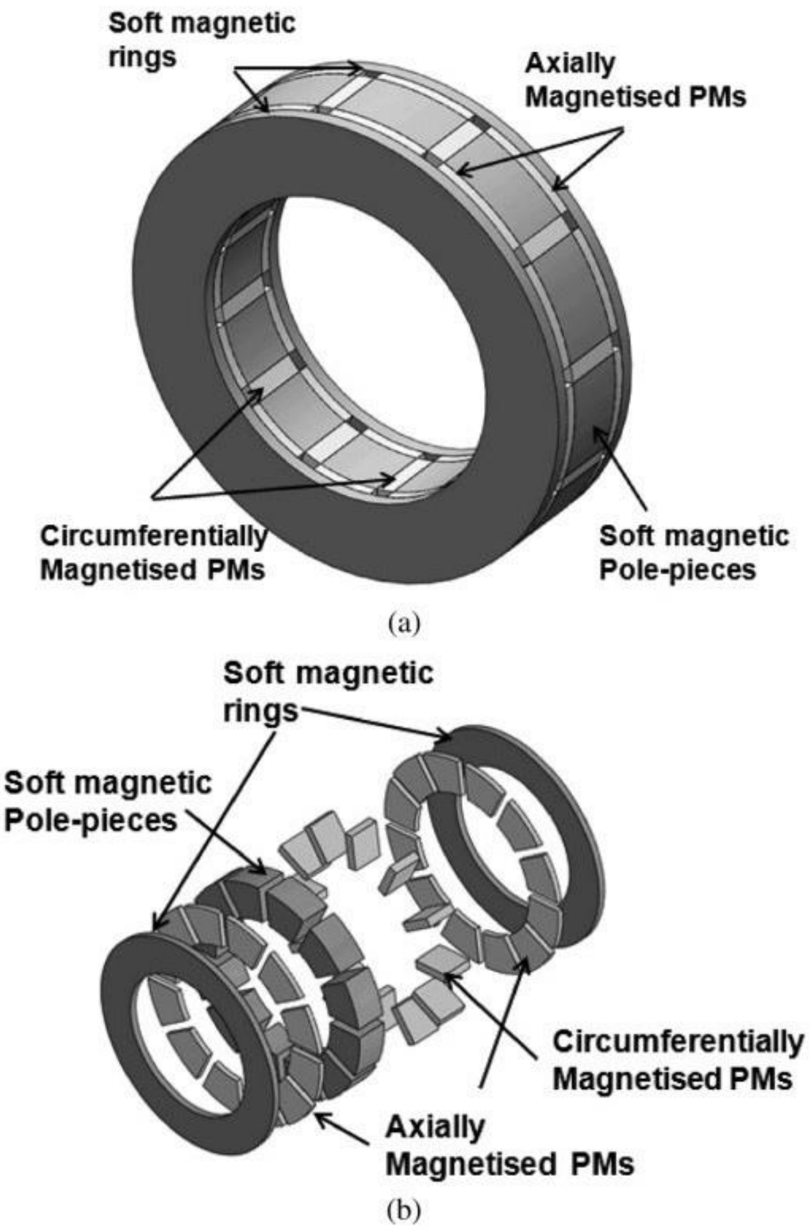

Fig. 1.8 Rotor with axially and circumferentially magnetised PMs (a) Assembled rotor, (b) Exploded view [12].

1.2 PM machines design review: Overview

Many researchers have introduced design and analysis methodologies using the analytical and finite element analysis (FEA) techniques for different topologies of PM machines. This enables key design parameters, such as pole number, PM and stator geometries, slot/pole number combinations etc. to be optimized, and the performance requirements of applications to be met. [7][13][14].

1.2.1 Surface mounted PM machines design

Surface mounted PM brushless machines are widely used in many applications. The definition of surface mounted PM machines comes from the location of the PM, which is fixed, on the surface of the rotor [7]. As shown in Fig. 1.4, there are two types of surface mounted SPM, a) inner rotor b) outer rotor, and the magnets can have radial, parallel or Halbach magnetizations. Simplicity and lower construction cost can be considered the main advantages of the SPM machines. Since, the (L_d, L_q) inductances of the stator windings of this type of machines are equal, the value of the reluctance torque is null. However, despite the mentioned advantages, the Inner rotor SPM machines has disadvantages, due to the location of the PM which make them exposed directly to the armature reaction field causing irreversible demagnetization of magnet which affects the output flux density. In addition, the magnets are exposed to centrifugal forces, which can damage them especially, at high speed. Therefore, this type of PM machine is mostly used in the industrial applications, which require relatively low speed [7], or application where stator banding is tolerated. Since, the instantaneous air gap flux density and torque are very important for obtaining good performance of this type of PM synchronous machines, significant researches have been proposed dealing with the analytical modeling of the instantaneous flux density in the air gap region taking the effect of different design parameters and operating conditions and validated using FEA analysis. The simplest description of the airgap flux density equation, electromagnetic torque-speed characteristics, magnetization and demagnetization process, winding distribution in the stator, iron losses, output power and efficiency have been presented in [6]. Many analytical methods have been developed for calculation the instantaneous magnetic field in the airgap/magnet region and airgap flux density for multi pole, inner and outer rotor radial magnetized slotless brushless

PM motor (SPM), using (2D) analytical solutions in the polar coordinate system. Firstly, on open circuit magnetic field [15], then the effect of stator slot (opening) is investigated, together with the effect of the magnetic field (armature reaction) from the stator winding current [16][17][18]. Another technique for calculating the flux produced by the stator and PM accurately and the airgap flux density in the (SPM) machine using lumped parameter magnetic circuit models as shown in Fig. 1.9, in which reluctance network is used to model the rotor, stator slots, stator yoke and teeth of the machine taking into account of the effect of leakage flux, magnetic saturation, etc. and validate the analytical results for airgap flux density under slot and tooth and the induced phase voltage using FEA and experimental results. [19][20][21].

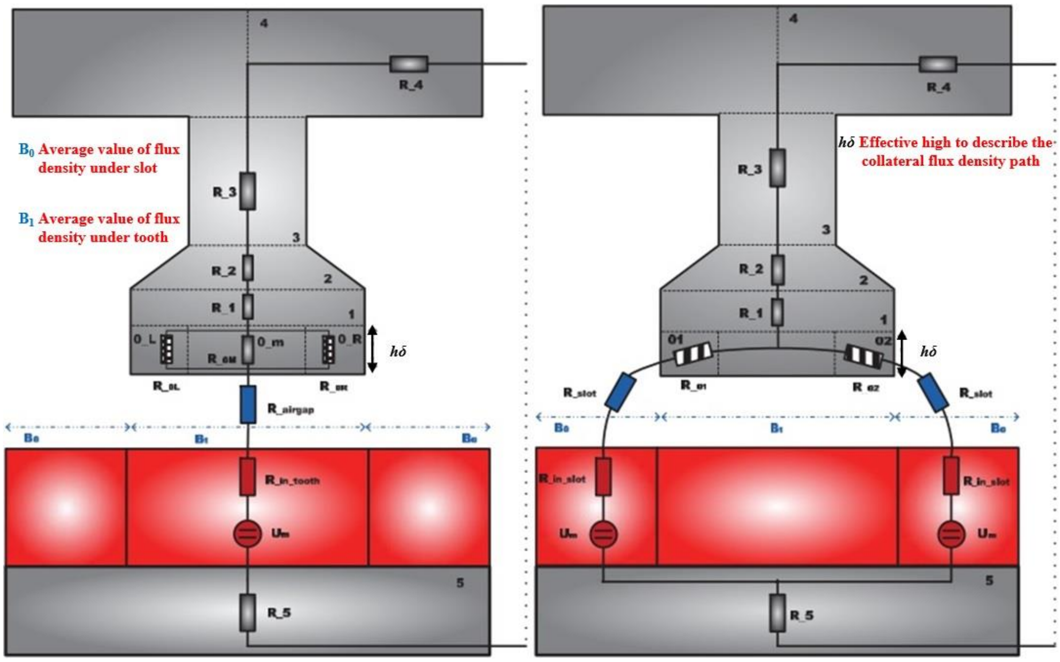

(a) (b)

Fig. 1.9 Reluctance network: tooth and slot region [20].

The shape and position of the magnet (flat magnet) or the classical single curved magnet in the SPM machine play an important role on the value of the fundamental airgap flux density, BEMF and the efficiency of the machines as shown in Fig. 1.10, in which six geometries of NdFeB magnet PM motor with different magnet shape and rotor configurations of internal and external rotor with 36 slots are designed and compared using FEA with respect to their topologies, magnetic field, airgap flux density, torque, losses and efficiency at constant power rate and different speed [22].

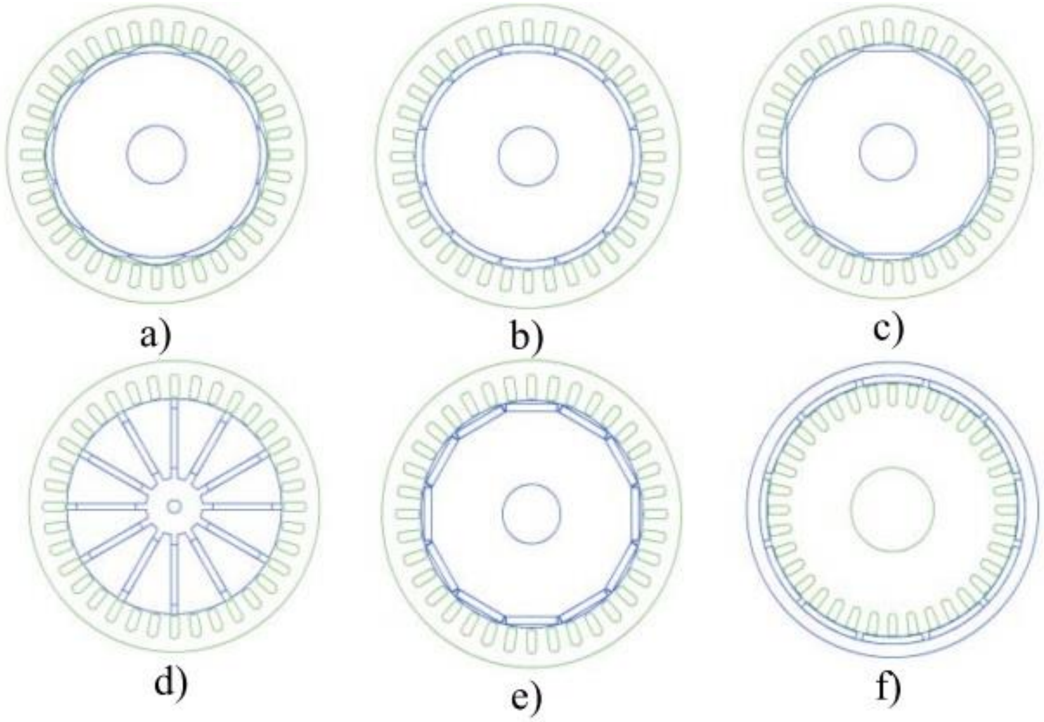

Fig. 1.10 Topologies SPM machine [22]

The material of the PM (Ferrite, SmCo, NdFeB etc.) and the distribution of the stator winding (distributed winding, concentrated winding, non-overlapped and overlapping winding) play an important factor in the losses (copper losses), linkage flux and BEMF harmonics, airgap flux density, fault tolerance, overload capability and the output properties for developing the required power and efficiency and then the cost of the SPM machines [6][8]. The effect of stator tooth length and width is also important and should be considered in the design of the SPM, by optimizing the tooth length and width with combination slot/pole number for getting the BEMF and increasing the linkage flux and achieving higher torque with reduced ripple torque [17][23]. The operation of the SPM motor and overload may cause mechanical damage for the machine; the mechanical torque will be high and can cause unsafe operation especially, when used in critical applications. To avoid high mechanical torque and overload, new topology for brushless permanent magnet motor equipped with all integrated magnetic torque limiter is designed by using two rotor each one carries a set of PM in order to achieve torque limiter capability without significantly affecting the size/weight [24]. For electric vehicle applications, the high power/torque density, high efficiency and good flux weakening capability are very important to satisfy the required characteristics and the reference driving cycles such New European Driving Cycle (NEDC). Therefore, a new topology of SPM machines with concentrated windings has been designed and optimized as shown in Fig. 1.11, taking into account the effect of different key parameter such as: slot-pole number, machines inductance, axial length, tooth width, stator back iron thickness, inner to outer diameter ratio and pole, pole pitch ratio and number of turn to meet the desired specifications [25].

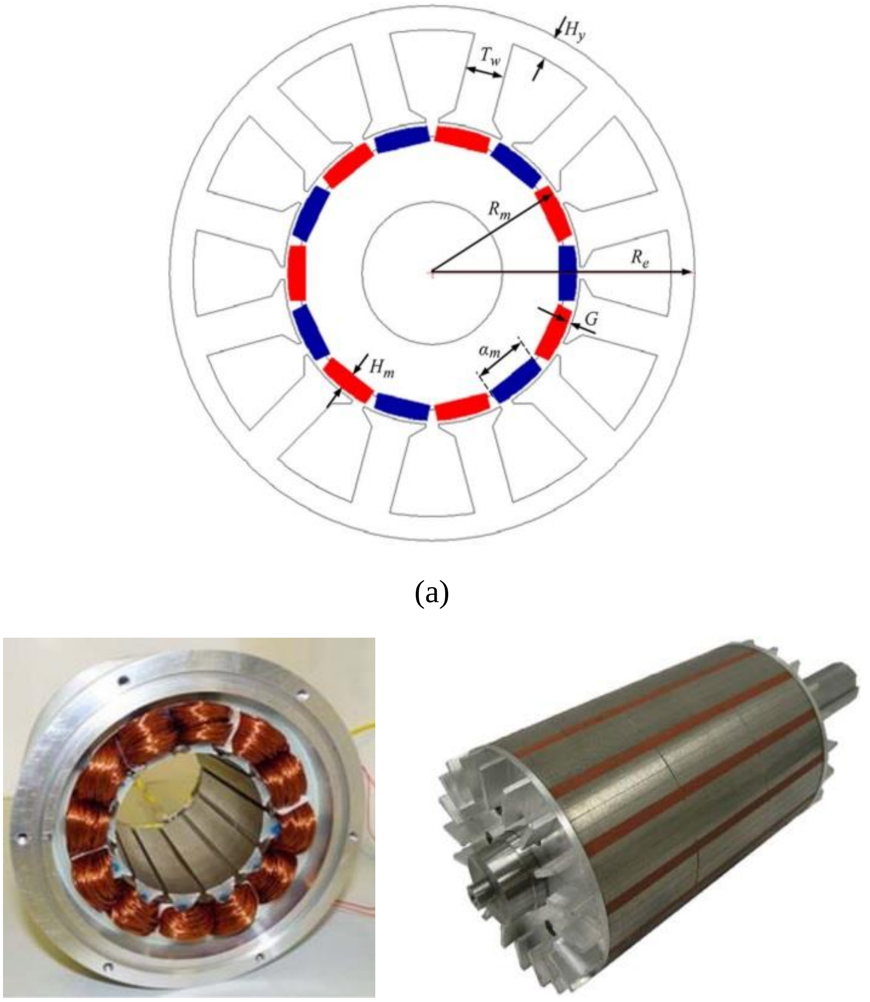

(a)

(b) (c)

Fig. 1.11 A new SPM motor topology a) Schematic of leading design parameter, b) Stator. c) Rotor [25].

1.2.2 Inner PM Machines design

The definition of inner PM comes from the location of the PM, which is buried into the rotor iron core. There are different types of inner PM machines depending on the position of magnet such as: V-shaped PM machines, W-shaped, segmented PM, spoke- rotor type etc.[8][9]. Each type has different properties which have been studied, and analyzed by many researchers in order to optimize the generated airgap flux density, torque production and efficiency [26][27]. This type of PM machines has many good features compared with SPM, since the PM is fixed inside the rotor, this make it robust and suitable for hybrid electric vehicle (HEV) [28][29][30]. Since it has a good torque smoothness, reliability and efficiency, IPM motor also used in the electrical power steering [31]. Due to the saliency of the rotor, the value of (L_d, L_q) inductances are not equal, this will increase the value of torque ripple which can be considered one of the main factors affecting the output characteristics of the machine (vibration, noise and losses) [32][33]. Therefore, this factor has been analyzed and calculated using different analytical techniques such as: (2-dimensional) equivalent magnet circuit which can be used for general synchronous machine and it's useful for the first step before using (FEA) [34][35]. Then, validate the analytical results using FEA techniques and experimental prototypes. Many constraints should be considered and analyzed in the design of IPM machines such as: air gap length, leakage flux at machines shaft for getting high linkage flux and airgap flux density [36][37][38]. To decrease the effect of the generated leakage flux, an auxiliary magnet with different thickness of rare earth magnet has been added to the rotor of new IPM geometry, which affects the air gap flux density as shown in Fig. 1.12 [39].

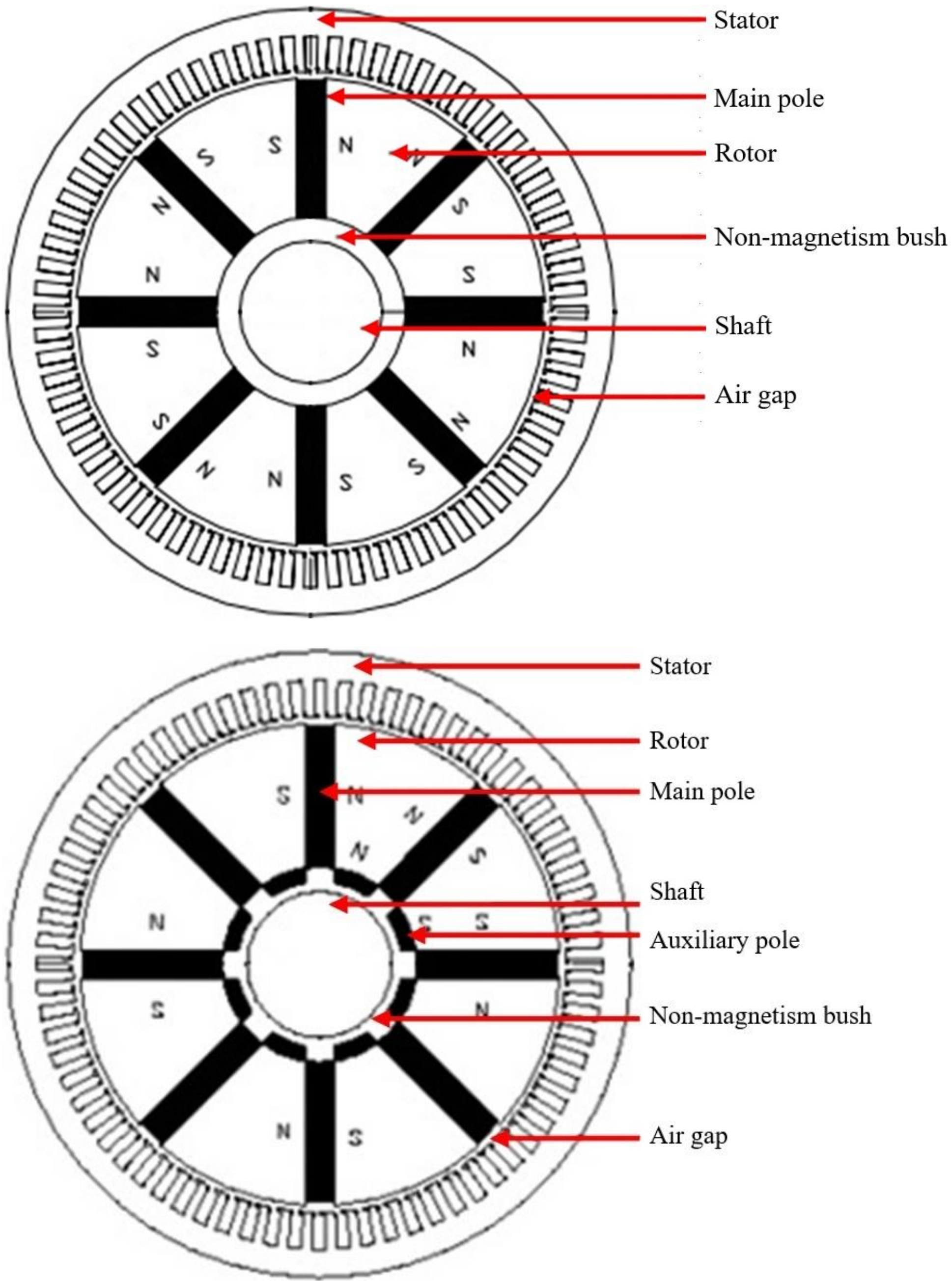

Fig. 1.12 Structure of the optimised spoke-type rotor PM machines [39].

To get a high air gap flux density and maximum torque which result in increased efficiency for the machine, the optimization of split ratio (Ratio of stator bore to outer diameter), and the winding type, should be considered in the design of IPM machines [40]. Pushing assistant and sub assistant ferrite PMs in the design of spoke rotor type can be considered on the novel method to maximize the torque density, air gap flux density and BEMF, with low cost compared with the initial IPM made of neodymium PM., as shown in Fig. 1.13 [41], in which new model of spoke-type rotor PM machine called (wing shaped spoke-type motor) is designed and analyzed using FEA and analytical model. The output characteristics such as BEMF, airgap flux density and torque are compared with other geometries so as to get novel reliable machine.

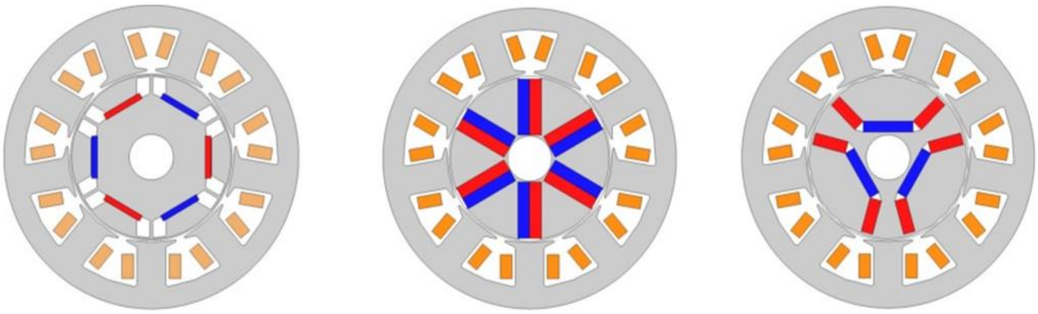

(a) Initial IPM-type motor (b) Spoke-type motor (c) V-type motor

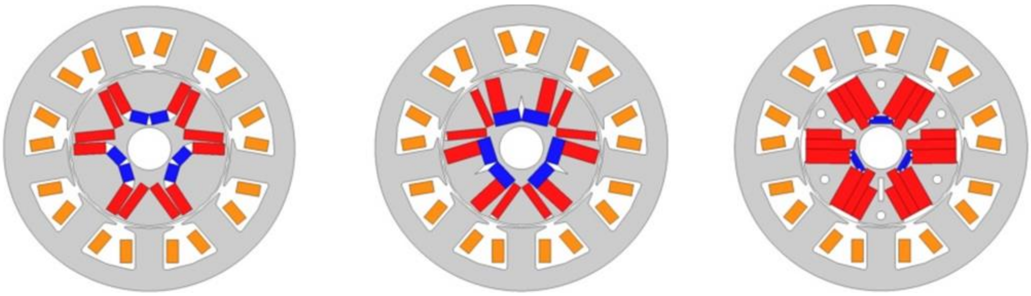

(d) U-type motor (e) Wing-type motor (f) Wing shaped spoke-type motor

(i) Initial and analyzed models

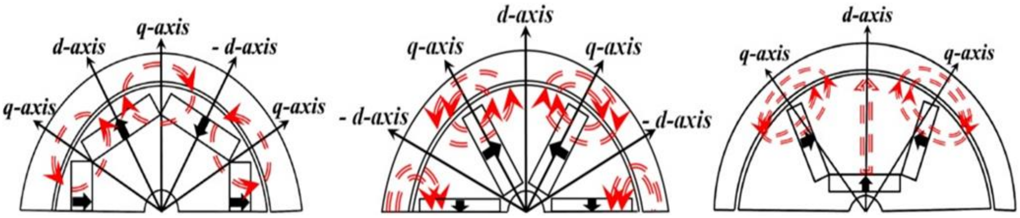

(a) IPM-type motor (b) SPOKE-type motor (c) V-type motor

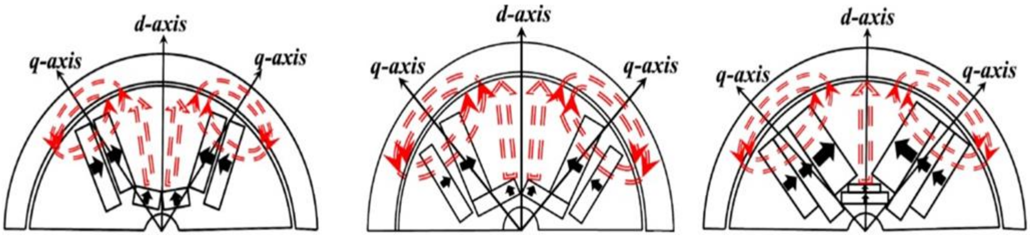

(d) U-type motor (e) Wing-type motor (f) Wing shaped spoke-type motor

(ii) Magnetic characteristics of the analyzed models

Fig. 1.13 Structure of different motors [41].

Since using 3D-FEA is still time consuming in simulating and analyzing the magnetic characteristics of the permanent magnet machines, an analytical model based on lumped circuit parameter model has been used to analyze a hybrid excitation synchronous machines and then compare the results with (3D-FEA) to optimize and build the prototype as shown in Fig. 1.14 [42]. The complete description of reluctance modeling of machines will be detailed in chapter 4 of the thesis.

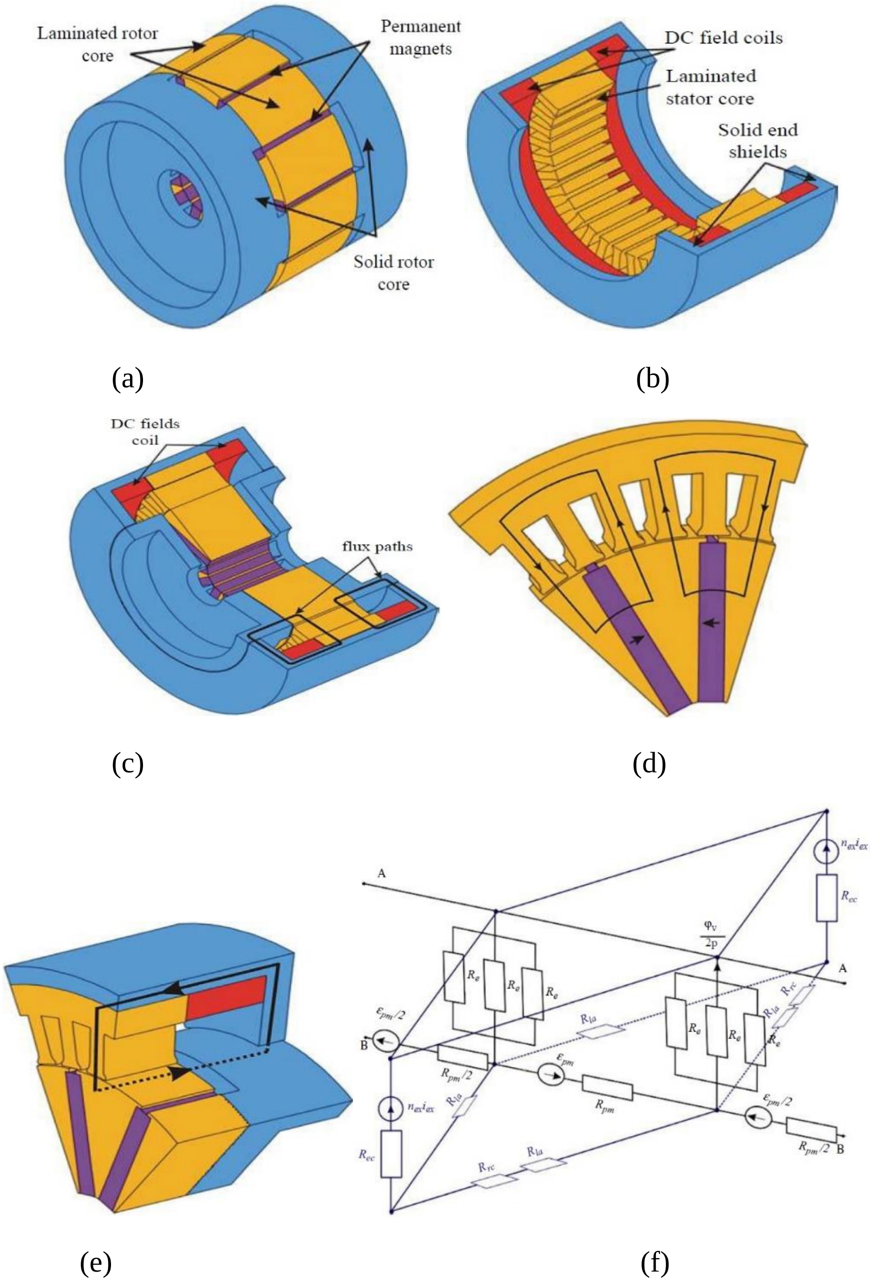

Fig. 1.14 Structure of hybrid excitation synchronous machine and its lumped circuit parameter model.

The nonlinear phenomena such as: cross coupling magnetic saturation, stator slotting effect has been taken into account in the calculating airgap flux density, back EMF, phase (d-q inductance), and torque of the interior PM motor by proposing specific lumped parameter magnetic circuit model (MCM), which can be applied in general for different types of rotors and stators of the IPM machines under both no-load (NI=0) and loaded (with external excitation) operation [43][44].

The effect of the material properties and the dimensions (length, thickness and the angle between the interior permanent magnets, auxiliary magnets) of the ferrite magnet used in the design of different type of the IPM machines is important, especially for spoke-type rotor machines. Therefore, it is analyzed in order to decrease the cogging torque and get a good flux concentration, by proposing a new spoke-type rotor BLDC motor as shown in Fig. 1.15, in which the inner magnet is divided with different adjusted angle in between so as to change the length and thickness of the magnet which cause variation of the ripple and cogging torque values [45].

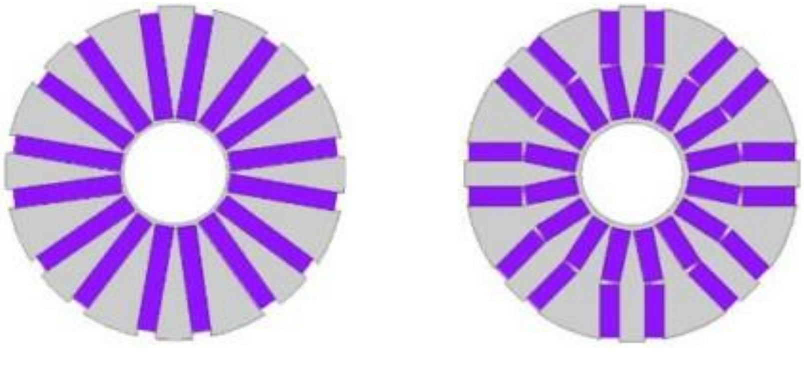

(a) Model 1 (b) Model 2

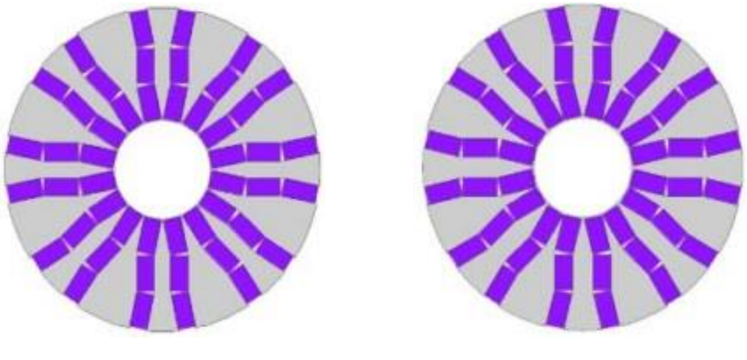

(c) Model 3 (d) Model 4

Fig. 1.15 Variable spoke-type BLDC motor models [45].

The eccentric shape of the pole pieces and the steel core between the splitted PMs plays a significant role on the electromagnetic performance of the spoke-type rotor machines. As shown in Fig. 1.16 the pole pieces of model (b) are eccentric in the shape causing the airgap length is larger than model (a). Beside that the pole pieces are not symmetric and having different thickness which will have an important effect on the generated BEMF, L_d and L_q values and their difference at different rated current [46].

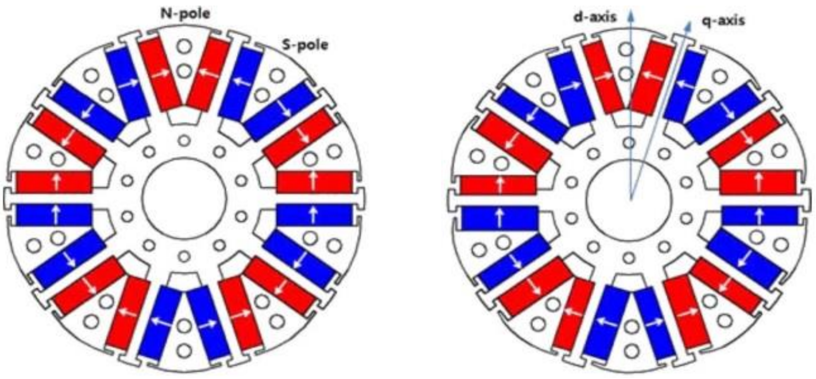

(a) (b)

Fig. 1.16 Rotor configuration of spoke-type rotor FMM [46].

Comparing with conventional spoke-type rotor machines, inserting auxiliary PMs have a significant effect on the magnetic field distribution and the output characteristics such as BEMF and torque waveforms. As shown in Fig. 1.17, four geometries of spoke-type rotor PM machines model (b), model (c), model (d) and model (e) are proposed and analyzed with auxiliary radial magnetized PMs. Comparing with model (a), the results show that model (b) and model (d) have less PM volume with improved electromagnetic torque and BEMF [47].

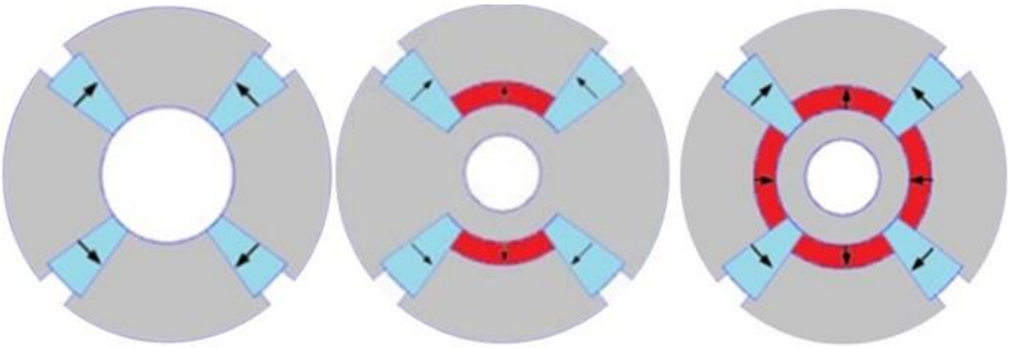

(a) Model 1 (b) Model 2 (c) Model 3

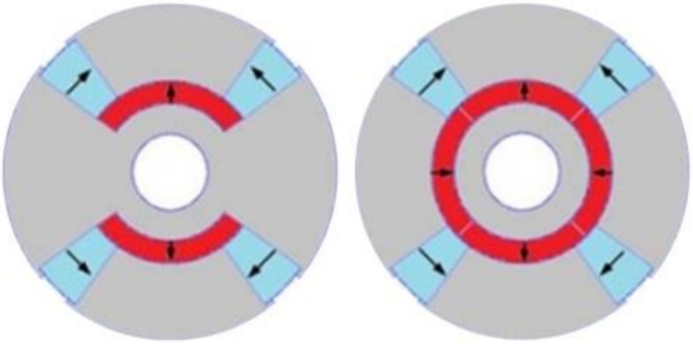

(d) Model 4 (e) Model 5

Fig. 1.17 Topologies of spoke-type PM machines [47].

Since the influence of magnetic saturation and cross coupling between the magnetic fields generated from the PM and the armature winding is very important in the calculation of the average electromagnetic torque and its components such as reluctance torque generated in the PM machine, a method has been used for separation the components of the torque using the concept of frozen permeability [48][49]. A detailed complete description of the frozen permeability concept will be in chapter 3 of the thesis.

The material of the motor iron core plays an important role in getting higher value of linkage flux with less losses, such as using (soft magnetic composite) (SMC) over the conventional silicon steels of the core in the design of the spoke rotor type PM motor [50].

1.2.3 Axial flux PM machines design

Since the generated magnetic field in this type of PM machines is parallel to the rotational axis (shaft axis), it is called axial flux PM machines. AFPM machine has many features which make it an important alternative technology used in different modern applications such as Joint modules for robot, instead of radial flux PM (conventional) machines, as shown in Fig. 1.18 in which a new AFPM motor has been proposed since it has high torque with short axial length [51][52].

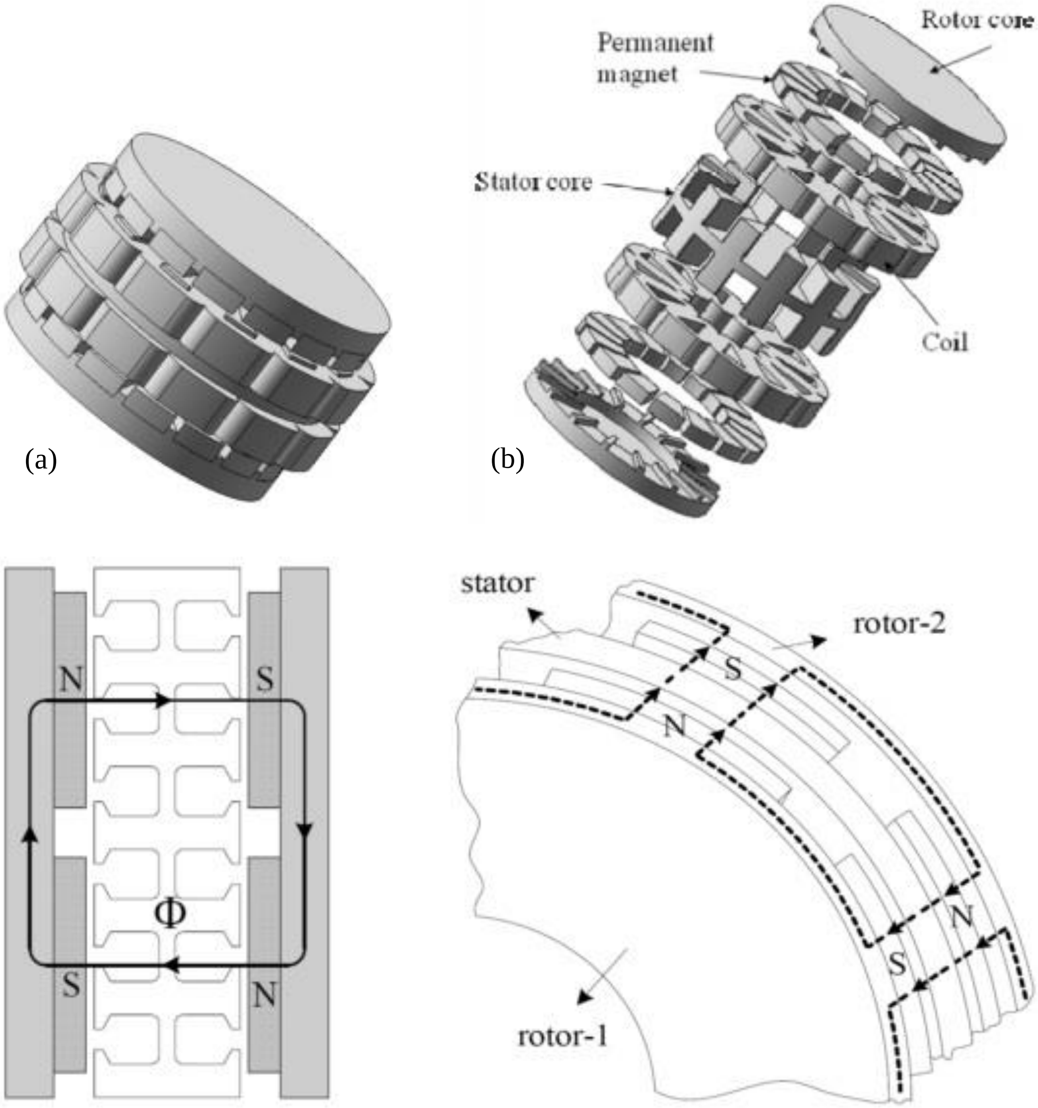

(a) (b)

(c) (d)

Fig. 1.18 New AFPM motor topology [51].

Comparing with RFPM machines, higher torque to weight ratio can be achieved since AFPM machines has less rotor core material and exhibit less rotor iron and copper losses [10][53]. To maximize efficiency and torque, many aspects of construction, electromagnetic design should be evaluated by using sizing equation, and/or FEA [11]. This can be done by using 3D-FEA techniques [54][55], as shown in Fig. 1.19, in which twenty-eight pole, three phase AFPM motor has been simulated and analyzed by 3D-FEA software, such as Flux3D, since it provides an accurate analysis of the magnetic devices taking into account geometric details and nonlinearity of magnetic characteristics.

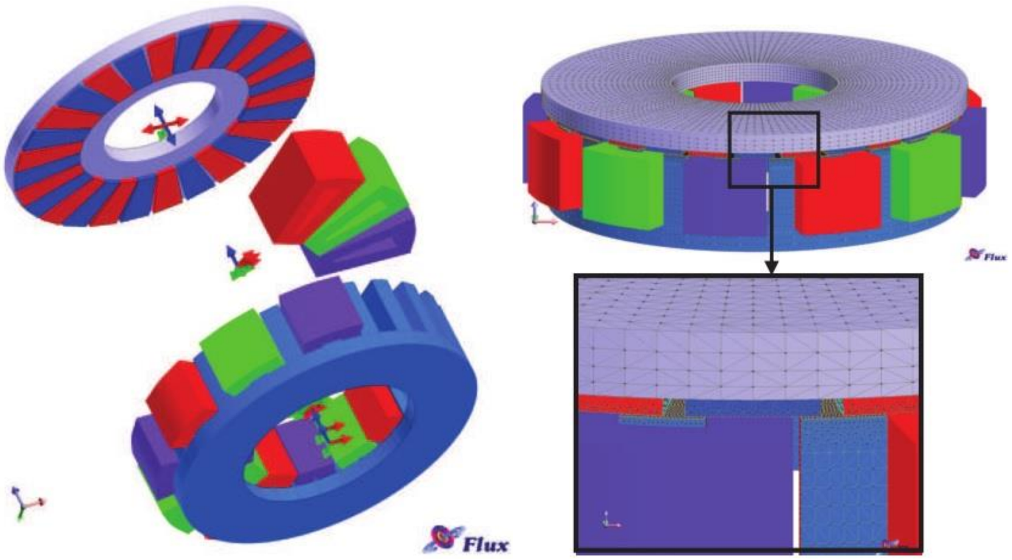

(a) (b)

Fig. 1.19 a) 28 pole AFPM motor, b) Three-dimensional mesh model, c) Distribution flux density in the stator [54].

Using sizing equations, a slotted (TORUS) (AFPM) motor has been designed for electric vehicles [56]. Like the radial flux PM machines, the effect of PM thickness on the machine output characteristic, flux distribution and air gap flux density is important and has been be considered [57], as shown in Fig. 1.20, in which a novel Six-phase with (22 poles and 24 slots), one-rotor-two-stators disc PMSM has been designed and simulated using FEA.

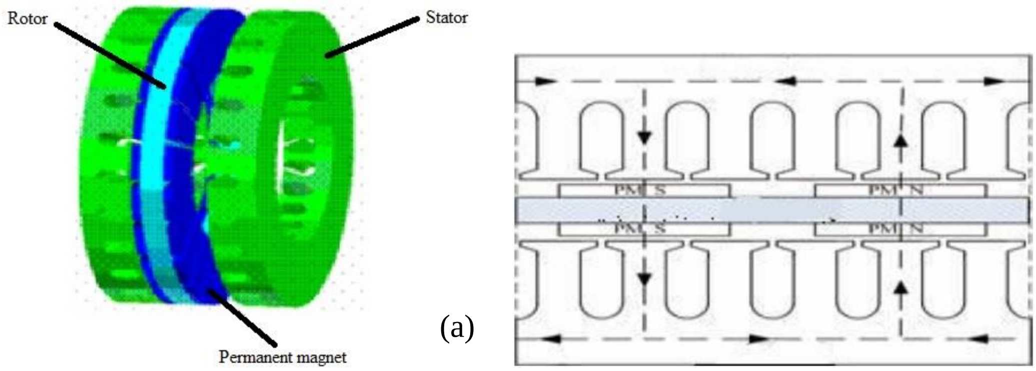

(a)

(b)

Fig. 1.20 a) Basic structure of disc PMSM, b) prototype and stator slots and winding [57].

The permeability of the permanent magnet, the finite permeability of iron has been accounted in the analytical calculation for the air gap flux density, back EMF and torque for (micro slotless axial flux permanent magnet motor (AFPM)), resulting in a quick way of determining and optimizing the performances of a slotless axial flux motor [58]. Air gap variation or (air gap deformity) due to the displacement of rotor from original position influences on the flux density and then the axial magnetic force between the stator and rotor of surface mounted axial flux permanent magnet motor (AFPM), which cause the bearing damage, reduce lifetime of the motor and cause vibration for the motor [59], as shown in Fig. 1.21.

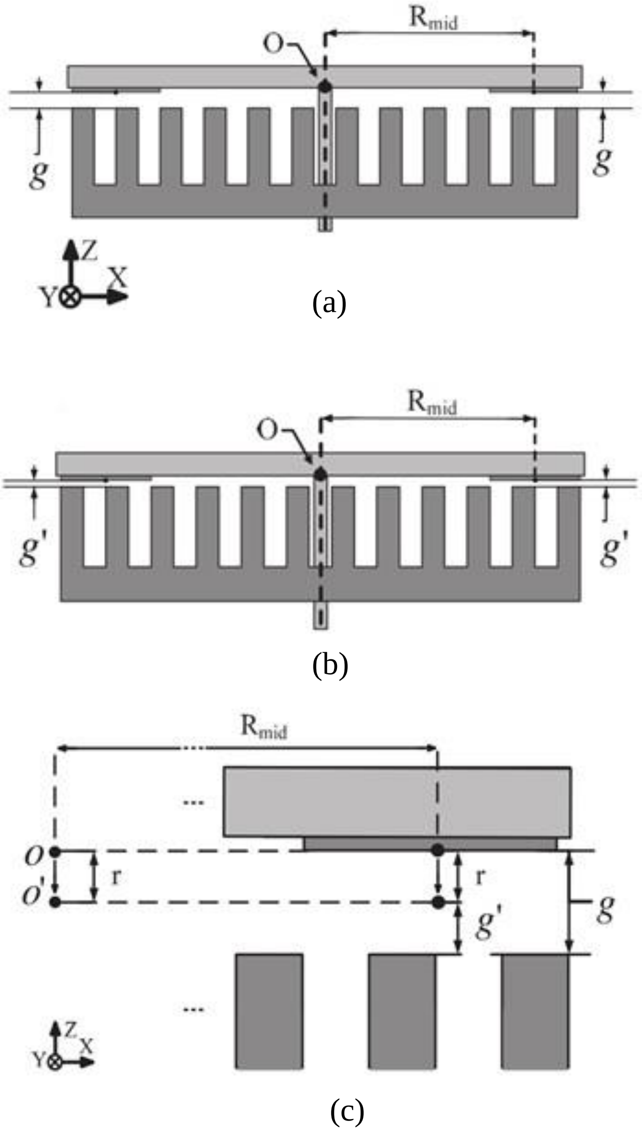

Fig. 1.21 Representation of rotor displacement in AFPM motor, a) healthy motor b) motor with airgap deformity. c) Representation of airgap displacement.

The effect of material of the used PM on the airgap flux density of AFPM machines and active length to rotor diameter ratio has been analyzed using the lumped parameter magnetic circuit model and compared with the results obtained with (3D-FEA) [12]. Since the effect of stator slot opening on the flux in the airgap is considerable, it has been analyzed and compared with FEA [60].

1.2.4 Summary

This chapter introduced a review about the design and analysis methodologies for different topologies of PM machines which are presented by many researchers, focusing on the effect of most important key design parameters such as of pole pairs number, rotor and stator geometries, distribution of stator windings, slots poles number, airgap length, stator active length ,PM geometry (length and thickness) etc. Using analytical and FEA techniques to investigate the electromagnetic performance of the machines and validate the output characteristics such BEMF, electromagnetic torque, cogging torque, phase voltage and airgap flux density with experimental results.

The definition and the properties of the main three types of the PM machines: SPM, IPM and AFPM machines is introduced and the investigation about the construction and the application of each type is presented considering the key design parameters mentioned above. Therefore, it employed an initial step in the design of PM machines.

Outline of this thesis

The work in each chapter of this thesis is as follows:

Chapter 2 - Investigation and design of different PM machines, the comparison between two PM rotor types has been introduced, these are the conventional IPM-Spoke type rotor and newly proposed rotor, equipped with axially and circumferentially magnetized PMs. The effects of different parameters, such as airgap length, pole number, pole arc to pole pitch ratio and the ratio of active inner to outer diameter of the rotor has been investigated using FEA and lumped parameter circuit model.

Chapter 3 - Design of axially and circumferentially magnetized PM machine to meet the requirements of a small personal mobility vehicle. In this chapter (3D) finite element method is the main method used for the design and analysis and the prediction of the BEMF, the output torque, efficiency etc. for different load condition.

Chapter 4 – Development of a new lumped parameter circuit model and evaluation of the machine characteristics, such as winding linkage flux and BEMF, torque etc. and compare the results with (3D) finite element at no load and full load conditions.

Chapter 5 – Description of the different components of the machine, and description of the methods adopted for the realization of the prototype and the test undertaken. The results are compared with prediction (3D-FEA).

Chapter 6 – Conclusion and recommendation for future work.

Chapter 2

An Investigation and design of different rotor PM machines

2.1 Introduction

In this chapter, a comparison between two PM rotor types is introduced, these are the conventional IPM Spoke-type rotor and newly proposed rotor, supplied by axially and circumferentially magnetized PMs. The procedure used for building the geometry of IPM machines (spoke-type rotor), slotless stator using 2D finite element flux software is introduced, and the values of the airgap flux density are compared with the analytical values derived using a simple lumped parameter magnetic circuit. The new PM rotor topology is introduced and modelled using 3D finite element and results are also compared with predictions from a lumped parameter magnetic circuit. A comparison between the two rotor topologies and the effects of different parameters are investigated, these are airgap length, pole number, pole arc to pole pitch ratio and the ratio of active inner to outer diameter of the rotor.

2.2 Spoke-Type Rotor

This section deals with the investigation of the performance IPM rotor, more specifically, a spoke-type rotor with slotless stator using (2D) Flux software. The purpose is to investigate the effect of parameters which include: airgap length, pole number, pole arc to pole pitch ratio and the ratio of active inner to outer diameter of the rotor on the airgap flux density and compare the finite element predictions of the airgap flux density with the analytical values from a simple lumped parameter magnetic circuit. The geometry and the parameters of the spoke-type rotor PM machines for different number of poles are shown in Fig. 2.1 and Table 2.1.

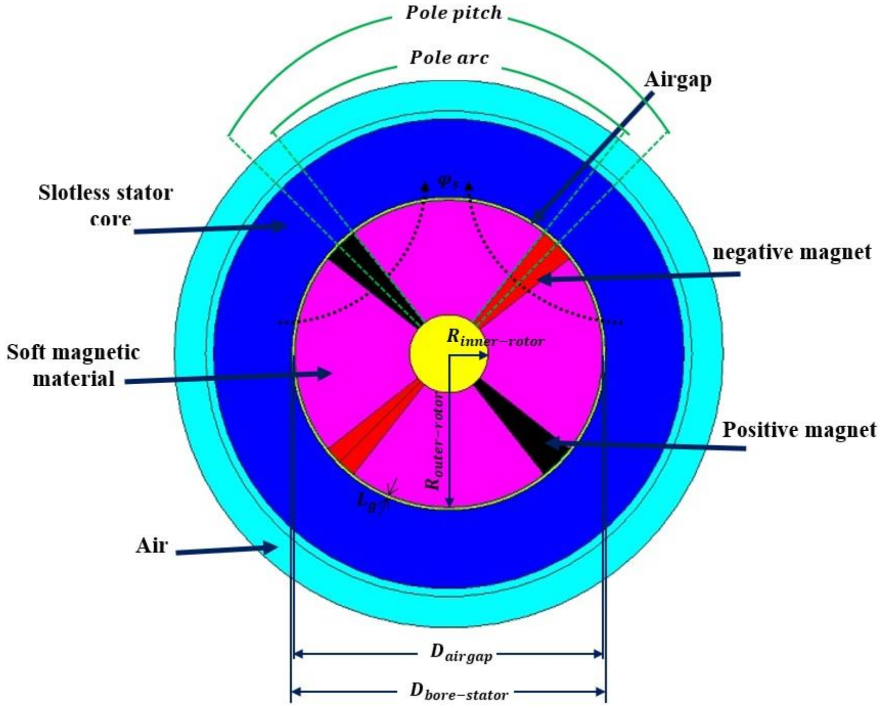

(a) 4 poles/slotless IPM machine

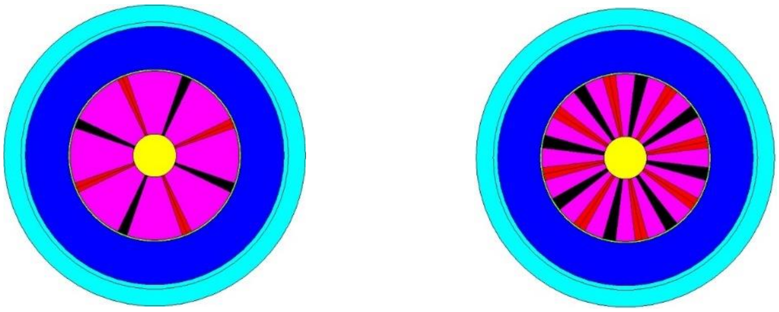

(b) 8 poles/slotless IPM machine (c) 16 poles/slotless IPM machine

Fig. 2.1 IPM Spoke-type rotor geometries

Stator active axial length	L_{axial} (mm)	30 mm
Airgap diameter	D_{airgap} (mm)	200 mm
Stator outer diameter	$D_{outer-stator}$ (mm)	300 mm
Number of poles	P	4, 6, 8, 10, 12, 14, 16, 18, 20
Airgap length	L_g(mm)	0.5 mm
Permanent magnet type		Ferrite
Remanence of permanent magnet	B_r(T)	0.39 T
Relative permeability	μ_r	1.2

Table 2.1 Parameter of the spoke-type rotor PM machine.

The flux per pole for spoke-type PM rotor is derived using equation Eq. 2.1, derived from the lumped parameter magnetic circuit in which the magnets are represented by MMF source F_m and reluctance R_m connected in series as shown in Fig. 2.2 [12][61].

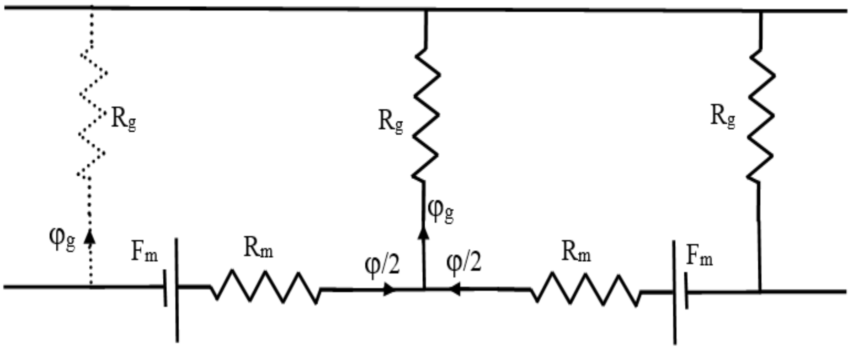

(a) 1- pole-pair shown

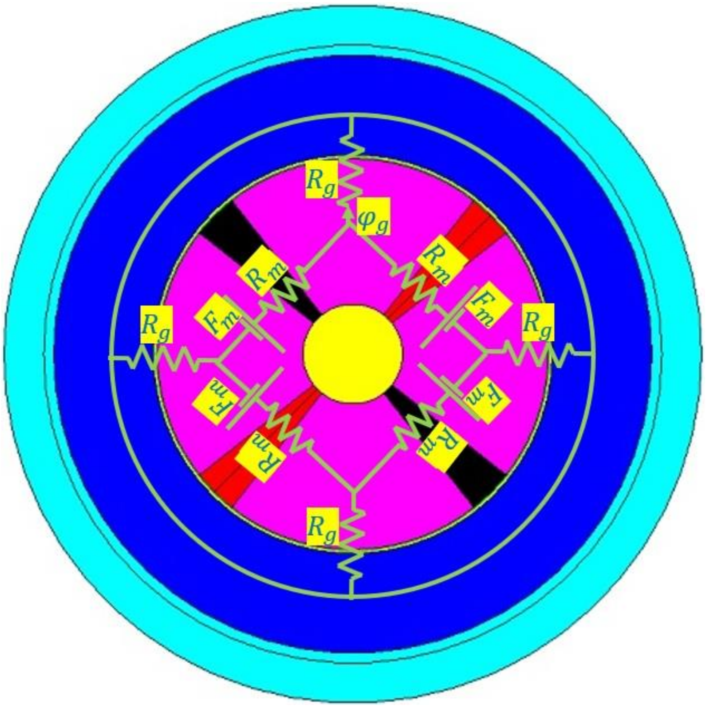

(b) Full geometry

Fig. 2.2 Lumped parameter magnetic circuit for spoke-type rotor

$$\varphi_g = \frac{F_m}{\left(\frac{1}{2}R_m + 2R_g\right)} \tag{2.1}$$

Where:

$$F_m = B_r \frac{L_m}{\mu_r \mu_0} \tag{2.2}$$

$$R_m = \frac{L_m}{\mu_r \mu_0 A_m} \tag{2.3}$$

$$R_g = \frac{L_g}{\mu_0 A_g} \tag{2.4}$$

The variation of the flux per pole with the ratio of the inner to outer diameter of the spoke-type rotor which is predicted using 2D-FEA and lumped parameter magnetic circuit is shown in Fig. 2.3, It can be noticed that the ratio of the inner to outer diameter of the rotor has a significant effect on the resulting flux per pole.

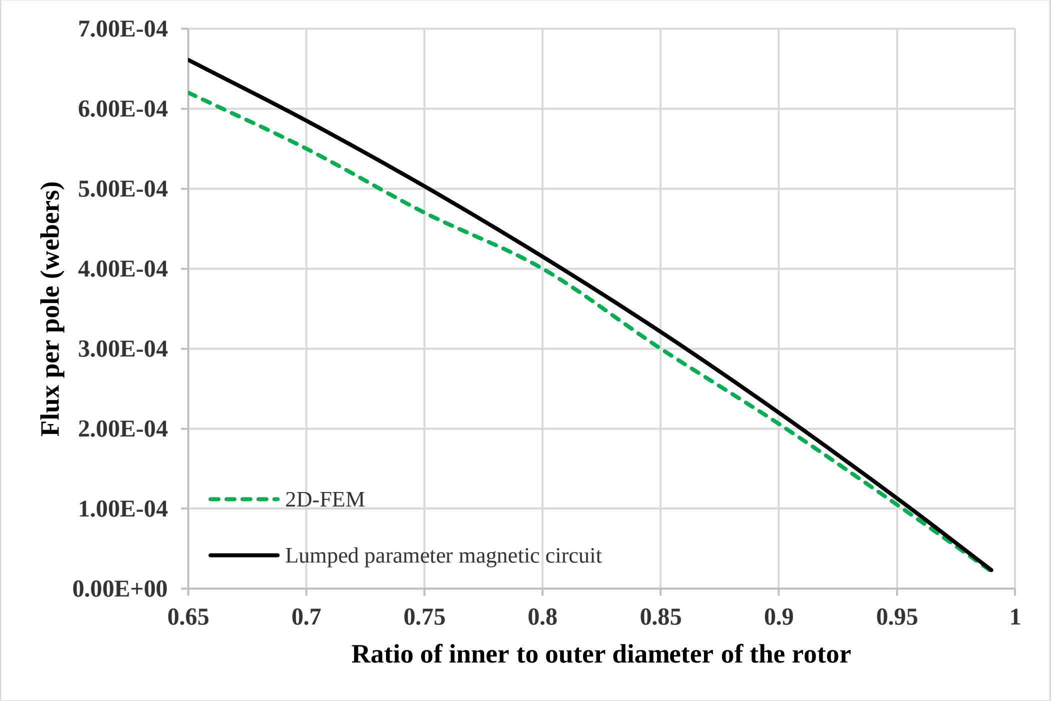

Fig. 2.3 Variation of the Flux per pole with the inner to outer diameter ratio of the spoke-type rotor for (12 pole, pole arc to pole pitch ratio = 0.8, L_g= 0.5 mm and stator active length = 30 mm).

Fig. 2.4, shows the variation of the fundamental airgap flux density for slotless stator with airgap length. At fixed stator inner diameter D_s when airgap length increases, the dimensions of the magnets of spoke-type rotor machine will be reduced causing reduction of the per pole flux and then B_g will be reduced. The fundamental value of the airgap flux density is:

$$B_1 = \frac{4}{\pi} B_g \sin\left(\alpha \frac{\pi}{2}\right) \qquad 2.5$$

It can be seen that the airgap length has a significant effect on airgap flux density. Fig. 2.5, shows the variation of the fundamental airgap flux density for slotless stator with different number of poles at different airgap length, using both lumped parameter magnetic circuit and 2D-FEA. It can be seen that for each airgap length, a pole number exist for which the value of fundamental airgap flux density is maximum.

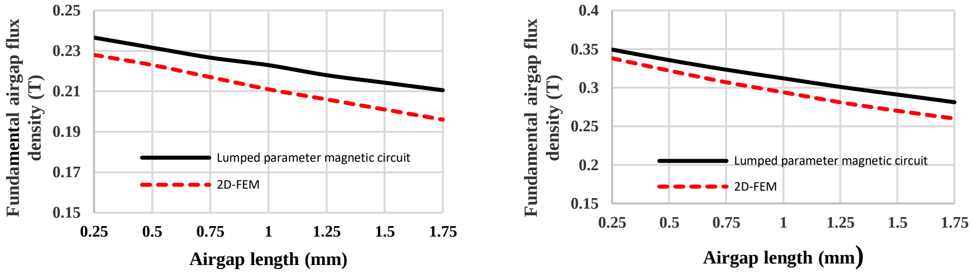

(i) 4 Poles (ii) 6 Poles

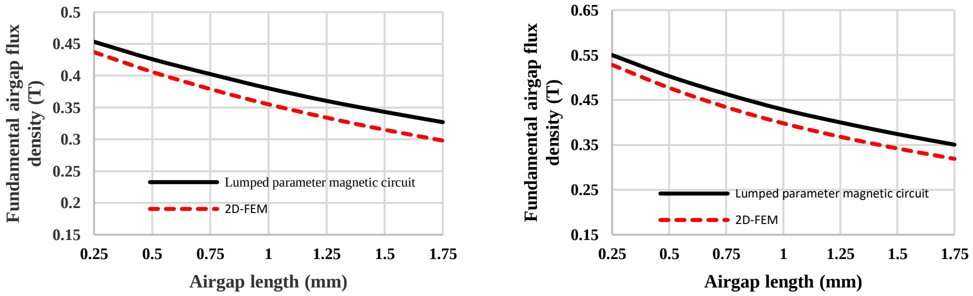

(iii) 8 Poles (iv) 10 Poles

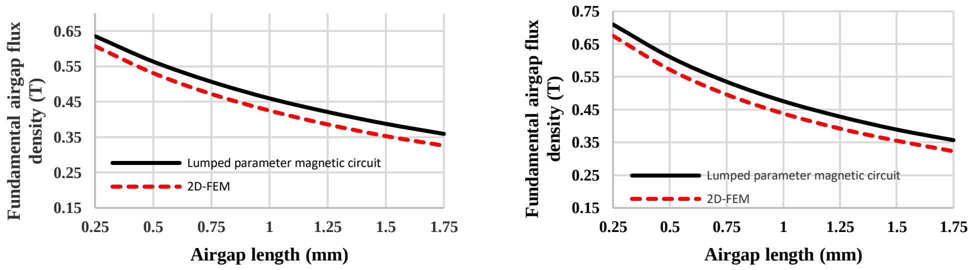

(v) 12 Pole (vi) 14 Pole

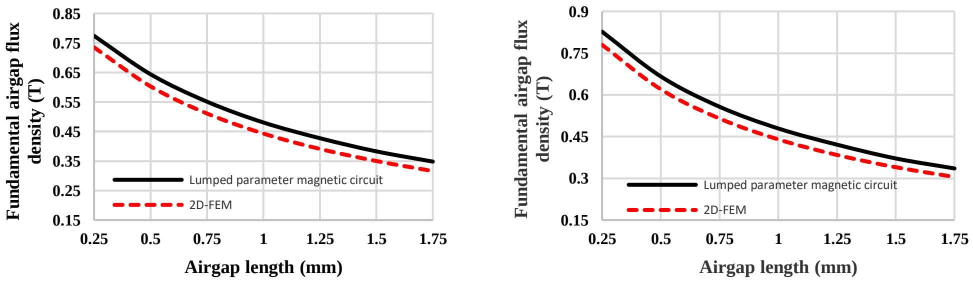

(vii) 16 Pole (viii) 18 Pole

Fig. 2.4 Variation of the fundamental airgap flux density with airgap length

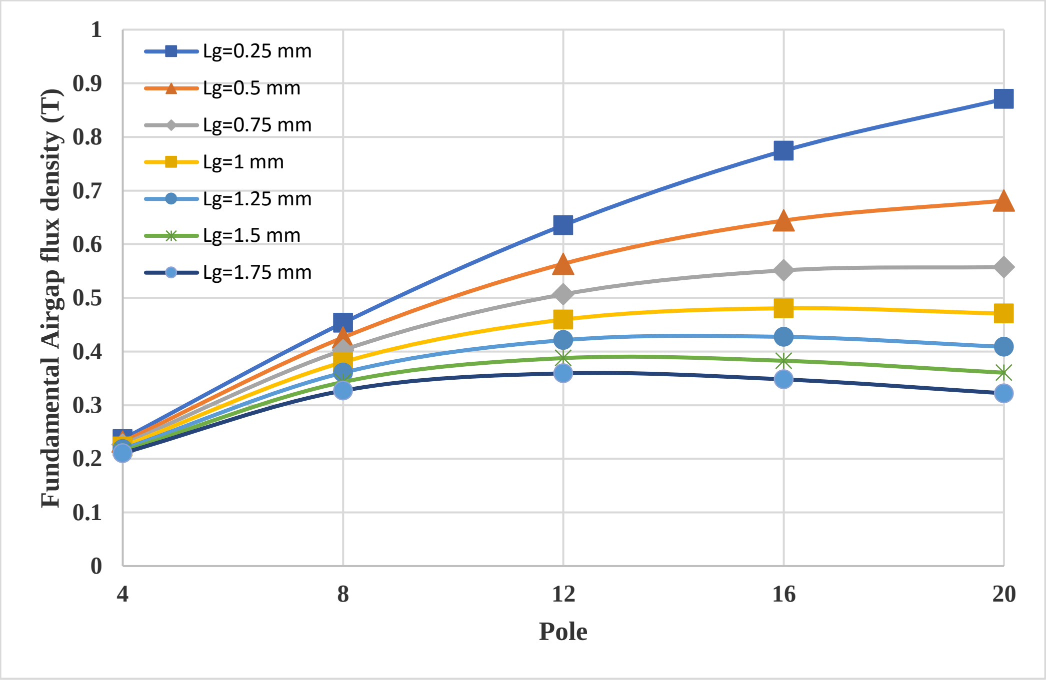

(i)

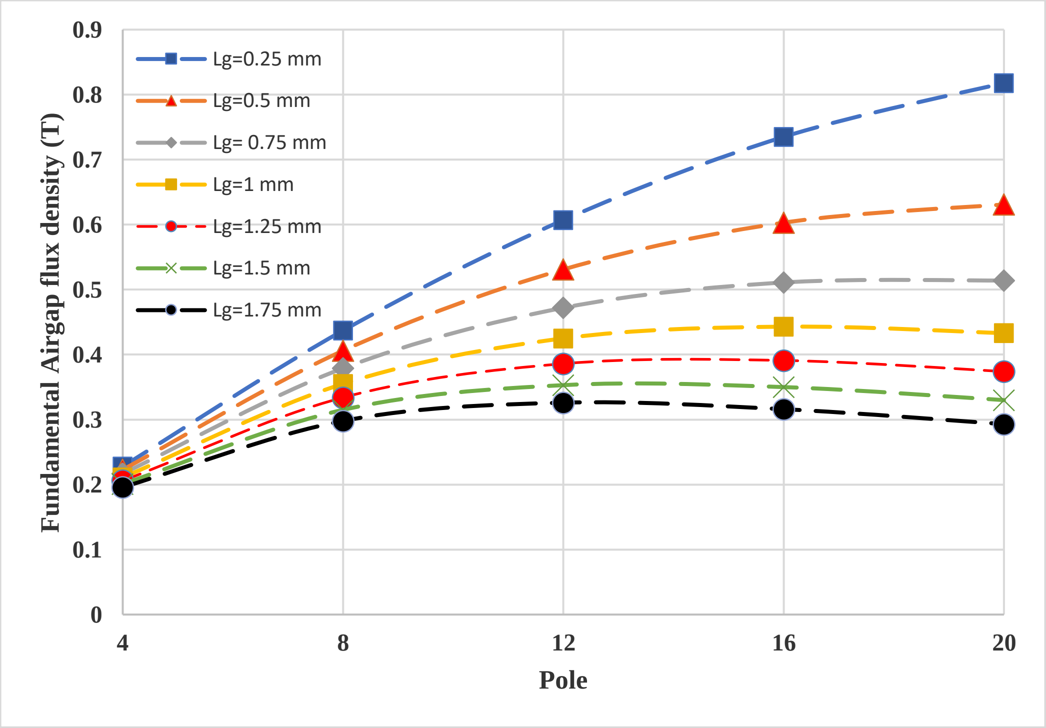

(ii)

Fig. 2.5 Variation of the fundamental airgap flux dentistry with number of poles for (Pole arc to pole pitch ratio =0.85, inner to outer rotor diameter ratio=0.66 and active length= 30 mm). (i) Lumped parameter magnetic circuit, (ii) 2D-FEA.

The effect of the pole arc to pole pitch ratio of the magnet (α) shown in Fig. 2.1, on the fundamental airgap flux density is shown in Fig. 2.6. The value of the fundamental airgap flux density is decreased when α increased, this due to the reducing of the magnet thickness L_m. Fig. 2.7 shows the effect of number of poles, where it can be seen that it has a significant effect on the achievable airgap flux density**.**

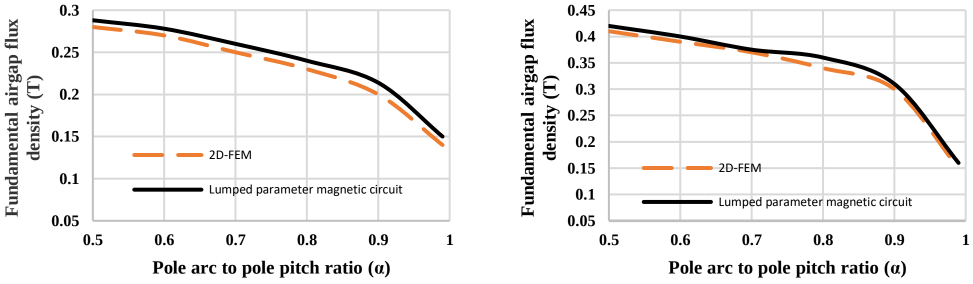

(i) 4 Poles

(ii) 6 Poles

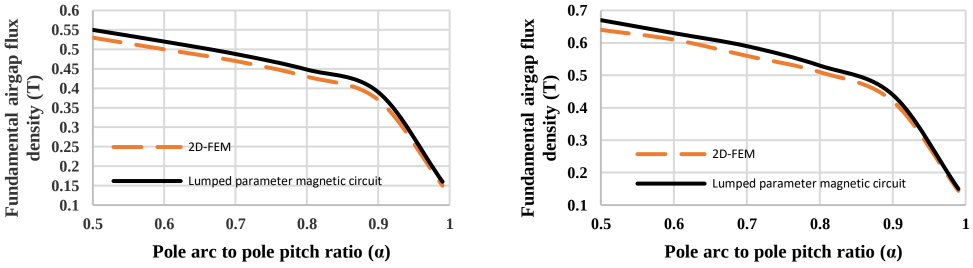

(iii) 8 Poles

(iv) 10 Poles

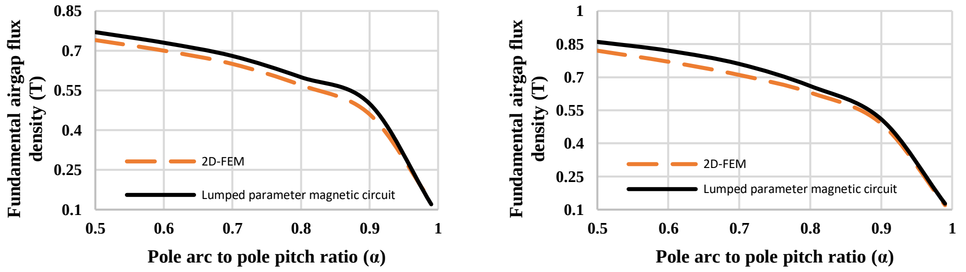

(v) 12 Pole

(vi) 14 Pole

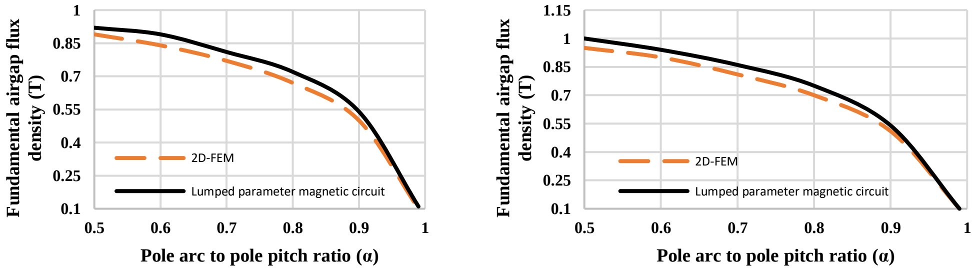

(vii) 16 Pole

(viii) 18 Pole

Fig. 2.6 Variation of the fundamental airgap flux density with the pole arc to pole pitch ratio of the magnet.

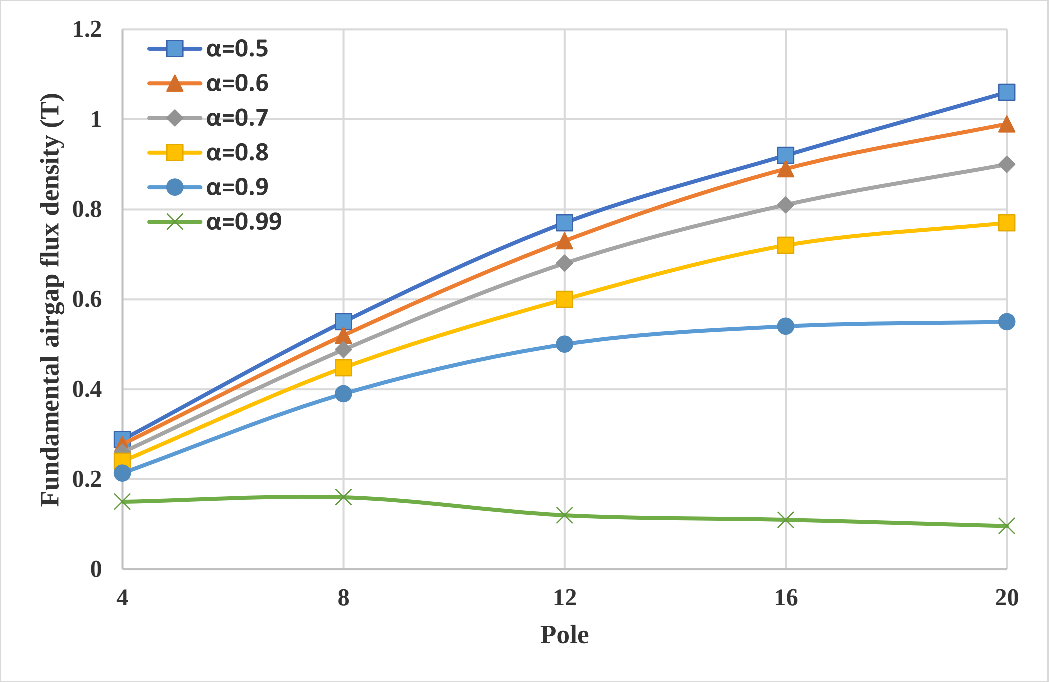

(i)

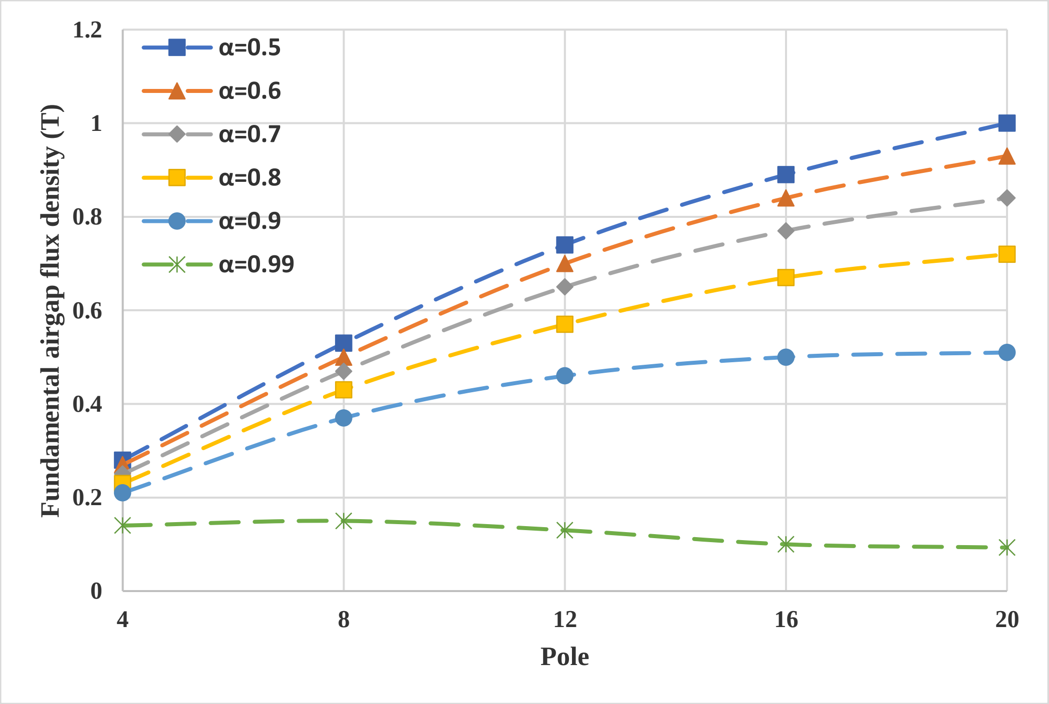

(ii)

Fig. 2.7 Variation of the fundamental airgap flux density with number of poles for (L_g= 0.5 mm, inner to outer rotor diameter ratio=0.66 and active length= 30 mm). (i) Lumped parameter magnetic circuit, (ii) 2D-FEA.

The dimensions of the magnets used in the machines will be changed if the ratio of the inner to outer diameter of the rotor is changed as shown in Fig. 2.8**.** When the ratio is increased at fixed airgap length and pole arc to pole pitch ratio $\boldsymbol{\alpha}$, the area of the magnet be reduced, and the thickness will be changed, and this will reduce the resulting fundamental airgap flux density. Similarly, Fig. 2.9 confirms that for different rotor inner active diameter to outer active diameter, the fundamental airgap flux density is significantly affected by number of poles.

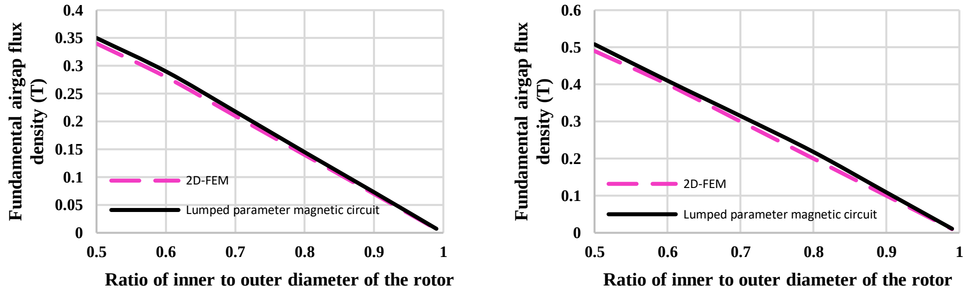

(i) 4 Poles

(ii) 6 Poles

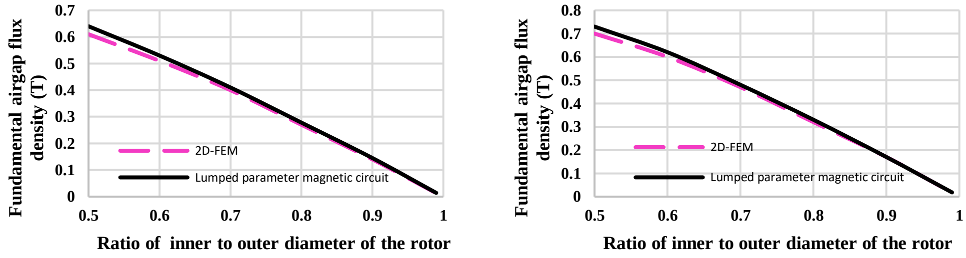

(iii) 8 Poles

(iv) 10 Poles

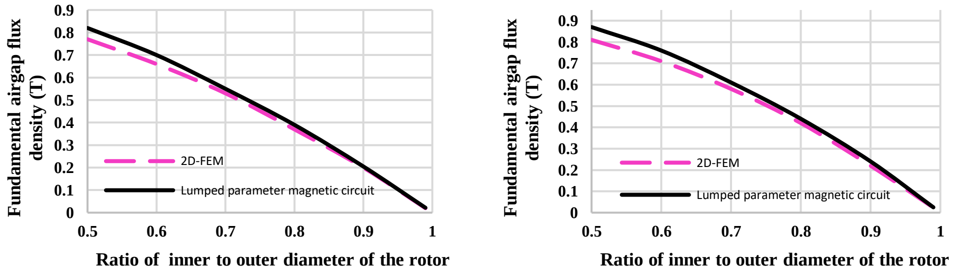

(v) 12 Pole

(vi) 14 Pole

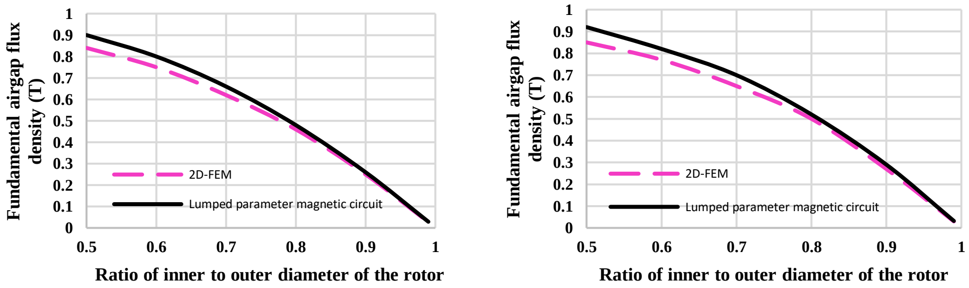

(vii) 16 Pole

(viii) 18 Pole

Fig. 2.8 Variation of the fundamental airgap flux density with the active inner to outer diameter ratio of the rotor.

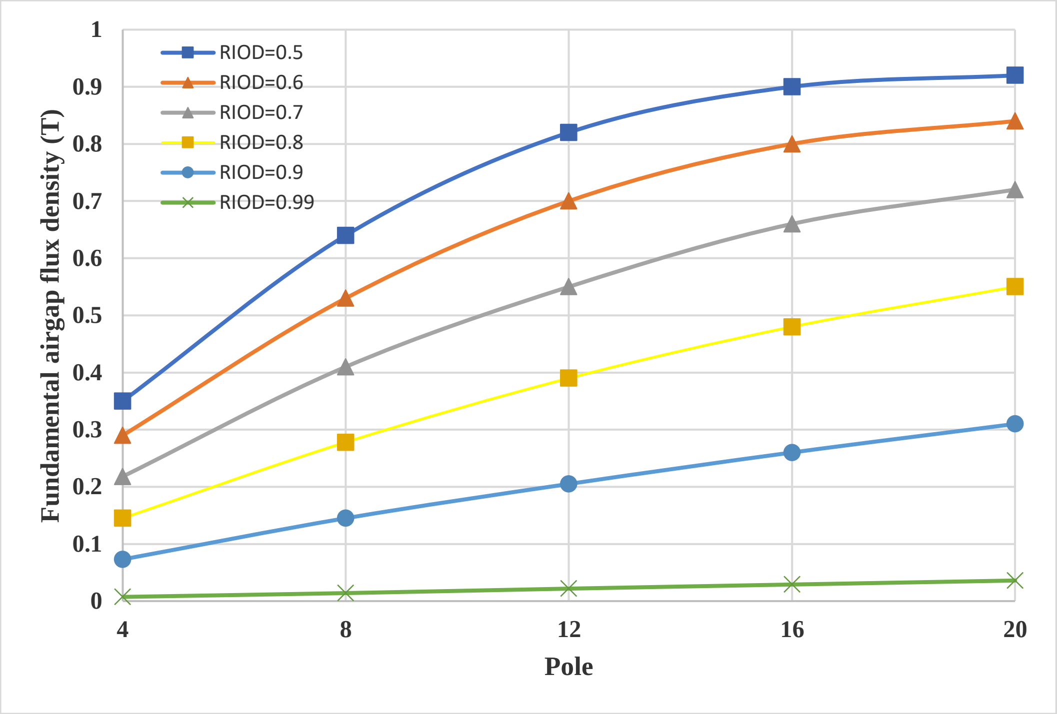

(i)

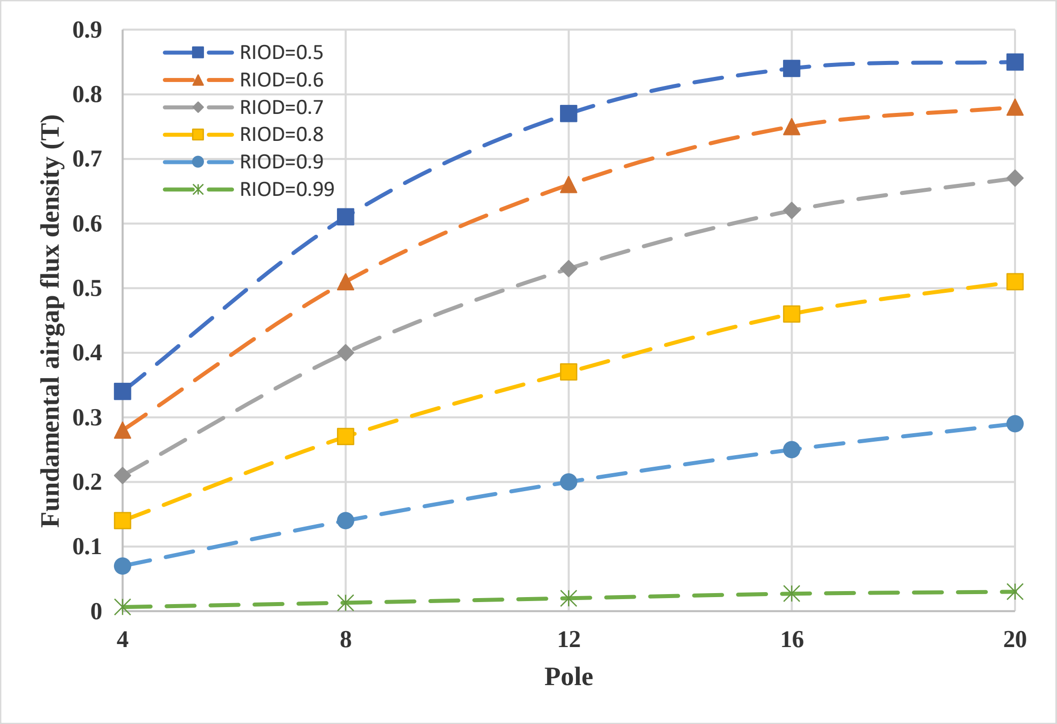

(ii)

Fig. 2.9 Variation of the fundamental airgap flux density with number of poles for (L_g= 0.5 mm, pole arc to pole pitch ratio =0.8 and active length= 30 mm). (i) Lumped parameter magnetic circuit, (ii) 2D-FEA.

2.2.1 Conclusion

The conventional spoke-type rotor machine is simulated using 2D-FEA and the important leading design parameters such as: number of poles, pole arc to pole pitch ratio, airgap length and the ratio of inner to outer diameter of the rotor are investigated to find the flux per pole and the fundamentals airgap flux density.

A simple lumped parameter magnetic circuit which neglects the leakage flux and assumes a slotless stator is employed to model the rotor and investigate the generated flux per pole. The output results show there is a good agreement between 2D-FEA and lumped parameter magnetic circuit which can be adopted as in the initial design stage.

2.3 Novel PM rotor

2.3.1 Introduction

Spoke-type rotor machines generate large airgap flux densities since they exhibit flux focusing geometries particularly, if large number of poles are used. These types of machines may enable to use of low-cost Ferrite PM to achieve high torque density and efficiencies compared with those using rare earth PM. Therefore, in this section the simulation and analysis of a novel rotor which contain axial and circumferential magnetized PMs using 3D flux software is presented, since 3D finite element method (FEM) allows precise analysis of magnetic device considering geometrical details and magnetic nonlinearity. A simple lumped parameter magnetic circuit model is also proposed to analyze the new rotor topologies assuming slotless stator, and where infinitely permeable soft magnetic rings and pole pieces are used.

2.3.2 A novel rotor with axially and circumferentially magnetized permanent magnet

The geometry of the novel rotor PM motor is shown in Fig. 2.10 and Fig. 2.11 respectively, the dimensions and parameters are shown in Table 2.2. In the proposed rotor, a sintered Ferrite PMs axially and circumferentially magnetized are used to achieve large airgap flux densities. When compared with spoke-type rotor, lower number of poles will be required to achieve higher airgap flux densities for smaller ratios of active length to diameter of the rotor. The proposed machine is initially simulated with slotless stator for active stator lengths, airgap lengths, pole arc to pole pitch ratio and different inner to outer rotor diameter ratios [12].

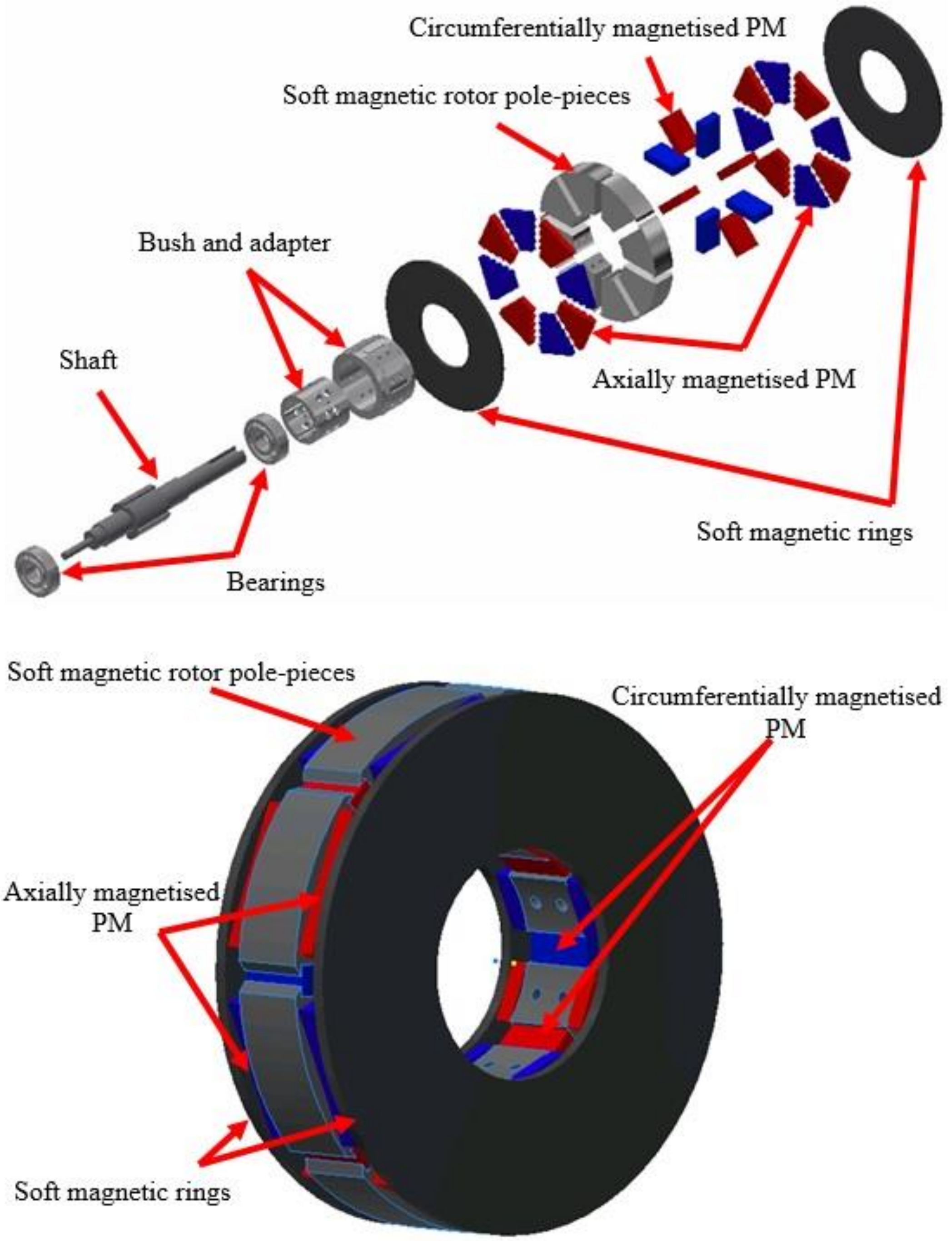

Fig. 2.10 Geometry of the novel PM rotor

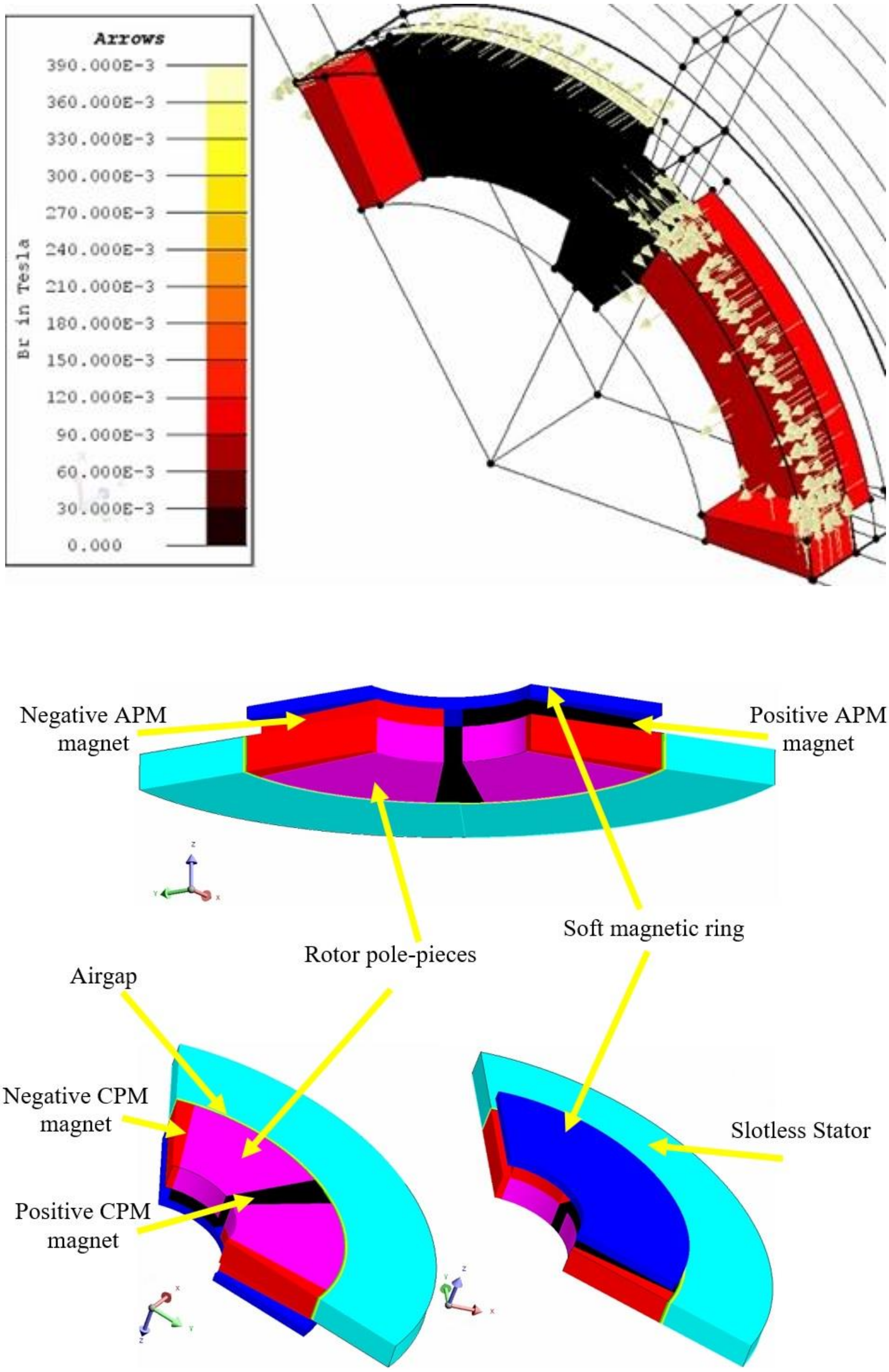

Fig. 2.11 Topology of the novel PM rotor-based 3D-FEA

Stator active axial length	L_{axial} (mm)	30 mm
Airgap diameter	D_{airgap} (mm)	200 mm
Stator outer diameter	$D_{outer-stator}$ (mm)	300 mm
Number of poles	P	6, 12, 18
Airgap length	L_g (mm)	0.5 mm
Axial PM length	L_{APM} (mm)	7.5 mm
Soft magnetic ring axial length	L_{ring} (mm)	5 mm
Permanent magnet type		Ferrite
Remanence of permanent magnet	B_r (T)	0.39 T
Relative recoil permeability	μ_r	1.2

Table 2.2 Parameters of the proposed rotor PM machine

2.3.3 Lumped parameter magnetic circuit model of the proposed rotor

The lumped parameter magnetic circuit which is used to model the new proposed rotor and derive the average air gap flux density B_g analytically is shown in Fig. 2.12, assuming the slotless stator, an infinitely permeable soft magnetic rings and soft magnetic pole pieces and neglecting the leakage fluxes [12].

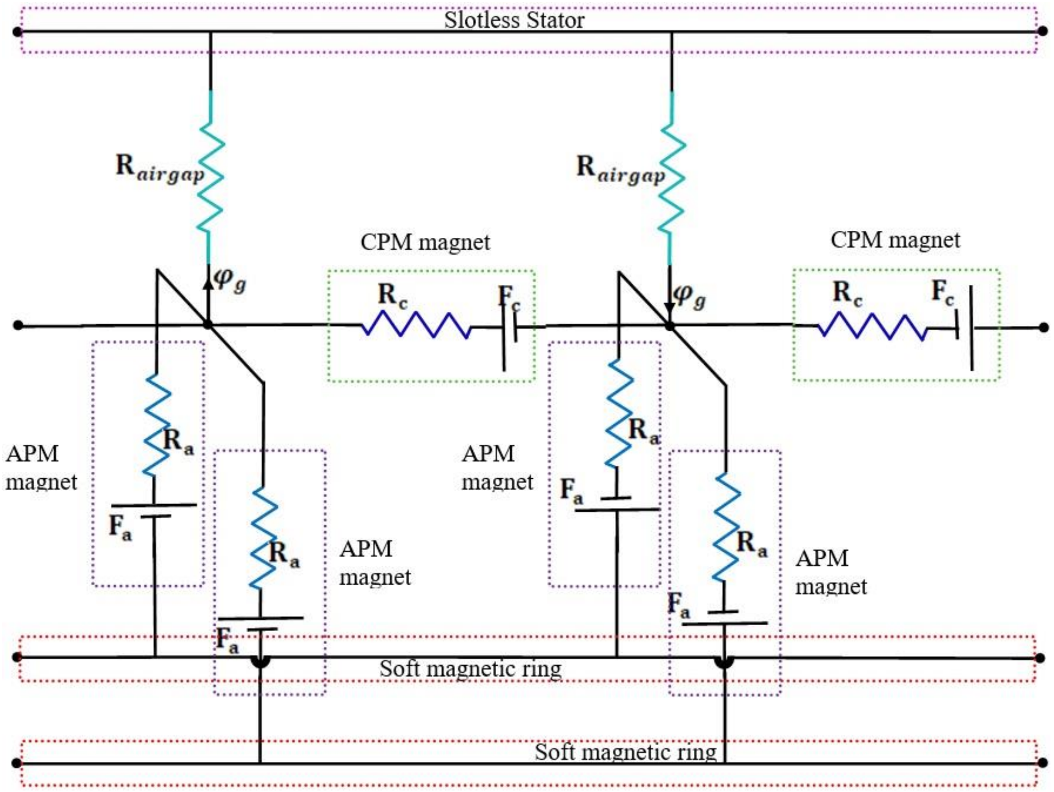

Fig. 2.12 Lumped parameter magnetic circuit of the proposed rotor.

Based on the above lumped parameter magnetic circuit, the flux per pole of the proposed rotor machine is derived as:

$$\varphi_g = \frac{(\lambda F_a + F_c)}{\left(\frac{1}{2}R_c + (2+\lambda)R_g\right)} \tag{2.6}$$

Where:

$$F_a = B_r \frac{L_a}{\mu_r \mu_0} \tag{2.7}$$

$$F_c = B_r \frac{L_c}{\mu_r \mu_0} \tag{2.8}$$

$$R_a = \frac{L_a}{\mu_r \mu_0 A_a} \tag{2.9}$$

$$R_c = \frac{L_c}{\mu_r \mu_0 A_c} \tag{2.10}$$

$$R_g = \frac{L_g}{\mu_0 A_g} \tag{2.11}$$

$$\lambda = R_c / R_a \tag{2.12}$$

For the spoke-type rotor machine, F_a=0. Fig. 2.13 shows the variation of the per pole flux with the of the inner to outer diameter ratio of the new proposed rotor which is predicted using 3D-FEA and lumped parameter magnetic circuit and compared with the conventional spoke-type rotor, it can be seen there is a good agreement between the predicted values using both methods. It can also be noticed that the inner to outer diameter ratio of the rotor affects significantly the resulting flux per pole. Furthermore, comparing with spoke-type rotor, a noticeable increase in the generated per pole flux can be achieved with the new proposed rotor.

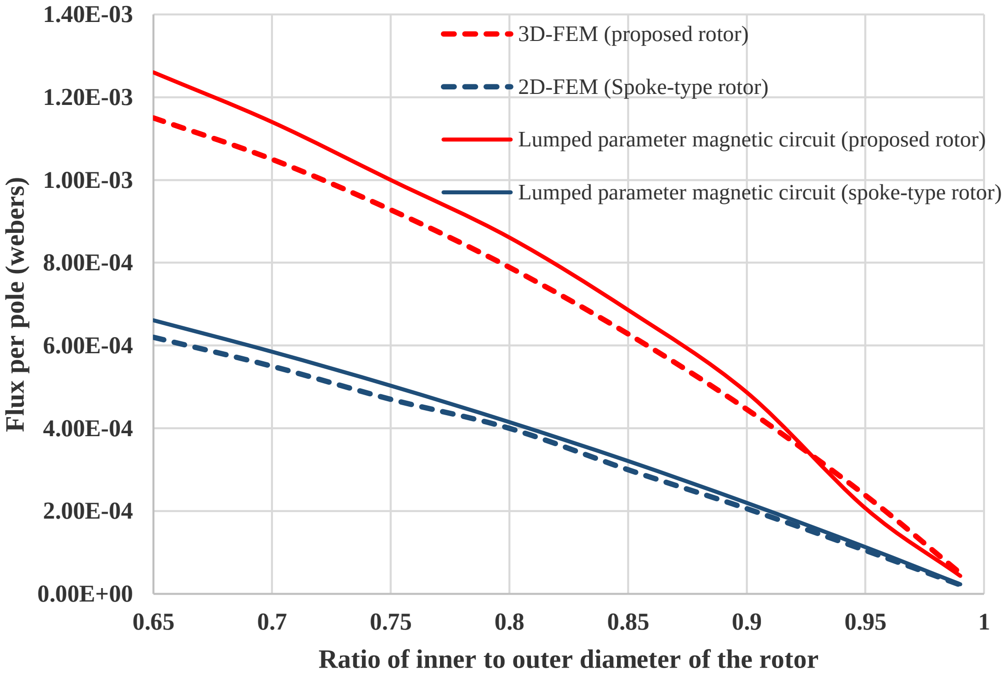

Fig. 2.13 Variation of the flux per pole for the (spoke-type rotor and proposed rotor) at different ratio of inner to outer diameter.

Fig. 2.14 shows the variation of the airgap flux density with the stator axial length. It can be noticed that the axial length of the stator has a significant effect on the airgap flux density resulting in a high flux density value at small ratio of stator axial length to the rotor diameter (L_{stator}/D_{rotor}).

Furthermore, good agreement exists between 3D-FEA and lumped parameter magnetic circuit. Fig. 2.15 shows the variation of the airgap flux density with the airgap length, it can be noticed that the airgap flux density has relative sensitivity to the airgap length.

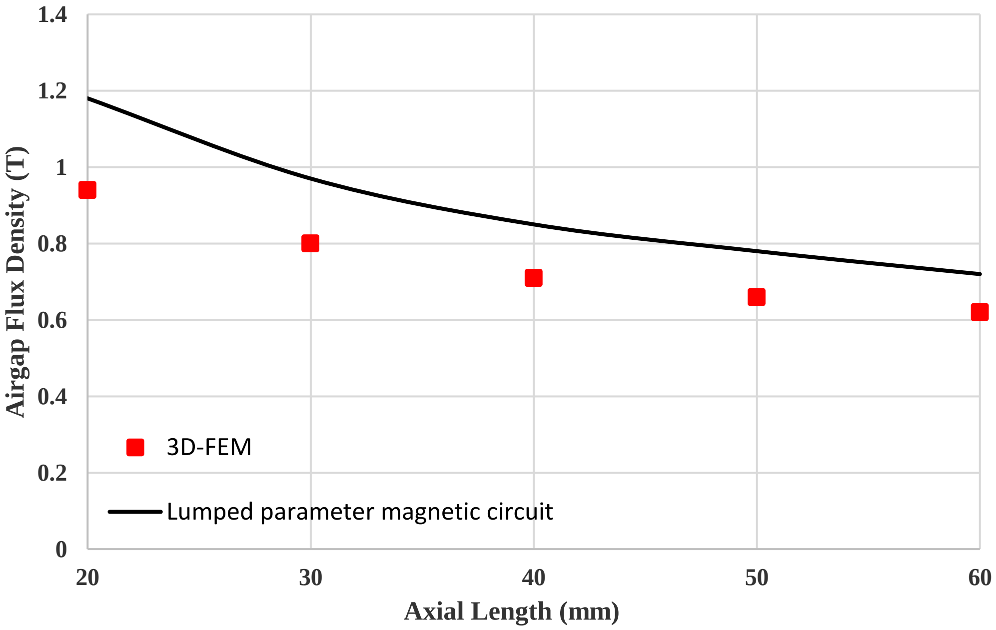

Fig. 2.14 Variation of the airgap flux density with stator active axial length for (12 pole, L_g = 0.5 mm and pole arc to pole pitch ratio =0.85).

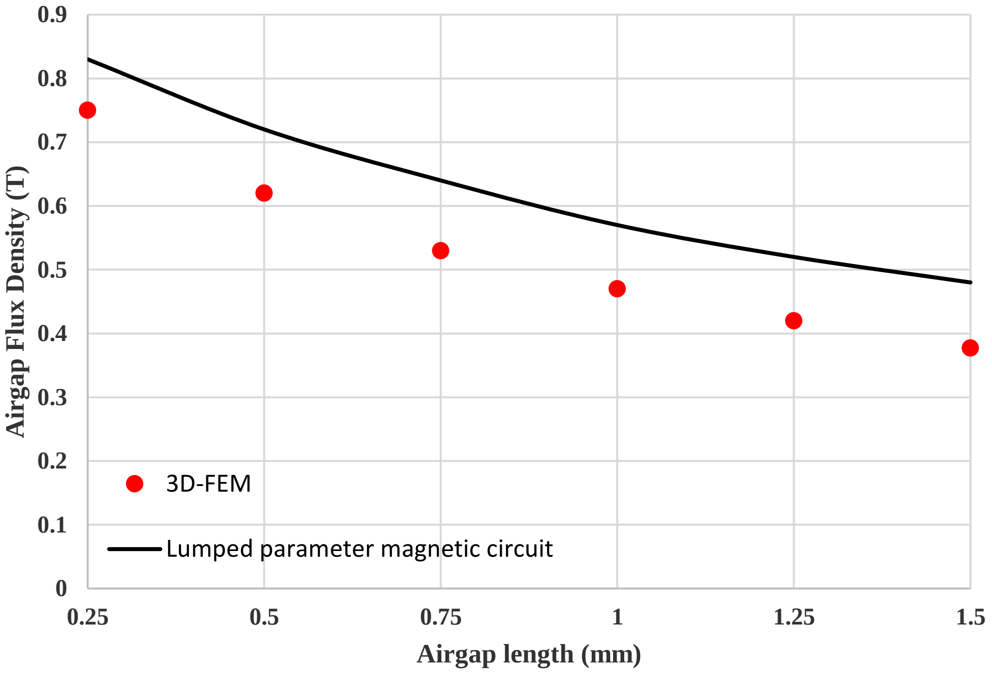

Fig. 2.15 Variation of the airgap flux density with airgap length for (12 pole, pole arc to pole pitch ratio =0.85 & stator active length = 60 mm).

Fig. 2.16 shows the variation of the fundamental airgap flux density for the proposed rotor at different pole arc to pole pitch ratio α and for different number of poles. It can be seen that there is significant increasing in the fundamental airgap flux density can be achieved when compared with spoke-type rotor for the same number of poles and airgap length**.** Fig. 2.17 shows the variation of the fundamental airgap flux density with the active inner to outer diameter ratio of the proposed rotor. The results show that compared with spoke-type rotor, a high value of the of the fundamentals airgap flux density can be achieved which can be ($\cong$ 1 T) at ratio = 0.75 depending on the number of poles.

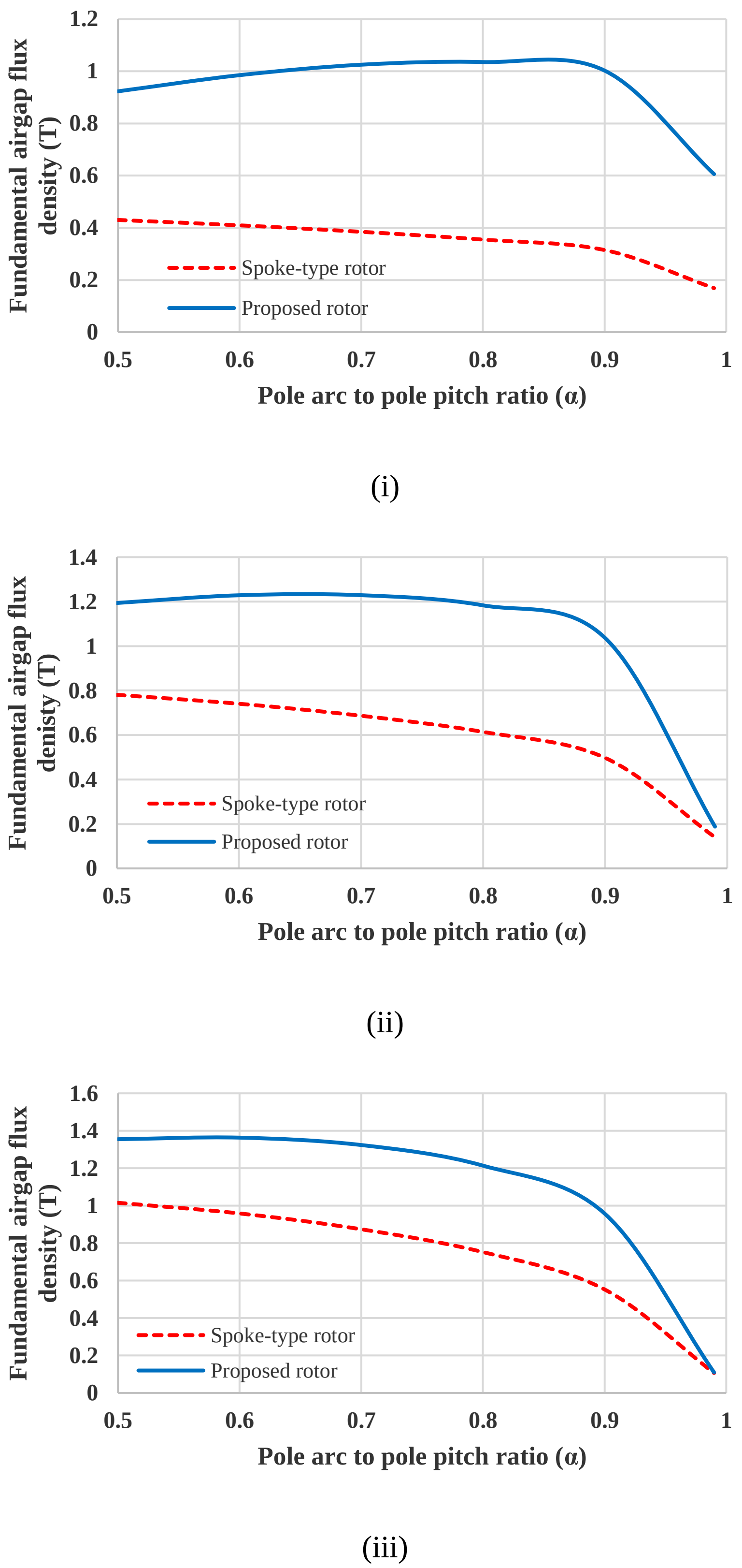

Fig. 2.16 Variation of the airgap flux density pole arc to pole pitch ratio (α) for (L_g =0.5 mm and stator active length =30 mm). (i) 6 poles. (ii) 12 pole. (iii) 18 pole.

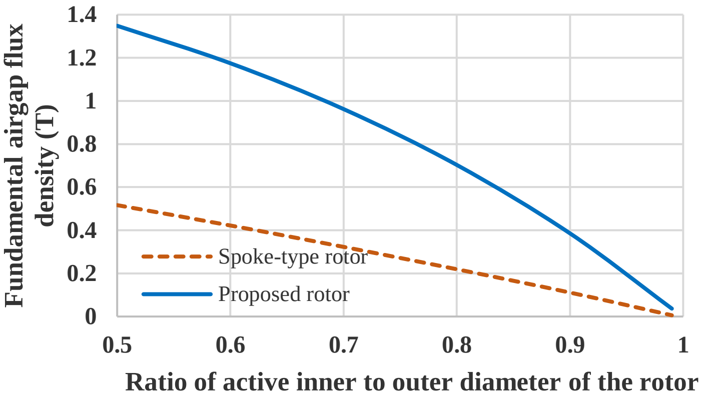

(i)

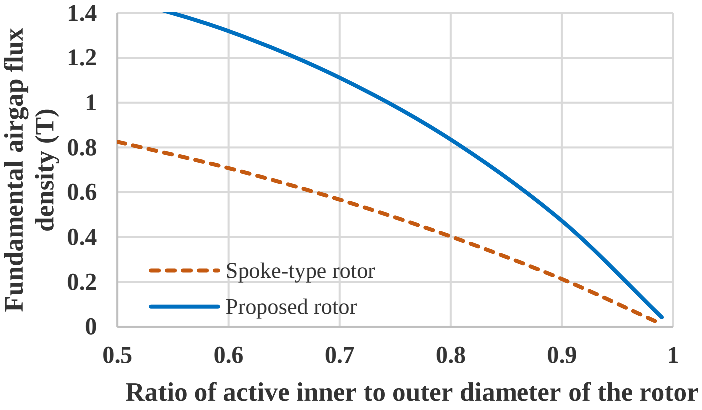

(ii)

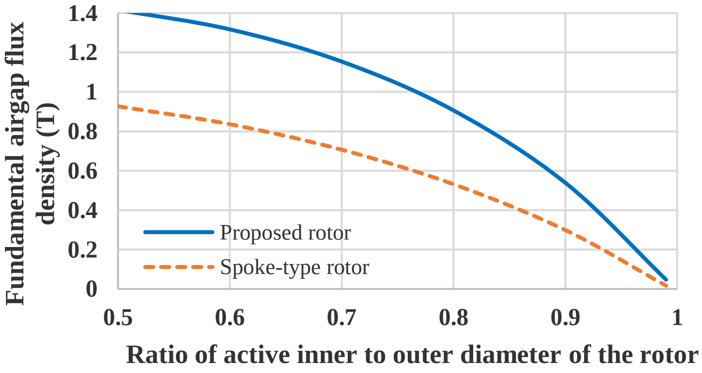

(iii)

Fig. 2.17 Variation of the fundamental airgap flux density with the inner to outer diameter ratio of the rotor for (L_g= 0.5 mm, pole arc to pole pitch ratio = 0.8 and stator active length = 30 mm). (i) 6 poles. (ii) 12 pole. (iii) 18 pole.

2.4 Conclusion

In this chapter, a novel rotor topology equipped with axially and circumferentially magnetized ferrite permanent magnets is investigated and compared with the conventional spoke-type rotor topology in term of achieved high airgap flux density considering the effect of many factors such as: stator active length, number of poles, pole arc to pole pitch ratio, airgap length and the ratio of inner to outer diameter of the rotor.

As the ratio of the inner to outer diameter of the rotor increases, the dimensions of the magnets of the conventional spoke-type rotor and the proposed rotor will be changed causing the flux per pole and then the fundamental airgap flux density to be reduced. In addition, the length of the airgap L_g has a great effect on the generated airgap flux density. As airgap length increases, the flux at No-load captured by the winding or also at slotless stator will be reduced causing the airgap flux density to be reduced. Therefore, at specific No. of poles the required airgap flux density should be chosen at specific airgap length. Furthermore, as the pole arc to pole pitch ratio increase, the thickness of the magnet of the spoke– type rotor will be reduced at fixed No. of poles causing airgap flux density to be reduced. As result the value of the pole arc to pole pitch ratio should be chosen with a suitable value (not very small), the reason is that the increase of the airgap flux density will cause saturation in the rotor and stator materials when pole arc to pole pitch ratio is very small.

Comparing with the conventional spoke-type rotor, high airgap flux density can be achieved from the new proposed rotor for relatively small ratio of axial length to diameter of the rotor which is can be about 2 times the remanence of the used ferrite PMs. Therefore, the proposed machine has the potential to be used in different cost sensitive applications, where torque/power density are important requirements, such as electric and hybrid vehicles.

A simple lumped parameter magnetic circuit which neglects the leakage flux and assumes a slotless stator is employed to model the rotor of the two topologies and investigate the flux per pole generated for different number of poles. Since it consumes less time comparing with FEA and can be used for different type of machines. The output results show there is a good agreement between FEA and lumped parameter magnetic circuit which can be adopted as in the initial design stage.

Chapter 3

Design of axially and circumferentially magnetized PM motor

3.1 Introduction

This chapter describes and analyses the performance and the characteristics of the new proposed rotor motor. Using 3D-FE, the geometry of the new proposed machine is simulated and optimised to obtain the desired output characteristics which enable it to be used in different cost sensitive applications, where torque/power density are important requirements, such as electric and hybrid vehicles.

3.2 Novel PM motor

The schematic of the proposed machine and its parameters are shown in Fig. 3.1 and Table 3.1 respectively.

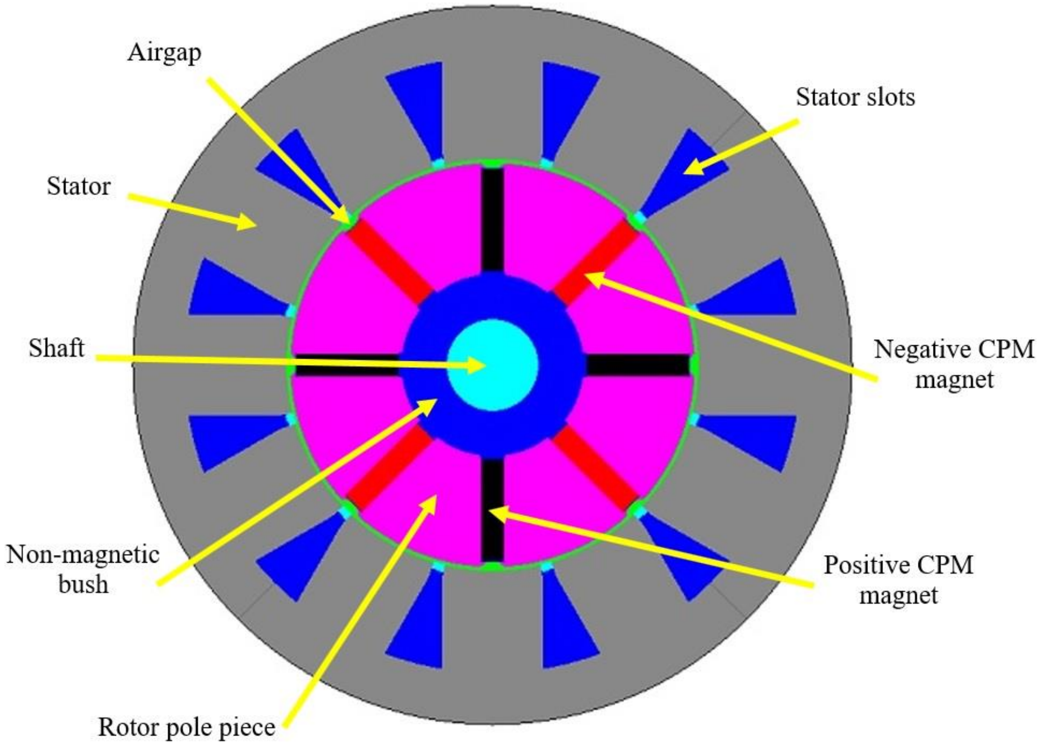

(i) View with CPMs

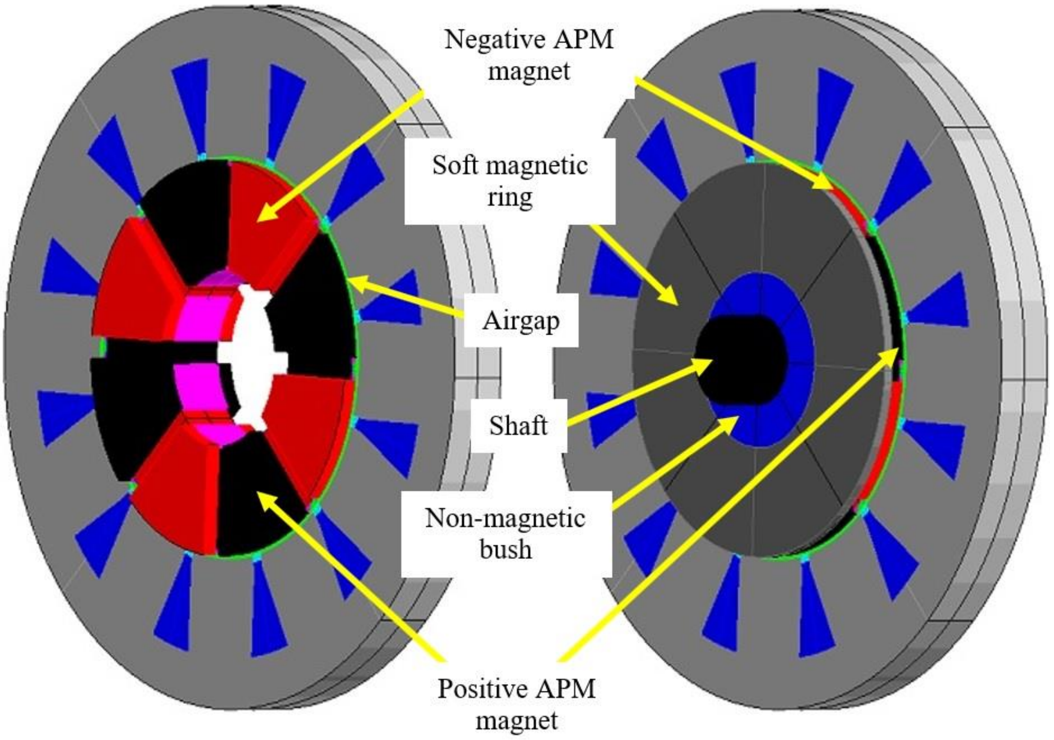

(ii) View with APMs

Fig. 3.1 Full geometry of the new proposed machine-based FEA.

Stator active axial length	L_{axial}	30 mm
Stator back iron width	d_c (mm)	25.25 mm
Tooth stalk width	T_s (mm)	50.0 mm
No. of winding turns	N	24 turn / 1 2 strands / FSCW
Airgap diameter	D_{airgap} (mm)	200 mm
Stator outer diameter	$D_{outer-stator}$ (mm)	350 mm
Number of pole pairs	P	4
Rotor outer active diameter	$D_{outer-rotor}$ (mm)	199 mm
Axial PM length	L_{APM} (mm)	7.5 mm
Circumferential PM length	L_{CPM} (mm)	30 mm
Circumferential PM width	W_{CPM} (mm)	49.75 mm
Circumferential PM thickness	L_C (mm)	11.7 mm
Soft magnetic ring axial length	L_{ring} (mm)	5 mm
Number of slots	N_s	12
Slot opening to slot pitch ratio		0.1
Airgap length	L_g (mm)	0.5 mm
Soft magnetic ring		Mild steel
Pole pieces material		SMC
Remanence of ferrite PM	B_r (T)	0.39 T
Relative recoil permeability	μ_r	1.2
Based speed	N_{base}	2250 r/min
Max. speed		4500 r/min
Max. current		880.27 A/turn
DC link voltage	V_{DC}	17 V/turn
Rated torque	T_{rated}	38.5 N.m
Rated power	P_{rated}	9 kW

Table 3.1 Parameters of the new proposed machine

Based on Fig. 3.2, the initial values of the stator teeth width and back iron thickness are calculated using Eq. 3.1 and Eq. 3.2, respectively. It can be noticed that the width of the tooth ($\mathrm{W_t}$) is limited by the airgap flux density ($\mathrm{B_{airgap}}$) and tooth density ($\mathrm{B_{tooth}}$) which depends on the value of flux per slot pitch ($\mathrm{\phi_s}$) and the active axial length of the machine (L_{axial}) as shown in Eq. 3.3. Whereas the back iron thickness ($\mathrm{d_c}$) is limited by the airgap flux density ($\mathrm{B_{airgap}}$) and the flux density in the back iron core ($\mathrm{B_{core}}$) which depends on the value of flux per pole-pitch ($\mathrm{\phi_p}$) and the axial length of the machine (L_{axial}) as shown in Eq. 3.4. These are subsequently refined to take into account the saturation of the magnetic circuit.

$$\mathrm{W_t} = \frac{\mathrm{B_{airgap}\lambda_s}}{\mathrm{B_{tooth}}} \qquad 3.1$$

$$\mathrm{d_c} = \frac{\mathrm{B_{airgap}\pi D_{airgap}}}{\mathrm{4PB_{core}}} \qquad 3.2$$

$$\mathrm{B_{tooth}} = \frac{\mathrm{\phi_s}}{\mathrm{W_t L}} \qquad 3.3$$

$$\mathrm{B_{core}} = \frac{\mathrm{\phi_P}/2}{\mathrm{d_c L}} \qquad 3.4$$

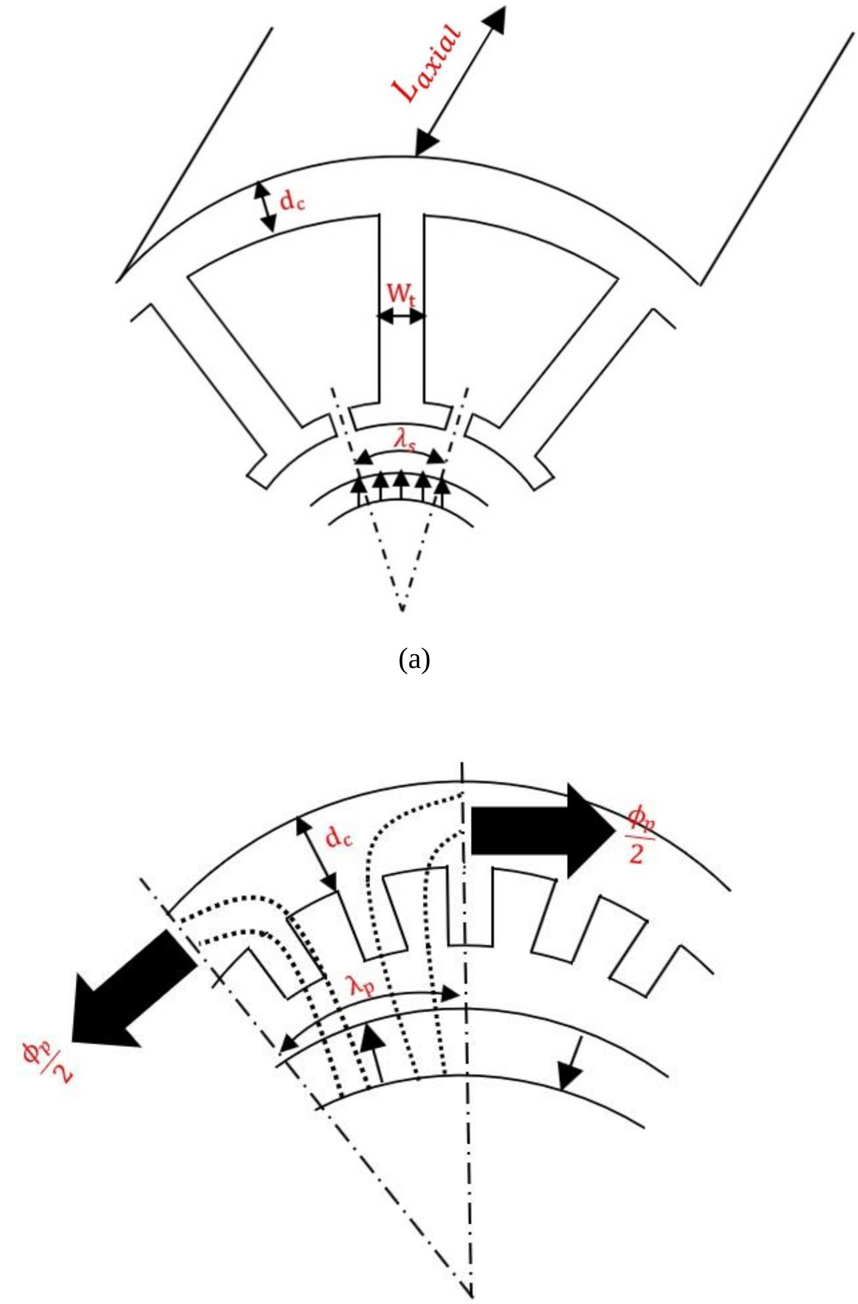

(a)

(b)

Fig. 3.2 Schematic diagram for (a) stator teeth (b) stator back iron.

In 3D-FEA, the stator windings (turn/coil) are represented using non- mesh coil option as shown in Fig. 3.3.

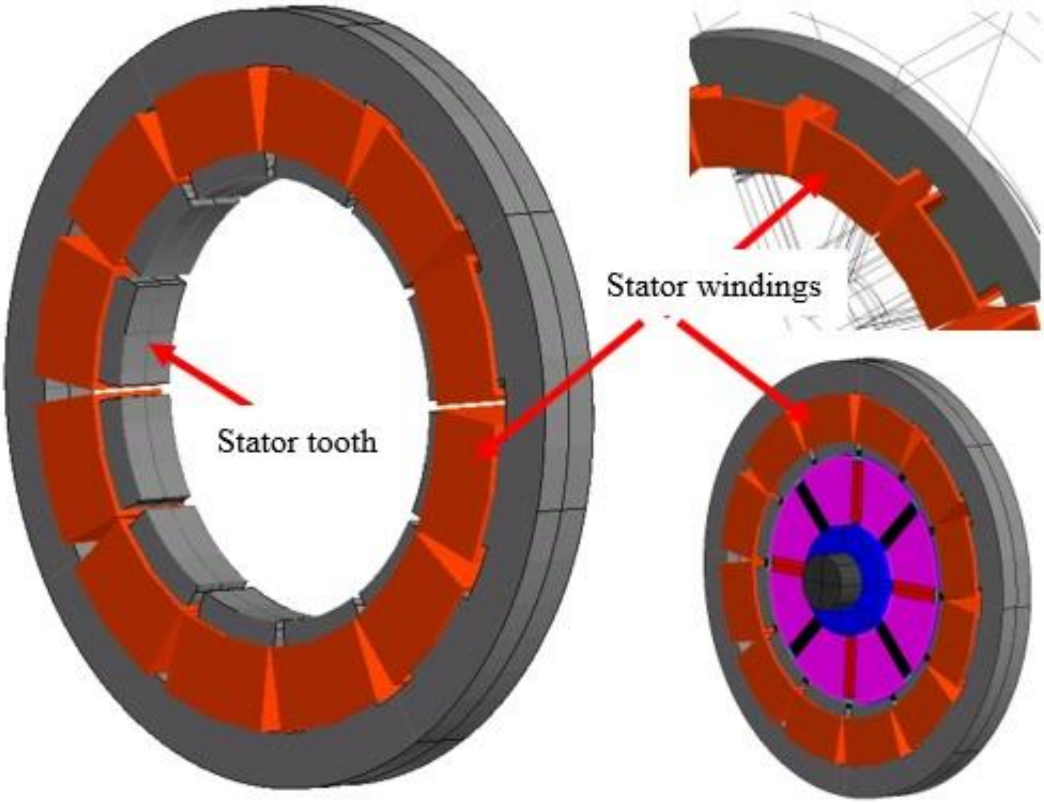

Fig. 3.3 3D-FEA based representing of stator winding (turn/coil).

3.3 3D-FEA Simulation and results

3.3.1 No-load condition

Fig. 3.4 - Fig. 3.6 shows the output characteristics of the new proposed machine such as linkage flux, BEMF voltages, It can be noticed that the fluxes produced by all the permanent magnets are focused in order to achieve large airgap flux densities compared to the conventional spoke-type rotor topologies, especially when a lower number of poles (8 poles) are used.

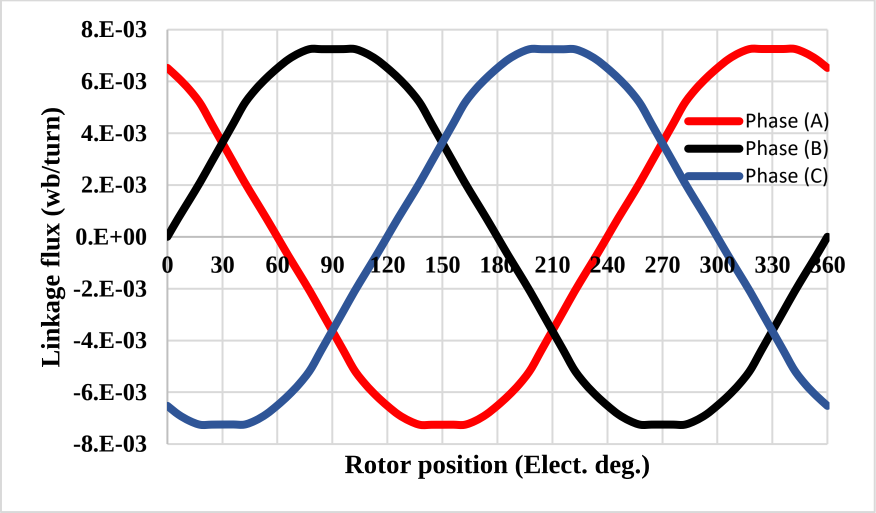

(a) 3-phase linkage flux waveforms

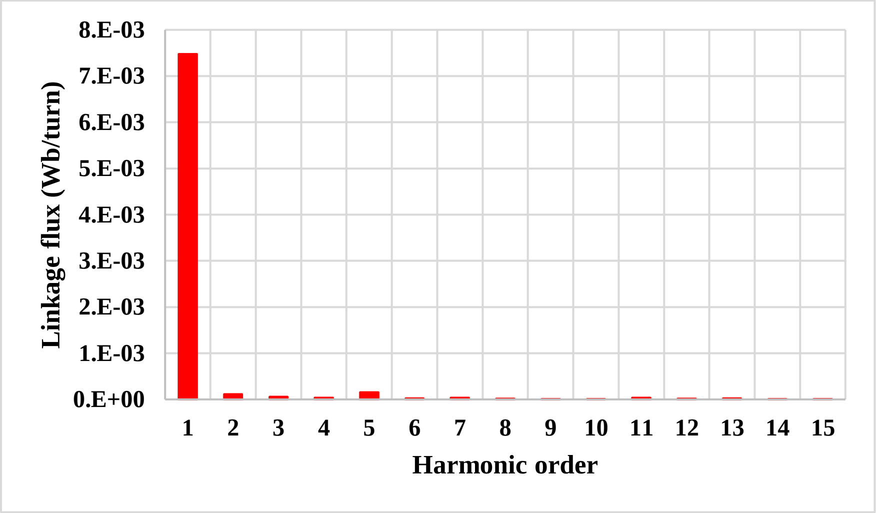

(b) Harmonic spectrum

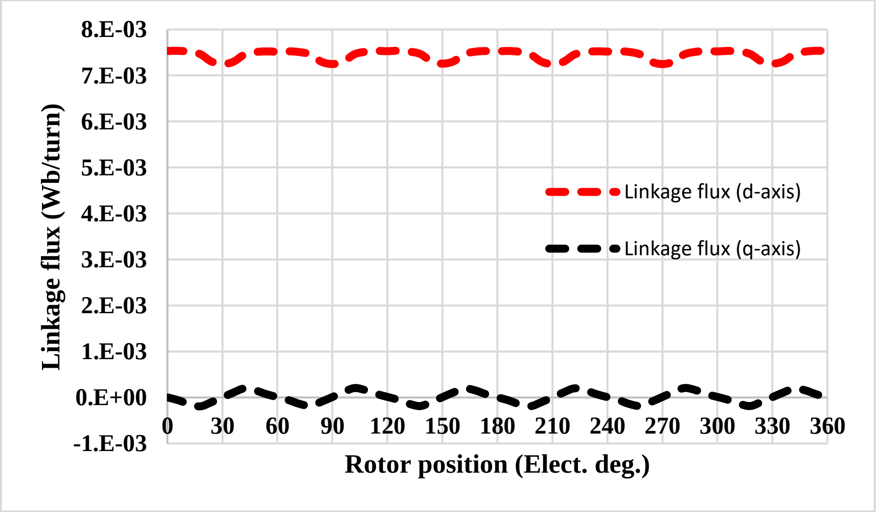

(c) d-q axes phase flux linkage waveforms

Fig. 3.4 Linkage flux wave forms under open circuit condition at speed =2250 r/min.

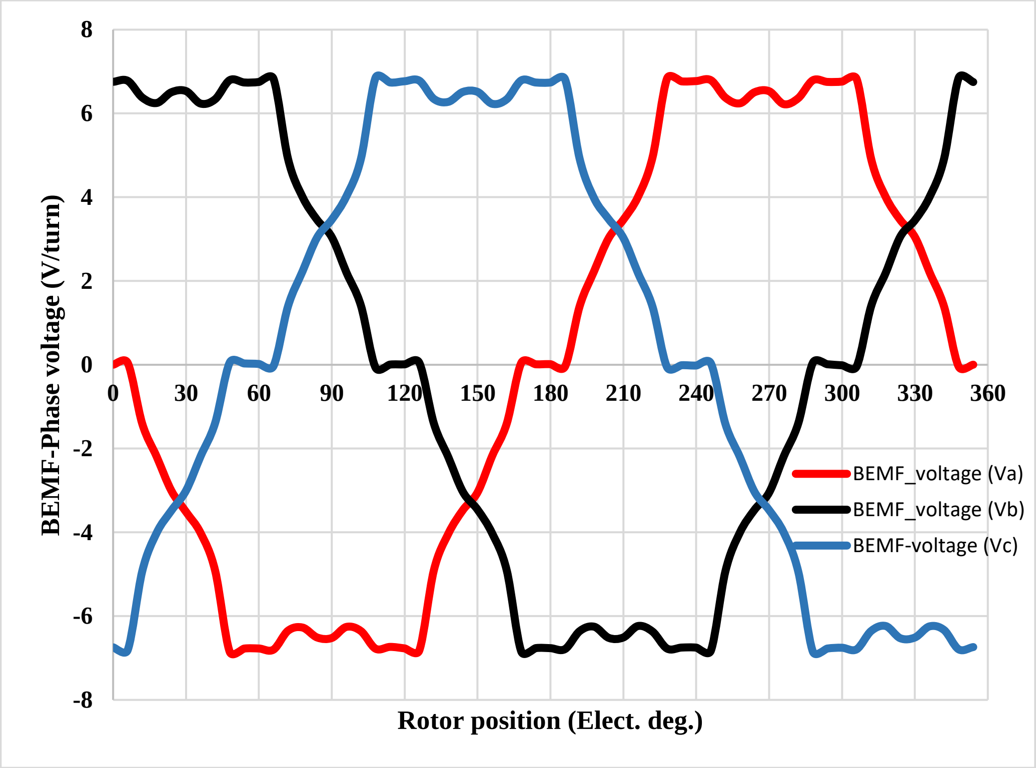

(a) 3-phase BEMF phase voltage waveforms

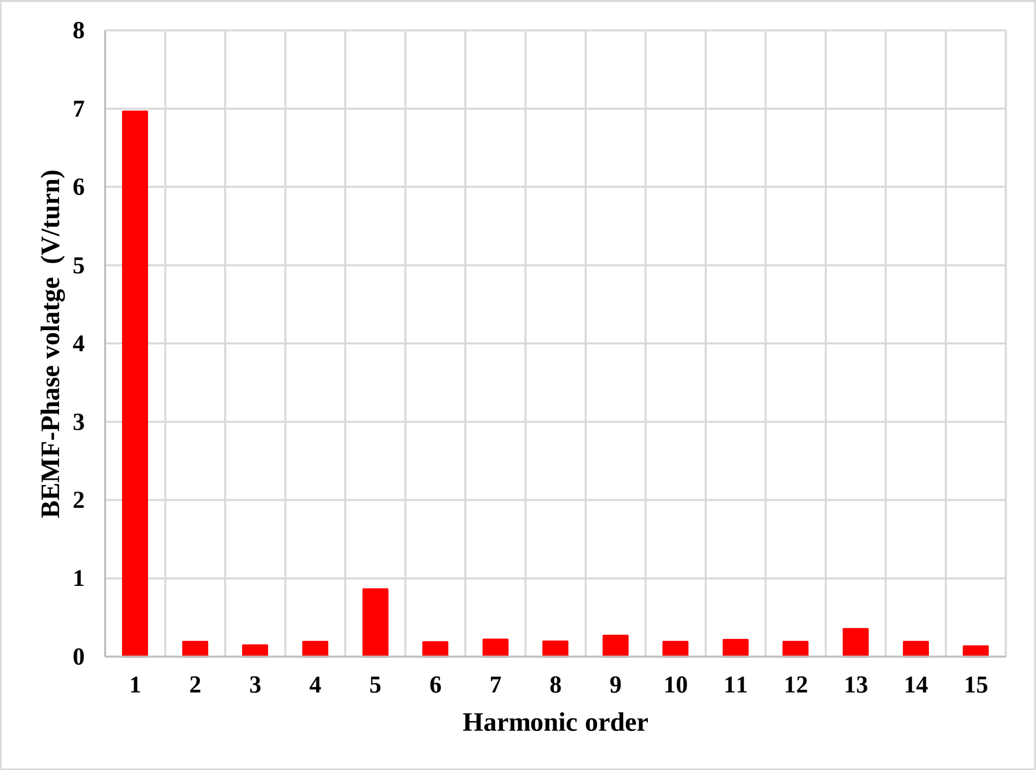

(b) Harmonic spectrum

Fig. 3.5 Three phase BEMF-Phase voltage waveforms at speed = 2250 r/min.

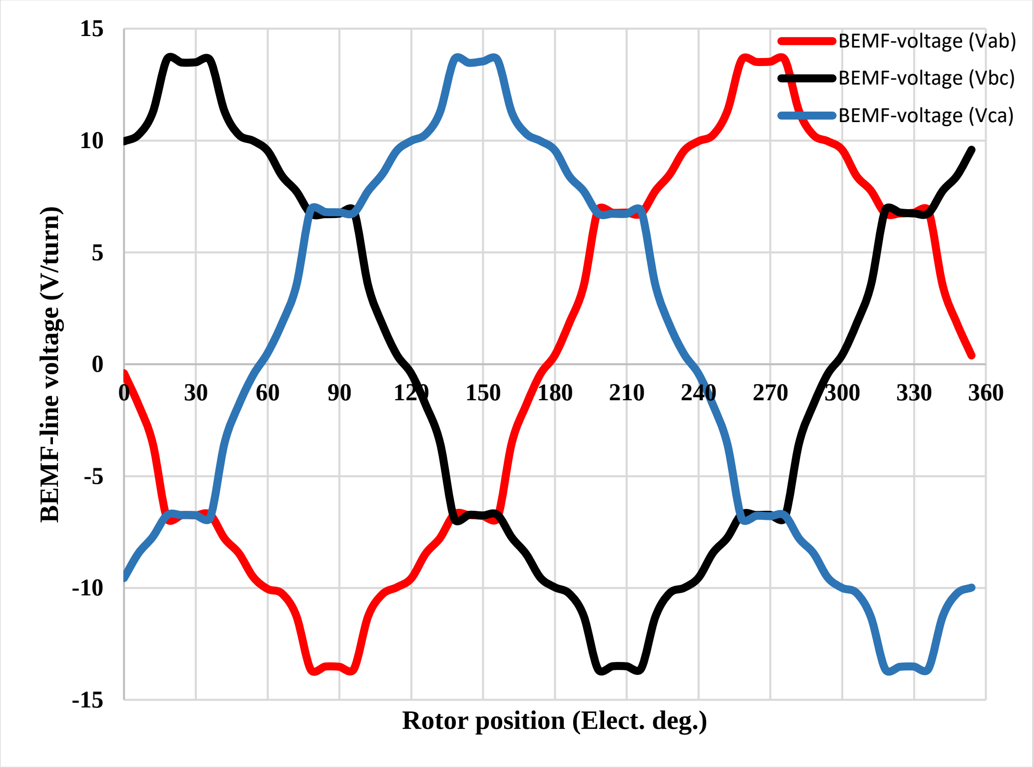

(a) 3-phase BEMF line voltage waveforms

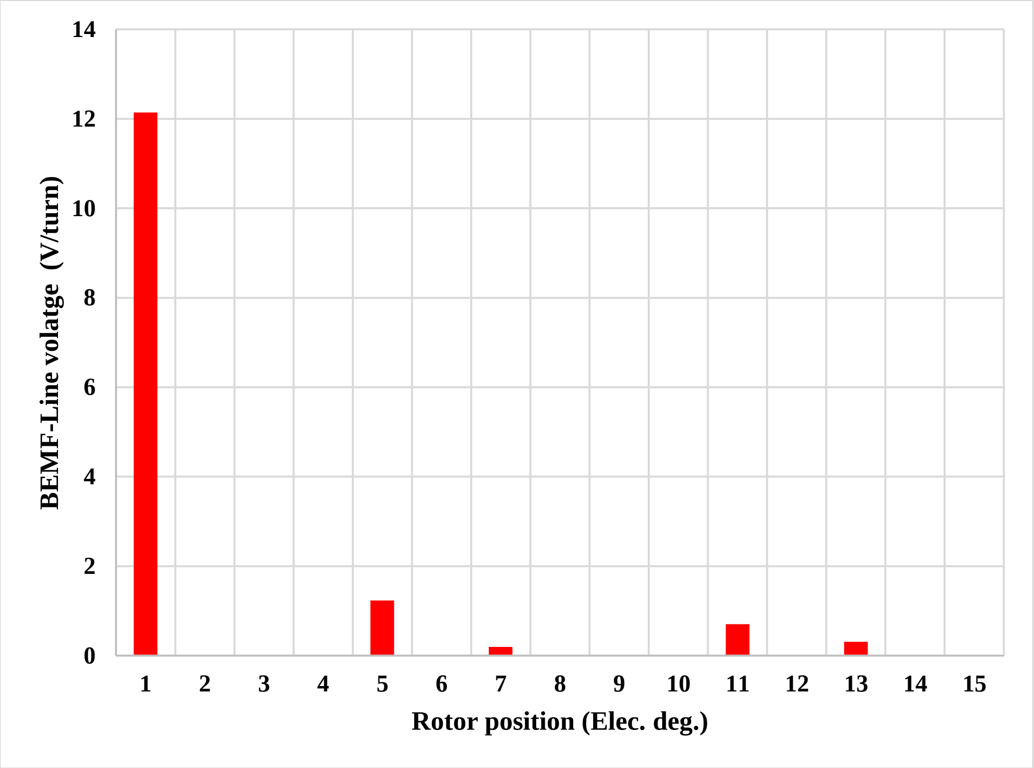

(b) Harmonic spectrum

Fig. 3.6 Three phase BEMF-Line voltage waveforms at speed = 2250 r/min.

Fig. 3.7 shows the NO-LOAD airgap flux density. As explained in chapter two, it can be noticed that a high value of the average flux density can be achieved which is more than 1.5 time of the remanence of the ferrite permanent magnet, especially at low ratio of the stator active length to rotor diameter which is very important characteristic of the novel machine. The waveform of cogging torque is predicted as shown in Fig. 3.8. It can be seen that low value of the cogging torque can be achieved.

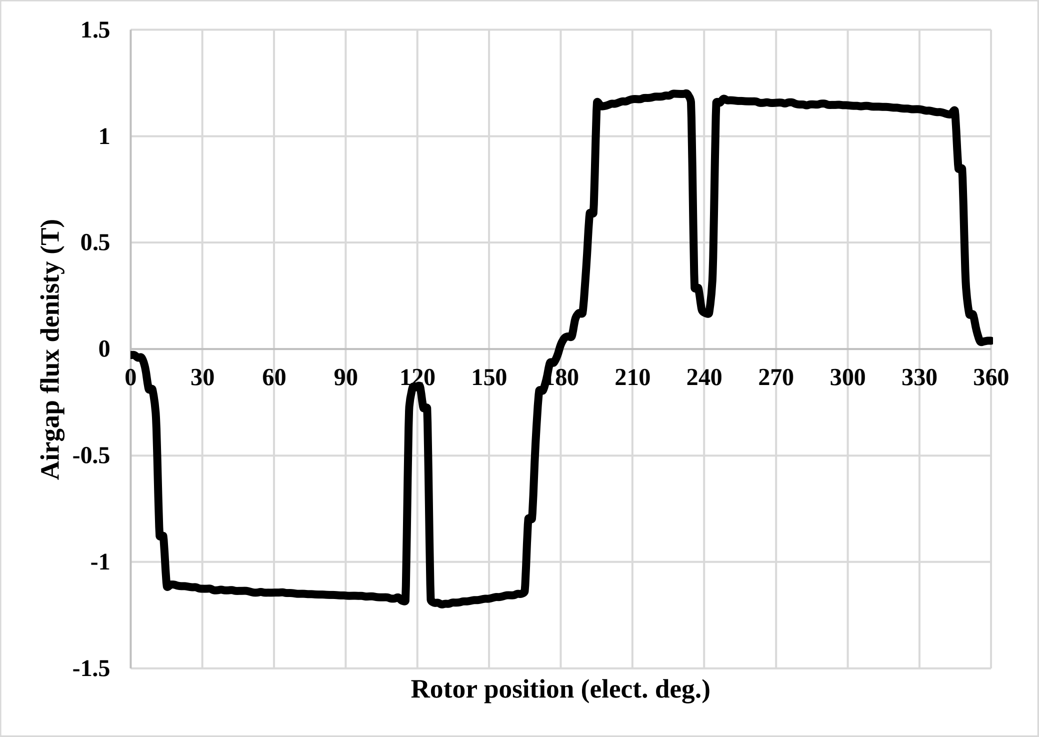

Fig. 3.7 Airgap flux density waveform for the new proposed machine.

Fig. 3.8 Cogging torque waveform for the new proposed machine.

3.3.2 Demagnetization characteristics of the ferrite magnet

The demagnetisation withstand capability for the Ferrite magnet used in the new proposed machine is estimated when full load current is applied at different working temperature so as to make sure that the magnet B-H characteristics will be within the linear region and to avoid working below the knee point as shown in Fig. 3.9. This has an important effect on the choosing of the correct type of sintered Ferrite magnet used in the prototype. The flux density B_m and the field intensity H_m for both the axially magnetised PM and circumferentially magnetised PM are shown in Fig. 3.10 & Fig. 3.11. As a result, Ferrite magnet grade (TDK FB6H) is chosen since it has linear working characteristics on the B-H curve at ambient and other working temperature at shown in Fig. 3.12 [62].

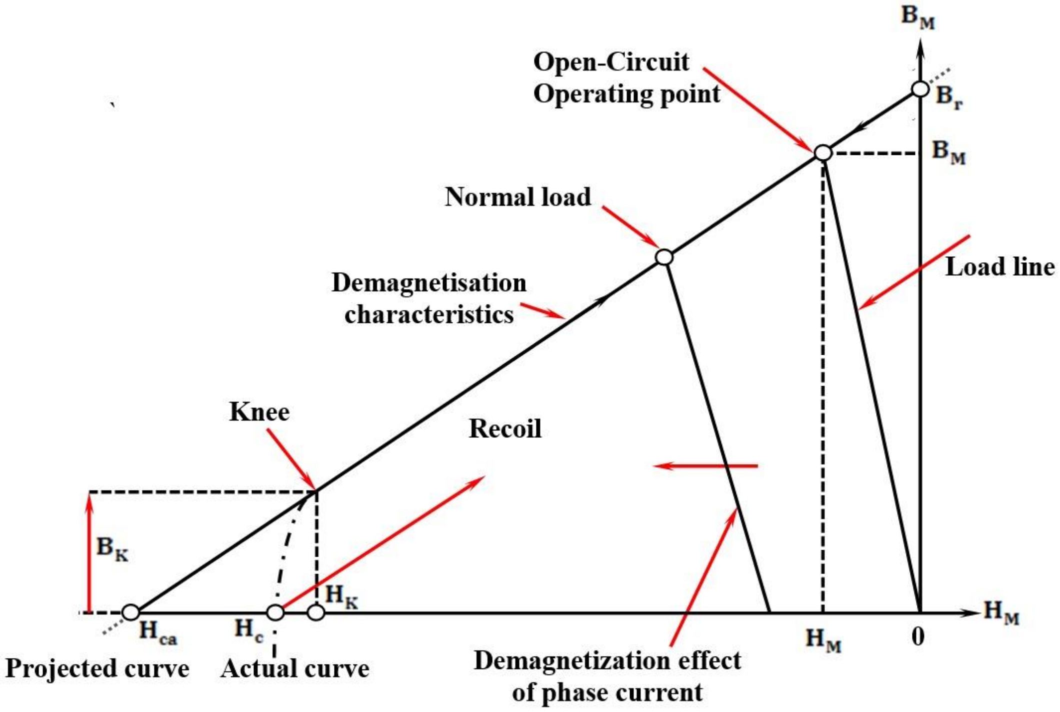

Fig. 3.9 B-H characteristics of the magnet material showing the demagnetization operating region [6]

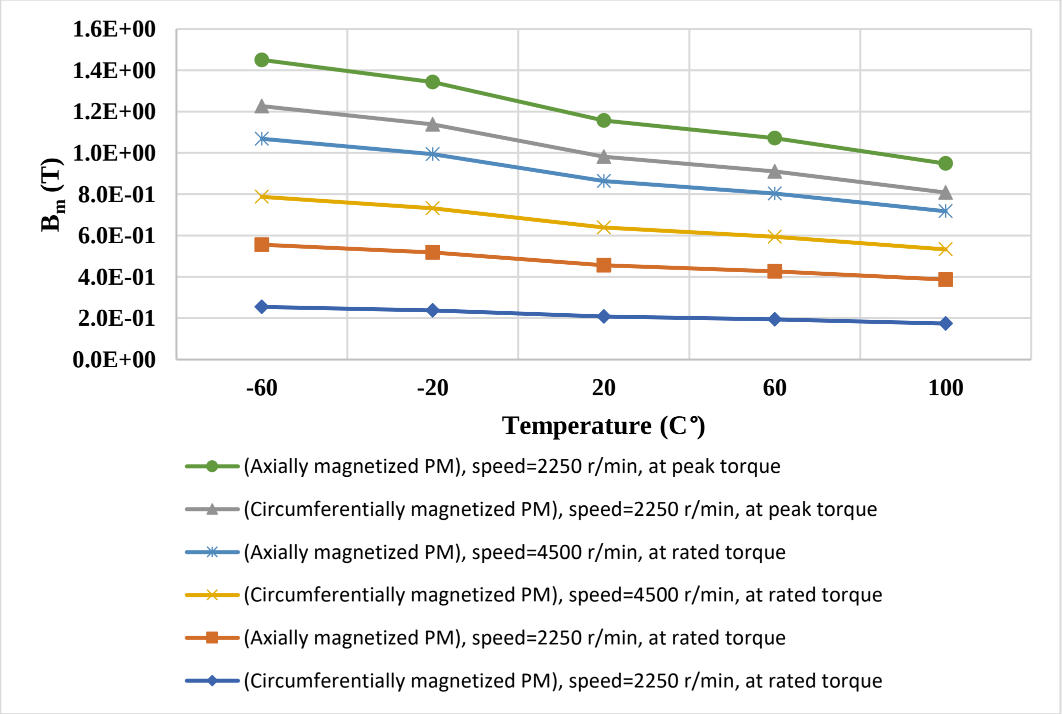

Fig. 3.10 Flux density of the ferrite PM used in the new proposed machine.

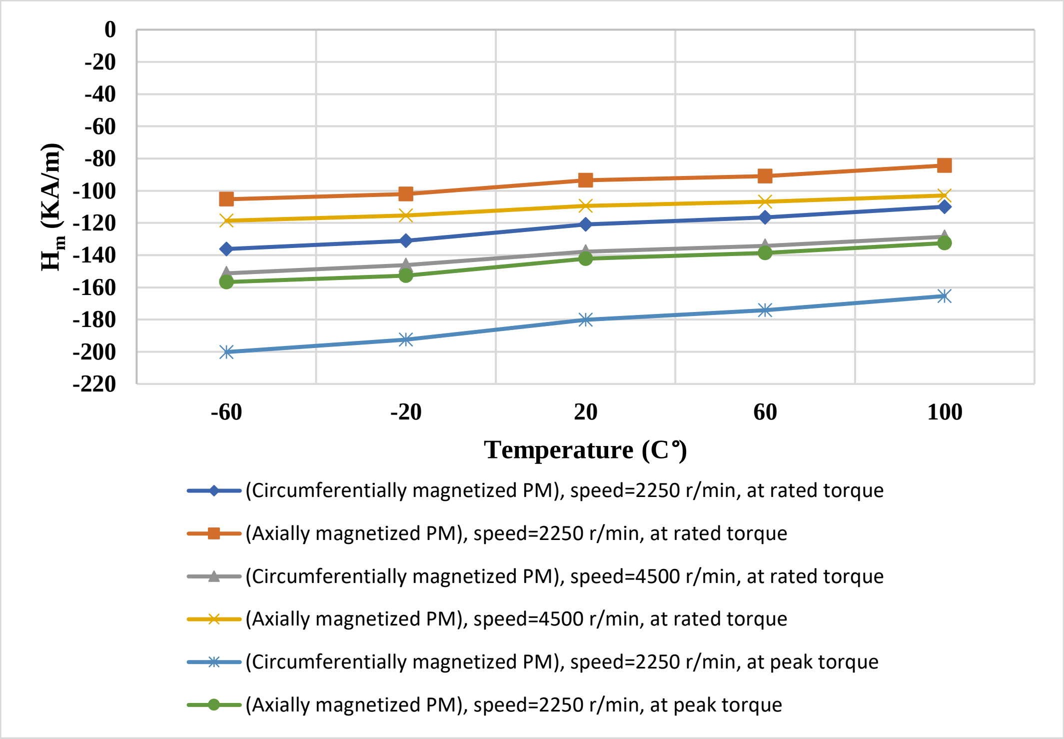

Fig. 3.11 Field intensity of the ferrite PM used in the new proposed machine.

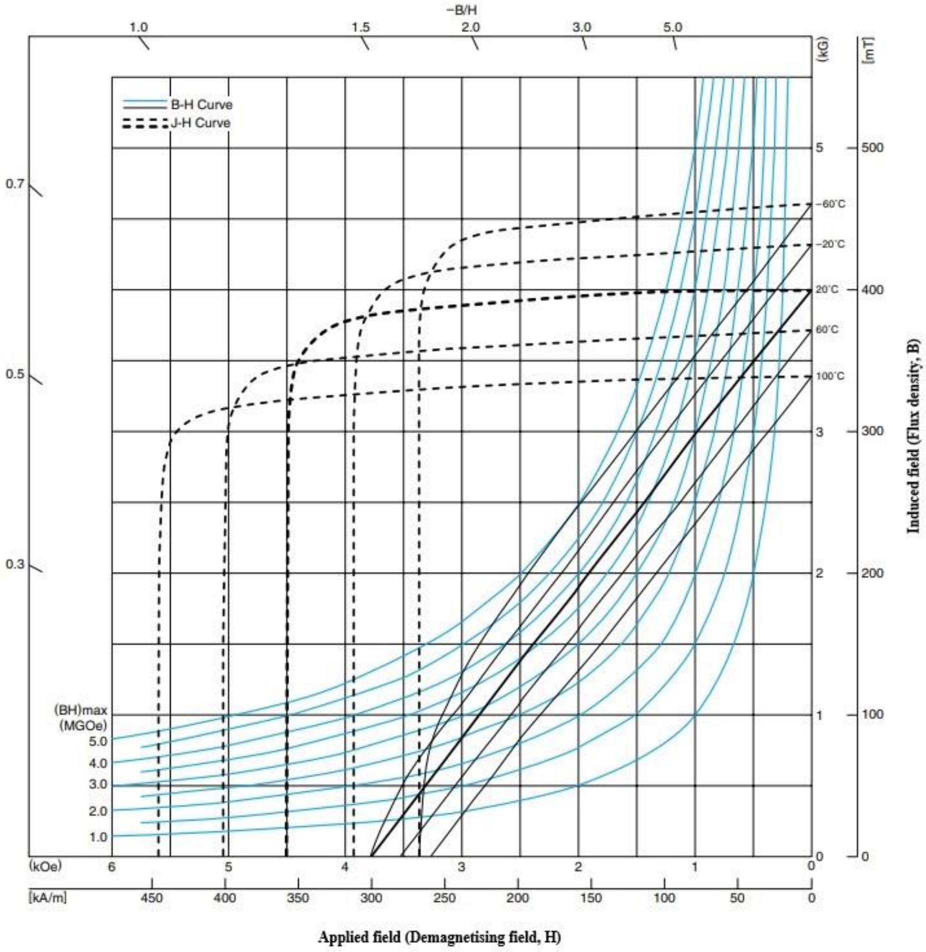

Fig. 3.12 B-H curve of the ferrite magnet grade (TDK FB6H) [62]

3.3.3 Simulation at load condition

In order to predict the output characteristics for the new proposed machine such as torque / speed and power / speed, efficiency envelopes and field weakening properties, it is simulated at load condition at I_{max} = 880.27A/turn (made from 24 turns of 12 strands of 0.75mm diameter wire) at maximum airgap shear stress = 20kPa. According to the 3D-FEA, the wave forms of the linkage flux, phase voltages, iron losses and maximum torque per ampere are investigated at different speeds to predict the required characteristics as shown in the below section.

3.3.3.1 Linkage flux waveforms at load condition

Fig. 3.13–Fig. 3.16, shows the three phase linkage flux waveforms for the new proposed machine which are predicted using 3D-FEA and its fundamental analysis at different rotational speed starting with base speed = 2250 r/min and in field weakening region at high speed. It can be noticed that the values of the linkage flux are decreased gradually as the rotational speed increases, due to field weakening in order to get a torque and output power within the limitation of the available voltage (DC link voltage). The value of current angle (γ) is determined based on the maximum value of the torque per applied load achieved (MTPA) which is predicted equal to (γ = 25°) at base speed (2250 r/min).

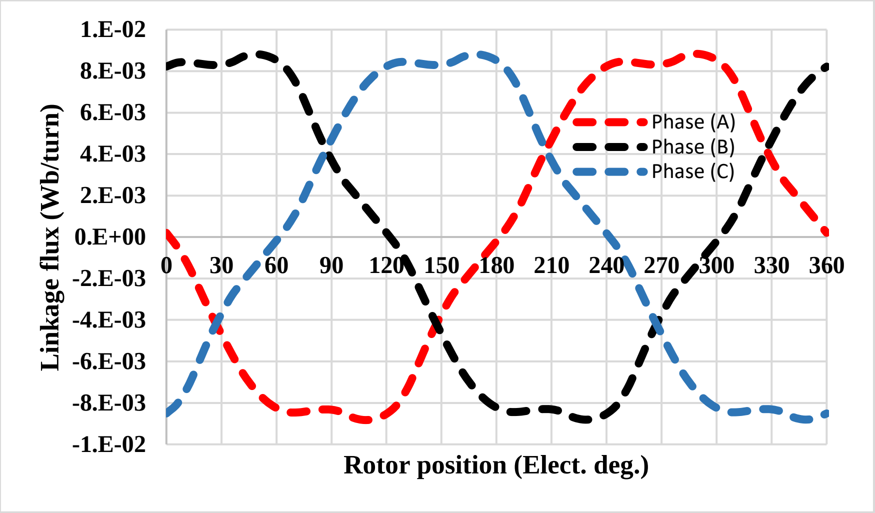

(a) 3-phase linkage flux waveforms

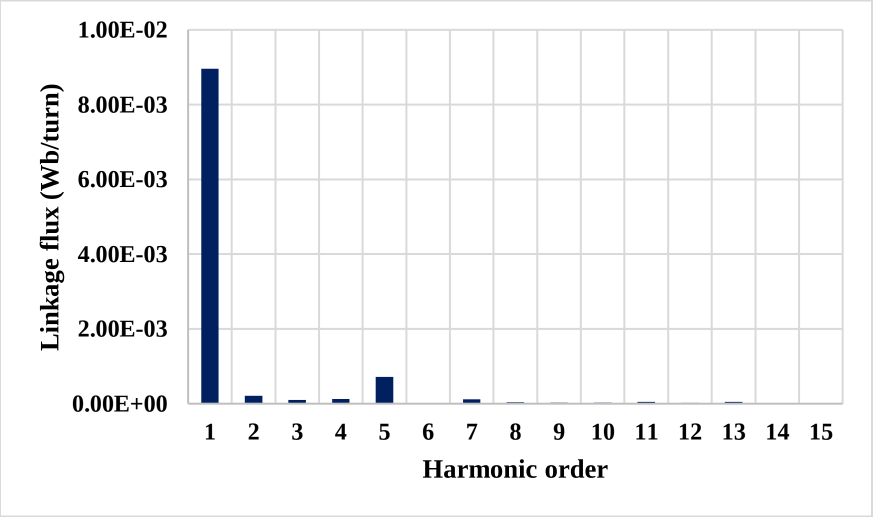

(b) Harmonic spectrum

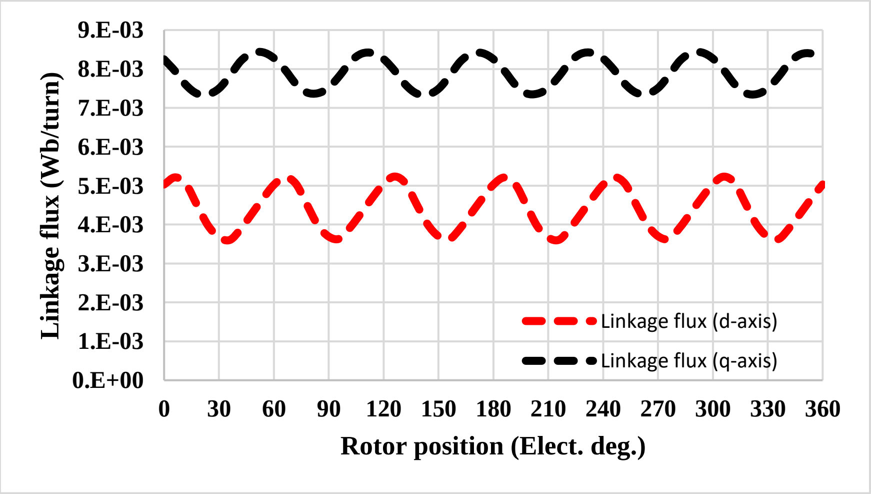

(c) d-q axes phase flux linkage waveforms

Fig. 3.13 Linkage flux at I_{max}=880.27 A/turn, speed = 2250 r/min, γ= 25°.

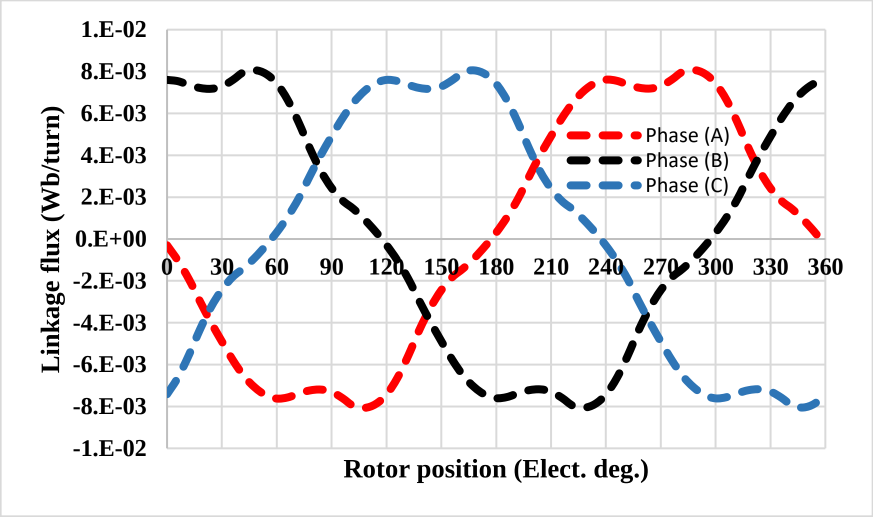

(a) 3-phase linkage flux waveforms

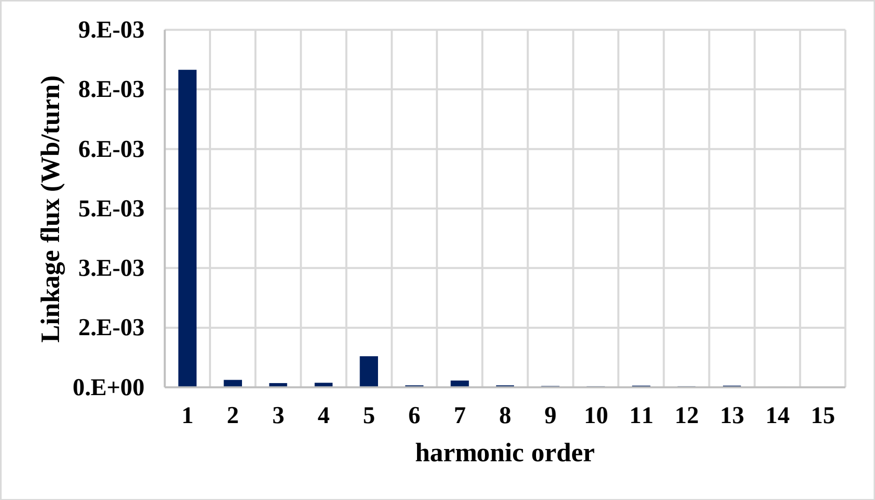

(b) Harmonic spectrum

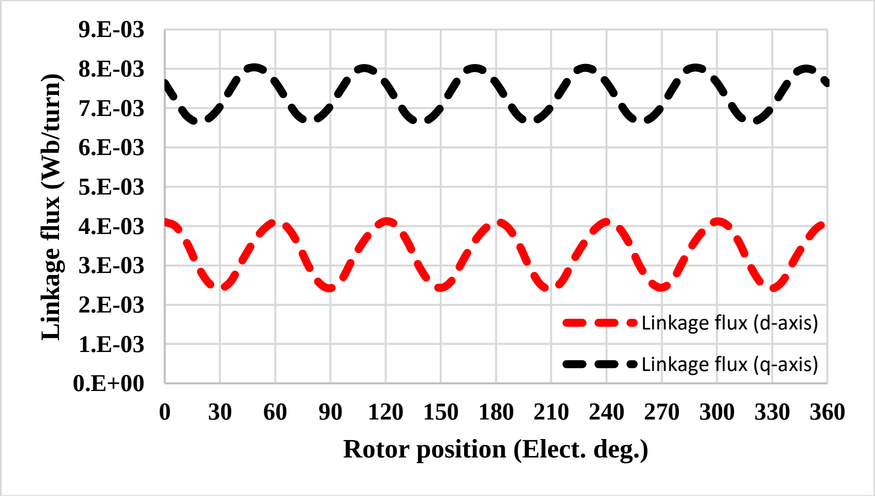

(c) d-q axes phase flux linkage waveforms

Fig. 3.14 Linkage flux at I_{max} = 880.27 A/turn, speed = 2500 r/min, γ = 35.65°.

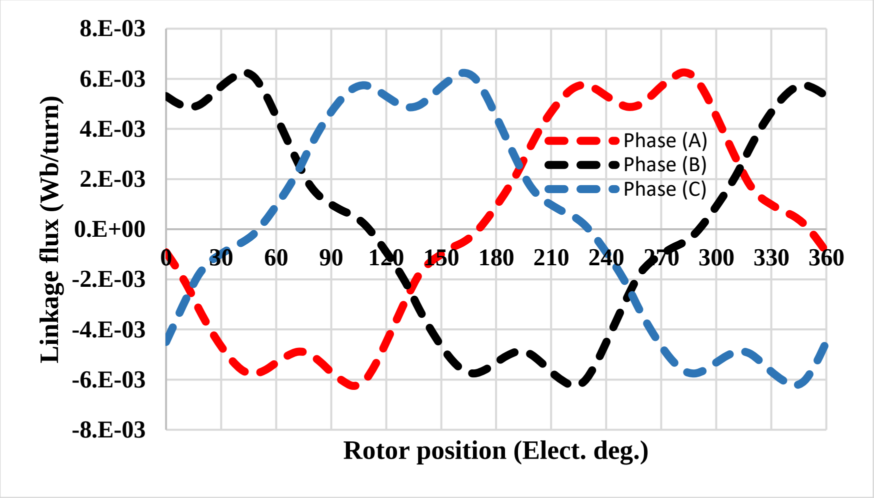

(a) 3-phase linkage flux waveforms

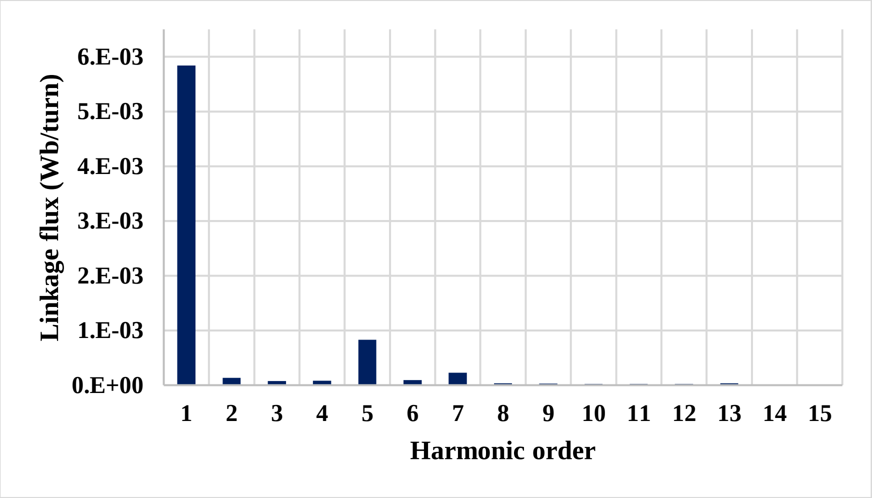

(b) Harmonic spectrum

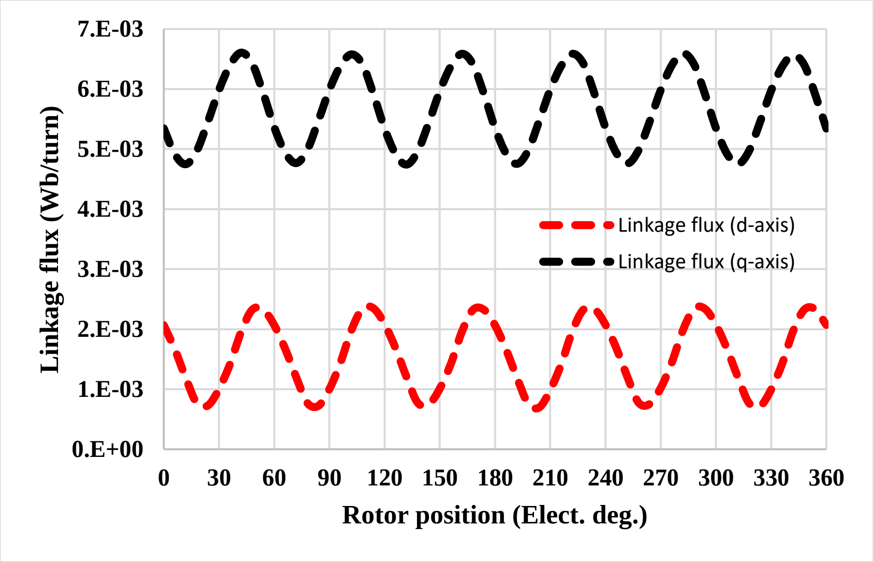

(c) d-q axes phase flux linkage waveforms

Fig. 3.15 Linkage flux at I_{max} = 880.27 A/turn, speed = 3500 r/min, γ = 52.39°.

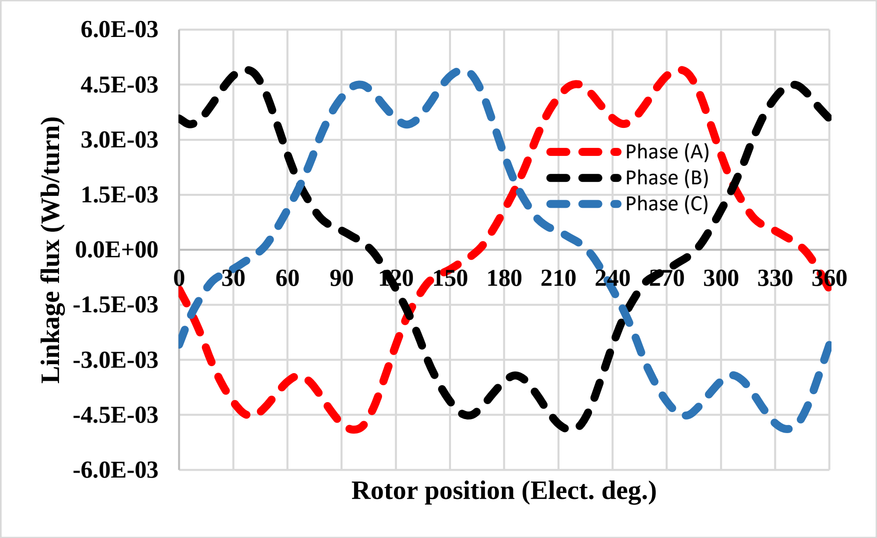

(a) 3-phase linkage flux waveforms

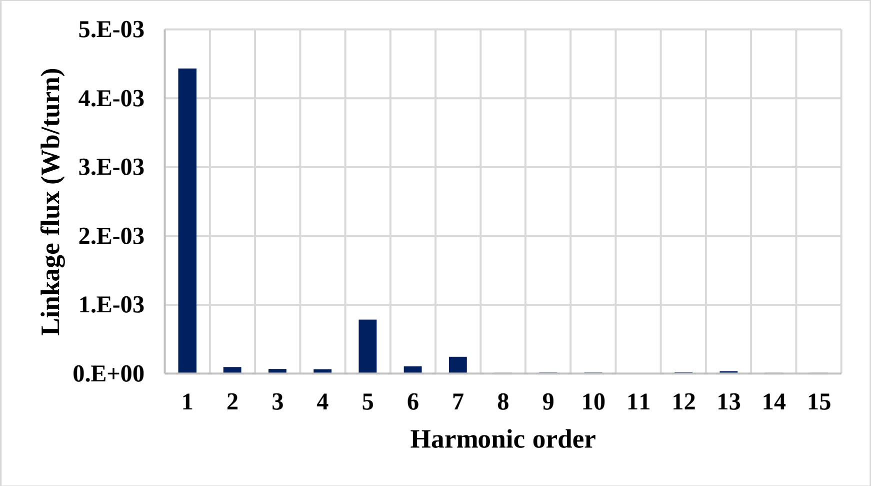

(b) Harmonic spectrum

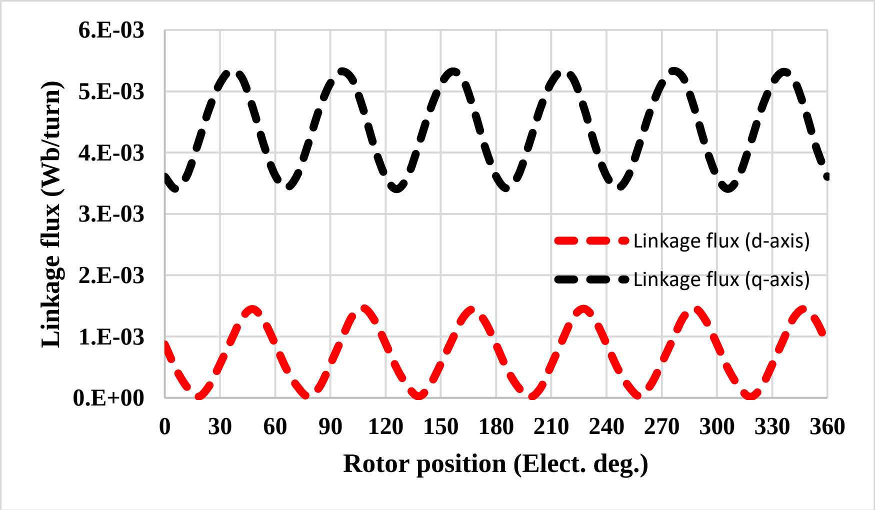

(c) d-q axes phase flux linkage waveforms

Fig. 3.16 Linkage flux at I_{max} = 880.27 A/turn, speed = 4500 r/min, γ = 62.07°.

3.3.3.2 Torque waveforms at load condition

The waveforms of the electromagnetic torque which are predicted using 3D-FEA at base speed = 2250 r/min and during the field weakening working region are shown in Fig. 3.17–Fig. 3.20. In the field weakening region as the speed increases the value of the torque will be reduced in order to work with constant power. In order to get maximum current per ampere the field weakening region, there will be d-axis current (I_d) injected as the as the maximum current angle (γ) will be $>$ zero). The average values of the torque will be maximum at the base speed = 2250 r/min and then started to decrease when working at the high speed in order to get the same required output power as much as possible, as will be seen in the generated torque speed envelopes later.

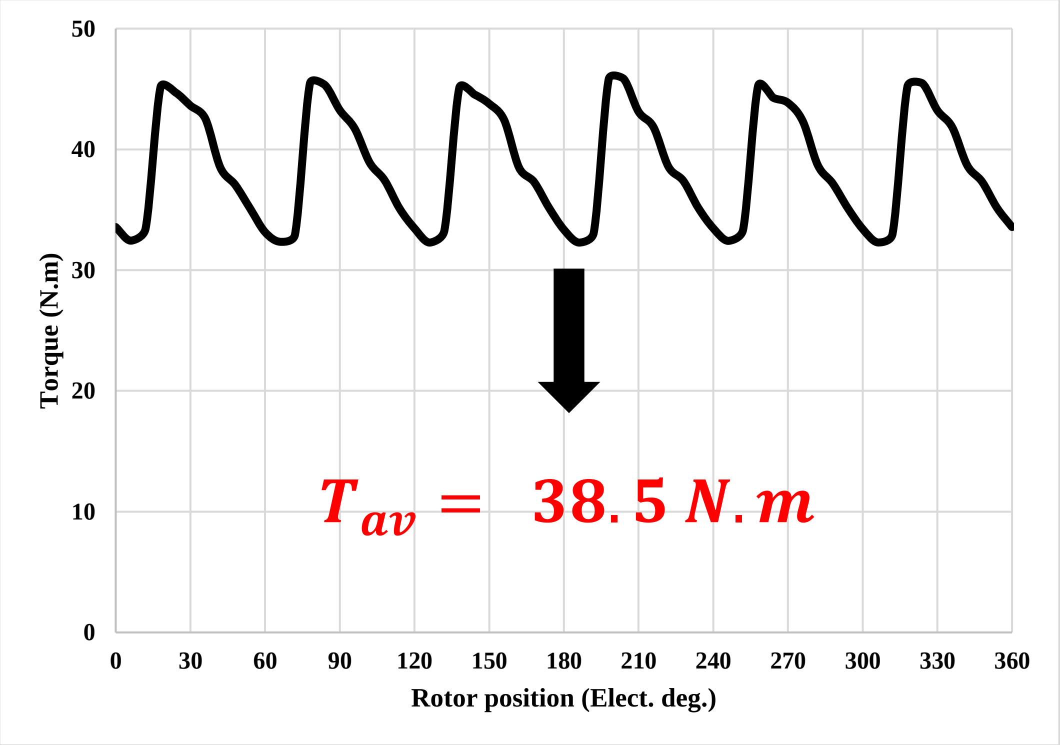

Fig. 3.17 Torque waveform at I_{max} = 880.27 A/turn, based speed = 2250 r/min, γ = 25°, I_d= -372.018 A/turn, I_q= 797.7956 A/turn.

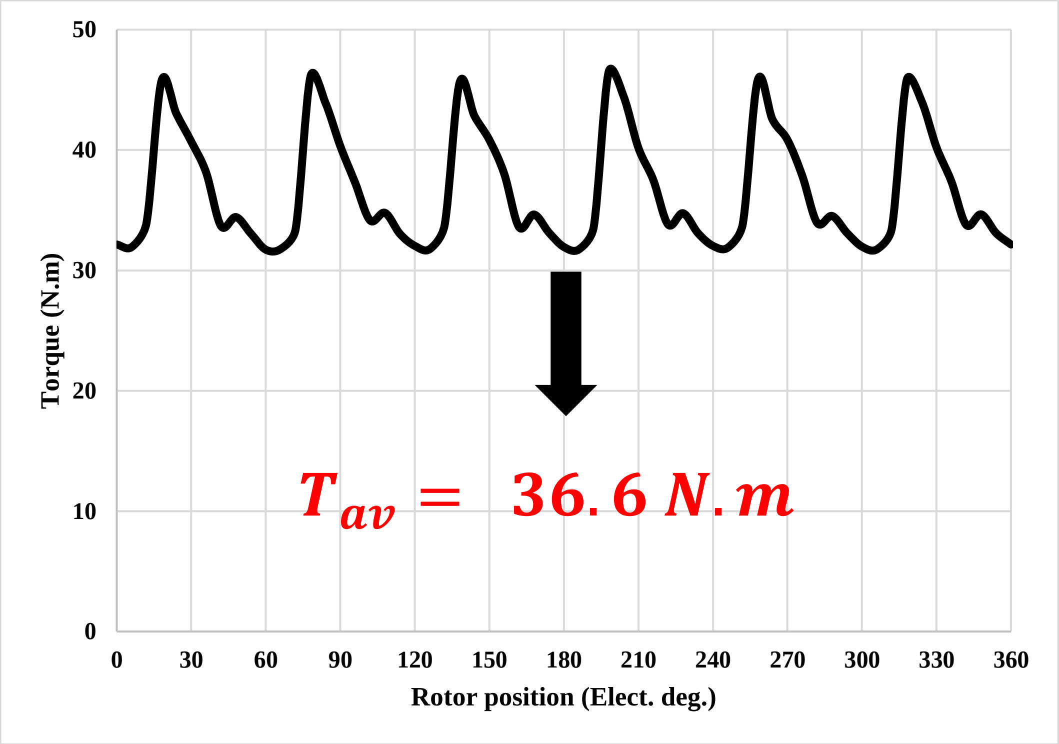

Fig. 3.18 Torque waveform at I_{max}= 880.27 A/turn, speed = 2500 r/min, γ = 35.65°, I_d = -513.161 A/turn, I_q = 715.2212 A/turn.

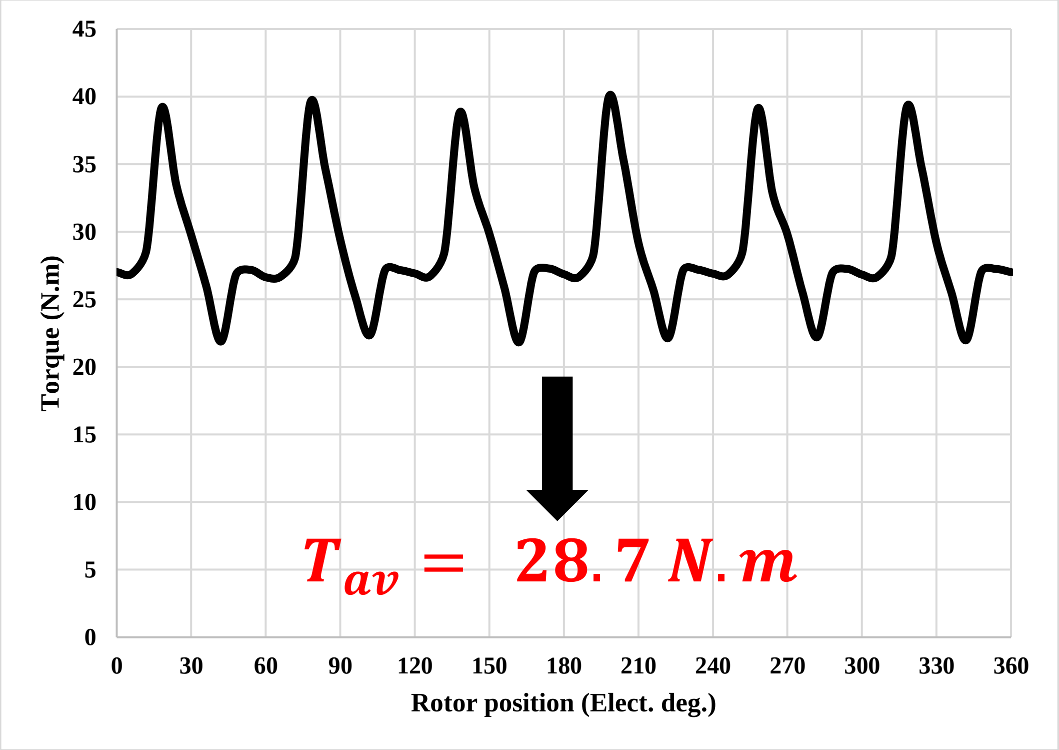

Fig. 3.19 Torque waveform at I_{max}= 880.27 A/turn, speed = 3500 r/min, γ = 52.39°, I_d= -697.349 A/turn, I_q = 537.1967 A/turn.

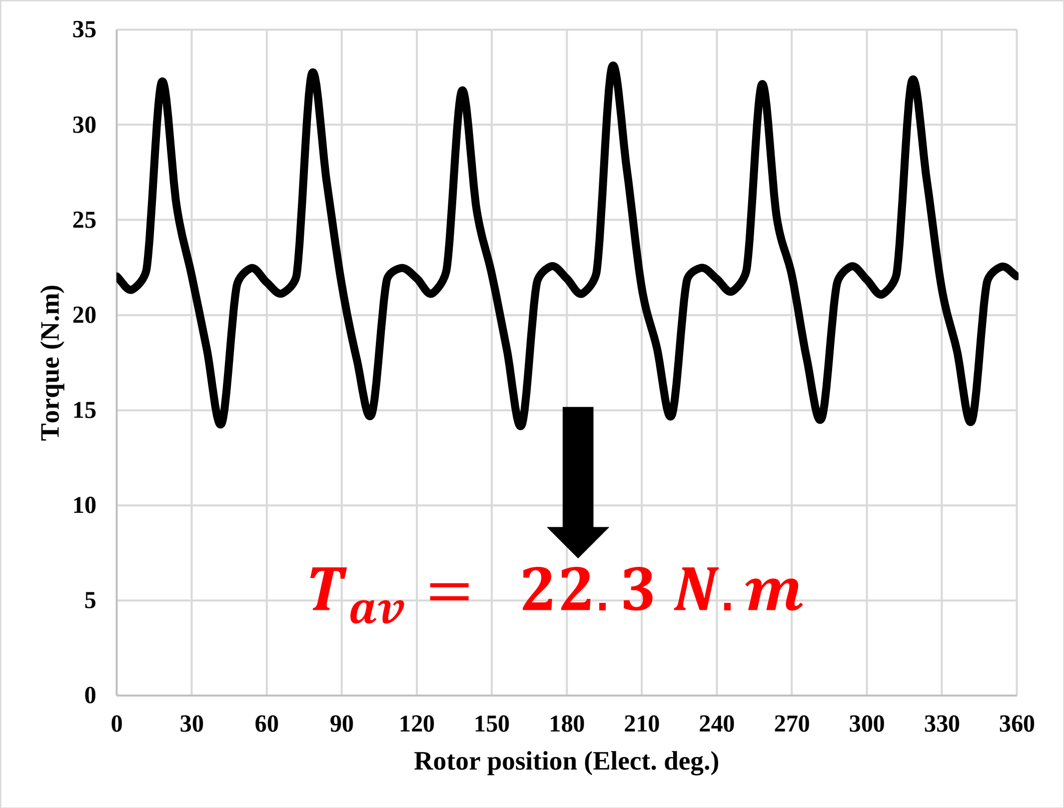

Fig. 3.20 Torque waveform at I_{max} = 880.27 A/turn, speed = 4500 r/min, γ = 62.07°, I_d = -777.796 A/turn, I_q = 412.19 A/turn.

3.3.4 Torque components separation using frozen permeability

The well-known equation of the electromagnetic torque of the machine is [48]:

$$T_{em} = \frac{m}{2} P\left[\Psi_d(i_d, i_q, \theta) i_q - \Psi_q(i_d, i_q, \theta) i_d\right] \qquad 3.5$$

Under low magnetic saturation (low load condition), the mutual coupling between the d and q axis of the magnetic circuit will be very small and negligible. Therefore, the d and q axis of the linkage flux are expressed using Eq. 3.6 [49].

$$\Psi_d = \Psi_m(i_d, i_q, \theta) + L_d(i_d, i_q, \theta) i_d \qquad 3.6$$

$$\Psi_q = L_q(i_d, i_q, \theta) i_q$$

On the other hand, at high load condition and if high value of torque is required, the magnetic saturation will be high. Therefore, the mutual coupling between the d and q axis of the magnetic path should be considered in the calculation of the d and q axis of the linkage flux equation as shown in Eq. 3.7 [49].

$$\begin{aligned} \mathit{\Psi}_d &= \mathit{\Psi}_{md}(i_d, i_q, \theta) + L_d(i_d, i_q, \theta) i_d + M_{dq}(i_d, i_q, \theta) i_q \qquad 3.7 \\ \Psi_q &= \Psi_{mq}(i_d, i_q, \theta) + M_{qd}(i_d, i_q, \theta) i_d + L_q(i_d, i_q, \theta) i_q \end{aligned}$$

Substituting Eq. 3.7 into Eq. 3.5, the resulting torque equation will be [49]:

$$T_{em} = \frac{m}{2} P\left[\Psi_{md} i_q - \Psi_{mq} i_d + (L_d - L_q) i_d i_q + M_{dq} {i_q}^2 - M_{qd} {i_d}^2\right] \qquad 3.8$$

Due to saturation effect, the reluctance of the d and q axis of the stator iron will be unequal due to the relative permeability change of the stator iron at different rotor position as shown in Fig. 3.21.

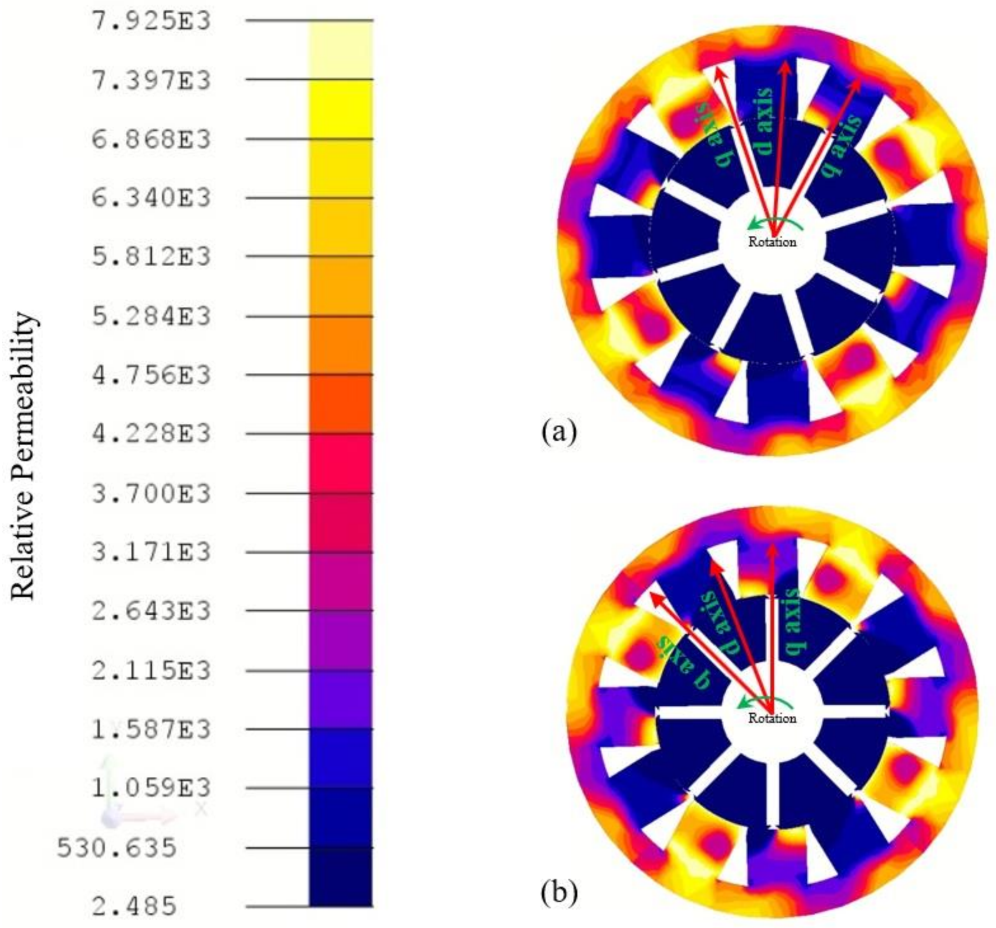

Fig. 3.21 Relative permeability contour at base rotation speed (a) Rotor position =15°, (b) Rotor position =43.5°.

As a result, the interaction between the rotor magnetic field with the unequal reluctances in the d and q axis will contribute torque component T_{mr}, which will be added to Eq. 3.8. and the final equation will be Eq. 3.9 [49].

$$T_{em} = \frac{m}{2} P\left[\Psi_{md} i_q - \Psi_{mq} i_d + \left(L_d - L_q\right) i_d i_q + M_{dq} {i_q}^2 - M_{qd} {i_d}^2\right] + T_{mr} \qquad 3.9$$

In this section, the instantaneous torque components shown in Eq. 3.9, are separated using frozen permeability process via FLUX 3D software as described below.

Fig. 3.22 illustrates the concept of the frozen permeability, where PM, i and *combined* refer to PM excitation, current excitation and the combination of both PM and current excitation respectively [48], $H_{combined}$ is the combined magnetic fields which is the combination of the H_{PM} and H_i. It can be noticed that the summation of $B_{PM} + B_i > B_{combined}$ which means $B_{combined}$ cannot be obtained by superposition B_{PM} and B_i respectively due to the difference of their relative permeability μ_{PM} and μ_i. Therefore, the concept of the frozen permeability assume that the relative permeability will be fixed at value of $\mu_{combined}$. In other words, the B-H relationship will be straight line with a slop of $\mu_{combined}$. As a result, the new combination of flux density $B_{combined} = B_{PM\_FP} + B_{i\_FP}$.

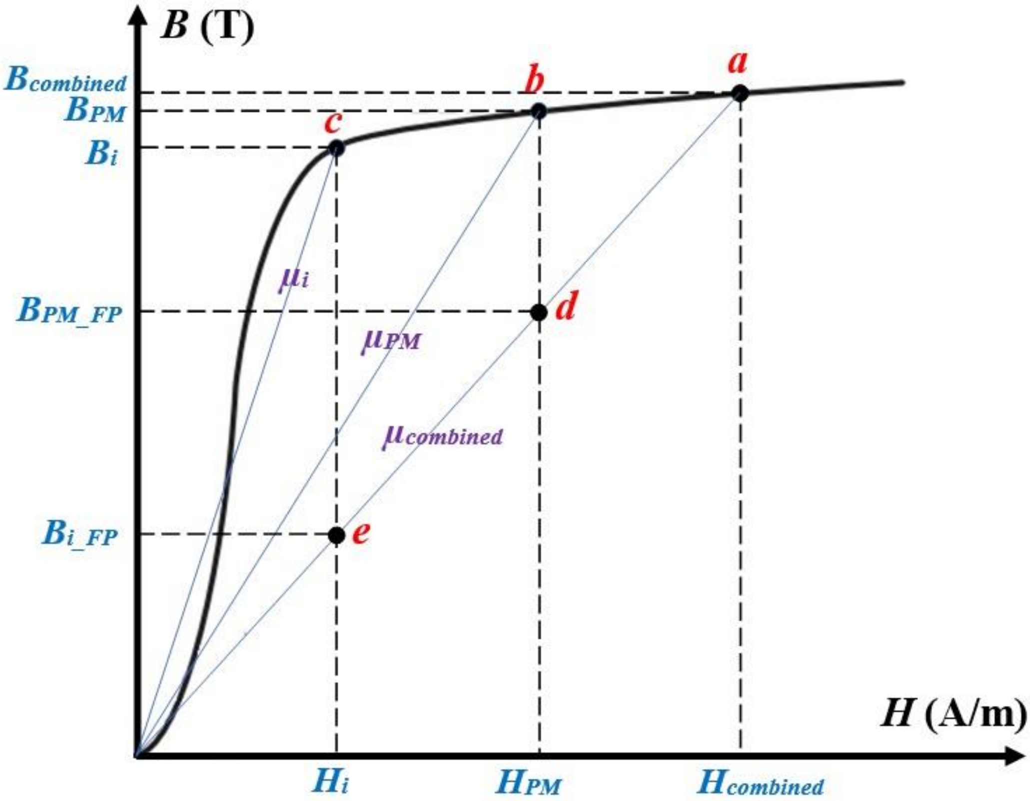

Fig. 3.22 Frozen permeability concept diagram [49]

The process for one electrical cycle using frozen permeability concept is deduced in the flow chart as shown in Fig. 3.23, where A-F are defined in Table 3.2. In this process, the frozen permeability concept is applied to stator part material. Therefore, the magnetic characteristic of stator material is updated from the original B-H curve to the spatial quantity at the present rotor position. This process will be continued until one electrical period is over.

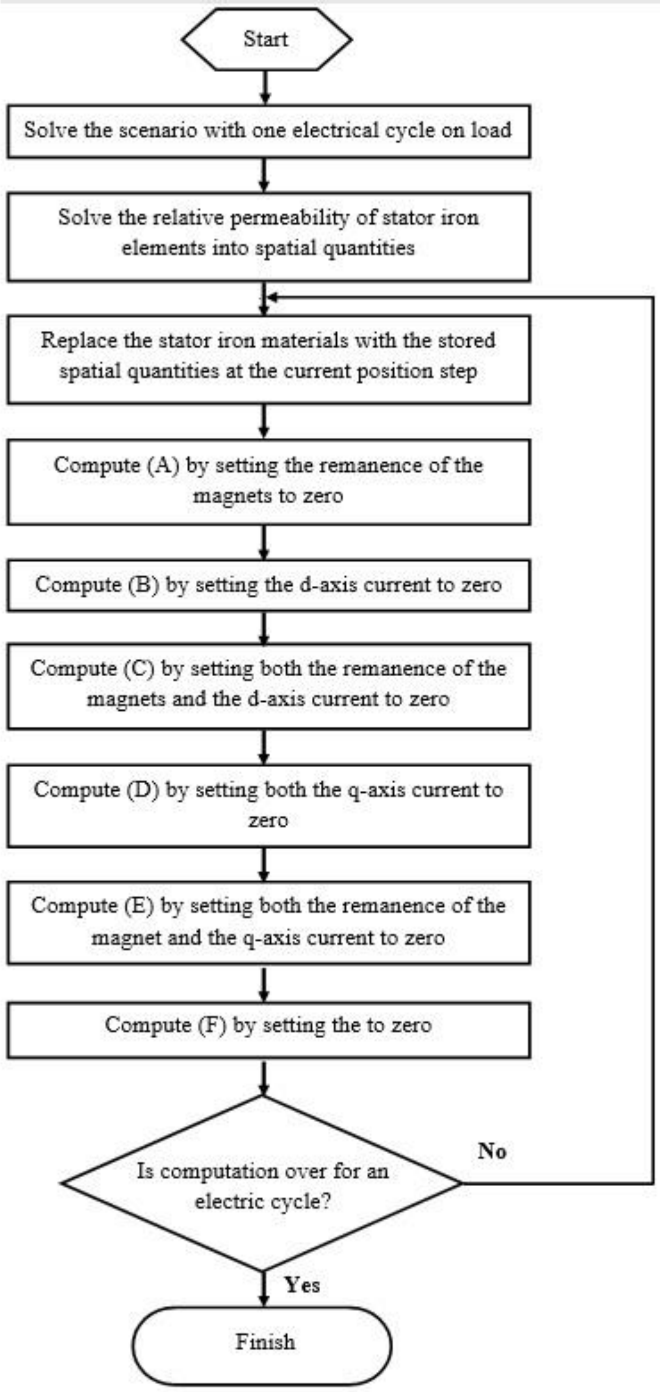

Fig. 3.23 Process of frozen permeability concept [49]

To compute the components of the electromagnetic torque at the rated speed, the excitation sources are changed in order to accurately compute the torque components resulted from this source as described in Table 3.2. It can be seen that the torque can be separated into six components and the final torque equation will be Eq. 3.10.

Torque components	Description	Equation
A	Remove magnets	$\frac{m}{2}P\left[\left(L_d-L_q\right)i_di_q+M_{dq}{i_q}^2-M_{qd}{i_d}^2\right]$
B	Just q-axis current as input load	$\frac{m}{2}P\left[\Psi_{md}i_q+M_{dq}{i_q}^2\right]+T_{mr}$
C	Remove magnets & Just q-axis current as input load	$\frac{m}{2}PM_{dq}{i_q}^2$
D	Just d-axis current as input load	$\frac{m}{2}P\left[-\Psi_{mq}i_d-M_{qd}{i_d}^2\right]+T_{mr}$
E	Remove magnets & Just d-axis current as input load	$-\frac{m}{2}PM_{qd}{i_d}^2$
F	No current	T_{mr}

Table 3.2 Torque components separation using frozen permeability process [49]

$$T_{em}=A+B-C+D-E-F \tag{3.10}$$

To achieve torque component (A), the rotor magnets are removed by setting the remanence of the magnets ($B_r =$ zero) and keep armature current as excitation source. Furthermore, the torque components (B and D) are achieved by exploiting just q-axis and d-axis of the armature current as input source respectively. Besides that, torque components (C and E) are achieved by removing the rotor magnets as for (A) but with only q-axis and d-axis of the armature current as input source, respectively. Finally, torque component (F) which represent the component contributed by the interaction of the rotor permanent magnet field with the unequal d and q direction in stator iron is achieved by removing the armature current source, in this case the rotor permanent magnet field will represent the only excitation source for the machine. To achieve each component mentioned above, the geometry is simulated and solved for one electric cycle based in the concept of the frozen permeability using 3D FLUX software developed by CEDRAT.

The waveforms of the torque components which are defined in Table 3.2, at rated speed are shown in Fig. 3.24 and the average torque values and the percentage values with rated torque average value are shown in Table 3.3.

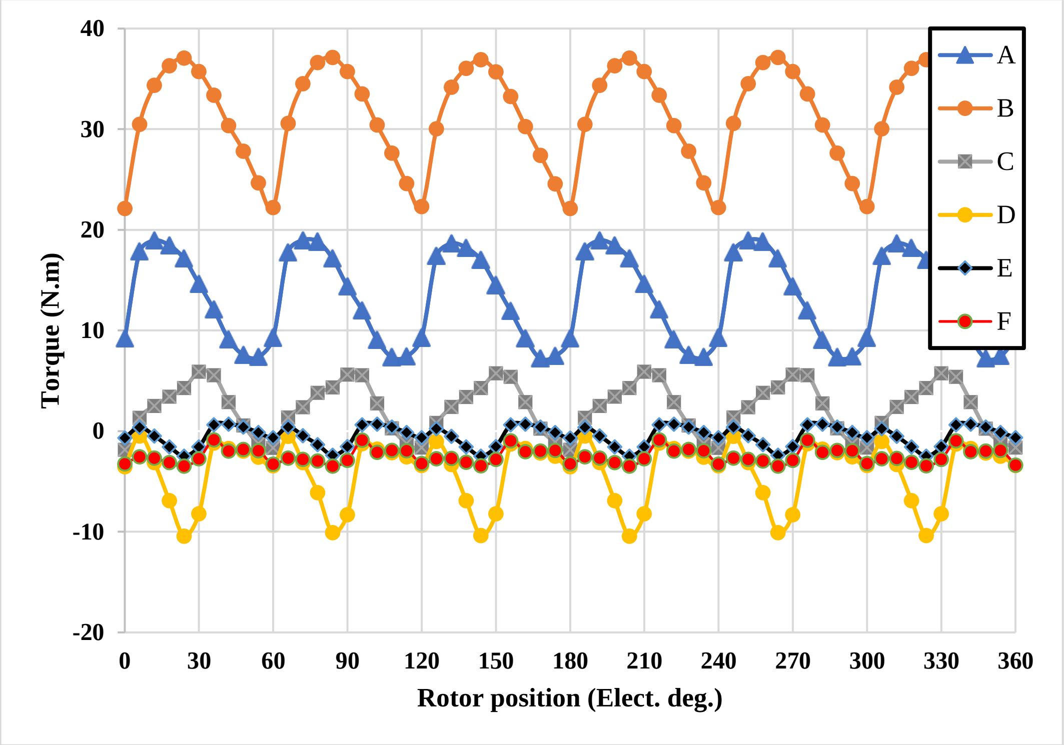

Fig. 3.24 Waveforms of torque components at base speed.

Torque components	Average torque (N.m)	Average torque ratio (%)
A	13.1	32.06 %
B	31	75.95 %
C	2.24	5.47 %
D	-4	-9.78 %
E	-0.46	-1.14 %
F	-2.49	-6.1 %
(A+B-C+D-E-F)	40.81	100 %

Table 3.3 Average value of the separated torque components.

Fig. 3.25 shows a comparison between the predicted torque waveforms using (with and without using frozen permeability concept) and the one obtained by 3D-FEA. (Model 1) represents the waveform of the electromagnetic torque which is predicted based on 3D-Flux software while (Model 2) represents the waveform of the torque predicted based on the frozen permeability concept and taken into account the effect of torque component (T_{mr}) as shown in Eq. 3.9 or Eq. 3.10. It can be noticed that (Model 2) and based on frozen permeability concept is accurately represented the waveform produced by 3D-FEA with small error comparing with the other predicted waveforms. In contrast, the classic model of the torque shown in Eq. 3.11 (Model 3) and based on frozen permeability has a large error comparing with 3D-FEA, since it neglects the effect of mutual inductance (M_{dq} and M_{qd}) and the torque component (T_{mr}). On the other hand, the classical model of the torque (Model 4) shown in Eq. 3.11 without using frozen permeability concept only matches the average value of the torque predicted by 3D-FEA.

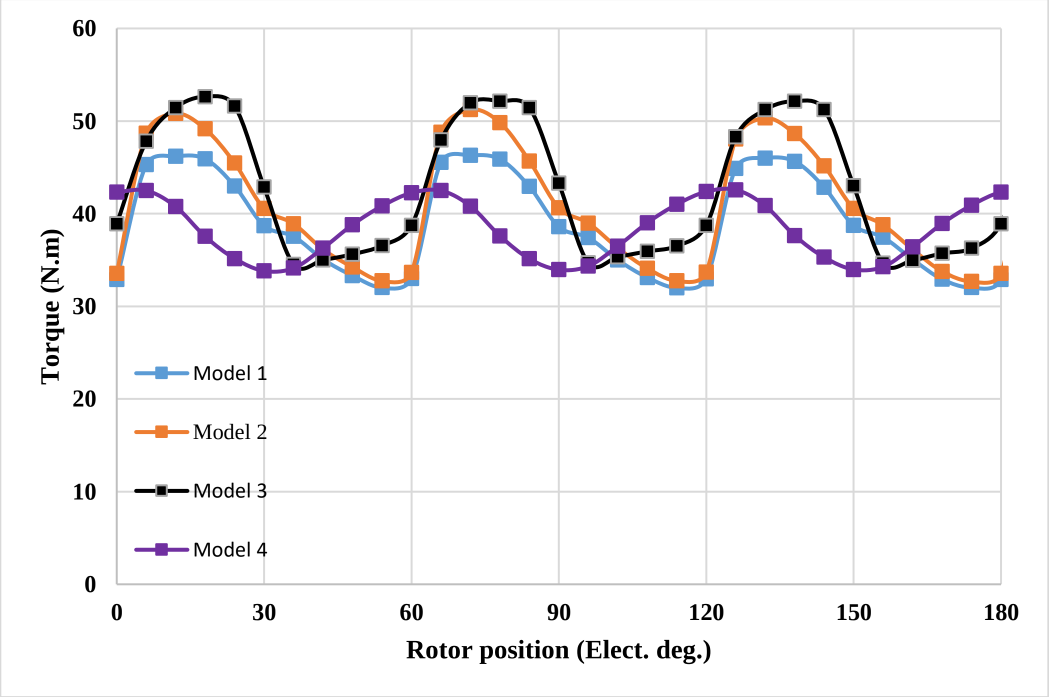

Fig. 3.25 Comparison of the calculated torque waveforms with 3D-FEA.

$$T_{em} = \frac{m}{2} P\left[\Psi_{md} i_q + \left(L_d - L_q\right) i_d i_q\right] \quad 3.11$$

$$= \mathrm{A} + \mathrm{B} - 2\mathrm{C} - \mathrm{E} - \mathrm{F}$$

The calculation of the reluctance torque (T_{rel}) is also done using classic torque model with and without frozen permeability process (Model 3 & Model 4) and the proposed model in [49] (Model 2) based on frozen permeability concept as shown in Eq. 3.12 & Eq. 3.13 respectively. The comparison between the three predicted waveforms of the reluctance torque is shown in Fig. 3.26 and Table 3.4. It can be noticed that the reluctance torque predicted based on (Model 2) with frozen permeability method is more accurate comparing with the other two components since, the classic model of the reluctance torque with and without using the frozen permeability process neglects the effect of the torque component resulted from mutual inductances. On the other hand, the effect of the torque (T_{mr}) on the reluctance torque component generated from (Model 2) and (Model 3) of the reluctance using frozen permeability is low, due to the fact that the value of (T_{mr}) is contributed by the alignment torque calculated using frozen permeability which is lower while the reluctance torque is higher compared with classic model of the reluctance torque without using frozen permeability process (Model 4) as shown in Table 3.4. Therefore, it can be concluded that the predicted torque using (Model 2) based on the frozen permeability concept, can accurately validate the torque produced by 3D-FEA.

$$T_{rel} = \frac{m}{2} P\left[\left(L_d - L_q\right) i_d i_q\right] = \mathrm{A} - \mathrm{C} - \mathrm{E} \quad 3.12$$

$$T_{rel} = \frac{m}{2} P\left[\left(L_d - L_q\right) i_d i_q + M_{dq} {i_q}^2 - M_{qd} {i_d}^2\right] = \mathrm{A} \quad 3.13$$

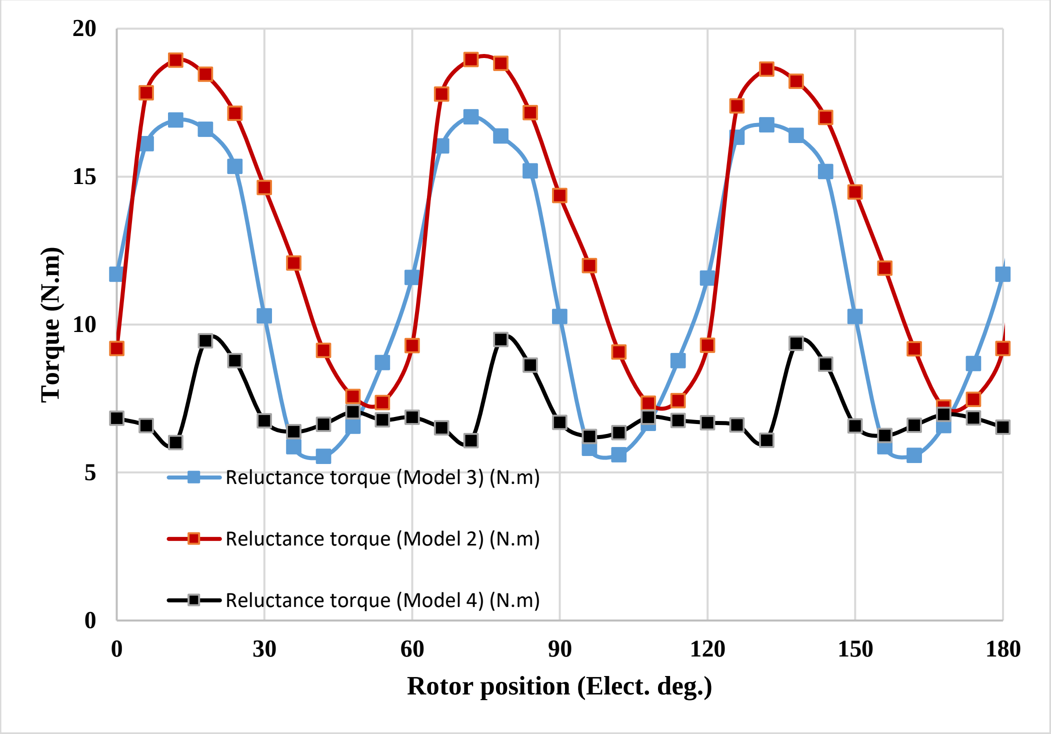

Fig. 3.26 Comparison of the reluctance torque waveforms.

	Model 3	Model 2	Model 4
Average reluctance torque (N.m)	11.3	13.1	7
Average reluctance torque ratio (%)	27.6 %	32 %	17.1 %

Table 3.4 Average values of the predicted reluctance torques.

3.4 Torque & power speed envelope

In this section, the generated torque & power speed envelops which are predicated based on 3D-FEA at different airgap shear stress are detailed. Fig. 3.27 shows the torque & power speed envelope at maximum airgap shear stress = 20kPa and $I_{max} =$ 880.27 A/turn. It can be noticed that a continuous torque of about 38 N.m can be getting below and at base speed = 2250 r/min and high output mechanical power of about 9 kW. The iron losses of stator material are computed using the 3D- FE based on Bertotti formula which including the computation of hysteresis losses, classical losses and excess losses as shown in Eq. 3.14.[63].

$$P_{fe} = \mathrm{K_f}\,[\text{Losses by hysteresis + Classical losses + Losses in excess}] \qquad 3.14$$

$$\text{Losses by hysteresis} = \mathrm{K_h B_m^{\alpha_h} f^{\beta_h}}$$

$$\text{Classical losses} = \sigma \frac{\mathrm{d^2}}{12}\left[\frac{\mathrm{dB}}{\mathrm{dt}}(\mathrm{t})\right]^{\alpha_\mathrm{c}}$$

$$\text{Losses in excess} = \mathrm{K_e}\left[\frac{\mathrm{dB}}{\mathrm{dt}}(\mathrm{t})\right]^{\alpha_\mathrm{e}}$$

$\mathrm{K_h}$: Hysteresis loss coefficient (130.245 (Ws/$\mathrm{T^2/m^3}$)).

σ: Classical losses coefficient (1923077 S/m).

$\mathrm{K_e}$: Excess losses coefficient (0.357 (W/$\mathrm{(T/s)^{1.5}/m^3}$)).

d: Stator lamination thickness (0.35E-3 m).

$\mathrm{K_f}$: Stacking factor (0.97).

α_h: B exponent for Hysteresis losses (2.0).

β_h: f exponent for Hysteresis losses (1.0).

α_c: B exponent for Classical losses (2.0).

α_e: B exponent for Excess losses (1.5).

Consequently, the predicted efficiency map over the rated torque and speed range is shown in Fig. 3.28. It can be noticed that the high efficiency of about 97% and above occurs over the torque range of (12.5 – 38.5) N.m at speed range of 1500 – 4500 r/min. It should be noted that the iron losses in the rotor pole pieces and magnet are not accounted in the prediction of efficiency map. since the material of the rotor pieces is soft magnetic composite (SMC) material which is featured with magnetic isotropy and powder metallurgy characteristics comparing with the conventional silicon steel material and the losses of the ferrite magnet is low comparing with rare earth.

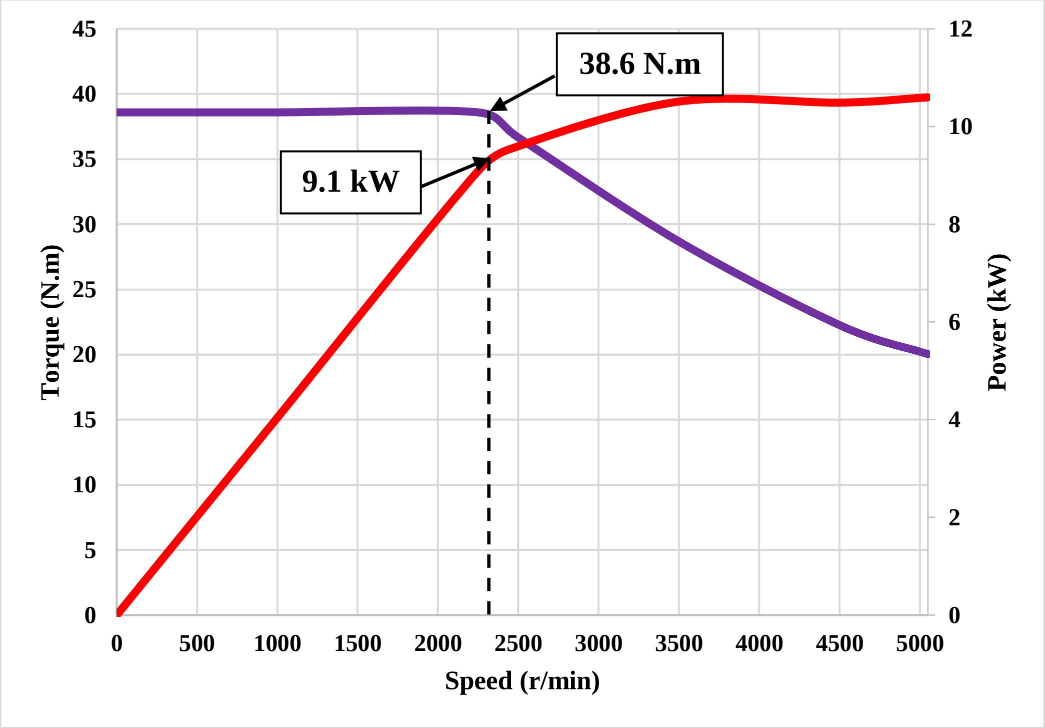

Fig. 3.27 Torque speed and power envelope at airgap shear stress 20kPa, I_{max}= 880.27 A/turn.

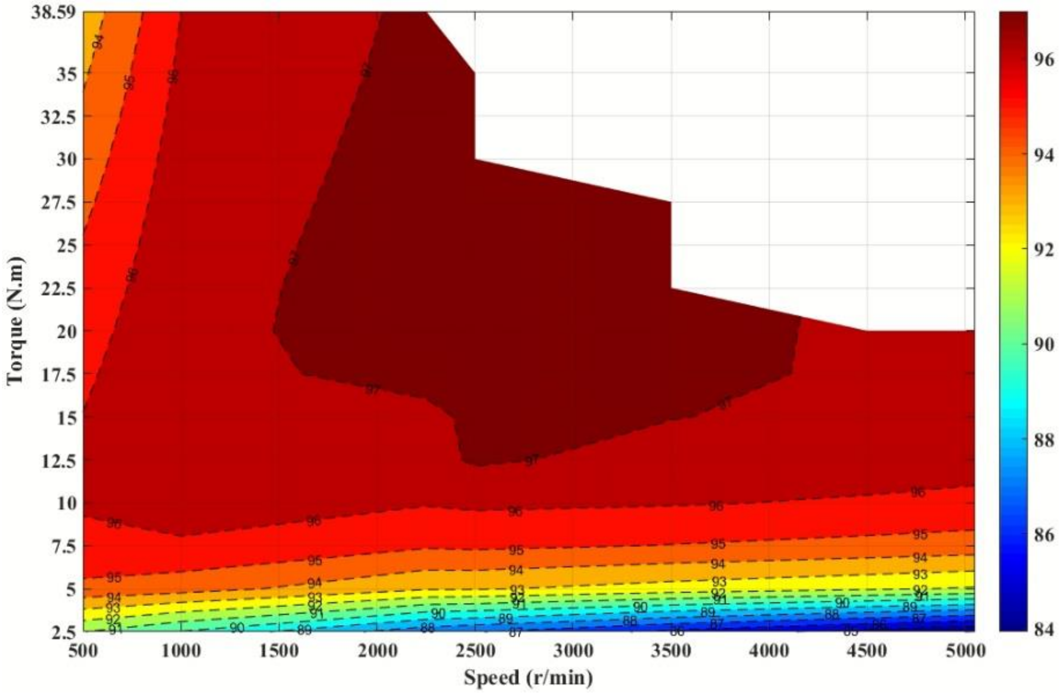

Fig. 3.28 Predicted efficiency map of the new proposed machine.

The predicted torque, power speed envelop and efficiency for the new proposed machine at different airgap shear stress are shown in Fig. 3.29 – Fig. 3.33. The value of the input current (I_{max}) is predicted at different shear stress as shown in the following equations:

The initial value of the electromagnetic torque (T_e) in firstly analytically calculated at different values of shear stress (σ) as shown in Eq. 3.15.

$$T_e = 2 \times V_{rotor} \times \sigma_{shear\ stress} \qquad 3.15$$

The value of the electrical loading ($Q_{r.m.s}$) is then predicted from the equation of the electromagnetic torque (T_e) as shown in 3.16.

$$T_e = \frac{\pi}{2\sqrt{2}} \times K_w \times {D_{bore-stator}}^2 \times L_{axial} \times Q_{r.m.s} \times B_1 \qquad 3.16$$

The input current (I_{max}) is set from the equation of the electrical loading ($Q_{r.m.s}$) as shown in Eq. 3.17.

$$Q_{r.m.s} = \frac{N_s \times I_{rms}}{\pi \times D_{bore-stator}} \qquad 3.17$$

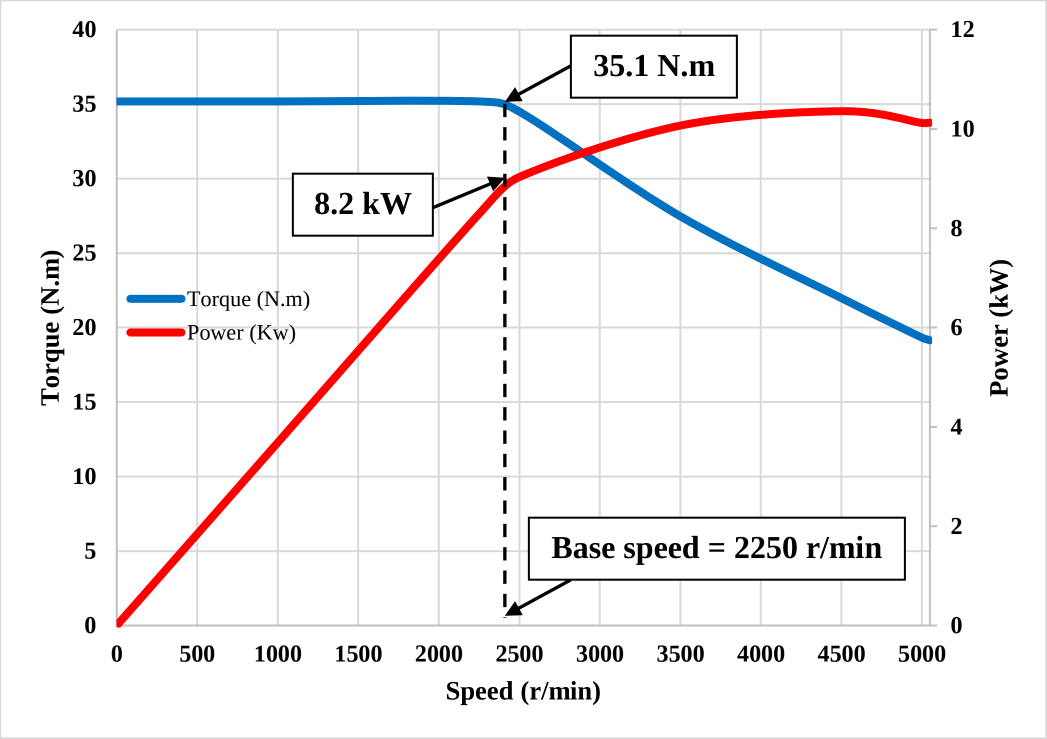

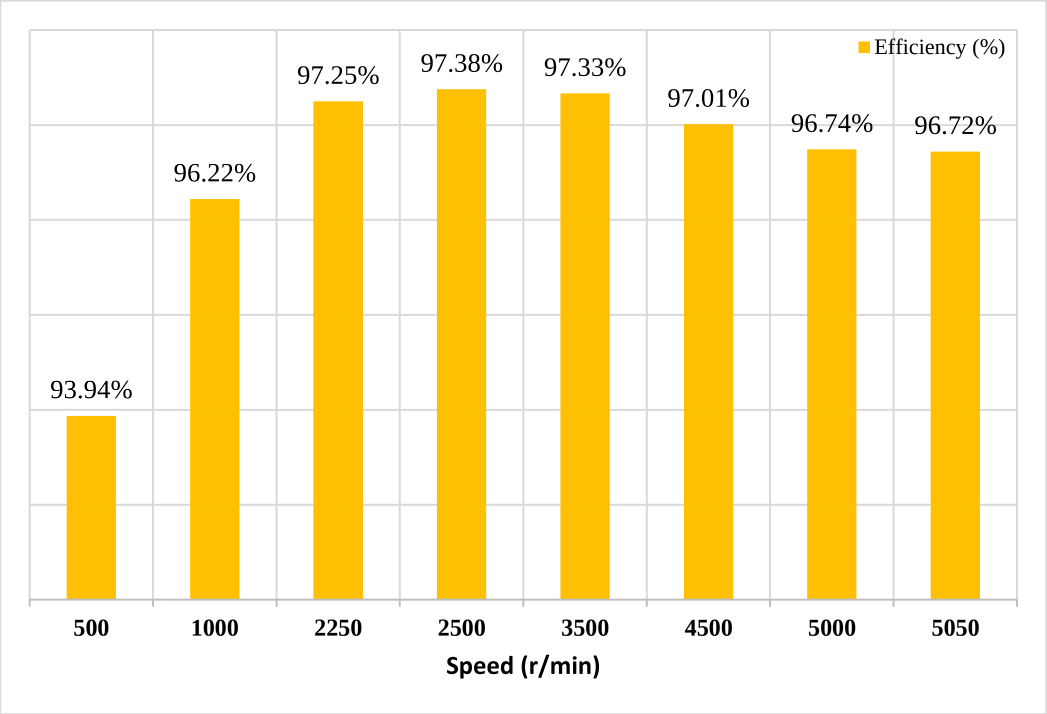

Fig. 3.29 Torque speed and power envelope and efficiency at airgap shear stress 18kPa, I_{max} = 792.24 A/turn.

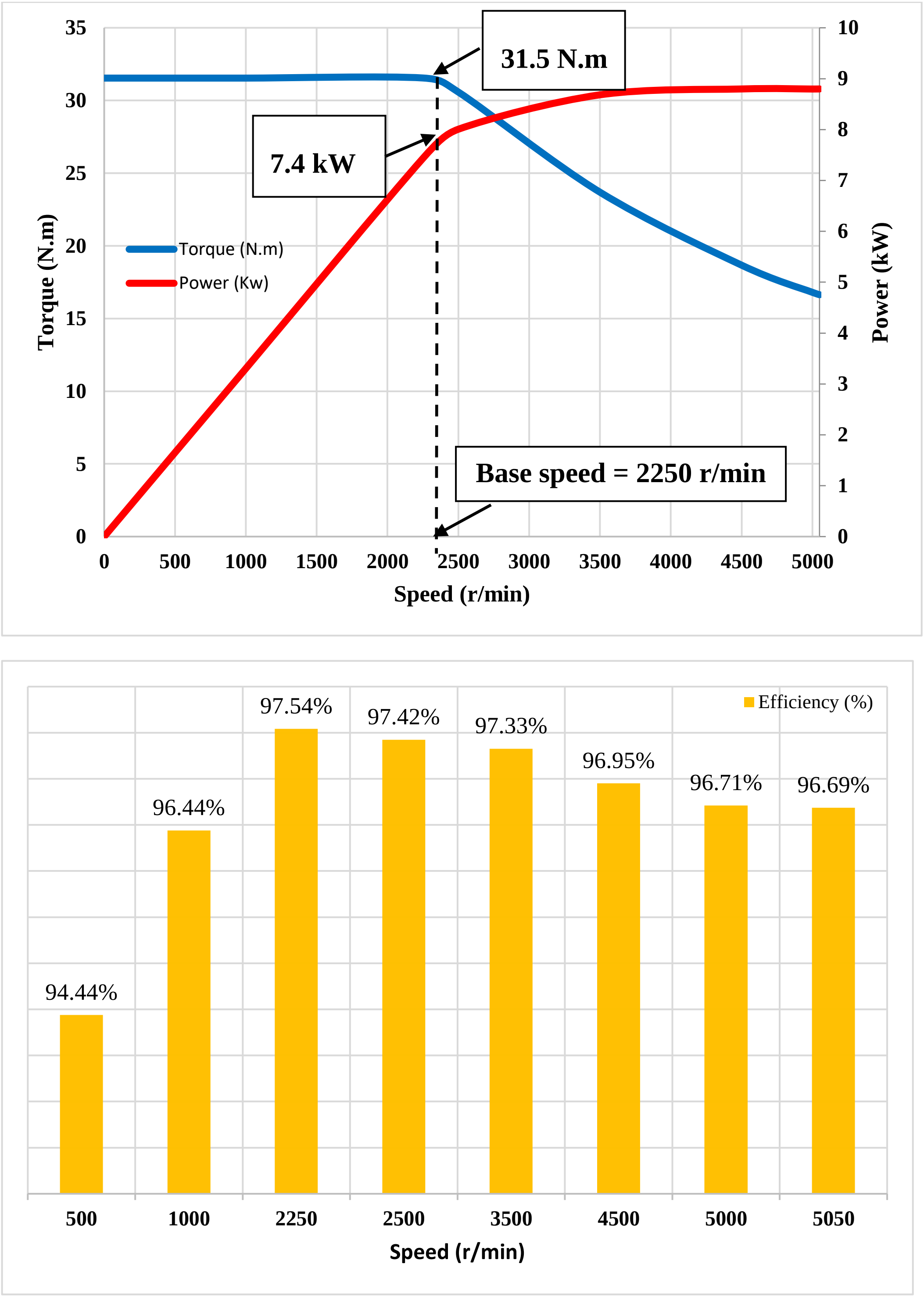

Fig. 3.30 Torque speed and power envelope and efficiency at airgap shear stress 16kPa, I_{max} =704.21 A/turn.

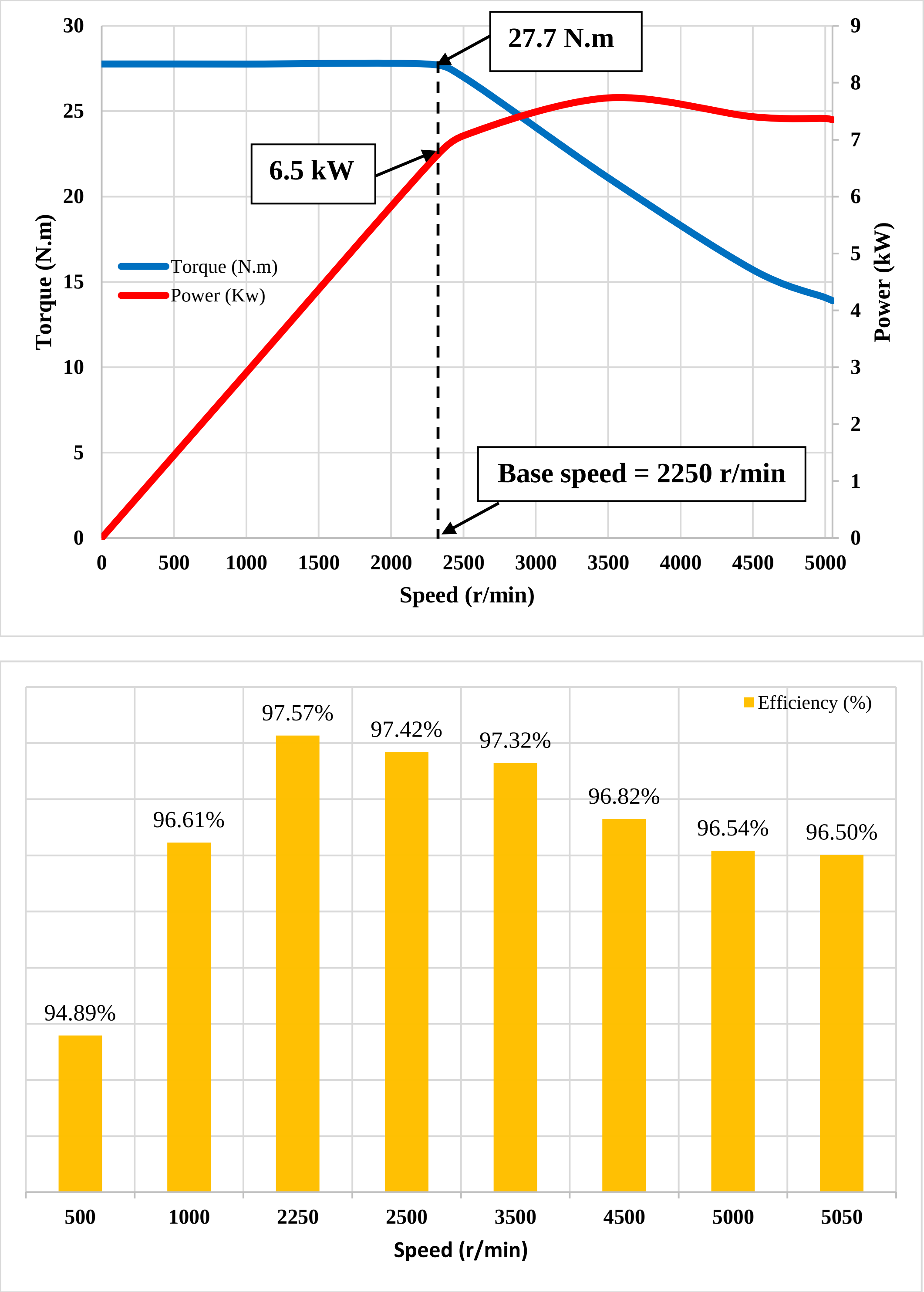

Fig. 3.31 Torque speed and power envelope and efficiency at airgap shear stress 14kPa, I_{max} = 616.19 A/turn.

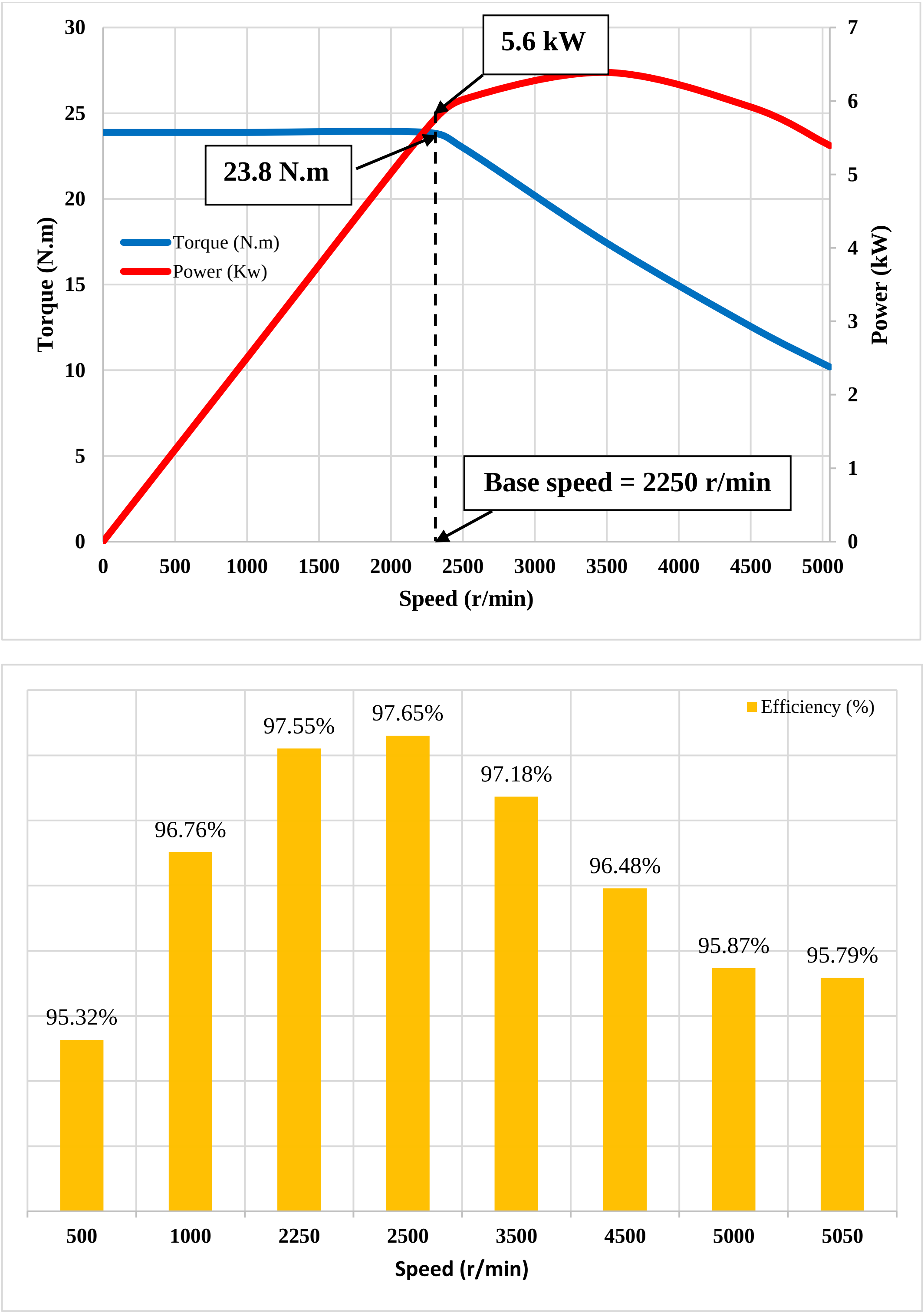

Fig. 3.32 Torque speed and power envelope and efficiency at airgap shear stress 12kPa, I_{max} = 528.16 A/turn.

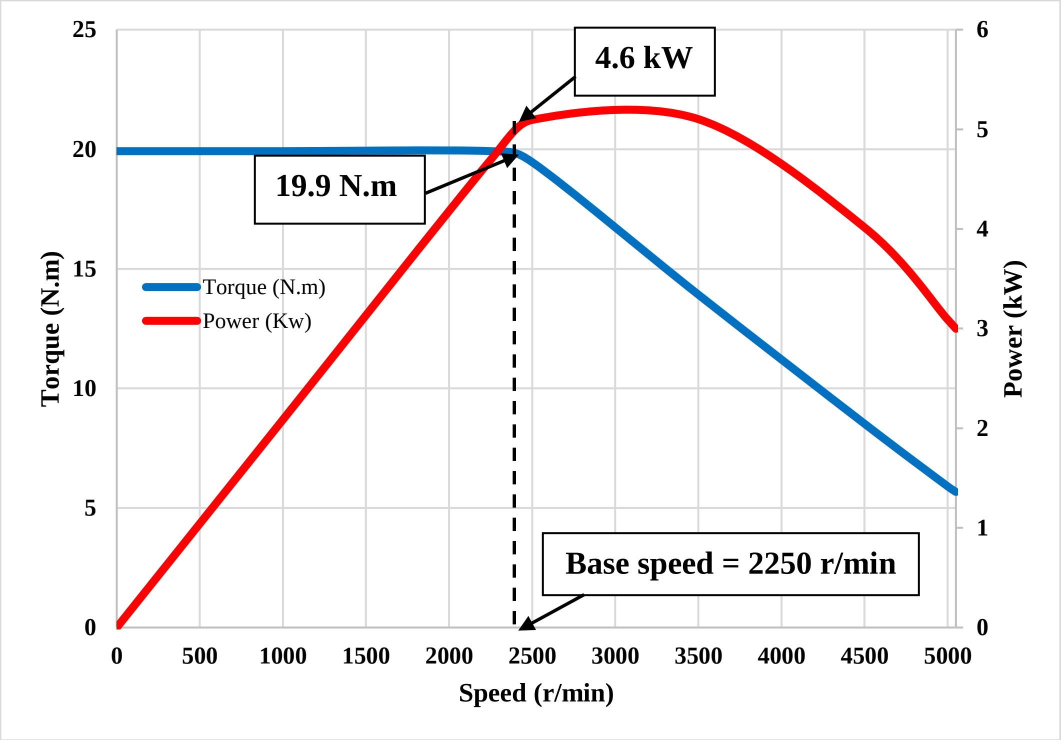

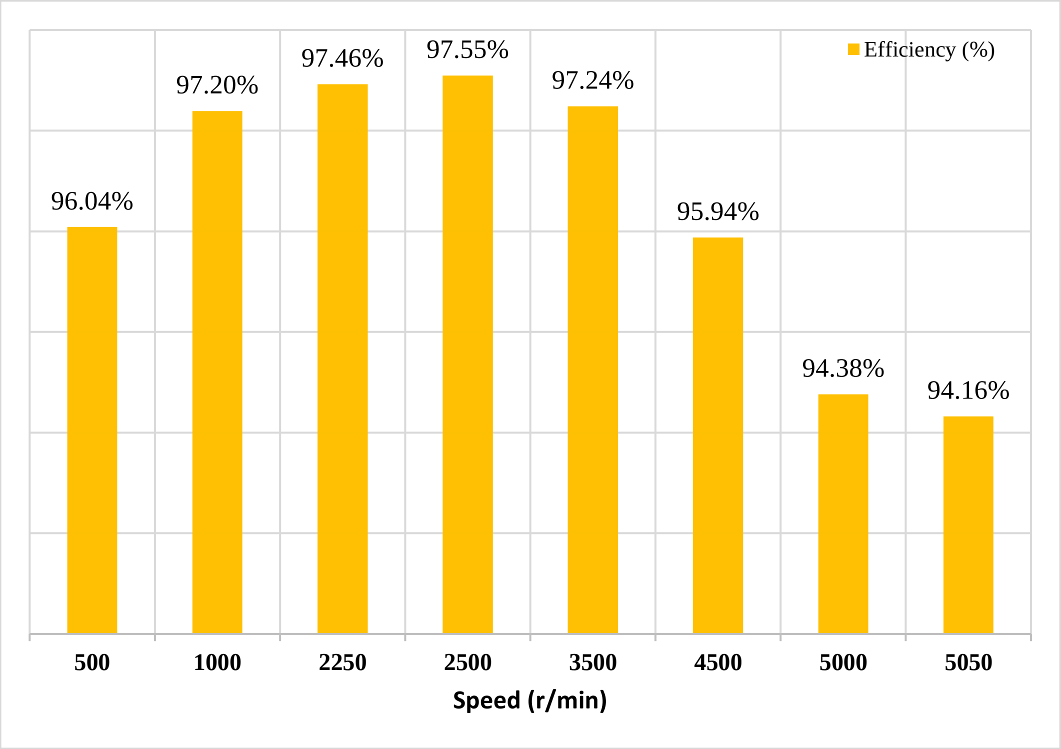

Fig. 3.33 Torque speed and power envelope and efficiency at airgap shear stress 10kPa, I_{max} = 440.13 A/turn.

3.5 Conclusion

In this chapter, the simulation and analysis of the new proposed machine is presented. Based on 3D-FEA, the required No-Load characteristics of the machine such as BEMF voltage, airgap flux density and cogging torque are predicted. The results show that a high airgap flux density with average value about 2 times the remanence of the used ferrite magnet can be achieved with low ratio of the stator active length to rotor diameter. The machine is simulated at different load conditions and the output characteristics such as the torque and power envelope are then predicted. Later on, the losses of the machines such as copper and iron losses are computed.

Based on 3D FLUX software and the with help of CEDRAT techniques a new prediction of the electromagnetic torque waveform is investigated using frozen permeability concept which considers the effect of magnetic saturation at high load condition, the mutual coupling between the d and q axis of the magnetic path and the interaction between the rotor magnetic field with the unequal reluctances in the d and q axis of the stator material. The validation of the predicted waveform of the torque is done with 3D-FEA. The results show that the predicted torque based on the frozen permeability concept, can accurately validate the torque produced by 3D-FEA.

Finally, the torque speed envelope and efficiency map are predicted. The predicted results show efficiencies in excess of 97% can be achieved.

Chapter 4

Lumped parameter circuit model

4.1 Introduction

Compared to finite element method, lumped parameter circuit model can also be considered a good method to represent, analyze and simulate electrical machines since it takes shorter time and can be used to estimate the performance different type of machines to predict parameters such as linkage flux, BEMF, torque etc. The accuracy of the lumped parameter circuit model depends on how the most important details are considered such as stator active axial length, leakage in stator slot, back iron, tooth tips and the (linear, nonlinear) magnetic characteristic of the stator iron material. In this chapter, a new non-linear lumped parameter circuit model (LPCM) is represented to simulate the new proposed machine using MATLAB/Simscape which enable to develop the models of different components. Therefore, the flux distribution and machine characteristics are predicted considering magnetic saturation and the above-mentioned parameters. The value of per phase linkage flux is evaluated at different rotor positions which is then used to predict the BEMF and the electromagnetic torque.

4.2 Basic concepts of LPCM approaches

The creation of the LPCM needs a prior knowledge to the flux pattern presented in the machines, Therefore, it is created to position lumped reluctances in the direction of the flux[43]. The governing equation at each lumped element is given by Eq. 4.1.

$$\varphi = \frac{F}{R} \tag{4.1}$$

Where φ, F and R, are flux, magneto-motive force (MMF) and reluctance, respectively. Reluctance is defined as:

$$R = \frac{L_m}{\mu A} \tag{4.2}$$

Where L_m, μ and A are thickness of the magnet in the direction of the flux, permeability of the material and the cross-sectional area perpendicular to flux flow, respectively.

Permanent magnets are represented by reluctance R in series with an MMF source. The MMF source and R are given by:

$$F_m = B_r \frac{L_m}{\mu_0 \mu_r} \tag{4.3}$$

$$R_m = \frac{L_m}{\mu_0 \mu_r A_m} \tag{4.4}$$

And the reluctance associated with the airgap is given by:

$$R_{airgap} = \frac{L_g}{\mu_0 A_g} \tag{4.5}$$

Where $\mu_r, \mu_0, L_m, A_m, L_g$ and A_g are relative recoil permeability of the magnet, permeability of the free space, thickness of the magnet in the direction of magnetisation, area of the magnet to which the magnetisation is perpendicular, airgap length and airgap area respectively.

4.3 LPCM of the proposed machine

The new LPCM which is used to represent the new proposed machine is shown in Fig. 4.1. It consists of three main regions: stator region, rotor region and airgap region. Each part will be detailed clearly in the next section. Due to magnetic symmetry, only a quarter part of the machine is represented taking the advantage of the periodicity of the machine as shown in Fig. 4.2. The parameters and dimensions of the proposed machine are given in Table 4.1. Accordingly, all the reluctances representing the stator teeth, back iron and tooth tips are modelled to include a nonlinear magnetic saturation, while the others which represent the airgap, stator slots and magnets are modelled as linear reluctances.

4.3.1 Stator modelling

In order to analyze the flux passing through the stator part of the proposed machine accurately taking into account the nonlinear magnetic saturation of the stator tooth, back iron and tooth tips (Non-linear permeability is derived from the B-H characteristics of the stator material), and the leakage flux between the stator pole at the end region, a new LPCM is used as shown in Fig. 4.3. It consist of five region (back iron region, teeth region, slots region, tooth tips region and leakage flux between adjacent stator teeth), each one is modelled using a specific lumped reluctance [21][64].

The lumped reluctances for stator back iron region $\mathbf{Rs_{back-iron}}$ and stator tooth region $\mathbf{Rs_{tooth}}$ are derived based on Eq. 4.2. Stator slot leakage path is represented by series of reluctance connections $\mathbf{Rs_{slot}}$ as shown in Fig. 4.4. The first term $\mathbf{R_{L1}}$ is the leakage reluctance between the stator teeth in winding area while the second term $\mathbf{R_{L2}}$ corresponds to the leakage reluctance in slot are excluding the winding area. Accordingly, it is modeled based on Eq. 4.6 [21] . Fig. 4.5 shows the leakge flux tube in the end region of the stator. It consists of semi-circular cylinder and half annulus. The leakage reluctance between adjacent stator teeth $\mathbf{Rs_{leakage}}$ is modelled based on Eq. 4.7. Stator tooth tips are modelled using nonlinear magnetic reluctance which is expressed based on Eq. 4.8**,** Eq. 4.9, Eq 4.10 and Eq. 4.11.

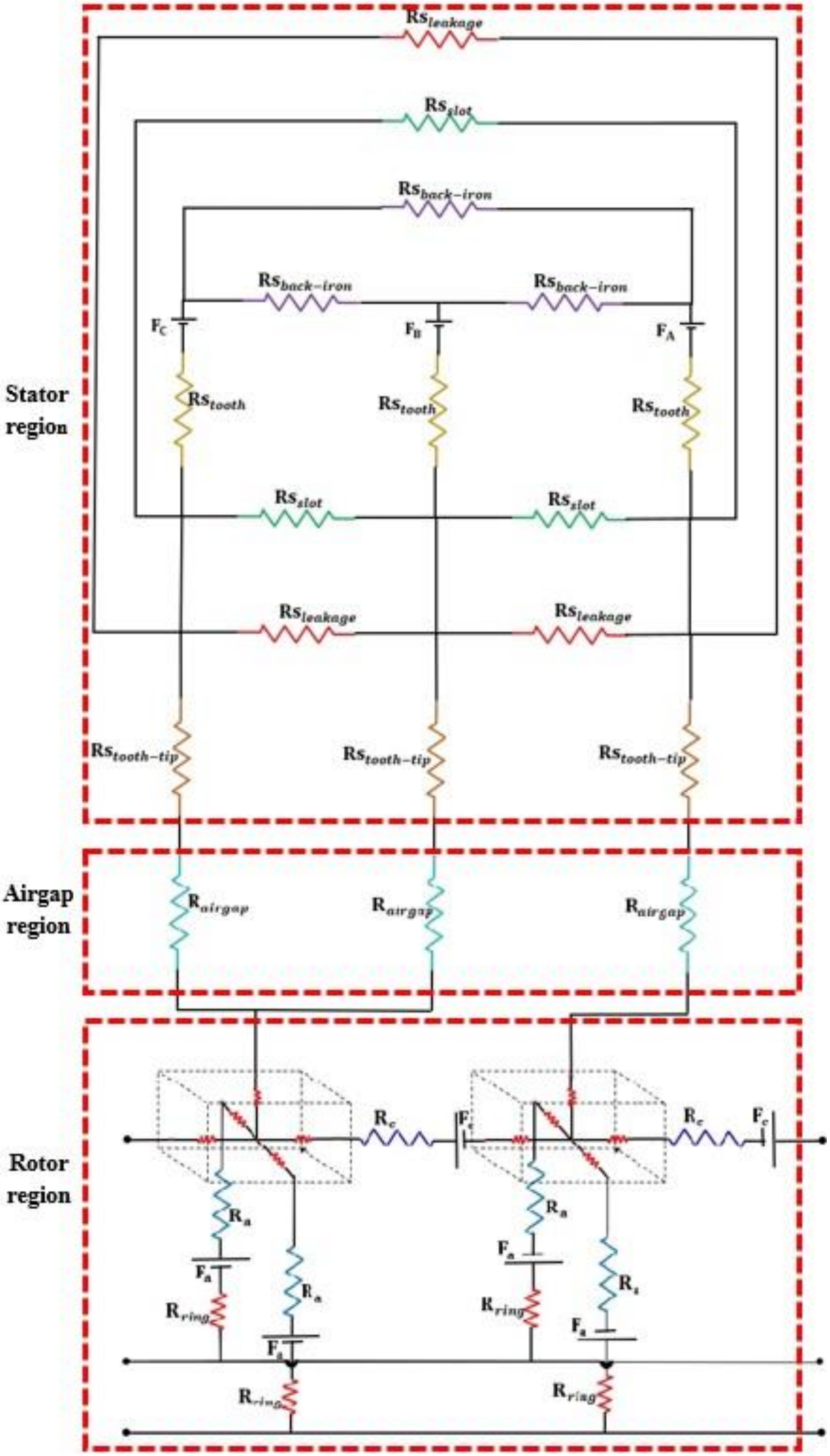

Fig. 4.1 Lumped parameter circuit model of the proposed machine.

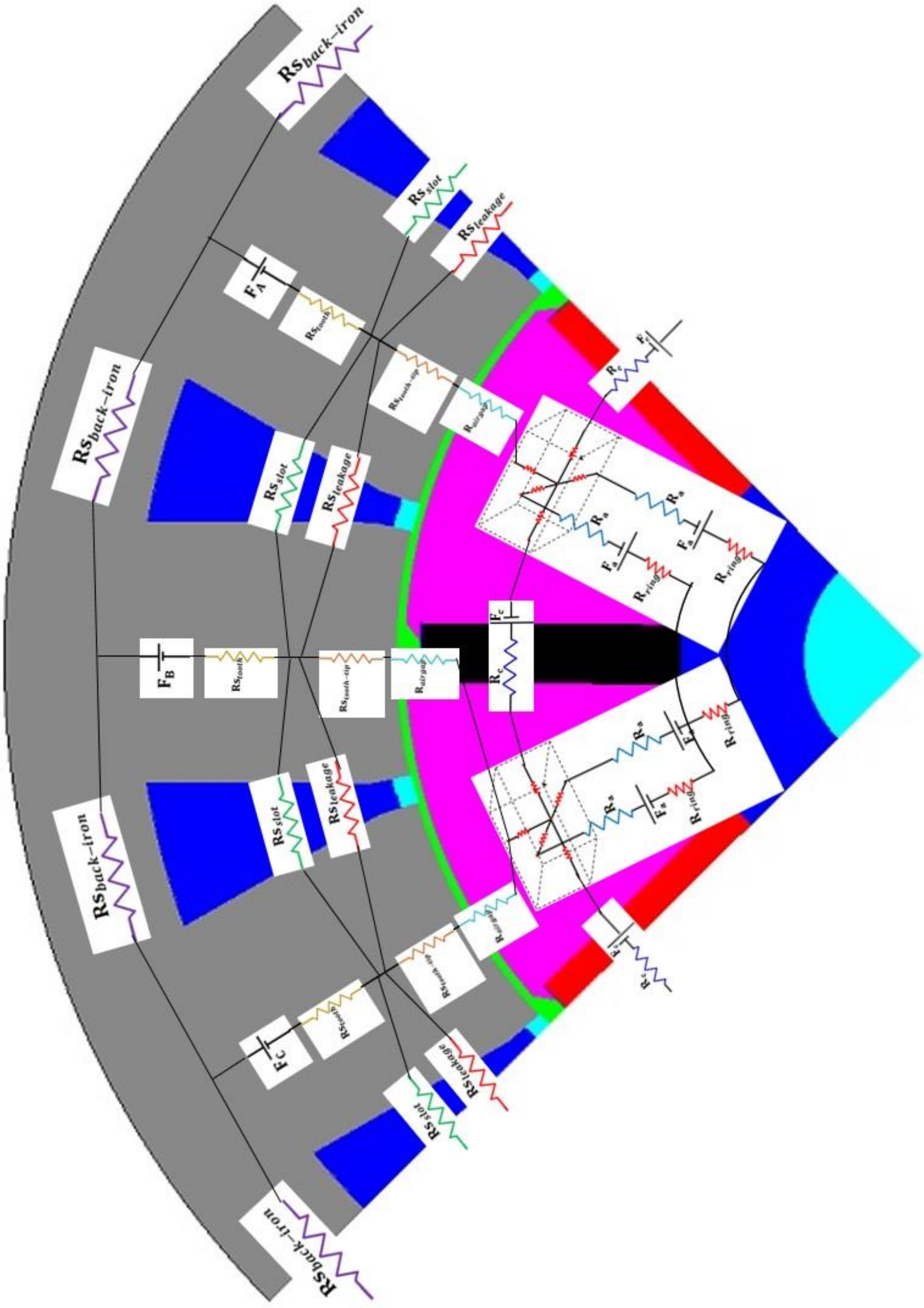

Fig. 4.2 Geometry of the new proposed machine.

Stator axial length	L_{axial} (mm)	30 mm
Stator back iron width	$\mathrm{d_c}$ (mm)	25.25 mm
Tooth width	T_s (mm)	50 mm
Tooth stalk length	T_{sl} (mm)	42.86 mm
Tooth tip thickness	$L_{tooth-tip}$ (mm)	7.73 mm
Tooth tip width	T_{tw} (mm)	5.58
Slot upper width	S_{uw} (mm)	28.15
Slot lower width	S_{lw} (mm)	5.92 mm
Slot opening angle		3°
Stator outer diameter	$D_{outer-stator}$ (mm)	350 mm
Stator bore diameter	$D_{bore-stator}$ (mm)	200 mm
Airgap diameter	D_{airgap} (mm)	200 mm
Airgap length	L_g (mm)	0.5 mm
Rotor inner diameter	$D_{inner-rotor}$ (mm)	88.18 mm
Rotor outer diameter	$D_{outer-rotor}$ (mm)	199 mm
Axial PM length	L_{APM} (mm)	7.5 mm
Circumferential PM length	L_{CPM} (mm)	11.698 mm
Soft magnetic ring axial length	L_{ring} (mm)	5 mm
Rotor Pole piece length	$L_{axial-rotor}$ (mm)	30 mm
No. of pole pairs	P	4
No. of slot	N_s	12
Type of magnet		Ferrite
Remanence of PM	B_r(T)	0.39
permeability of air	μ_0 henry per meter	$4\pi * 10^{-7}$

Table 4.1 Parameters of the new proposed machine required for LPCM.

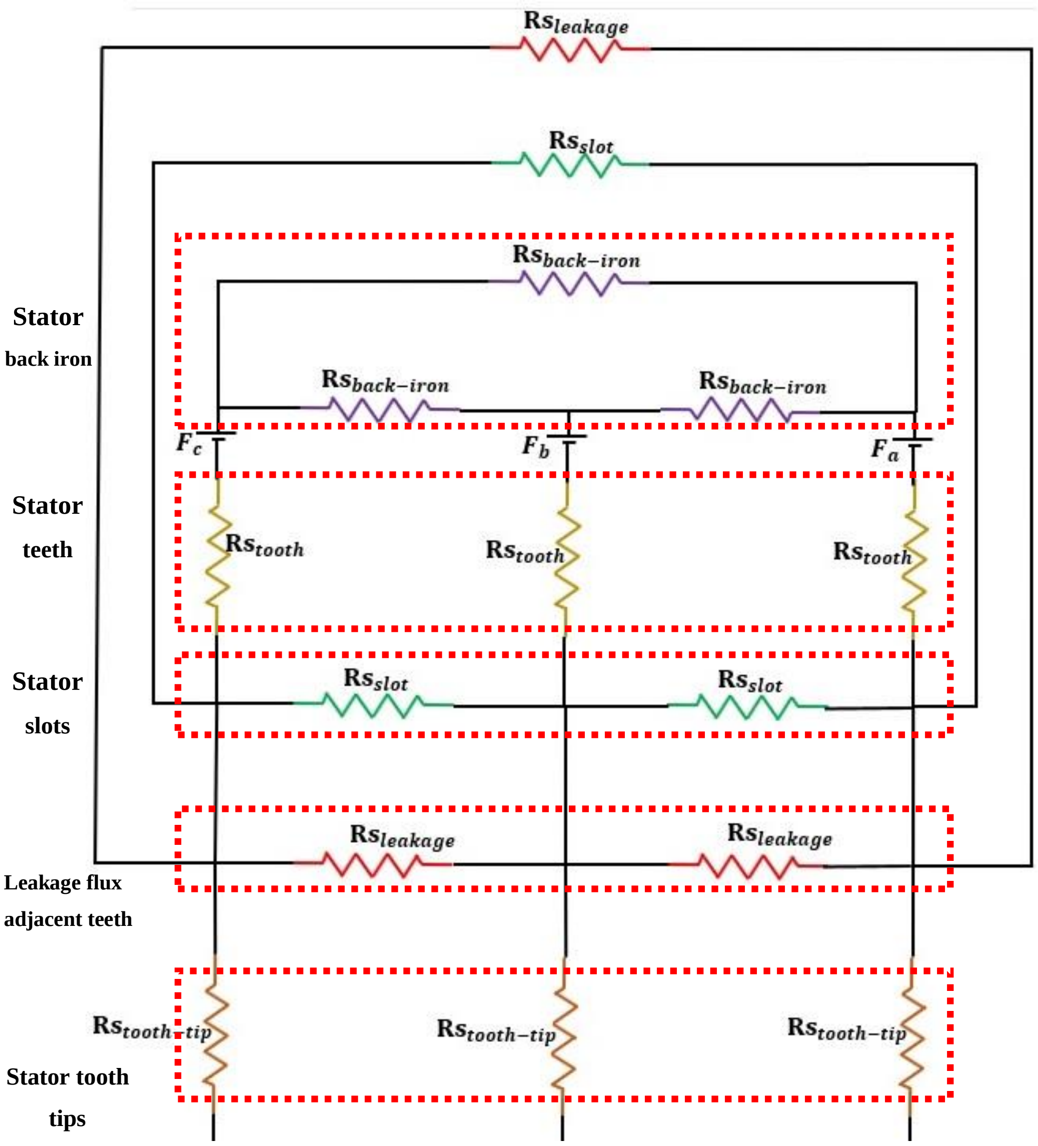

Fig. 4.3 Lumped parameter circuit model for the stator of the proposed machine.

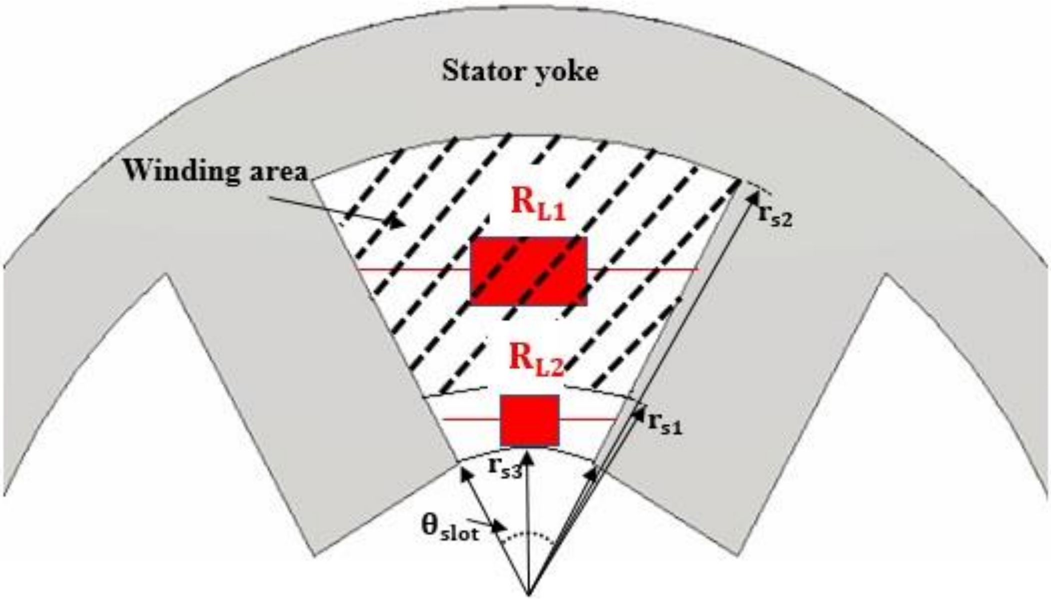

Fig. 4.4 Flux tube between adjacent stator poles [21]

$$\mathrm{Rs_{slot}} = \left(1/\left((\mu_0 k_i L_{axial}/\theta_{slot} r_{s1})(r_{s2} - r_{s1})\right)\right) + \left(1/\left((\mu_0 k_i L/\theta_{slot}) \ln\frac{r_{s1}}{r_{s3}}\right)\right) \qquad 4.6$$

$$= R_{L1} + R_{L2}$$

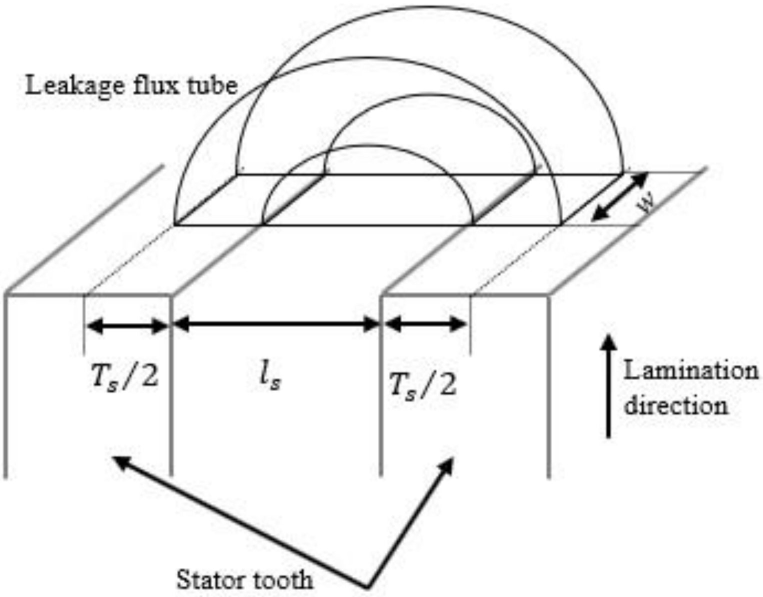

Fig. 4.5 Leakage flux tube between adjacent stator teeth [21]

$$\mathrm{Rs_{leakage}} = \left(1/\left(2\mu_0 w\left(0.268 + 0.318\ln\left(1 + \frac{T_s}{l_s}\right)\right)\right)\right) \quad 4.7$$

$$\mathrm{R_{tooth-tip}} = \frac{L_{tooth-tip}}{\mu_0\mu_r A_{tooth-tip}} \quad 4.8$$

Where:

$L_{tooth-tip}$, μ_0, μ_r and $A_{tooth-tip}$ are tooth tip length, air permeability, relative permeability respectively and tooth tip area, respectively. $A_{tooth-tip}$ is expressed as:

$$A_{tooth-tip} = k_i L(T_s - X) \quad 4.9$$

$$L_{tooth-tip} = X \text{ if } \left(0 \le X < \frac{T_s}{2}\right) \quad 4.10$$

$$L_{tooth-tip} = T_s - X \text{ if } \left(\frac{T_s}{2} \le X < T_s\right) \quad 4.11$$

X is the shifting value between the magnet magnetisation axes and the stator pole.

4.3.2 Airgap modelling

The flux path in the airgap region is expressed by reluctance R_{airgap} which has been derived based on Eq. 4.5. The airgap area A_g is calculated at each rotation step of the rotor with respect to the stator as shown in Eq. 4.12 . Furthermore, the value and connection of airgap reluctances R_{airgap} will be change based on the position of the magnets in the rotor with respect to the stator winding as shown in Fig. 4.6.

$$A_g = W_{airgap} \times L_{axial} \quad 4.12$$

W_{airgap}: Airgap width surrounding between rotor pole-pieces and stator tooth.

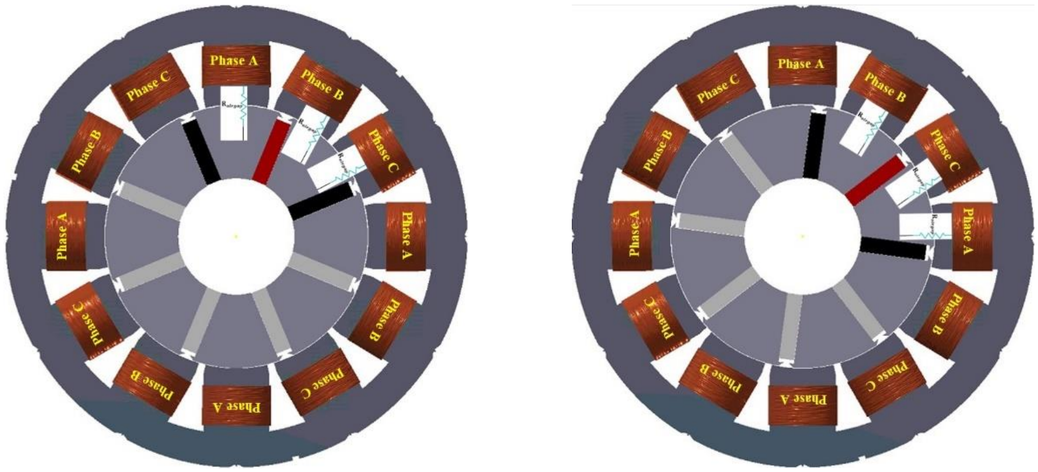

(a) Rotor position = 0° mech. Deg.

(b) Rotor position = 30° mech. Deg.

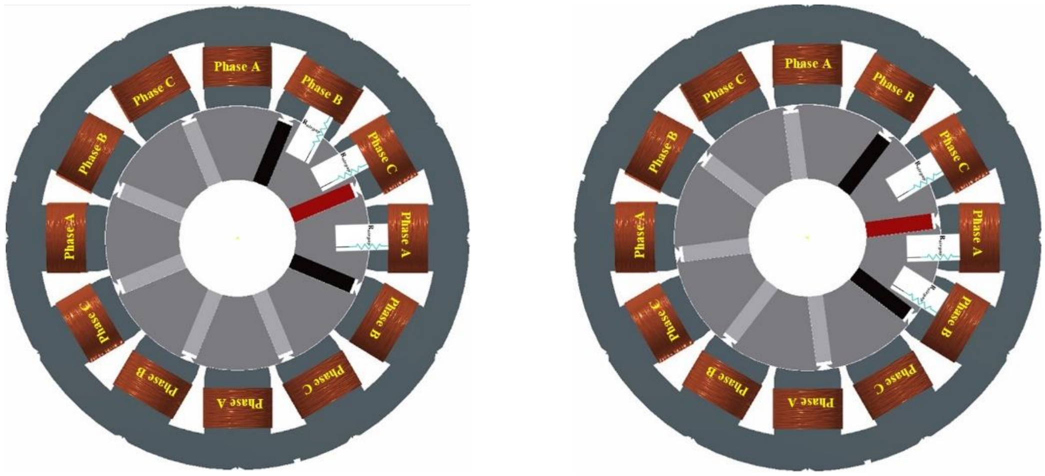

(c) Rotor position = 45° mech. Deg.

(d) Rotor position = 60° mech. Deg.

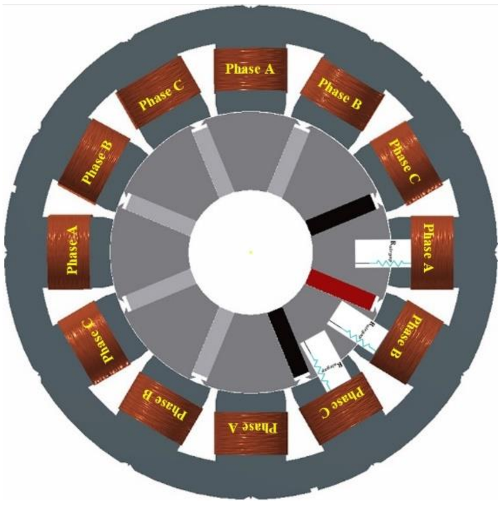

(e) Rotor position = 90° mech. Deg.

Fig. 4.6 Airgap reluctance connections at different rotor positions

The effect of the stator slot on the calculation of the airgap length (actual airgap) is considered. Therefore, the new airgap length is expressed by Eq. 4.13 using Carter coefficient [61].

$$l_{gc} = k_c l_g \qquad 4.13$$

Where:

l_{gc}: Airgap length with carter factor.

l_g: Mechanical airgap length.

k_c: Carter coefficient.

4.3.3 Rotor modelling

The LPCM which is used to represent the rotor of the proposed machine is shown in Fig. 4.7. As previously mentioned, the axially and circumferentially magnetized PMs are represented by MMF source in series with reluctance. The rotor pole piece reluctance is represented by 3D reluctance element which consist of five reluctances as shown in Fig. 4.8 [65]. The soft magnetic ring reluctance $\mathrm{R_{ring}}$ is calculated based on Eq. 4.2.

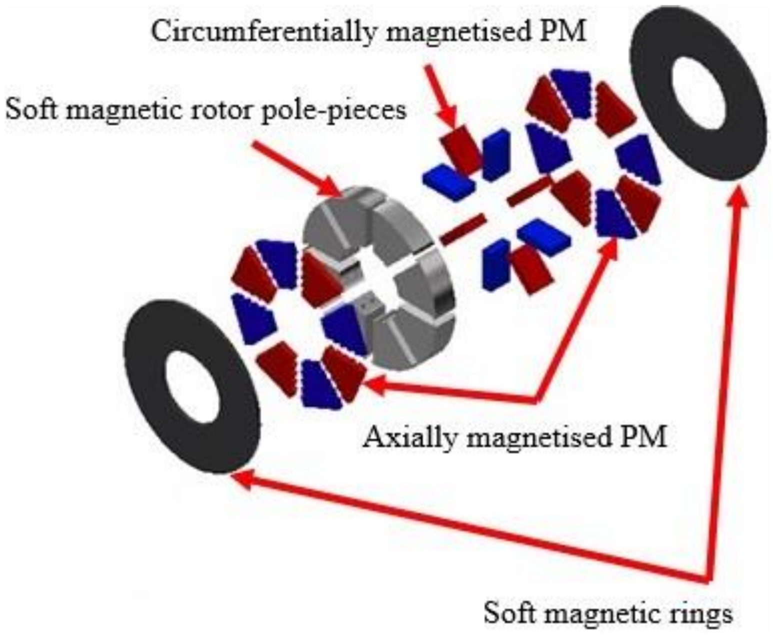

(a) Rotor expolded view

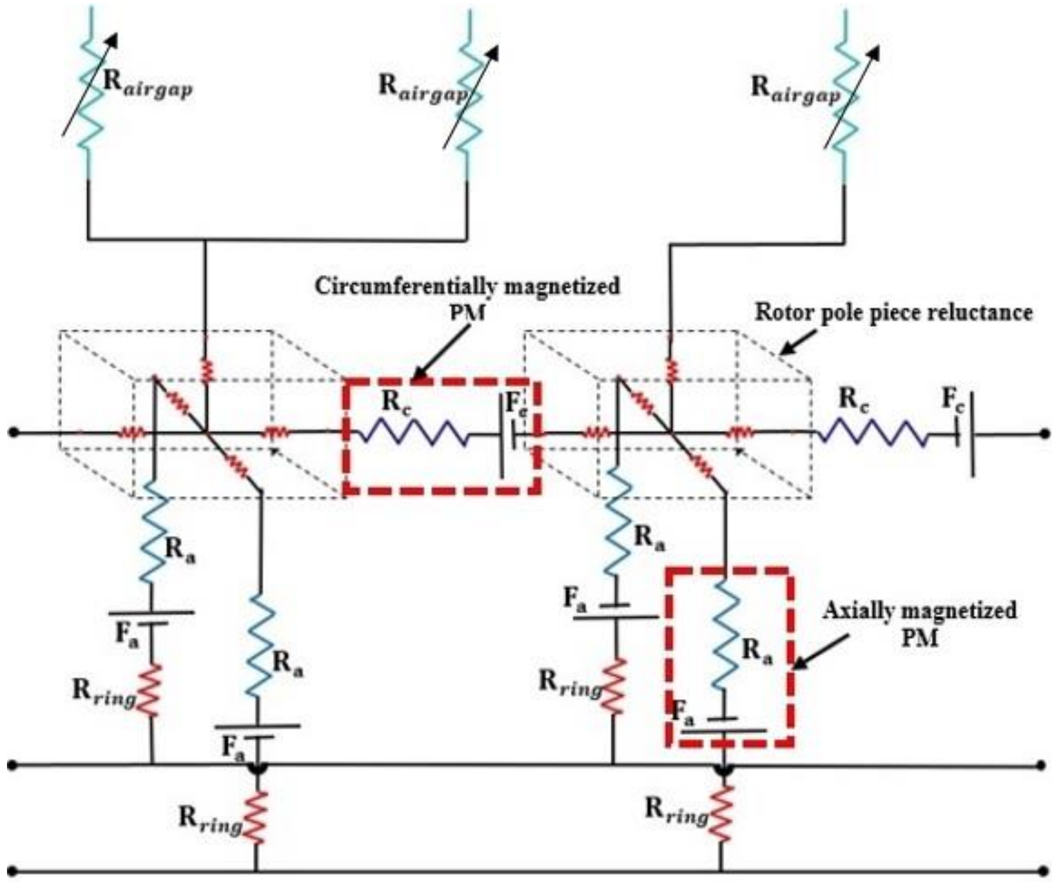

(b) LPCM of the rotor

Fig. 4.7 Lumped parameter circuit model for the rotor of the proposed machine.

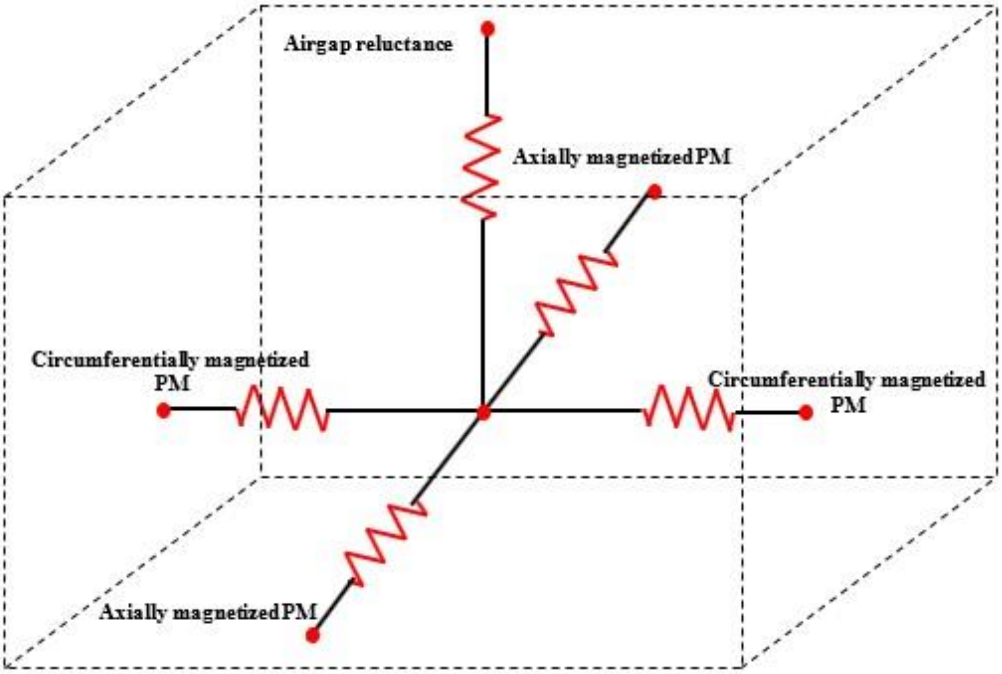

Fig. 4.8 Rotor pole-pieces reluctance (3D reluctance element).

4.4 LPCM results and discussion

The validation of the proposed LPCM shown in Fig. 4.1 is done by comparing the output waveforms such as phase flux linkages, BEMF and phase voltages with FEA results under open circuit condition and in the presence of armature current (load condition). Furthermore, the electromagnetic torque is predicted and compared with FEA under different load conditions at different current control angles. The instantaneous value of the flux linkages is computed and converted into d, q axis at each position step as in FEA.

4.4.1 No-load condition

Fig. 4.9 & Fig. 4.10 show a comparison between predicted phase flux linkage waveform at no load (open circuit condition) using the LPCM and FE. It can be noticed that a small difference exists in the fundamental values as shown in Fig. 4.11. Fig. 4.12 & Fig. 4.13, show the BEMF voltage waveform at electrical frequency of (150 Hz) and the harmonic spectrum respectively, corresponding to rotor speed of 2250 r/min. It can be seen that a very good agreement exists between the predicted values using both methods.

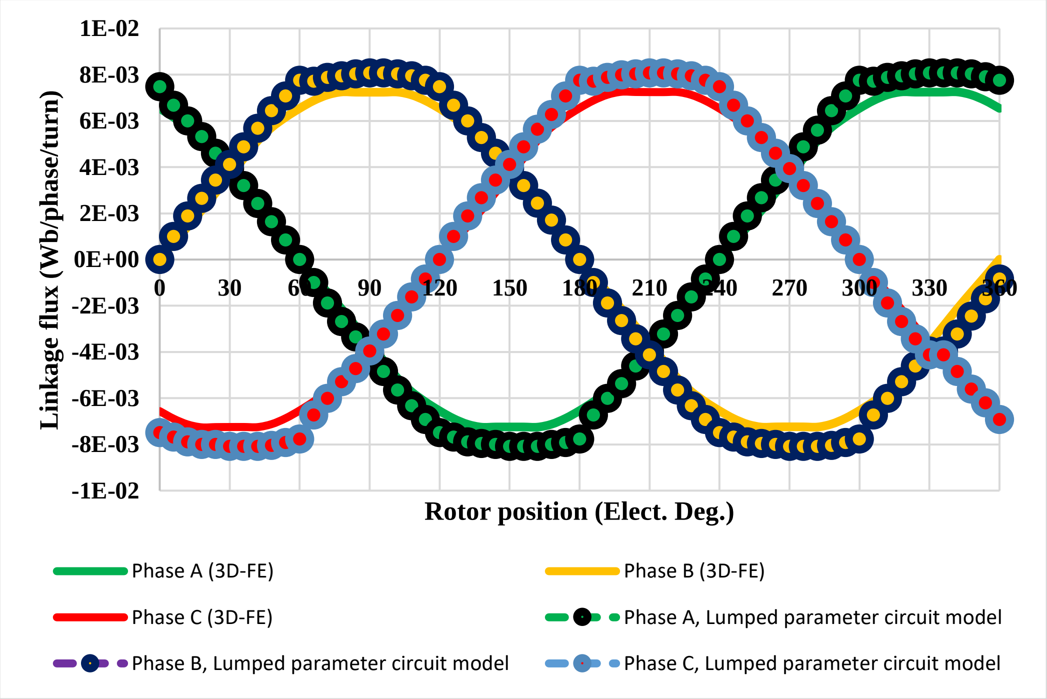

Fig. 4.9 Phase flux linkage waveforms under No-load condition.

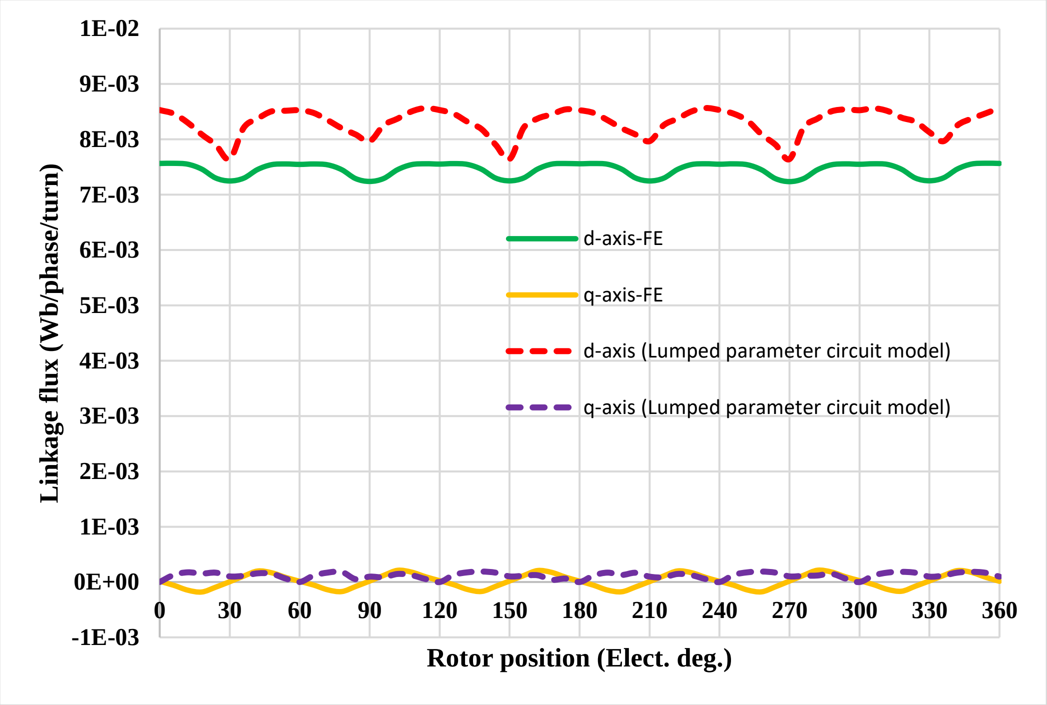

Fig. 4.10 d-q axes phase flux linkage waveforms under No-load condition.

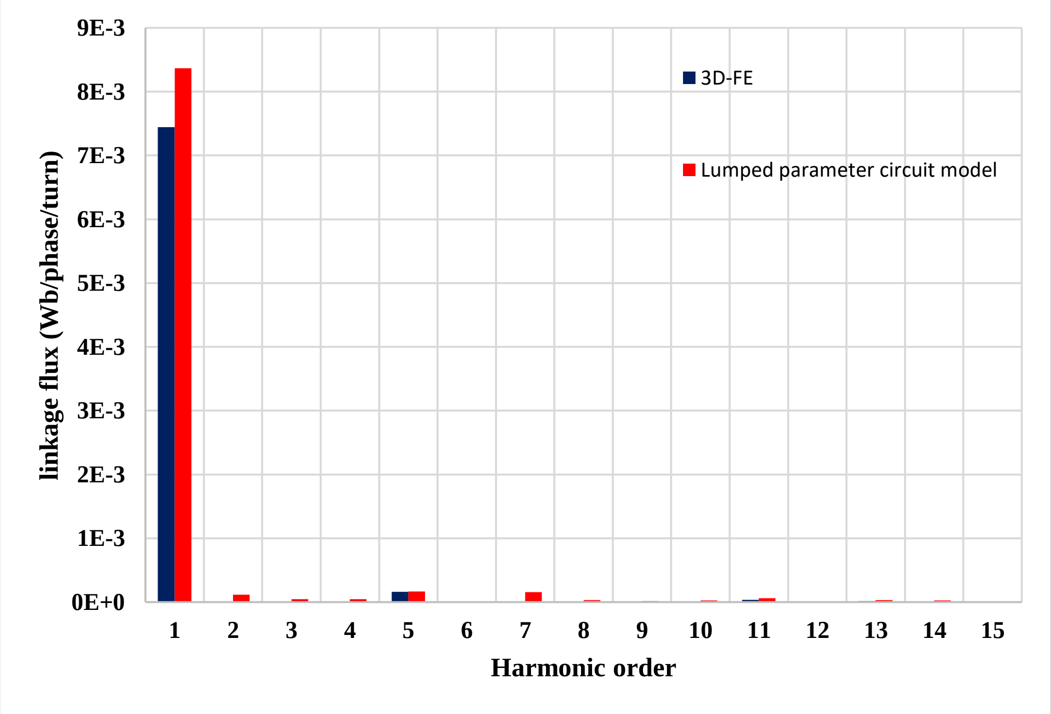

Fig. 4.11 Harmonic spectrum of the linkage flux waveform under No-load condition.

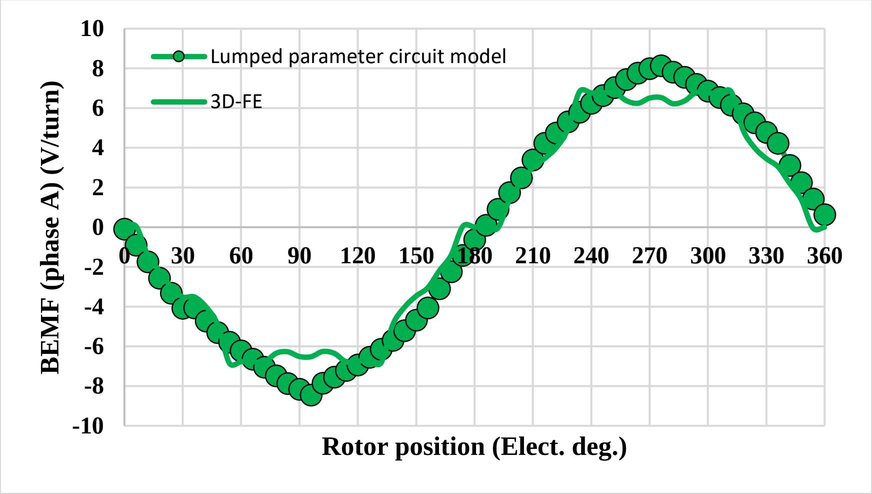

(i) BEMF waveform – phase A

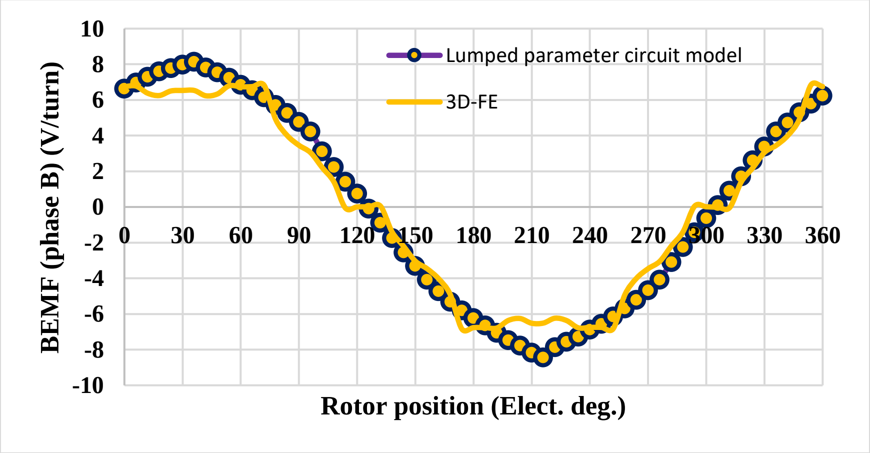

(ii) BEMF waveform – phase B

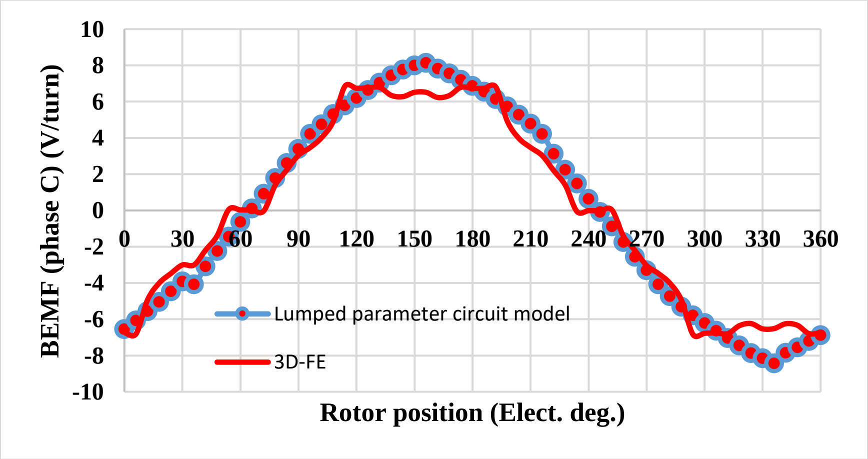

(iii) BEMF waveform – phase C

Fig. 4.12 Phase BEMF voltage waveform under No-load condition at base speed =2250 r/min.

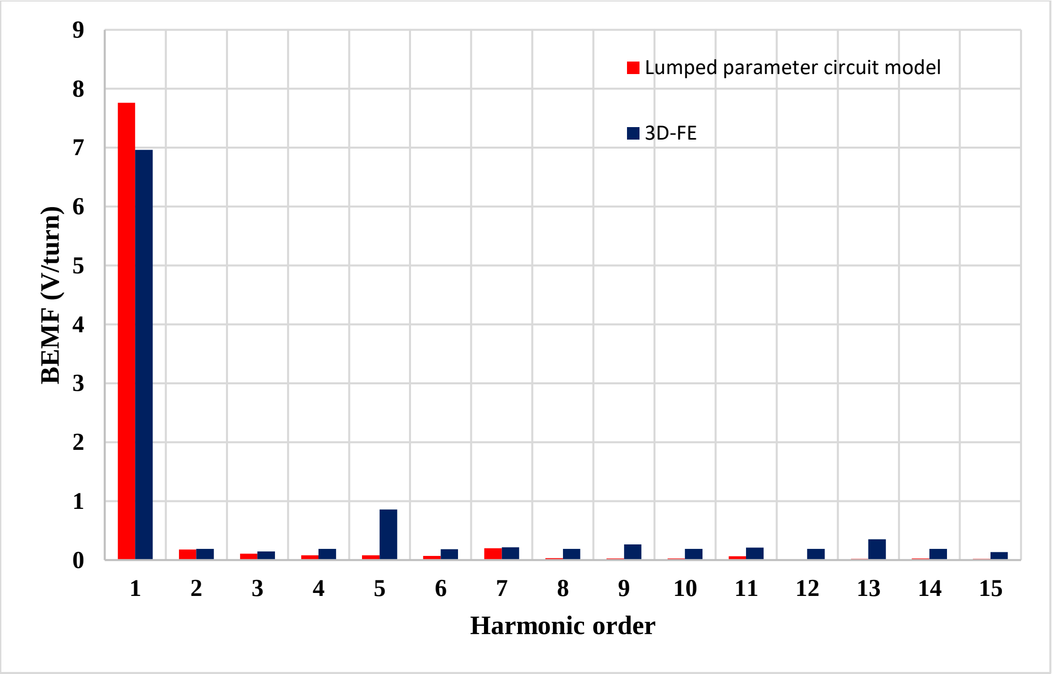

Fig. 4.13 Harmonic spectrum of the BEMF waveform.

4.4.2 Load condition

Fig. 4.14 - Fig. 4.28 show the waveforms of the phase flux linkages and phase voltages which are predicted using proposed LPCM and compared with FE as a function of rotor angle at different rotor speeds (electrical frequency) and current control angles. The results show that the harmonics especially the fifth harmonics of the linkage flux waveforms is high at the base speed 2250 r/min and reduced at the field weakening working region of the machine. Therefore, comparing with the finite element waveforms, there is a difference between the two waveforms as can be noticed in the harmonic analysis, and this difference in values is reduced when working at the maximum speed = 4500 r/min. The difference also can be noticed in the phase voltage waveforms at different rotation speeds, since they are calculated depending on the predicted linkage flux waveforms from the lumped parameter circuit model.

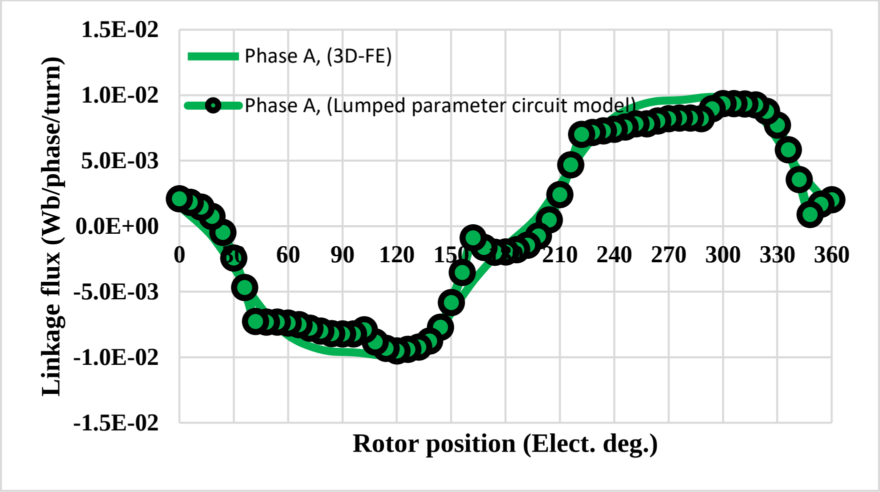

(i) Linkage flux waveform – phase A

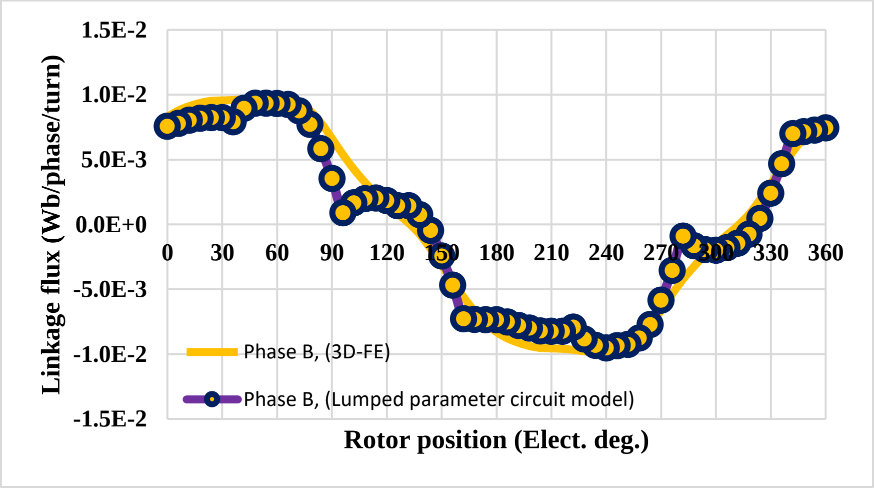

(ii) Linkage flux waveform – phase B

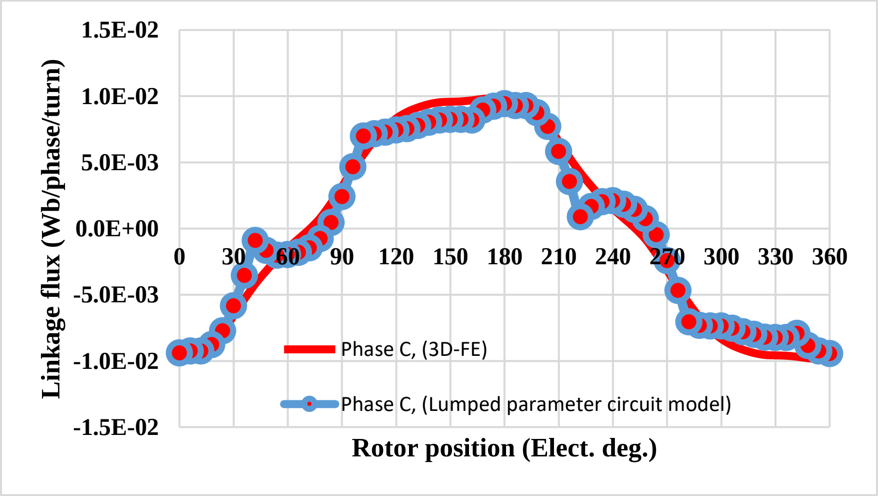

(iii) Linkage flux waveform – phase C

Fig. 4.14 Phase flux linkage waveforms at speed = 2250 r/min, I_{max}= 880.27A, γ = 0°.

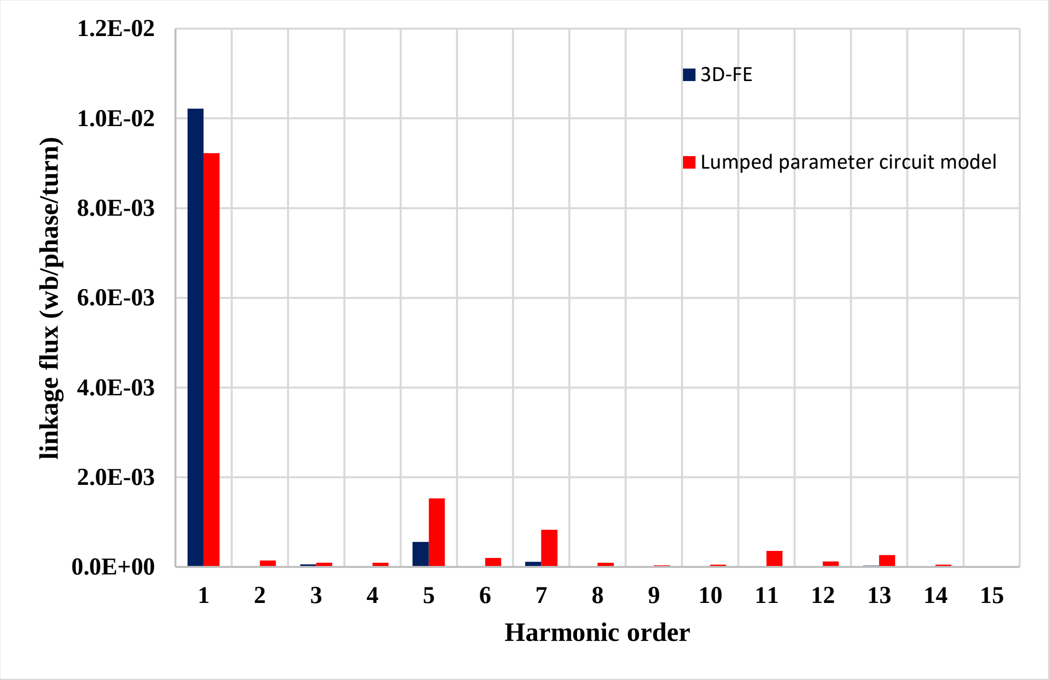

Fig. 4.15 Harmonic spectrum of the linkage flux at speed 2250 r/min, I_{max}= 880.27A, γ = 0°.

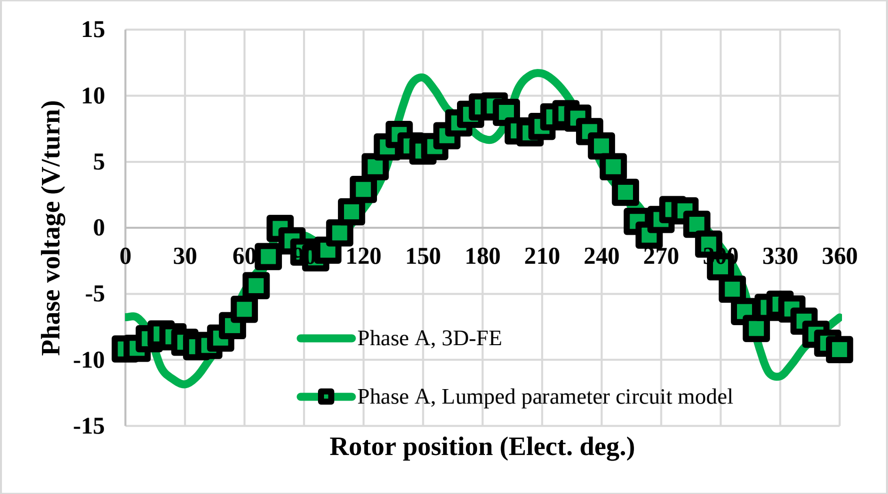

(i) Phase voltage waveform – phase A

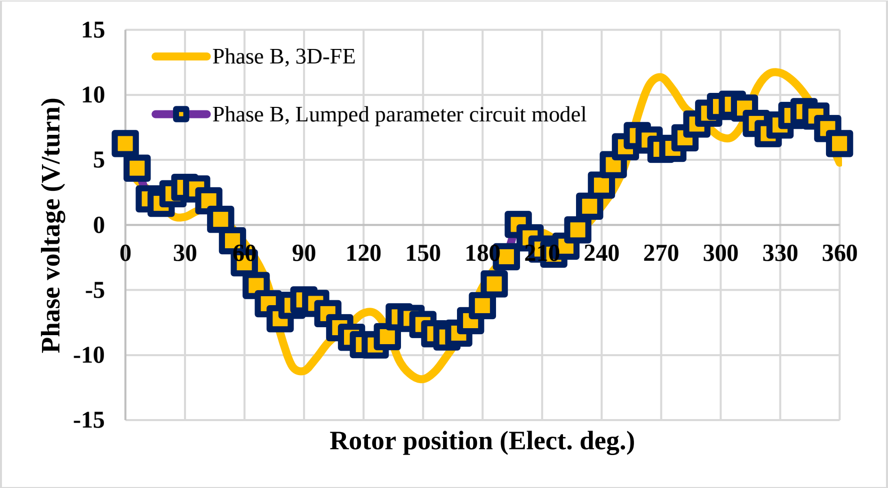

(ii) Phase voltage waveform – phase B

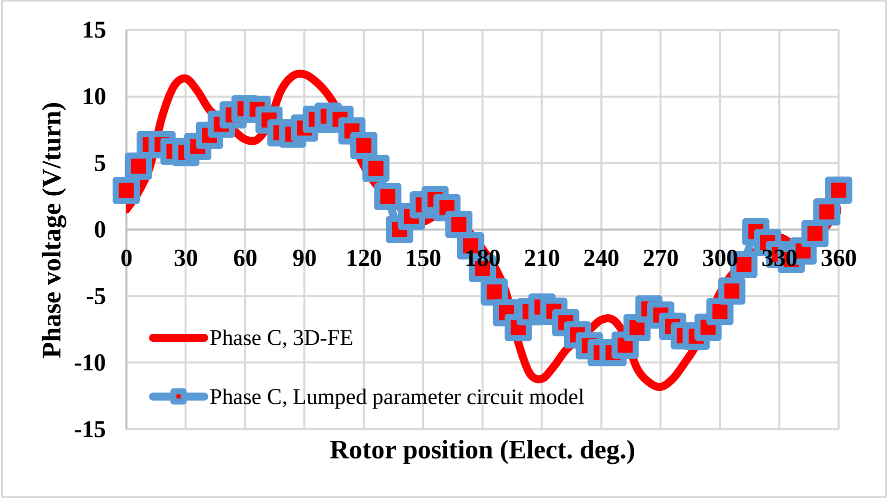

(iii) Phase voltage waveform – phase C

Fig. 4.16 Phase voltage waveforms at speed 2250 r/min, I_{max}= 880.27A, γ = 0°.

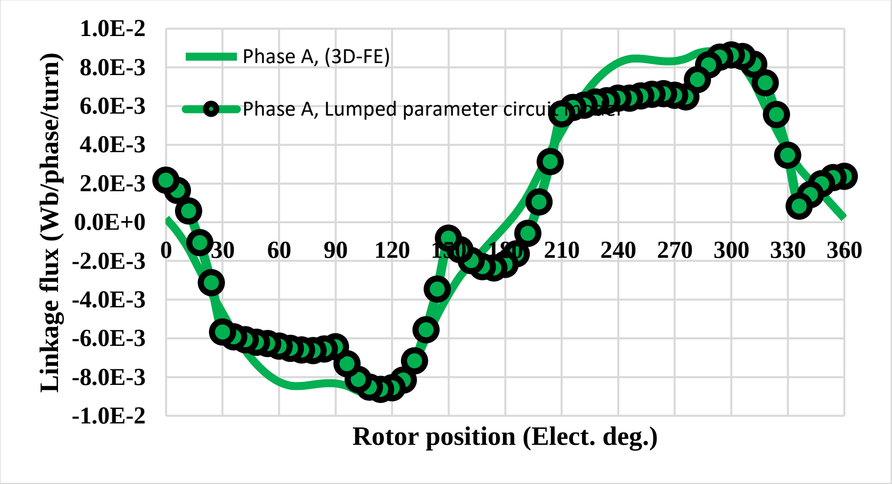

(i) Linkage flux waveform – phase A

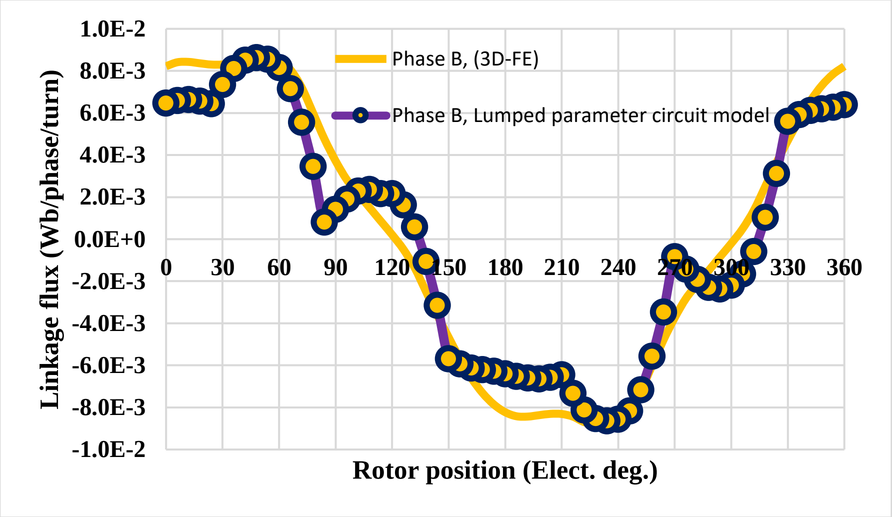

(ii) Linkage flux waveform – phase B

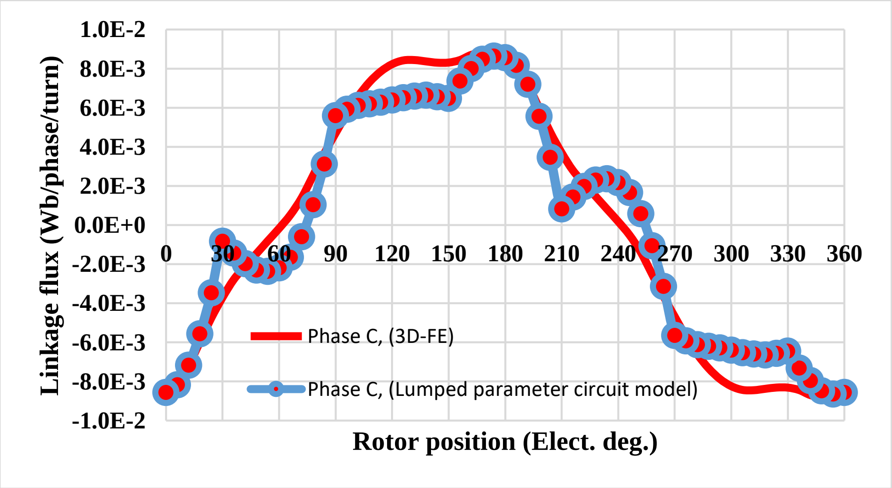

(iii) Linkage flux waveform – phase C

Fig. 4.17 Phase flux linkage waveforms at speed = 2250 r/min, I_{max} = 880.27A, γ = 25°.

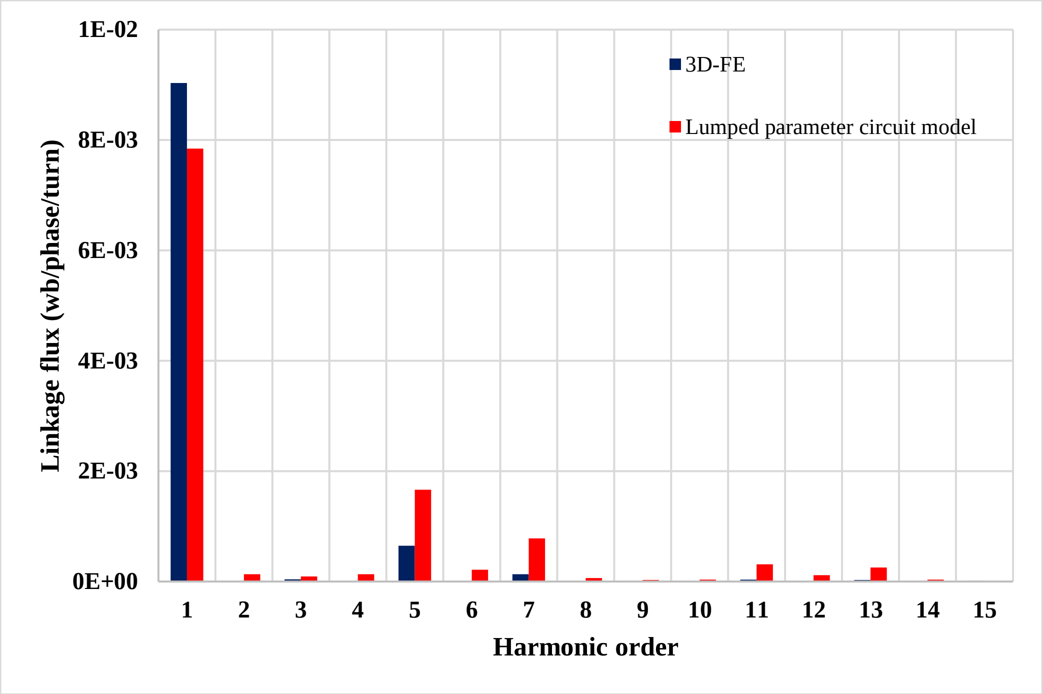

Fig. 4.18 Harmonic spectrum of the linkage flux at speed = 2250 r/min, I_{max} = 880.27A, γ = 25°.

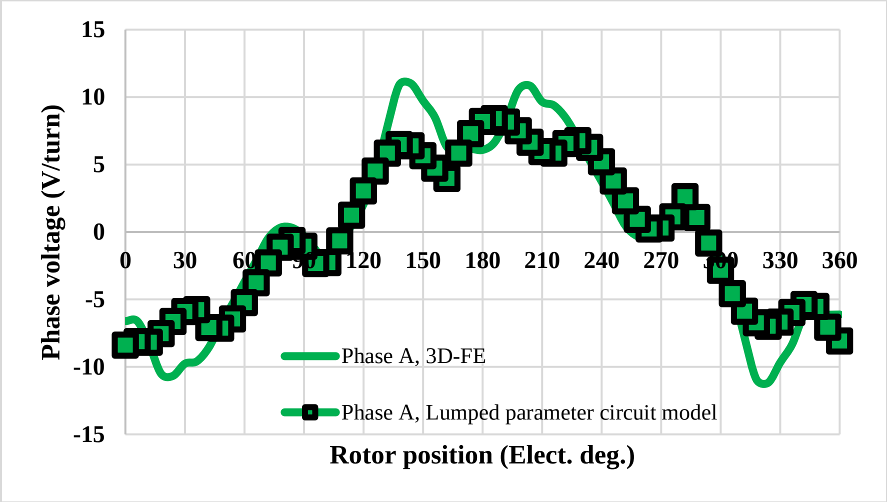

(i) Phase voltage waveform – phase A

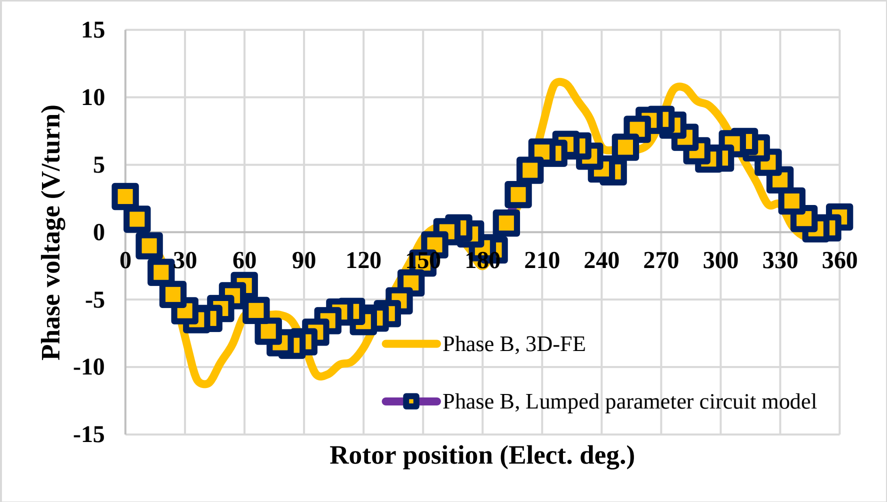

(ii) Phase voltage waveform – phase B

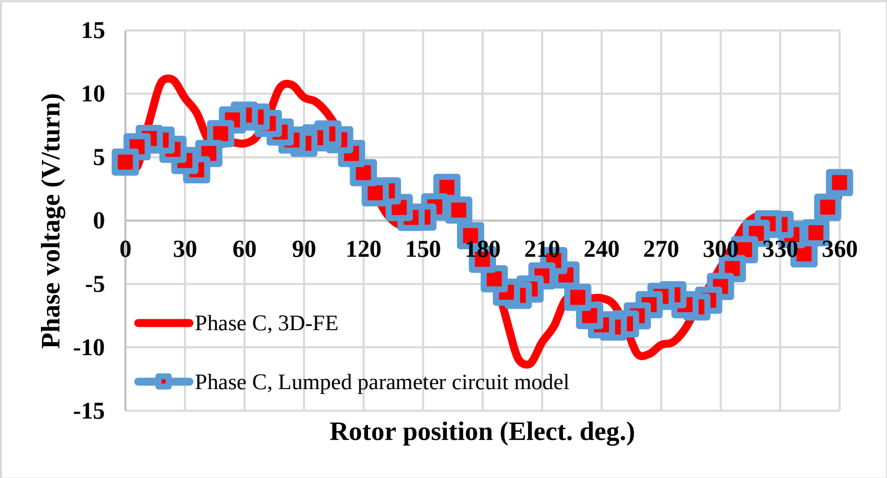

(iii) Phase voltage waveform = phase C

Fig. 4.19 Phase voltage waveforms at speed 2250 r/min, I_{max} = 880.27A, γ = 25°.

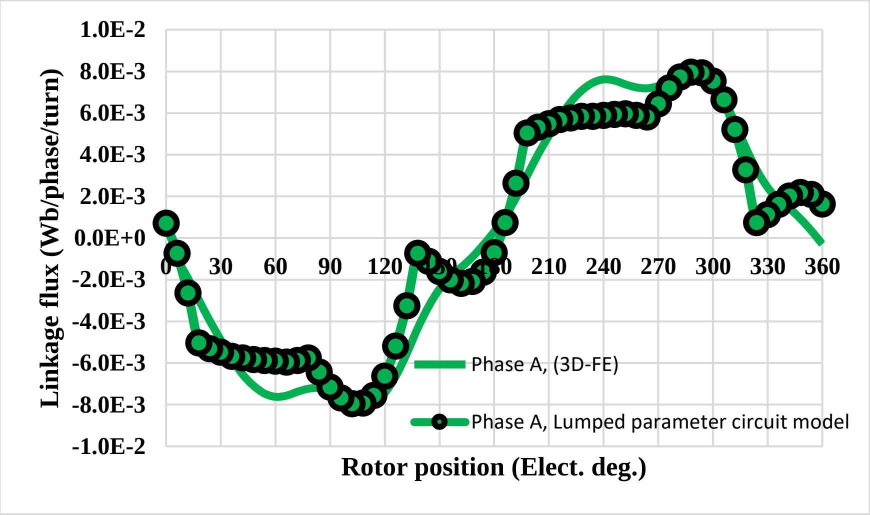

(i) Linkage flux waveform – phase A

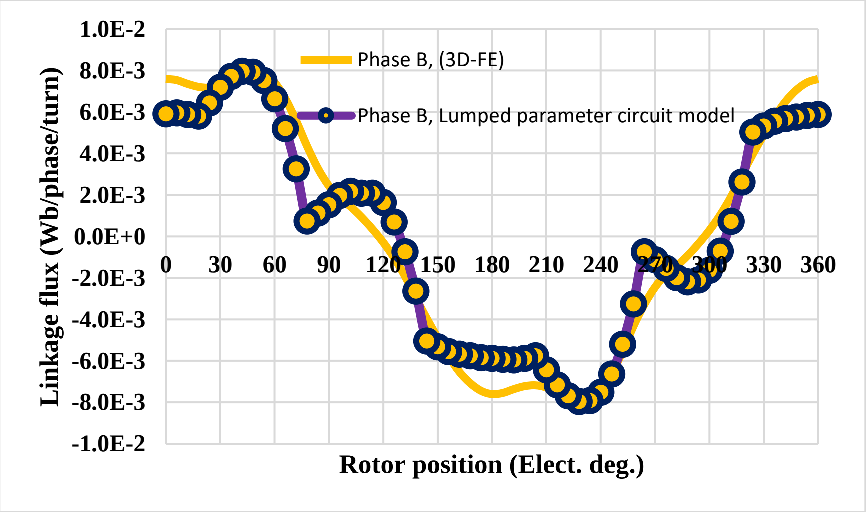

(ii) Linkage flux waveform – phase B

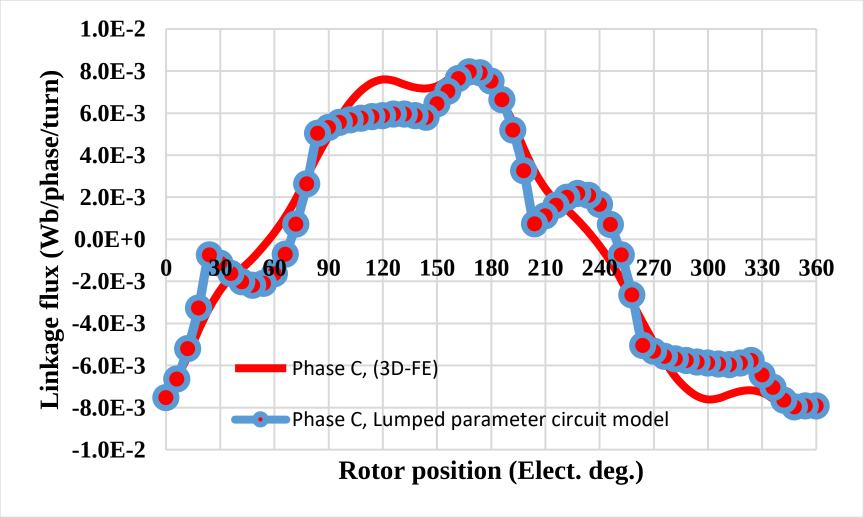

(iii) Linkage flux waveform – phase C

Fig. 4.20 Phase flux linkage waveforms at speed = 2500 r/min, I_{max} = 880.27A, γ = 35.65°.

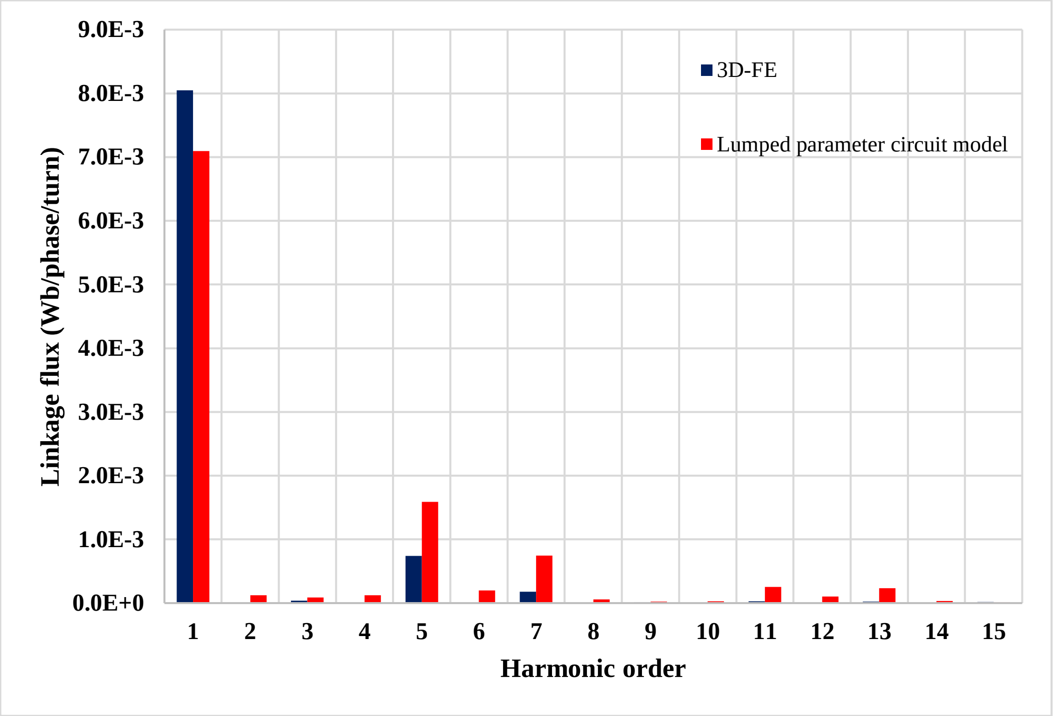

Fig. 4.21 Harmonic spectrum of the linkage flux at speed = 2500 r/min, I_{max} = 880.27A, γ = 35.65°.

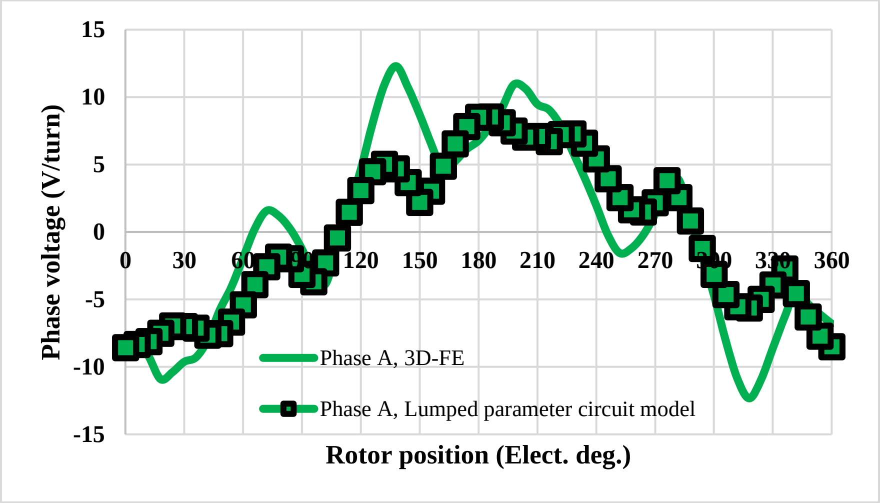

(i) Phase voltage waveform – phase A

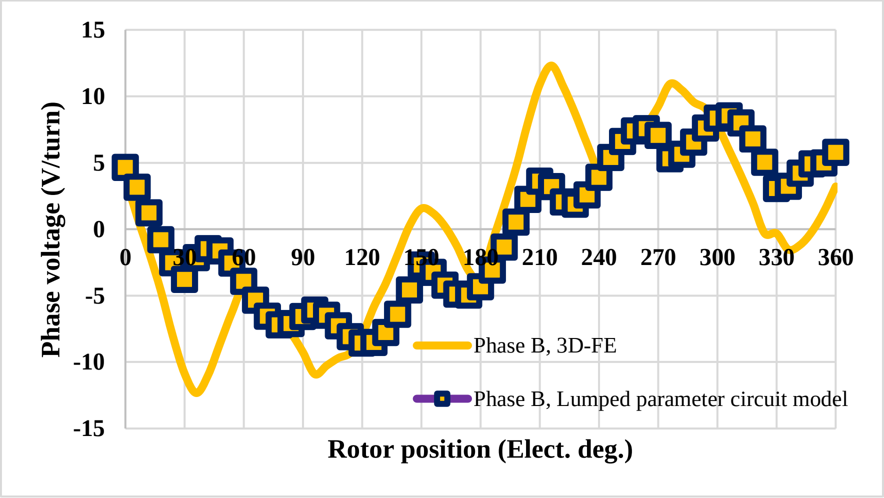

(ii) Phase voltage waveform – phase B

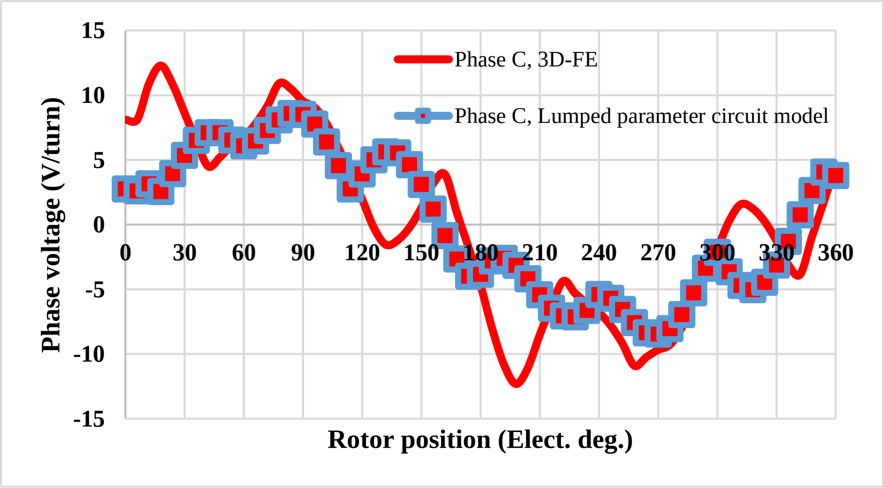

(iii) Phase voltage waveform – phase C

Fig. 4.22 Phase voltage waveforms at speed 2500 r/min, I_{max} = 880.27A, γ = 35.65°.

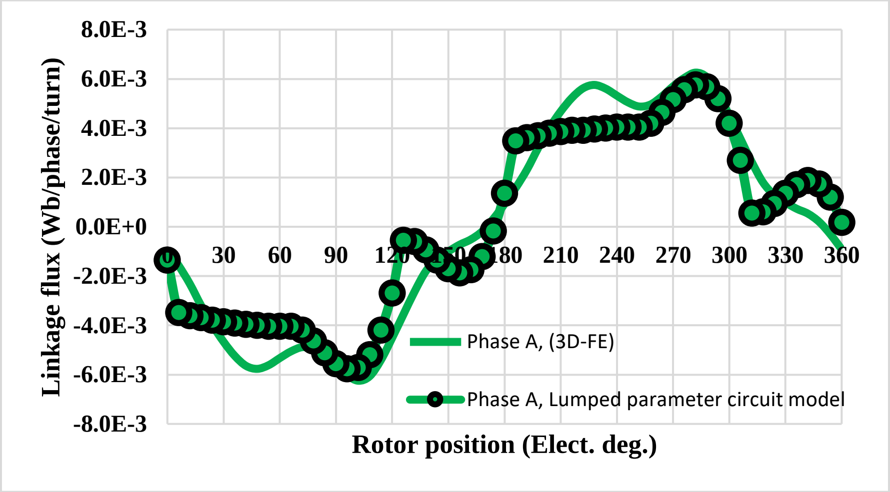

(i) Linkage flux waveform – phase A

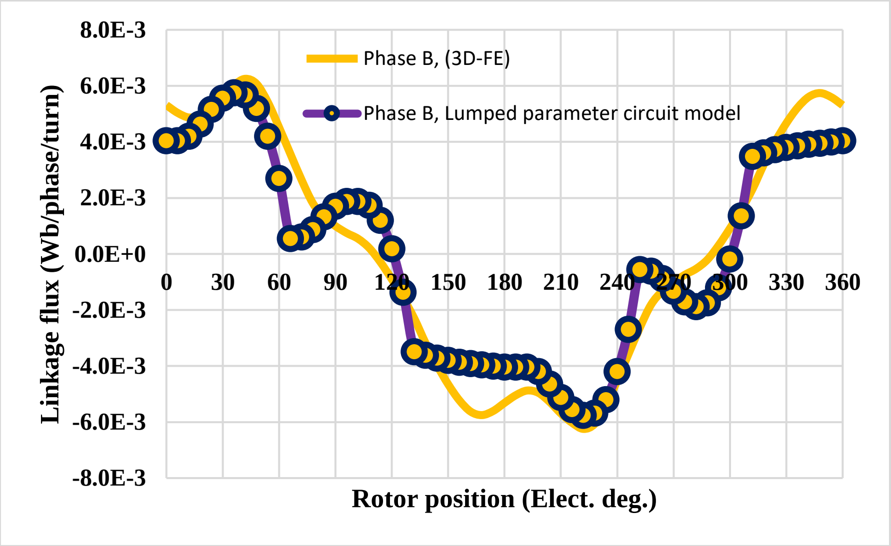

(ii) Linkage flux waveform – phase B

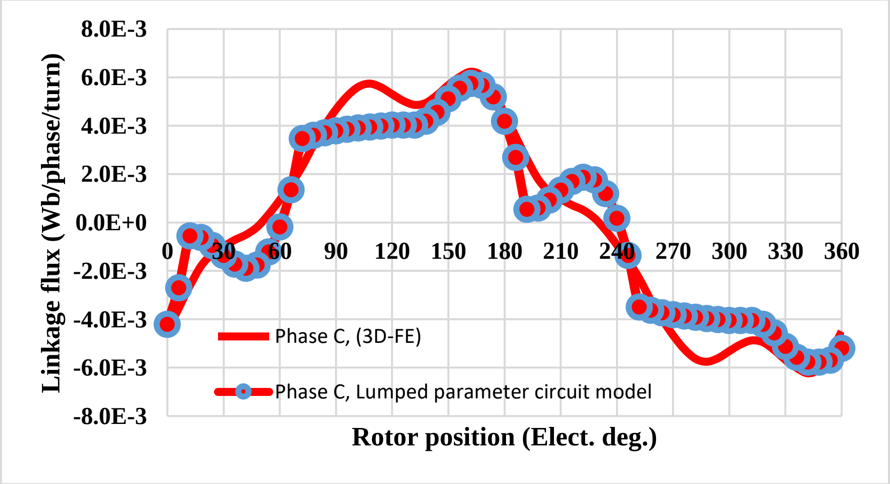

(iii) Linkage flux waveform – phase C

Fig. 4.23 Phase flux linkage waveforms at speed = 3500 r/min, I_{max} = 880.27A, γ = 52.39°.

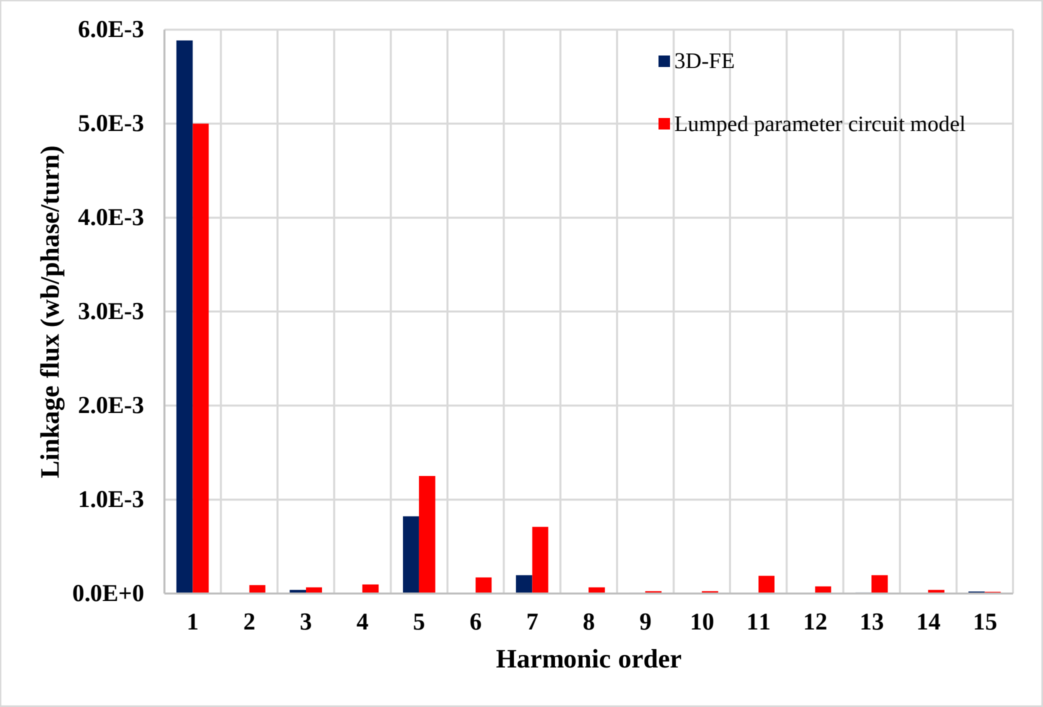

Fig. 4.24 Harmonic spectrum of the linkage flux at speed = 3500 r/min, I_{max}= 880.27A, γ = 52.39°.

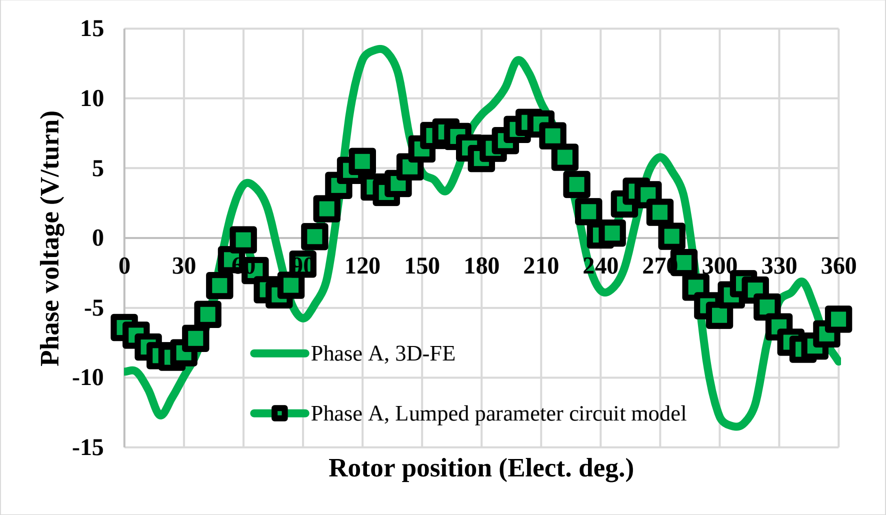

(i) Phase voltage waveform – phase A

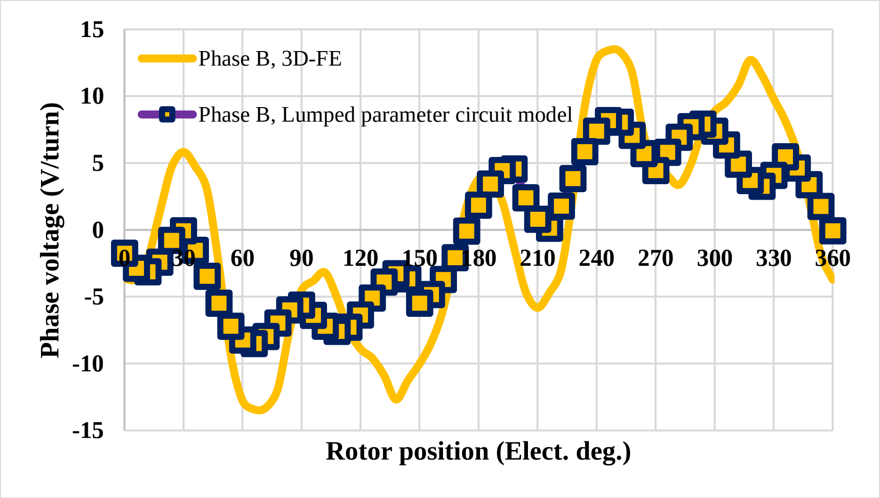

(ii) Phase voltage waveform – phase B

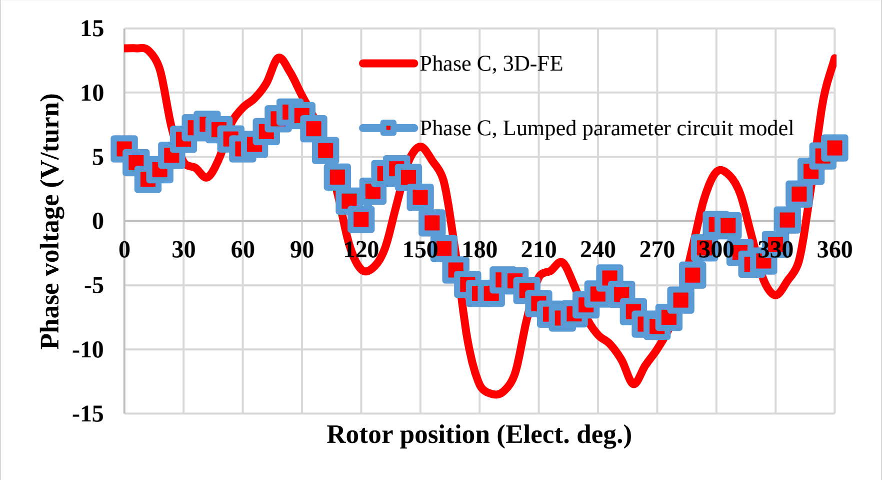

(iii) Phase voltage waveform – phase C

Fig. 4.25 Phase voltage waveforms at speed 3500 r/min, I_{max}= 880.27A, γ = 52.39°.

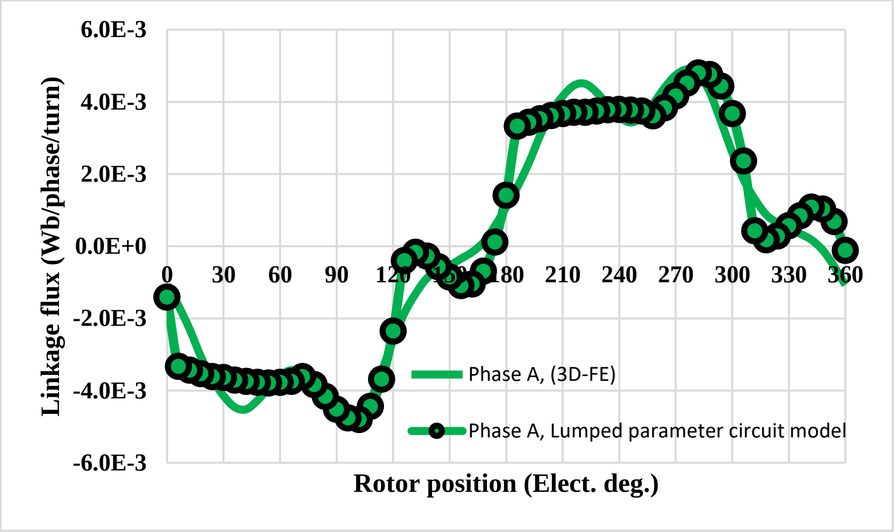

(i) Linkage flux waveform – phase A

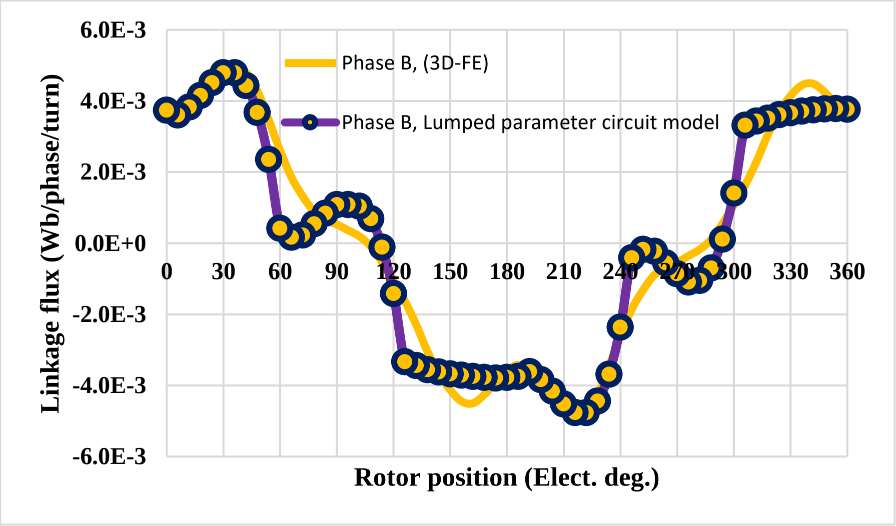

(ii) Linkage flux waveform – phase B

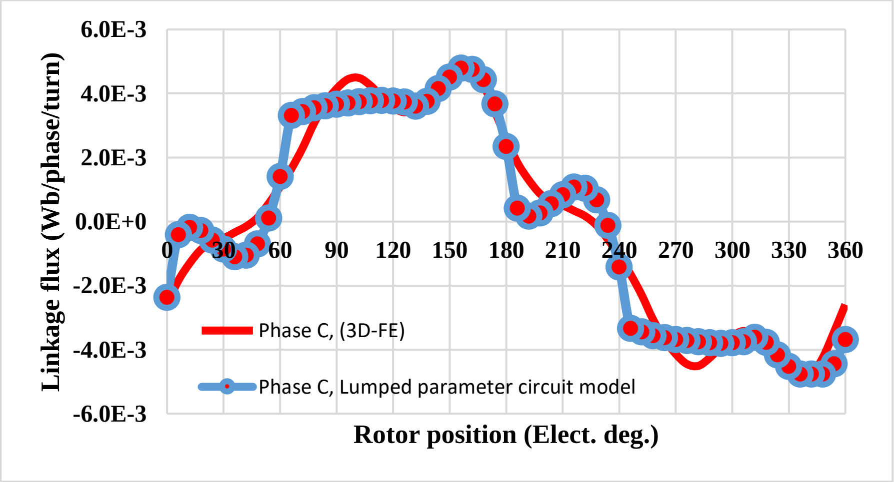

(iii) Linkage flux waveform – phase C

Fig. 4.26 Phase flux linkage waveforms at speed = 4500 r/min, I_{max} = 880.27A, γ = 62.07°.

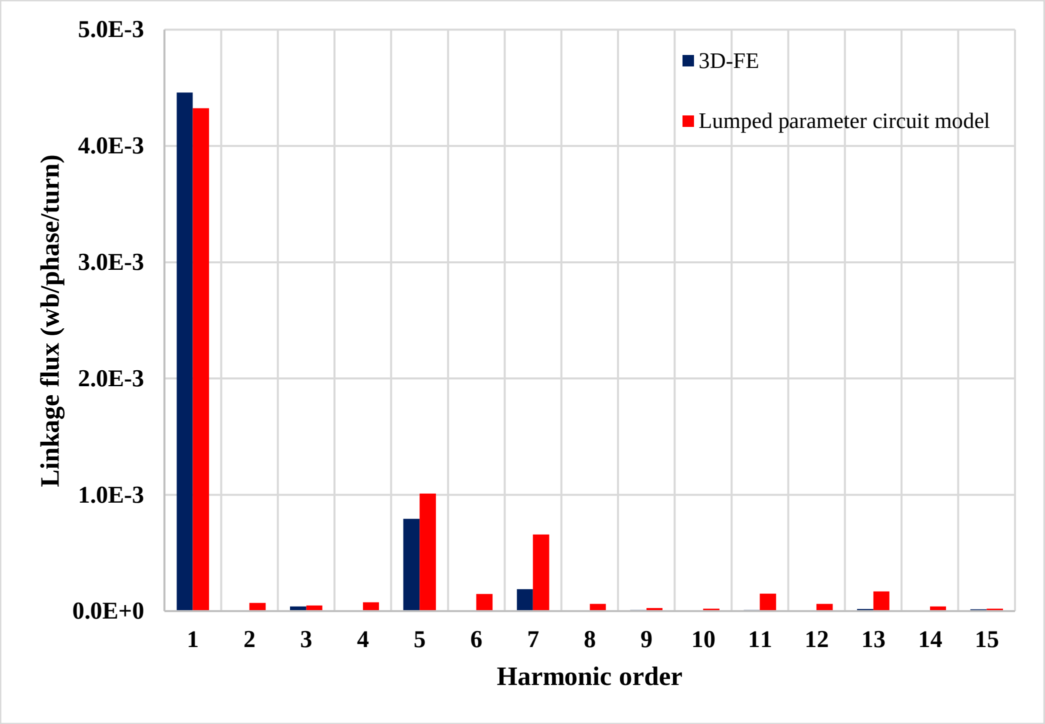

Fig. 4.27 Harmonic spectrum of the linkage flux at speed = 4500 r/min, I_{max} = 880.27A, γ = 62.07°.

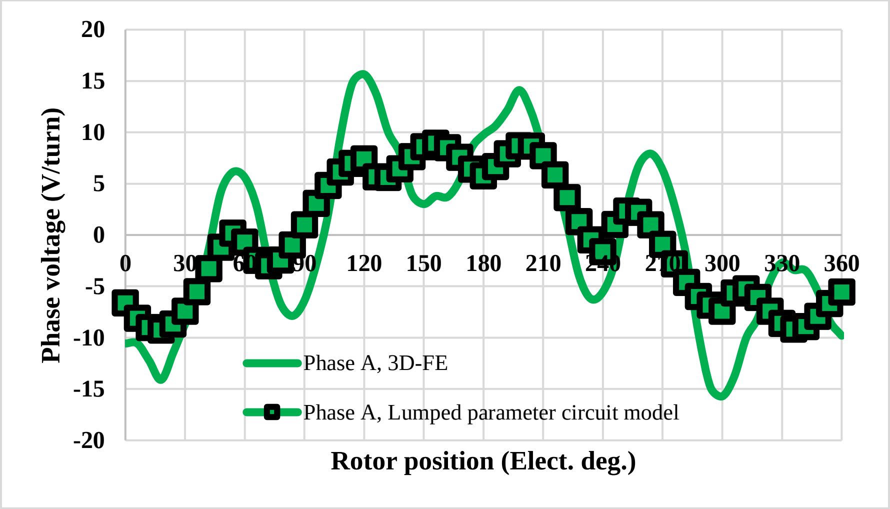

(i) Phase voltage waveform – phase A

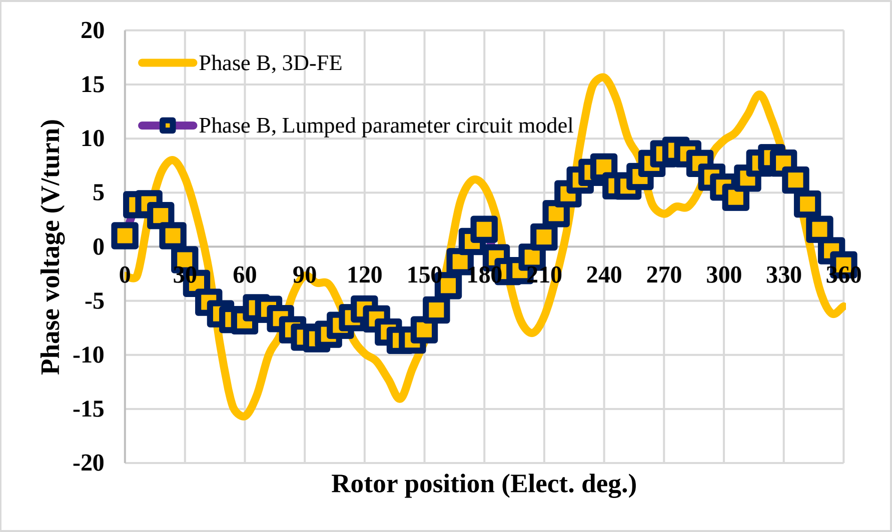

(ii) Phase voltage waveform – phase B

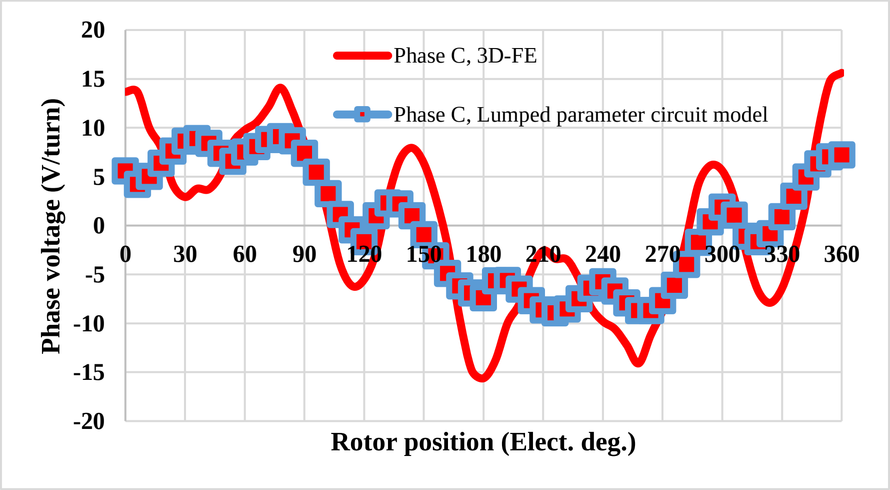

(iii) Phase voltage waveform – phase C

Fig. 4.28 Phase voltage waveforms at speed 4500 r/min, I_{max} = 880.27A, γ = 62.07°.

4.4.3 Torque at (load condition)

Fig. 4.29 - Fig. 4.33, show a comparison between the output torque waveforms which are predicted using LPCM and FE analysis for amplitude of current (I_{max} = 880.27 A/turn) at different speeds and current control angles (γ). Comparing with FEA, the average value of the predicted torque using lumped parameter circuit model at different rotation speeds is a slightly smaller as shown in Fig. 4.34 and Fig. 4.35, which show a comparison between the torque speed envelopes predicted by the proposed lumped parameter circuit model and finite element at different current angles (γ**)**. The LPCM predicted torque is calculated based on Eq. 4.14 or Eq. 4.15 [49]**.**

$$T_{(I_{max},\gamma)}=\frac{3}{2}P\left(\psi_d(I_{max},\gamma)*I_{max}*\cos(\gamma)-\psi_q(I_{max},\gamma)*I_{max}*\sin(\gamma)\right) \tag{4.14}$$

$$T_{(\psi_{(d,q)},i_{(d,q)})}=\frac{3}{2}P\left((\psi_d*i_q)-(\psi_q*i_d)\right) \tag{4.15}$$

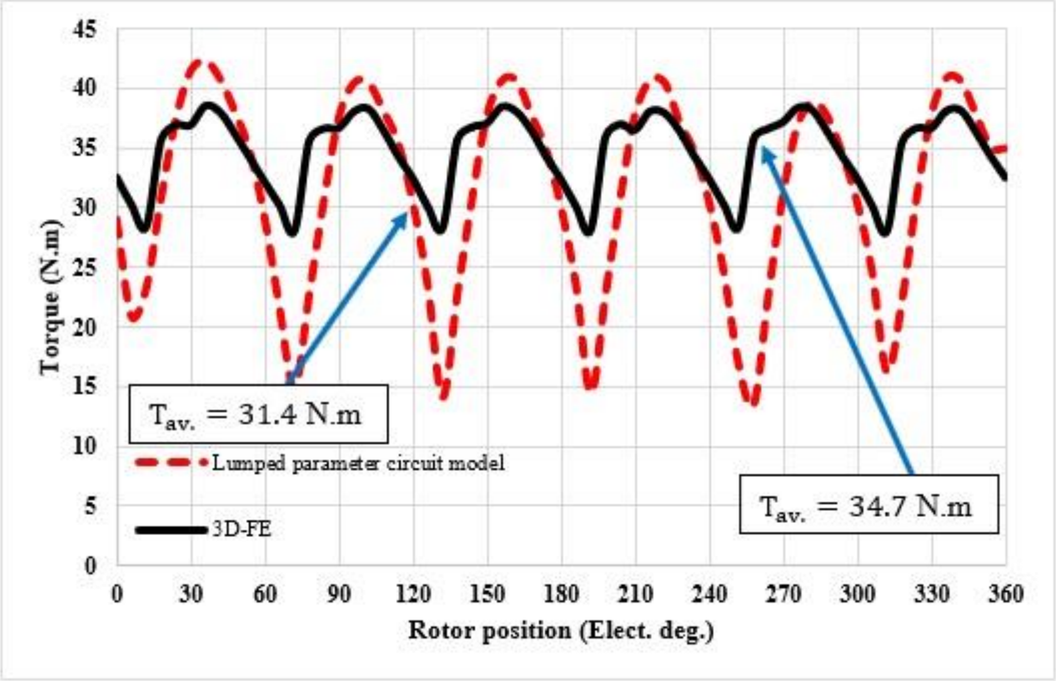

Fig. 4.29 Torque waveform at speed 2250 r/min, I_{max} = 880.27A, γ = 0°.

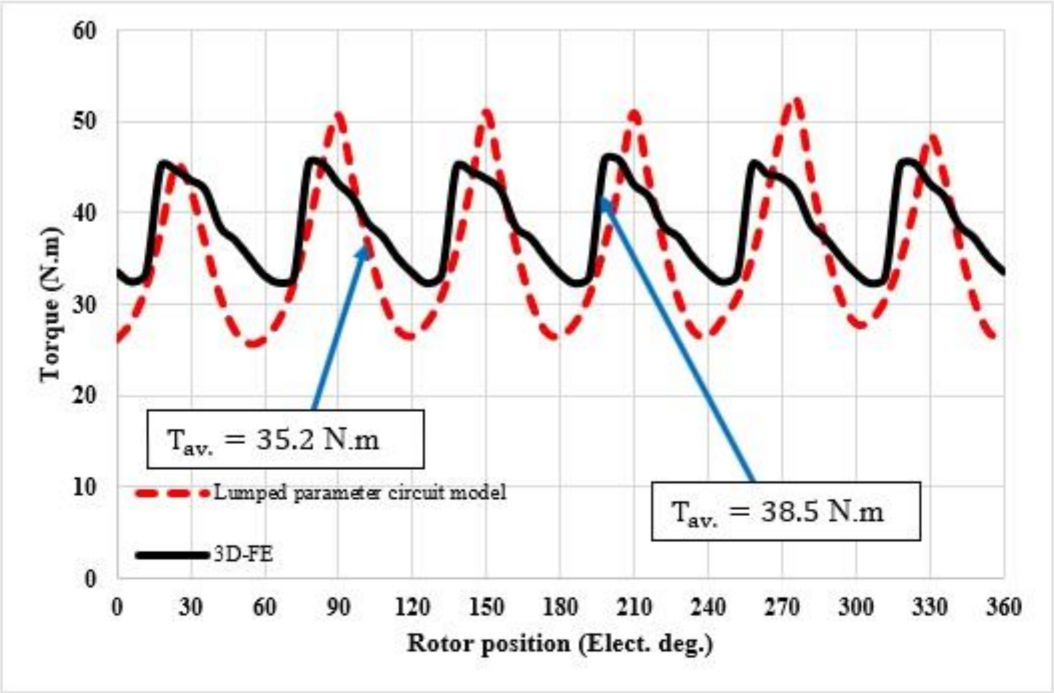

Fig. 4.30 Torque waveforms at speed 2250 r/min, I_{max} = 880.27A, γ = 25°.

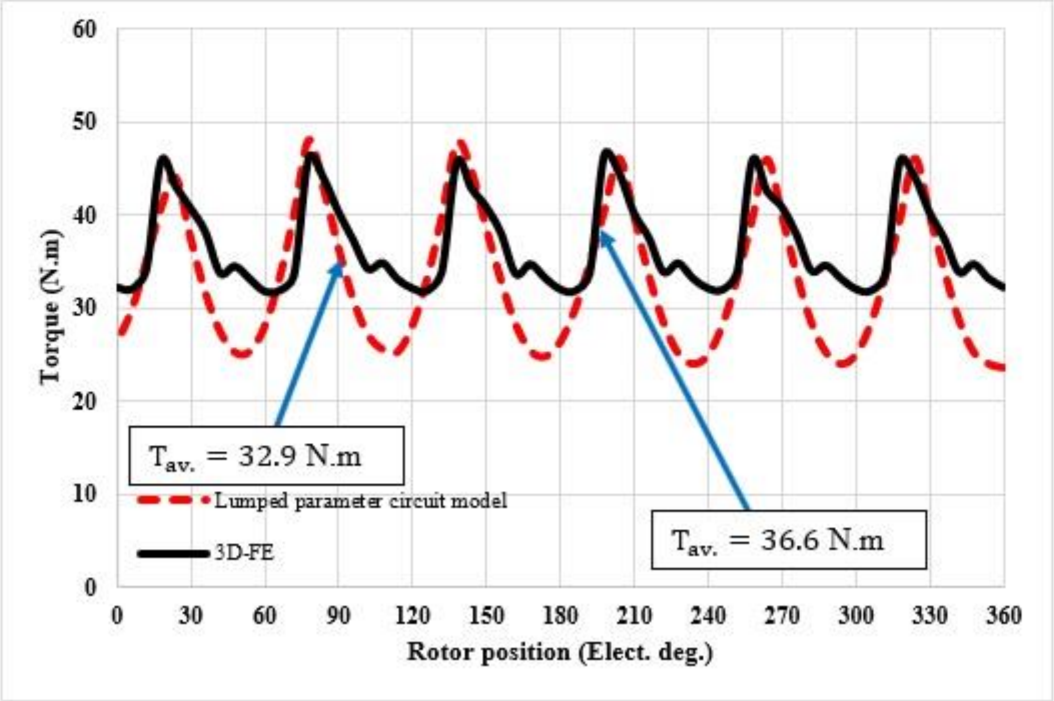

Fig. 4.31 Torque waveforms at speed 2500 r/min, I_{max} = 880.27A, γ = 35.65°.

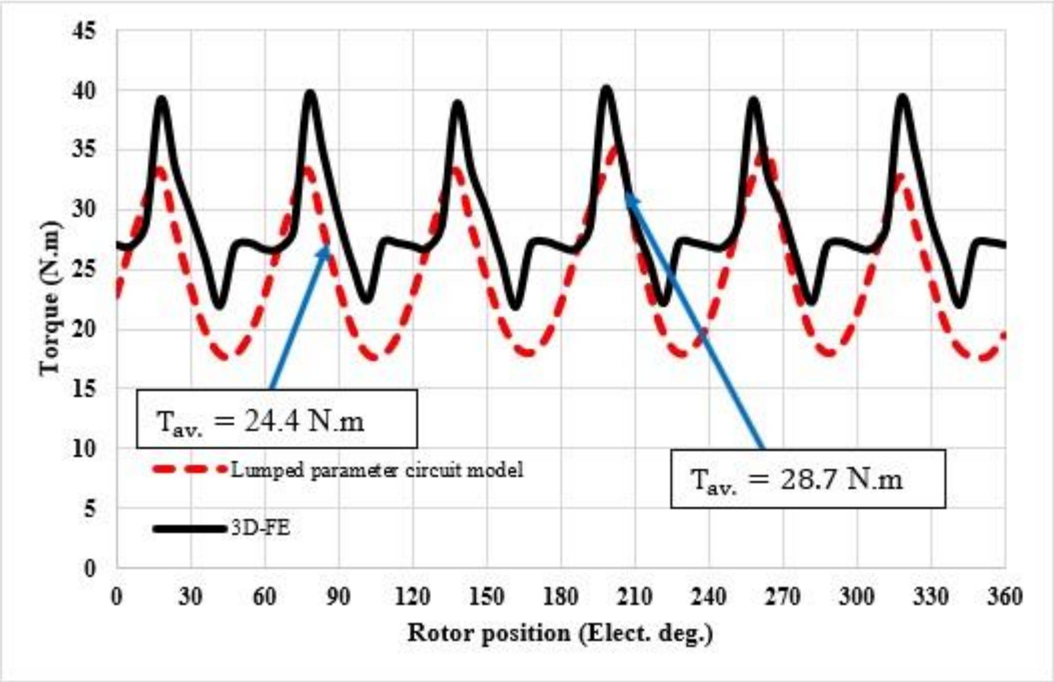

Fig. 4.32 Torque waveforms at speed 3500 r/min, I_{max} = 880.27A, γ = 52.39°.

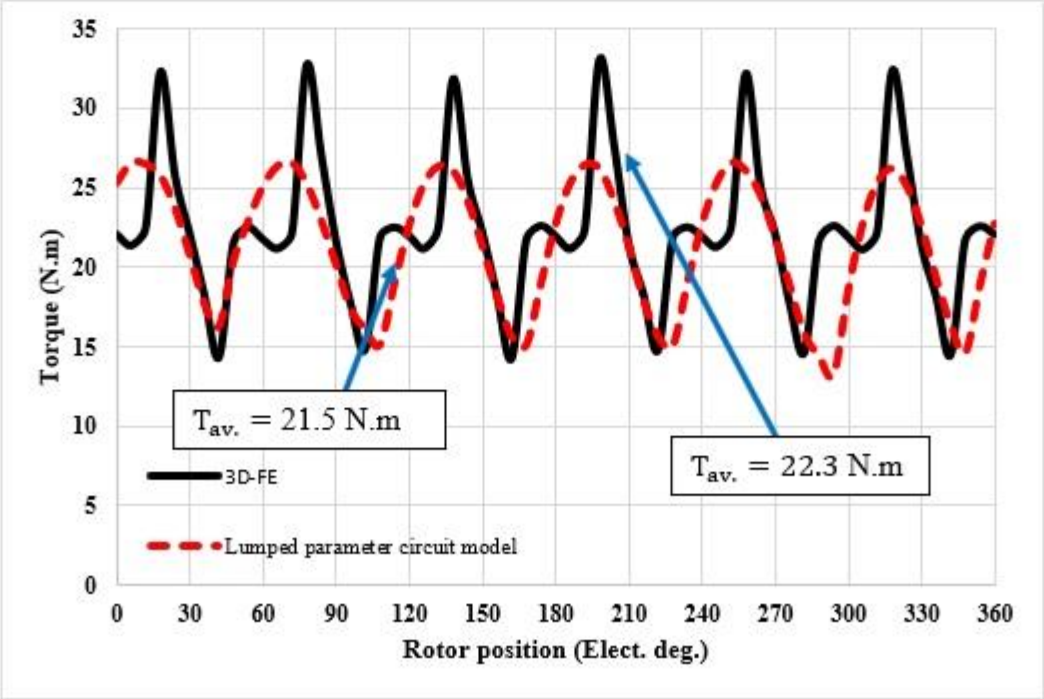

Fig. 4.33 Torque waveform at speed 4500 r/min, I_{max} = 880.27A, γ = 62.07°.

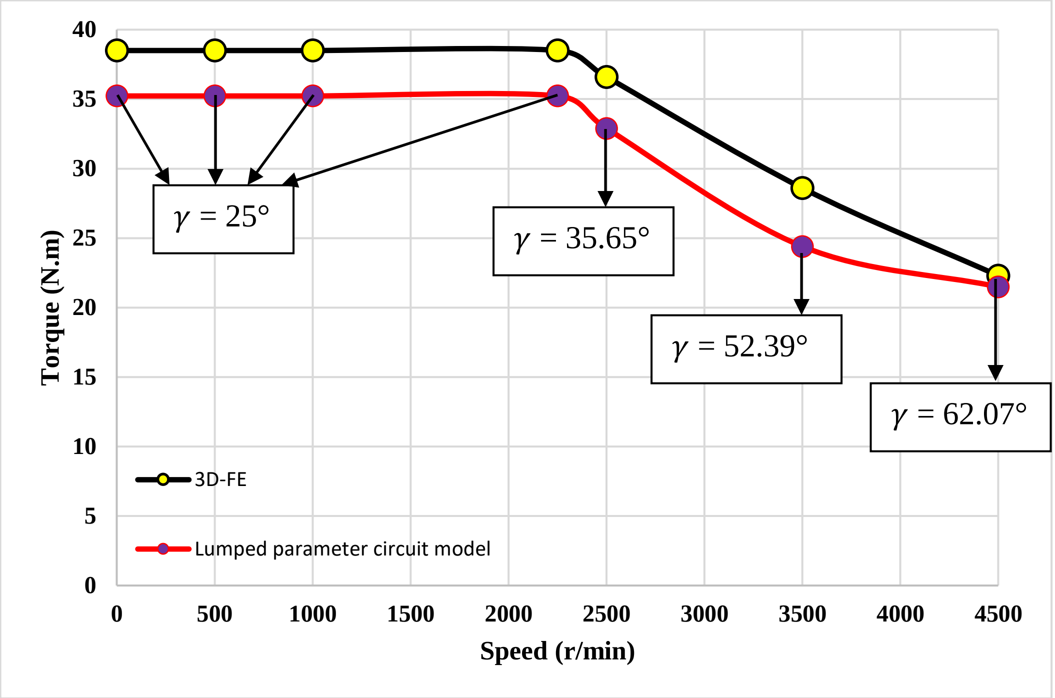

Fig. 4.34 Predicted average torque at different speed.

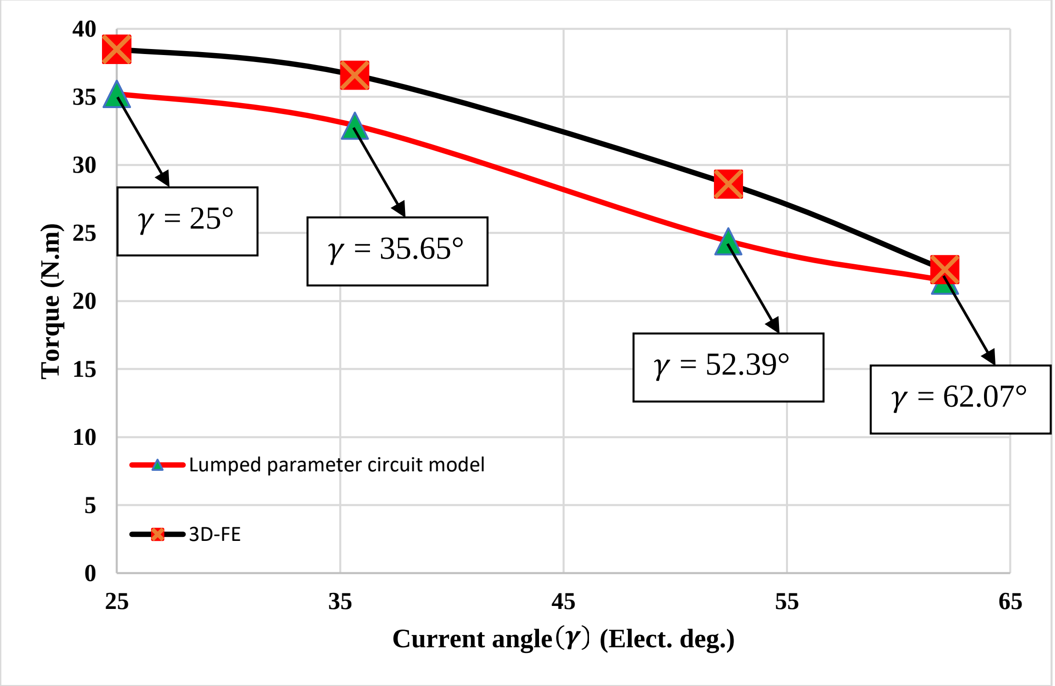

Fig. 4.35 Predicted average torque at different current control angle (γ).

4.5 Conclusion

A new lumped parameter circuit model is developed to simulate and analyze the new proposed rotor machine which is able to predict the machine characteristics with significantly shorter time compared with finite element. In addition, the nonlinear characteristics of the stator and rotor material, slot leakage, and tooth tip leakage are considered.

The predicted results including flux linkage, BEMF, phase voltage and torque waveforms are compared with finite element at no-load condition and at different current angles (γ) which show a relatively good agreement in particular for the no-load linkage flux and BEMFs.

Although nonlinear characteristics of stator are considered, there are a still noticeable differences between the predicted linkage flux waveforms between the LPCM and the finite elements, particularly for harmonics, and for the phase voltage on load conditions. One of the reasons is LPCM struggling with airgap flux with rotor/tooth alignment as R_{airgap} is only approximated. Nevertheless, the value of the predicted linkage flux when working in the field weakening region are closer to that predicted by finite element specially at high speeds of 3500 r/min and 4500 r/min.

The average value of torques predicted using LPCM generally smaller than those predicted value by finite element and it is about (8%) at based speed, albeit the difference being smaller at larger rotational speeds, as can also be confirmed by the results in Table 4.2, which shows that the values of inductances L_d and L_q are closer at higher speed under field-weakening operation.

Speed (r/min)	Current angle (γ)	L_d (FE)	L_d (LPCM)	L_q (FE)	L_q (LPCM)	L_d (%) (FE reference)	L_q (%) (FE reference)
2250	25	8.28E-06	1E-05	9.9E-06	8.25E-06	-31.7 %	17.1 %
2500	35.65	8.15E-06	1E-05	1.03E-05	8.9E-06	-25.8 %	13.4 %
3500	52.39	8.5E-06	9.84E-06	1.06E-05	8.69E-06	-15.6 %	17.7 %
4500	62.07	8.69E-06	9.9E-06	1.06E-05	1E-05	-14.3 %	2.75 %

Table 4.2 Results for L_d and L_q inductances.

Chapter 5

Experimental tests and validations of the novel prototype

5.1 Introduction

In this chapter the manufacture and description of the different components and assembly of the Ferrite prototype electrical machine are represented. Furthermore, the description for the methods adopted for the realization of the prototype and tests undertaken is investigated and the results are compared with 3D-finite element predictions.

5.2 Novel machine prototype

The overall geometry of the novel prototype is shown in Fig. 5.1. Each part of the prototype construction will be detailed as shown in the following:

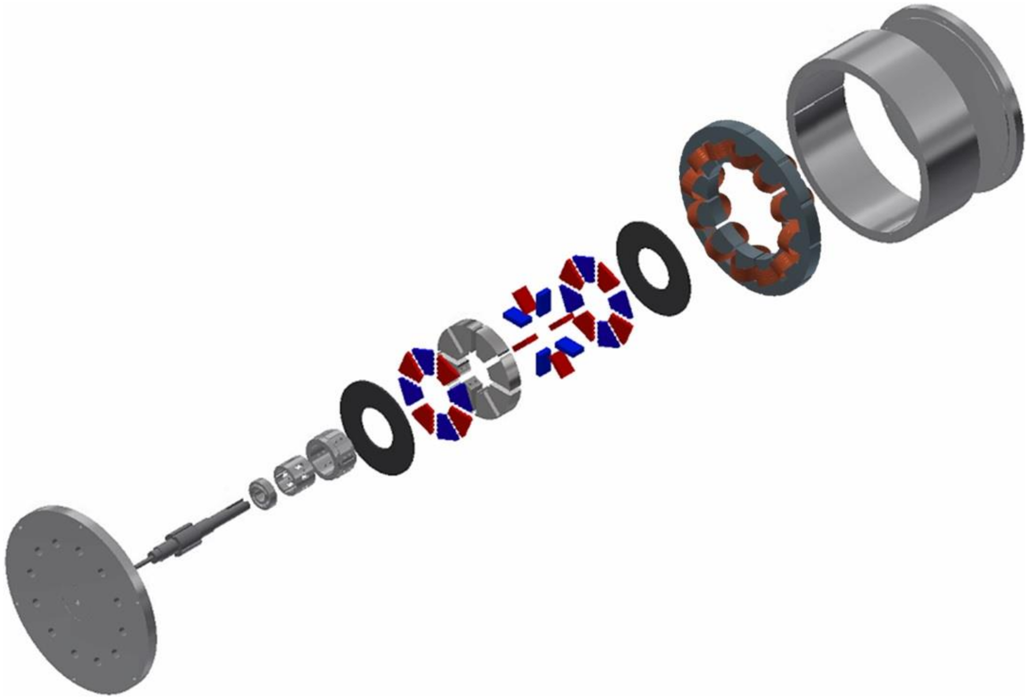

Fig. 5.1 Schematic diagram of the novel prototype.

5.2.1 Stator

The stator part of the new prototype is shown in Fig. 5.2. It consists of steel lamination type (M270-35A) with (0.35 mm) thickness and (30 mm) active axial length with 12 slots, fractional slot concentrating windings (FSCW) with 24 turn/tooth, 0.75 mm winding diameter are wounded as shown in Fig. 5.3 & Fig. 5.4 respectively. The overall dimensions will be shown in Appendix A.

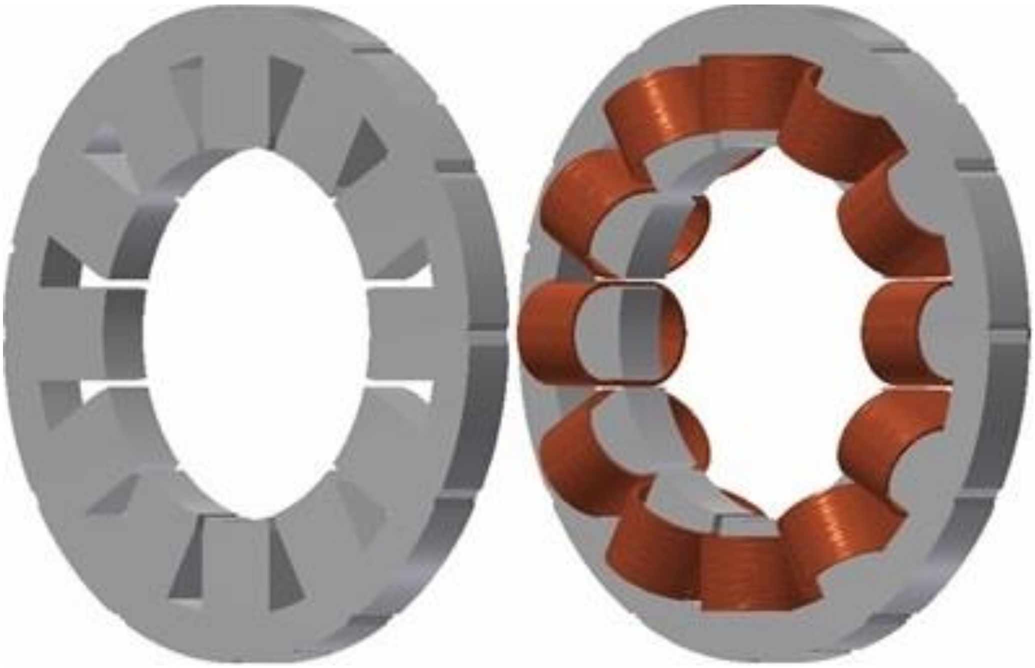

(a) (b)

Fig. 5.2 Stator modelling for the new proposed prototype.

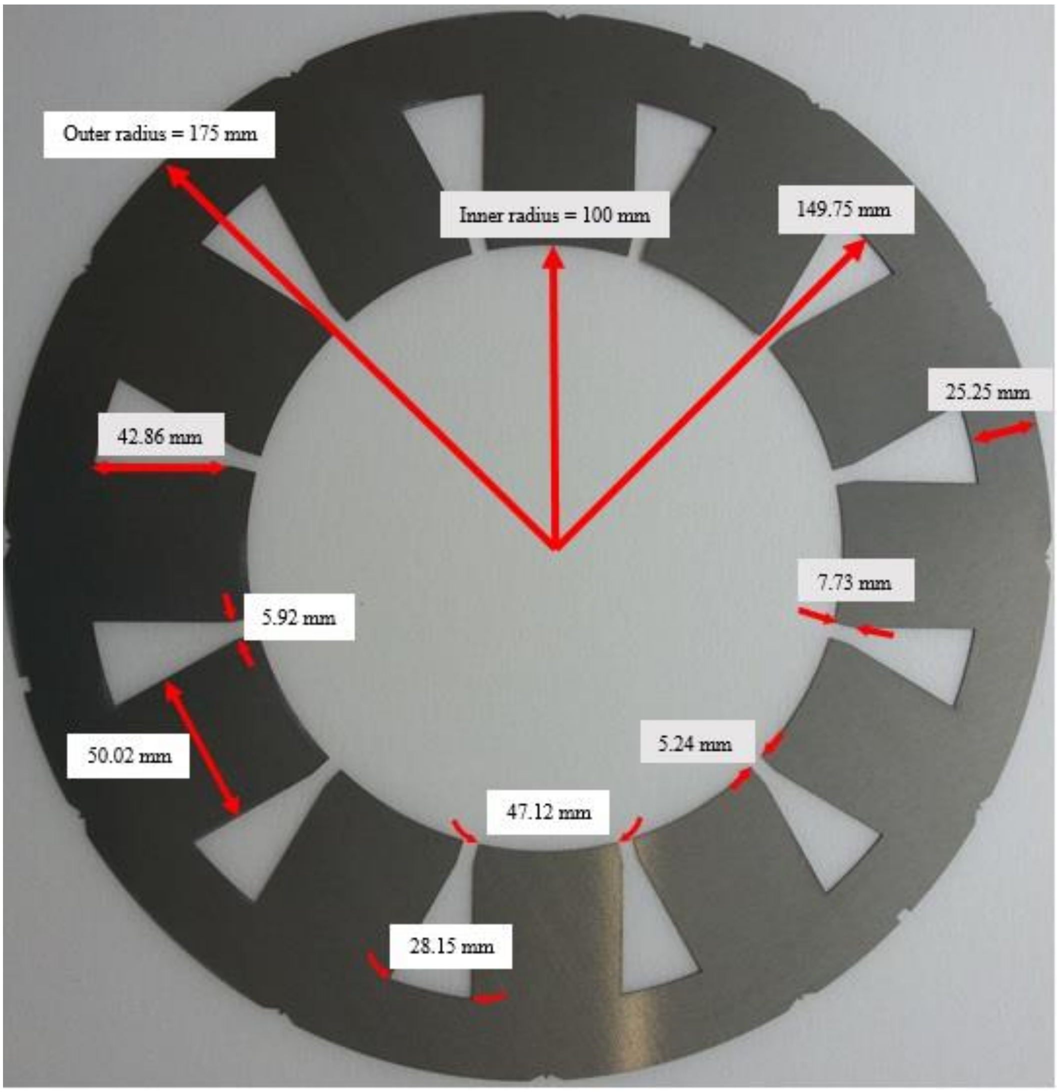

Fig. 5.3 Stator steel lamination type (M270-35A).

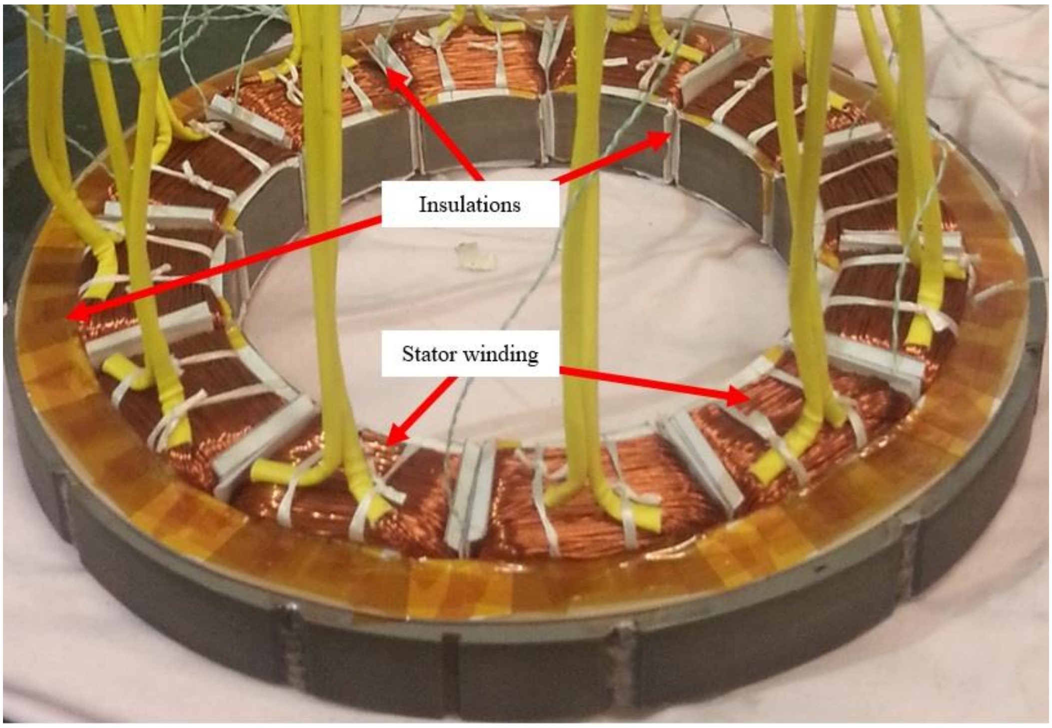

(a)

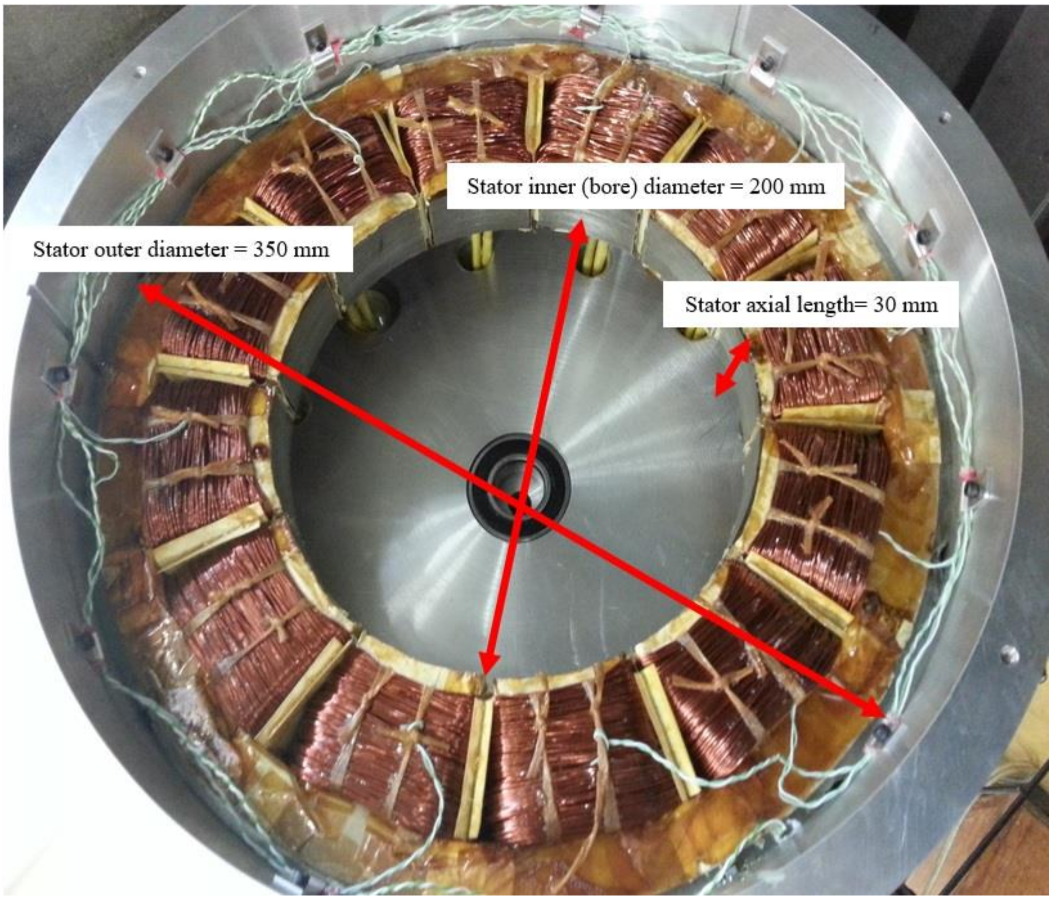

(b)

Fig. 5.4 Proposed stator with windings.

5.2.2 Rotor

The rotor part of the new proposed machine is shown in Fig. 5.5 & Fig. 5.6. It consists of:

- Rotor pole pieces.
- Axially and circumferentially magnetised permanent magnets.
- Soft magnetic rings.
- Shaft.
- Cylindrical bush and adapter.

Due to cost and machining difficulties, the axially magnetised permanent magnets are assembled from rectangular pieces, resulting in total area smaller than originally assumed. The description of each part will be detailed below and the overall dimensions and schematic diagram for the rotor pole pieces, axially and circumferentially magnetised permanent magnets and the cylindrical bush will be shown in Appendix A.

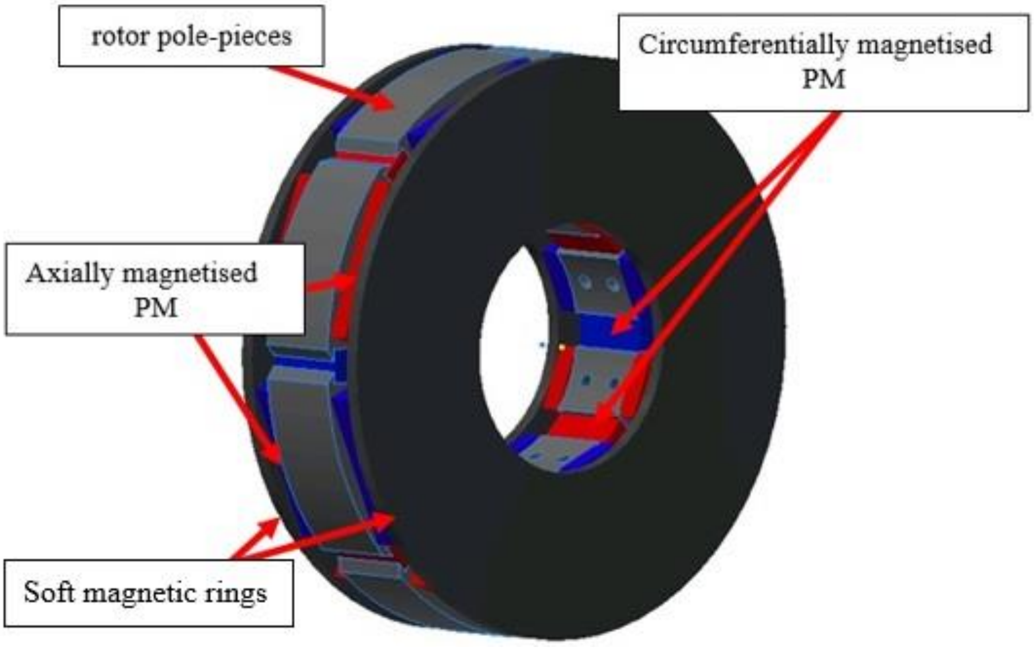

(i) Assembled rotor

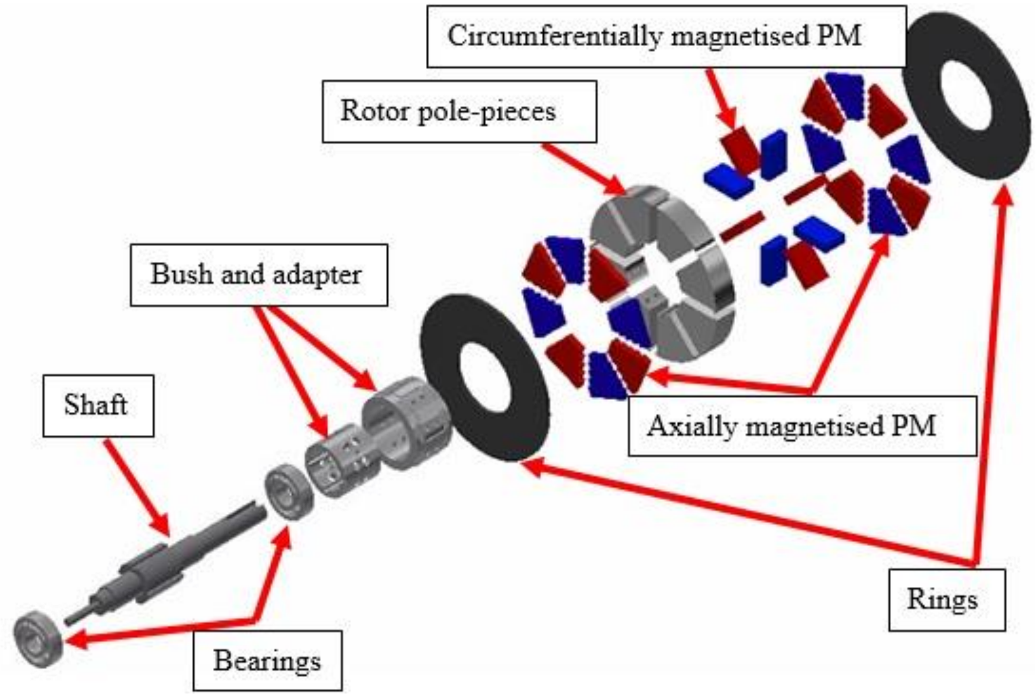

(ii) Exploded view

Fig. 5.5 Schematic diagram of the proposed rotor.

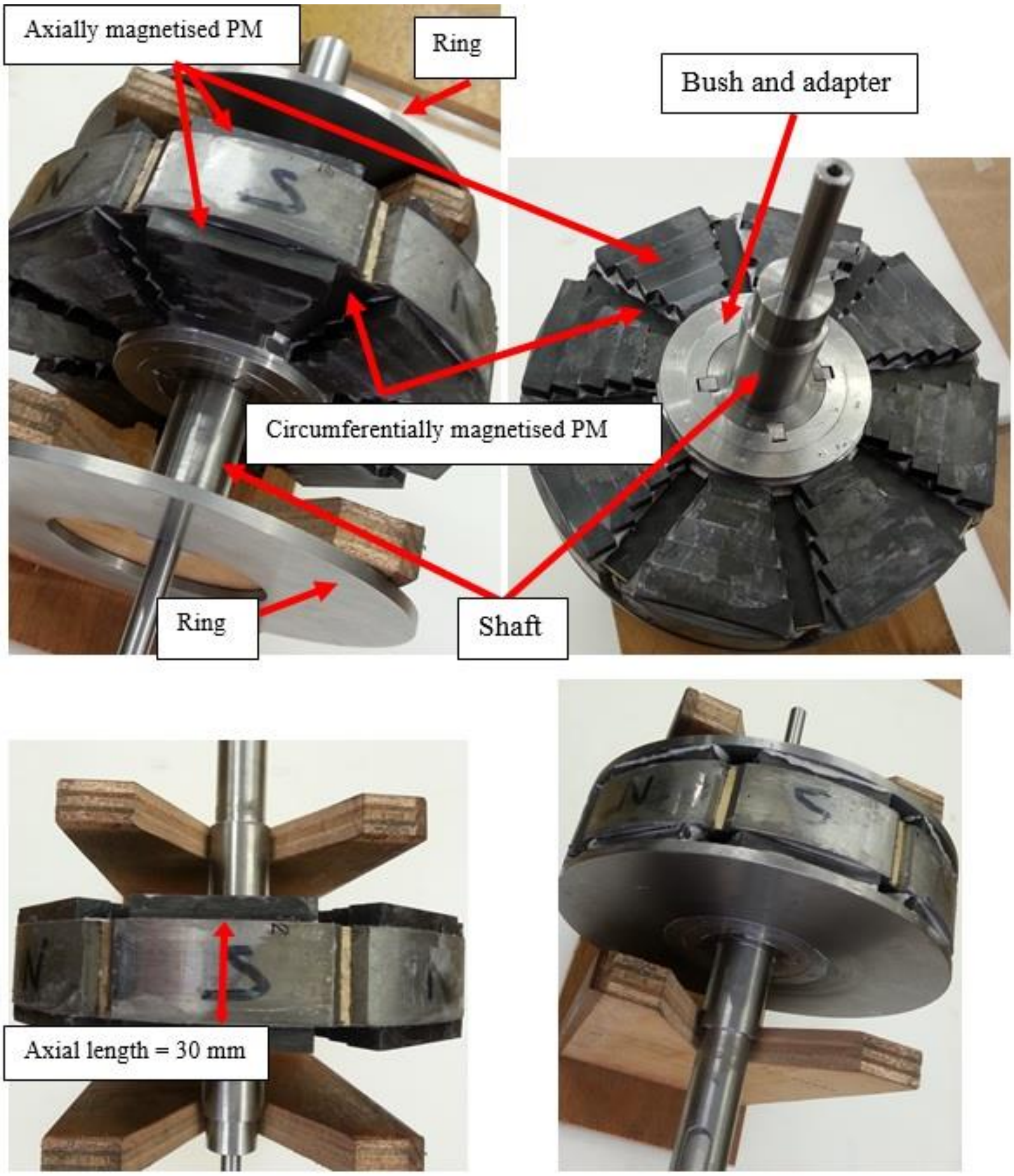

Fig. 5.6 Proposed rotor.

Fig. 5.7 & Fig. 5.8 show the rotor pole-pieces which are built using (mild steel EN1) and fixed on a non-magnetic aluminium bush using non-magnetic stainless screws to minimise the leakage flux. At the outer diameter of the moulds there are two features which are used to protect the circumferential PM from being thrown out by the centrifugal force at high-speed operation.

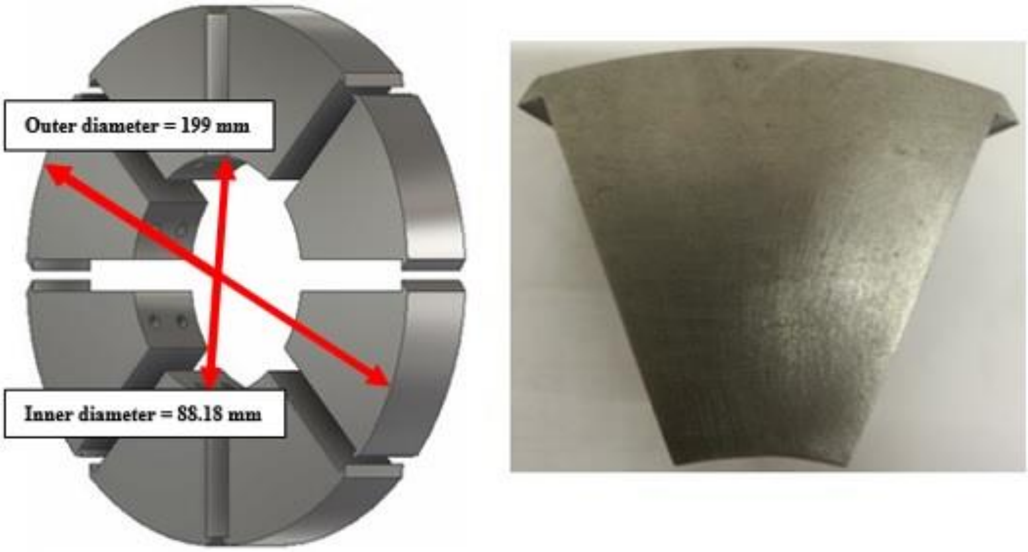

Fig. 5.7 Schematic diagram of the proposed rotor pole-pieces.

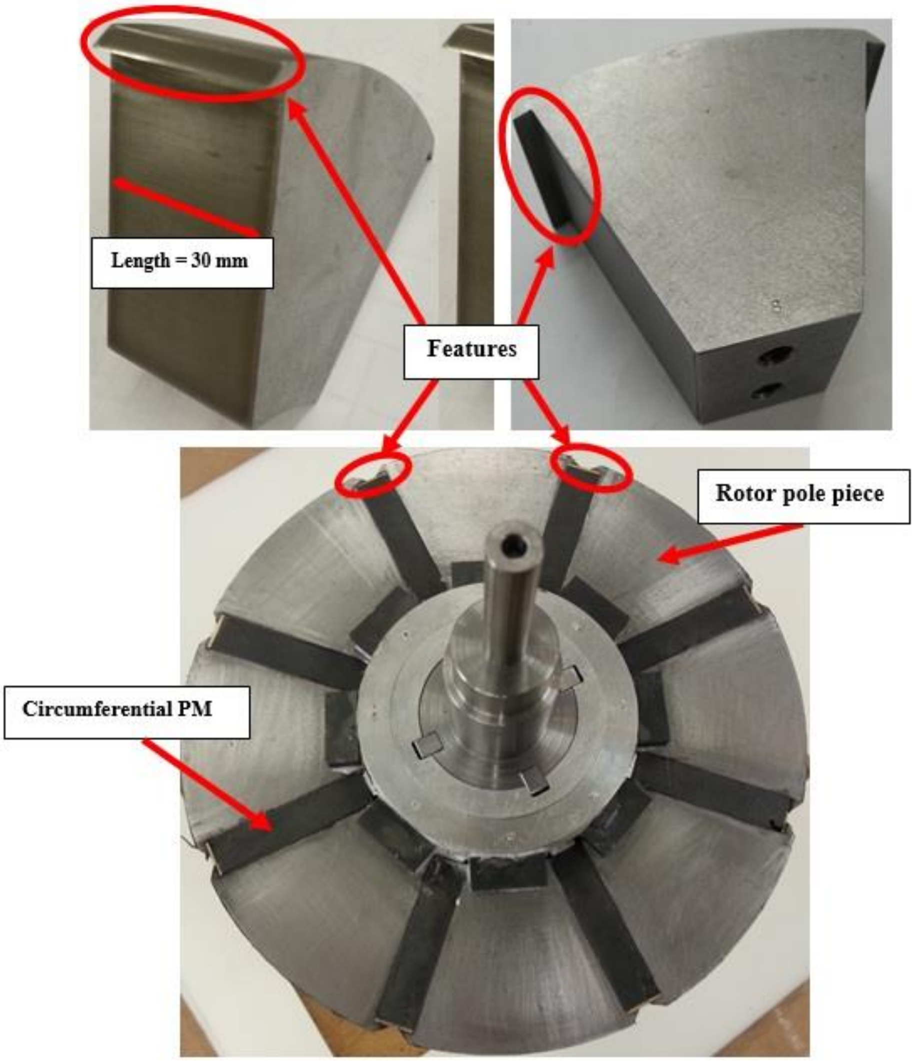

Fig. 5.8 Proposed rotor pole-pieces.

Fig. 5.9 shows the geometry of the axially and circumferentially magnetized sintered ferrite permanent magnets which are used in the new proposed machines with Br about (0.39) and linear at 20° in the 2^{nd} quadrant B-H characteristics. As shown in Fig. 5.6, there will be two layers of axially magnetised PM distributed and fixed on both sides of the rotor pole pieces using specific high strength glue. It may worth mentioning that the axially magnetised PM provide a leakage bath for circumferentially magnetised PM and vice versa.

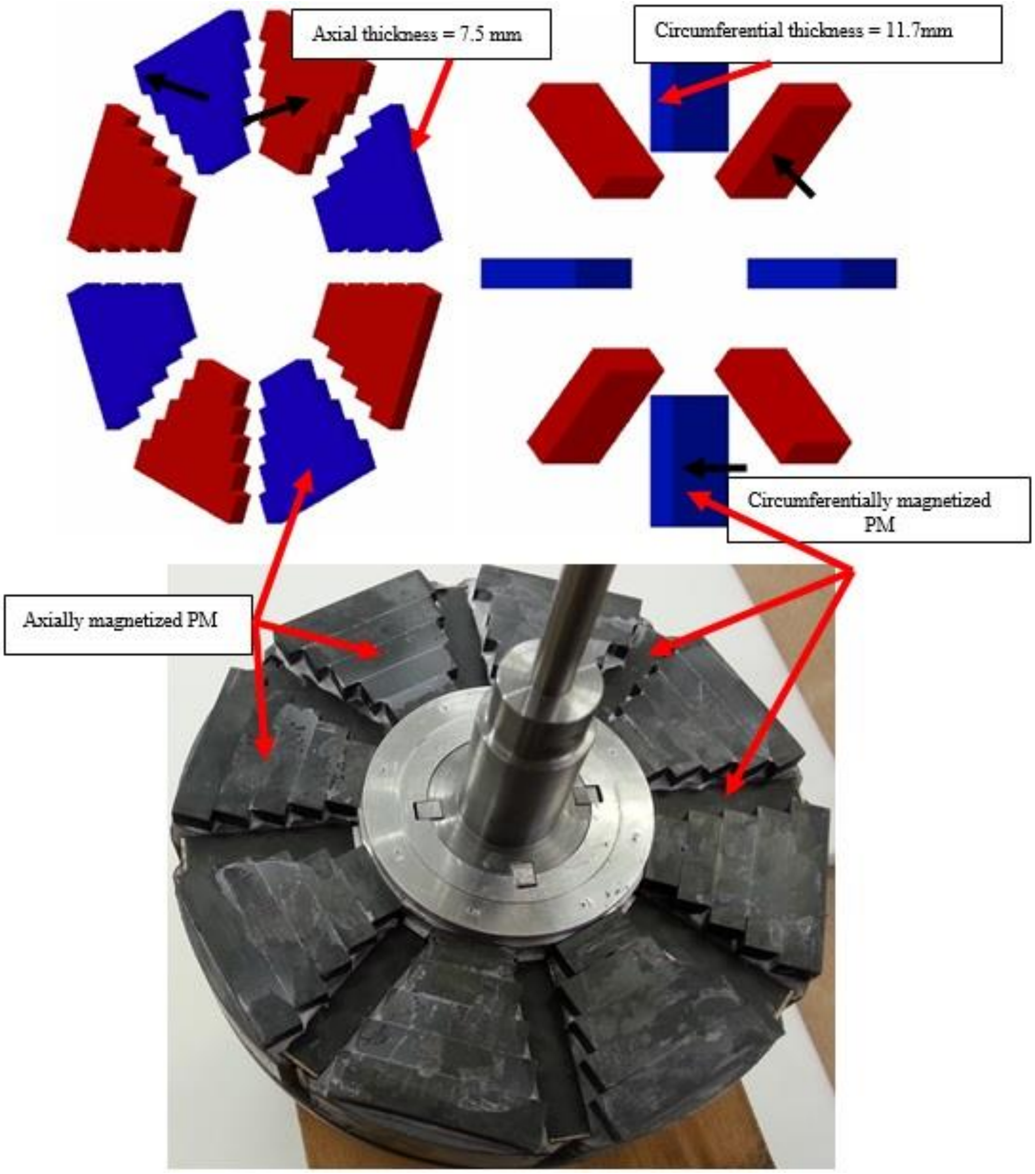

Fig. 5.9 Geometry of axially and circumferentially magnetised PM.

As shown in Fig. 5.5, the two soft magnetic rings with high permeability steel are used and fixed over each axially magnetised PM to provide a good path for the magnetic flux as well as supporting the rotor parts. The geometry of the soft magnetic ring is shown in Fig. 5.10.

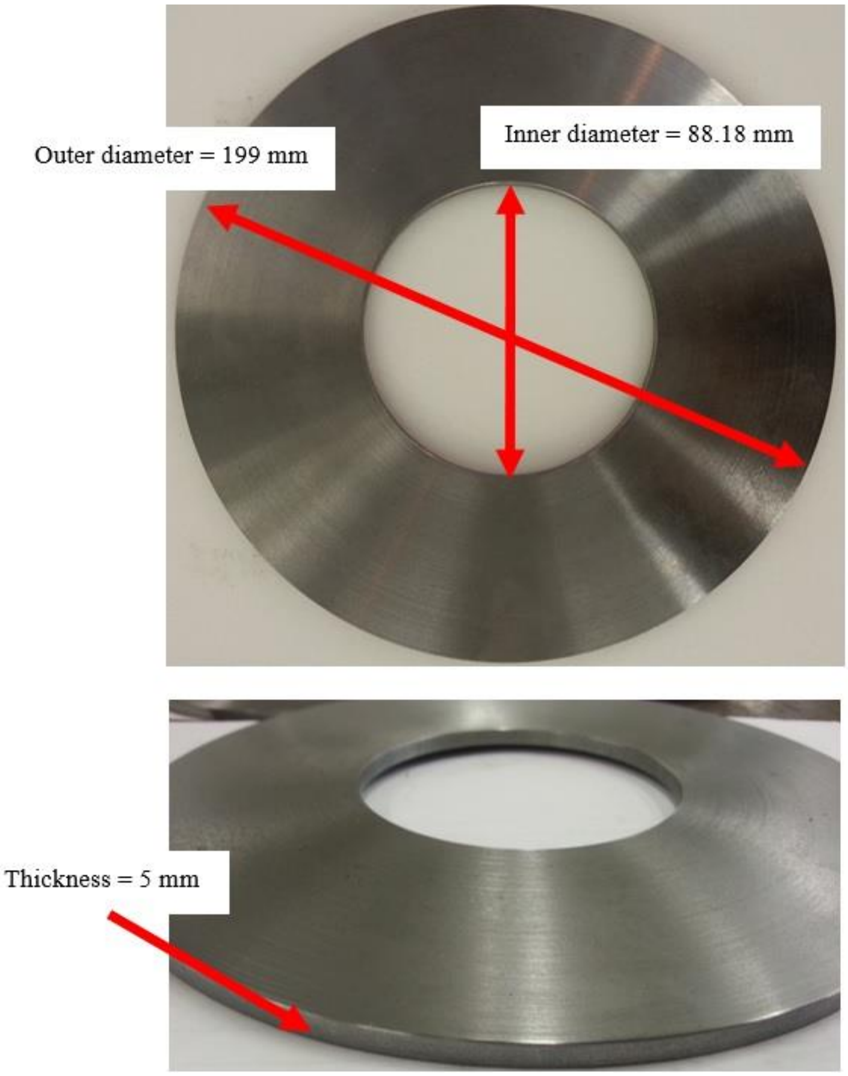

Fig. 5.10 Geometry of the soft magnetic ring.

The geometry of the used shaft is shown in Fig. 5.11. Due to the combined weight of the shaft and the (attached parts fixed over the shaft), a deflection in the shaft may happen during rotation which will creates resonant vibration at certain speed which is called critical speed. The magnitude of shaft deflection depends on 1) stiffness of the shaft and its support. 2) total mass of the shaft and attached parts. 3) unbalance of the mass with respect to the axis of rotation [66]. The calculation of the critical speed is shown in Eq. 5.1.

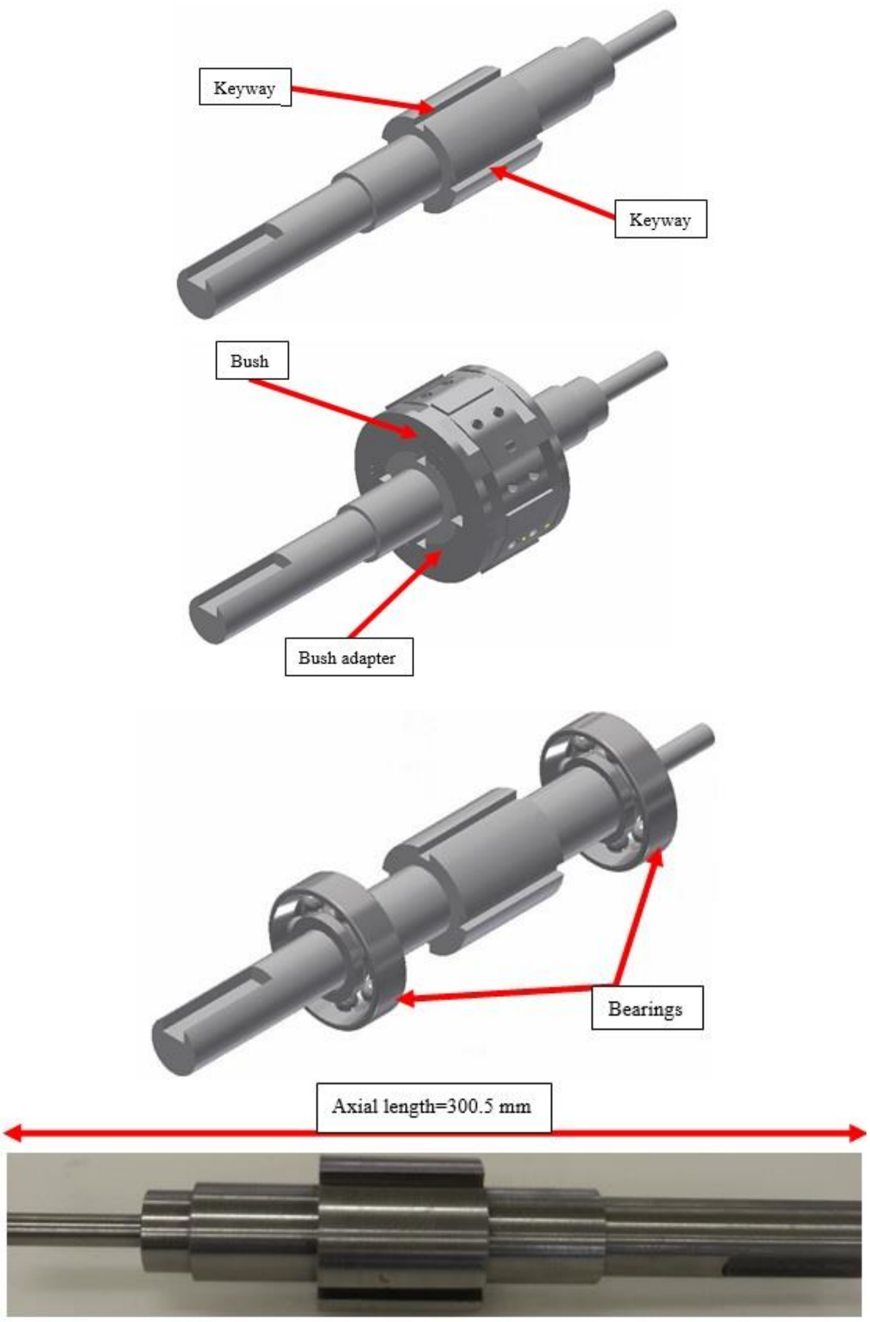

Fig. 5.11 Proposed Shaft geometry of the machine.

$$\text{Critical speed (Nc)} = \frac{30}{\pi}\sqrt{\frac{g}{\delta_{st}}} \qquad 5.1$$

Where:

g = gravity acceleration (9.81 m/s^2).

δ_{st} = total maximum static deflection.

The total maximum static deflection (δ_{st}) consists of a) Maximum static deflection on shaft (δ_{st1}) based on Fig. 5.12 and Eq. 5.3 [66]. (b) Maximum static deflection on load (δ_{st2}) based on Fig. 5.13 and Eq. 5.4 [66].

$$\delta_{st} = \delta_{st1} + \delta_{st2} \tag{5.2}$$

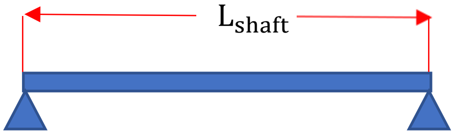

Fig. 5.12 Static deflection on shaft.

$$\delta_{st1} = \frac{5w\mathrm{L_{shaft}}^3}{384EI} \tag{5.3}$$

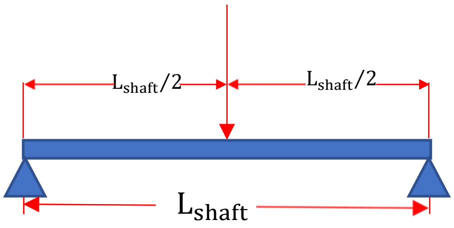

Fig. 5.13 Static deflection on load.

$$\delta_{st2} = \frac{W\mathrm{L_{shaft}}^3}{48EI} \tag{5.4}$$

Where:

w = weight of the shaft in kg, (1.657 kg)

W = weight of the wheel (attachment parts over the shaft) in kg, (9.5 kg).

E = modulus of elasticity, kg/m^2, for shaft C40= $200\times10^8\,\mathrm{kg}/m^2$.

I = moment of inertia = $\pi D^4/64$, m^4.

$\mathrm{L_{shaft}}$ = length of the shaft, m. (300.5 mm).

According to Eq. 5.1, the critical speed (Nc) is (18000 r/m) at total maximum static deflection is about (1.5E-6 m).

An aluminium bush and adapter are fixed over the shaft using key material which are fixed through the keyways paths to avoid sliding. On the both ends of shaft there are two deep groove bearings type (6205-2RSLTN9/C3VT162). The diameter of the bearing and its type is chosen depending on the total load (dynamic and static load) on the shaft and its diameter. Fig. 5.14 shows the bush and bush adapter material**.** The material which has been used for the shaft is (steel EN8) and for the bush and bush adapter is (aluminium).

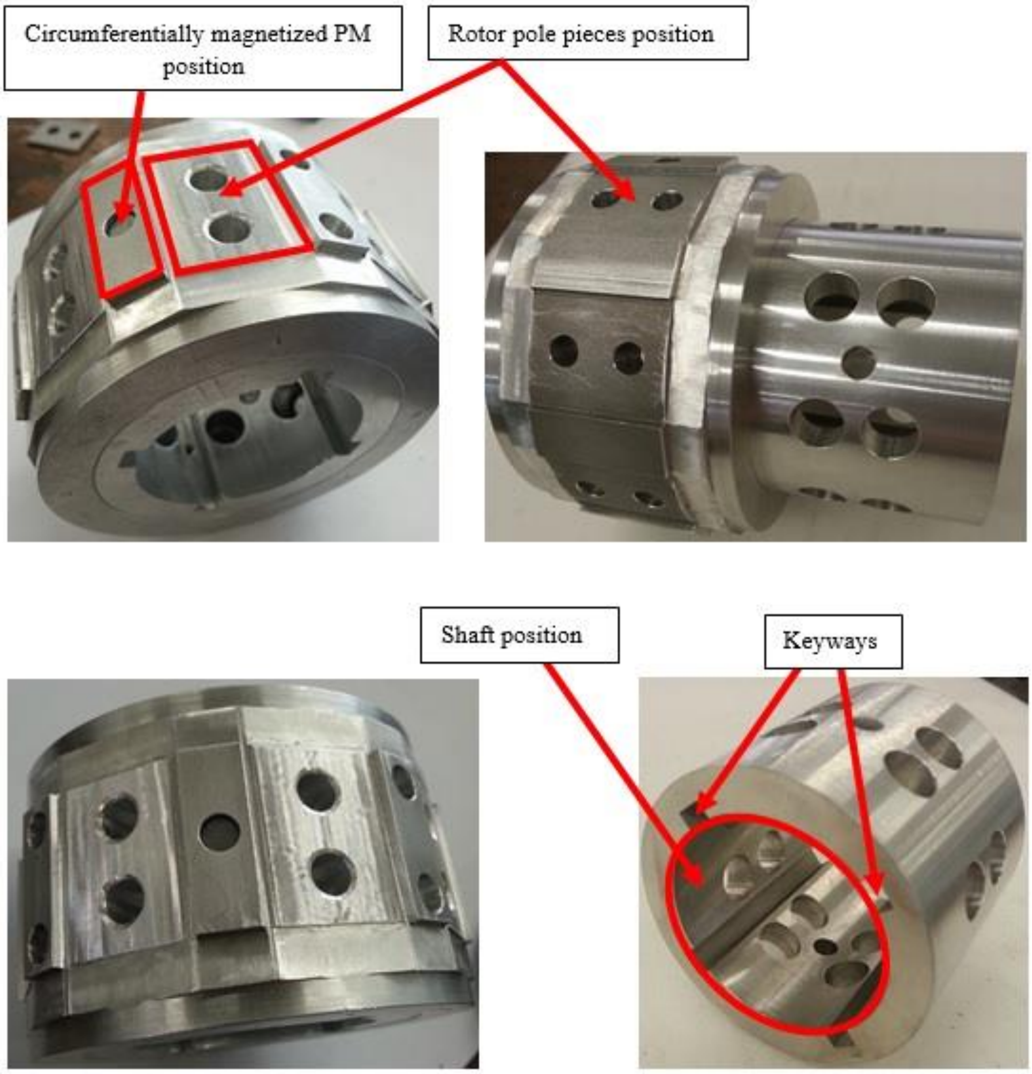

Fig. 5.14 Bush and adapter fixed over the shaft.

5.3 Experimental results and validations

Experimental tests are undertaken to measure the output characteristics of the new proposed machine such as (cogging torque, static torque and BEMF) and compared with those obtained from finite elements.

5.3.1 Cogging torque measurements

For any slotted permanent magnet machines, due to the interaction between the PM and slot permeance there will be a cogging torque generated which has an important effect on the speed ripple and may cause acoustic noise and vibration. Therefore, it is important to separately quantify the cogging torque accurately. In this section a specific simple test is applied on the new proposed machine to measure the cogging torque wave form as in [67].

The schematic diagram of the cogging torque measurements rig is shown in Fig. 5.15.

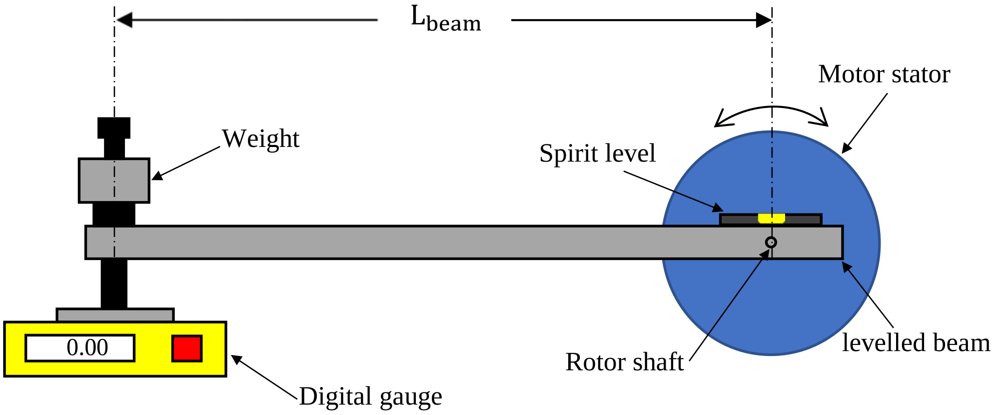

Fig. 5.15 Schematic diagram of cogging torque measurements.

The stator is fixed in the jaws of lathe which enable it to turn in different (precise) steps. A levelled beam is attached to the rotor shaft and the and one end is rested on the tray of weight scale which is fixed on support table. Firstly, the beam is levelled at the weight scale was zero, then the weight is added and fixed at the end of the bar as preload to ensure the bar is always in contact with the scale, and to obtain measurement of positive and negative the cogging torque waveform, i.e. getting always positive waveform of the measured cogging torque. Secondly, the stator is turned in the lathe at fixed steps (1.5°-90°). The experimental installation to measure the cogging torque is shown in Fig. 5.16.

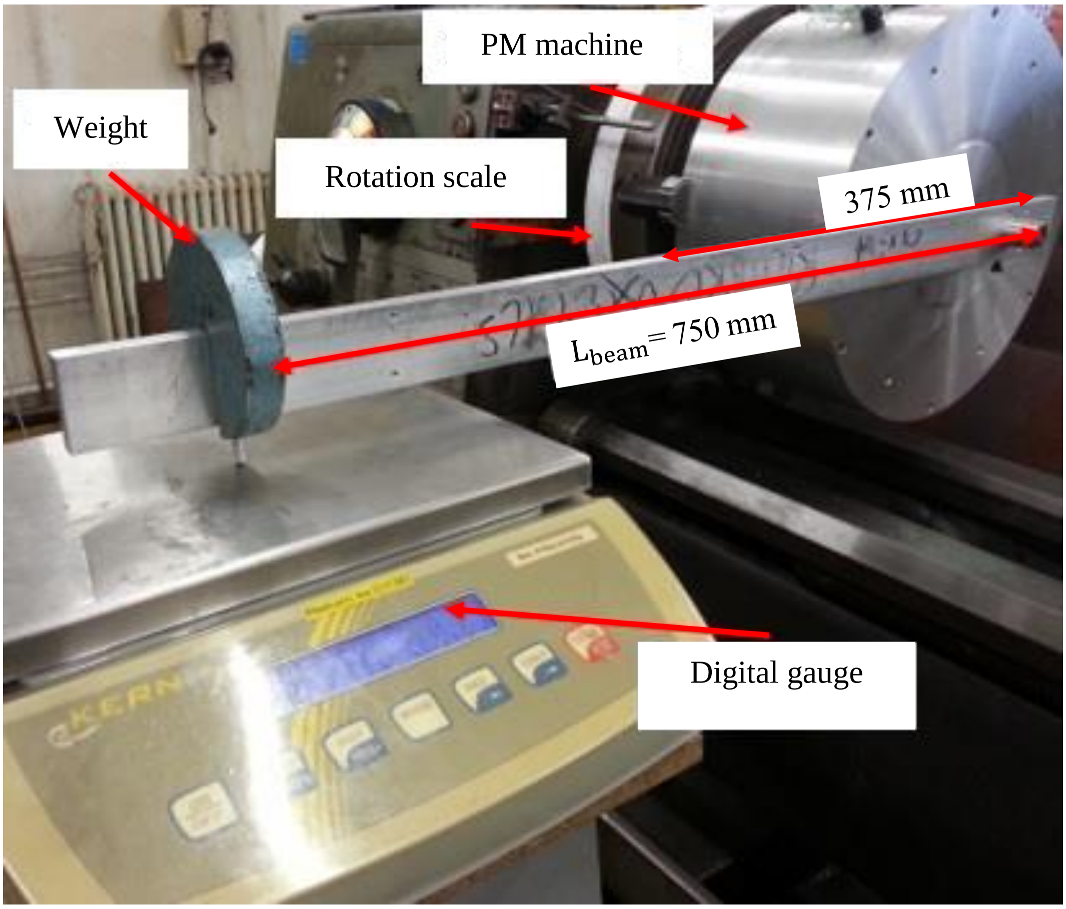

(i) Cogging torque measurement with preload weight = 1.36 kg

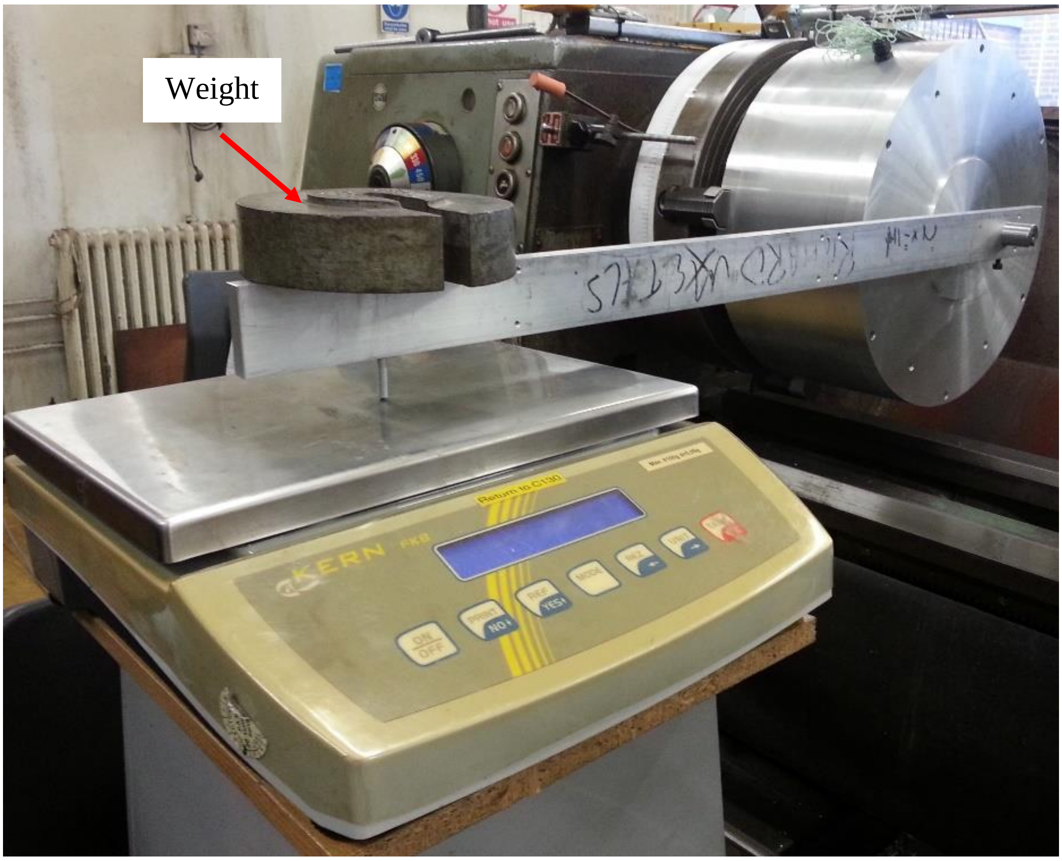

(ii) Cogging torque measurement with preload weigh = 4.56 kg

Fig. 5.16 Installation for cogging torque measurement (experimentally).

Due to the position changing between the stator and rotor relatively, the measured force is asserted with the changing cogging torque value acting on the bar. For symmetrical permanent magnet machine which having equal positive and negative cycles of the cogging torque waveform and zero average value, the equation of the cogging torque can be obtained from the reading of the weight scale $\left(F_{reading}\right)$ and the length of the bar (L_{beam}) after subtracting the pre-load force $\left(F_{pre-load}\right)$ as shown in Eq. 5.5 – Eq. 5.8.

$$T_{cogging} = \left(\left(L_1\left(F_{reading} - F_{pre-load}\right)\right) - \left(L_2 F_{bar}\right)\right) \quad 5.5$$

$$F_{reading} = w_{scale\ reading}(\mathrm{kg}) \times g \quad 5.6$$

$$F_{pre-load} = w_{pre-load}(\mathrm{kg}) \times g \quad 5.7$$

$$F_{bar} = w_{bar}(\mathrm{kg}) \times g \quad 5.8$$

Where:

$L_1 =$ The total length of the beam from the centre of the rotor shaft to the centre of the weight (mm)

$L_2 =$ The length of the beam from the centre of the rotor shaft to the middle of the beam.

$g =$ Gravity acceleration (9.8 m/s^2).

Fig. 5.17 shows the variation of measured and predicted cogging torque waveforms with rotor position. It can be noticed that although the shape of the waveforms is very similar, the measured cogging torque is larger than predicted, with predicted cogging torque considering the realisation of the axial permanent magnet Fig. 5.18 being ever smaller. Nevertheless, the results show that the maximum value of the cogging torque is very small and about 5.5% of the rated torque value. The modification of the shape of the axially magnetized permanent magnet is represented in 3D-FEA by changing the value of the remanence flux density B_r of the magnet. The area of the modified shape of the axial magnetized permanent magnet is reduced to about 19% comparing with the original shape, Therefore, the modified value of the B_r is equal to:

$$B_r\ (\text{modified}) = B_r\ (\text{original}) - (0.19 \times (B_r\ (\text{original}))) \quad 5.9$$

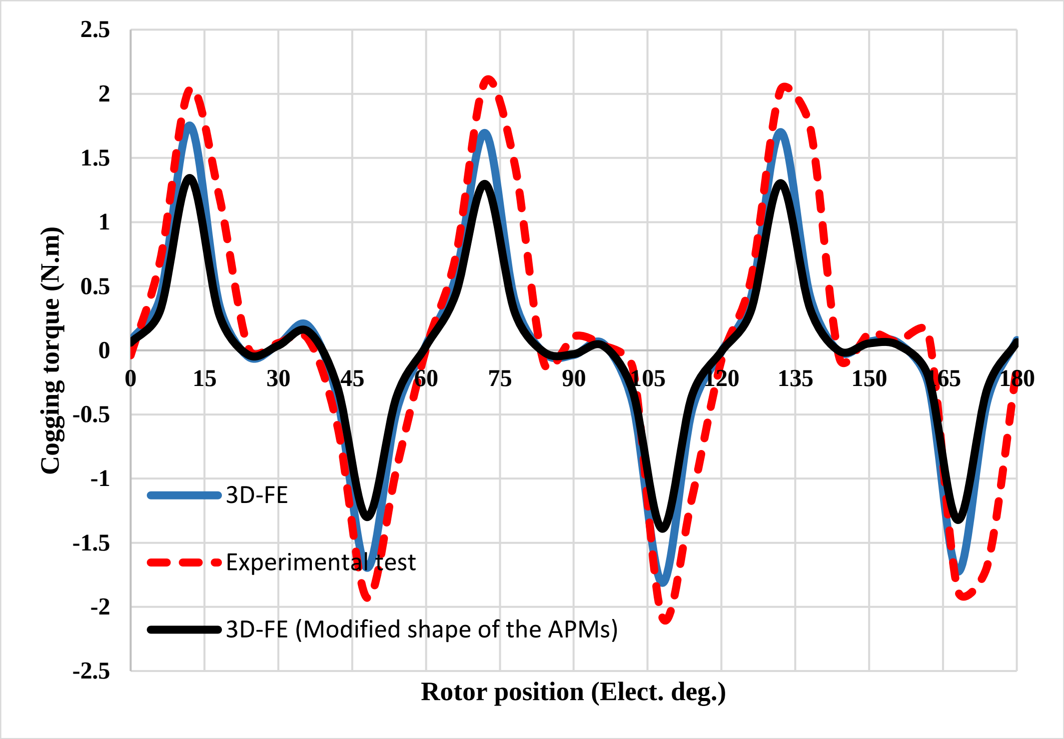

Fig. 5.17 Cogging torque waveforms.

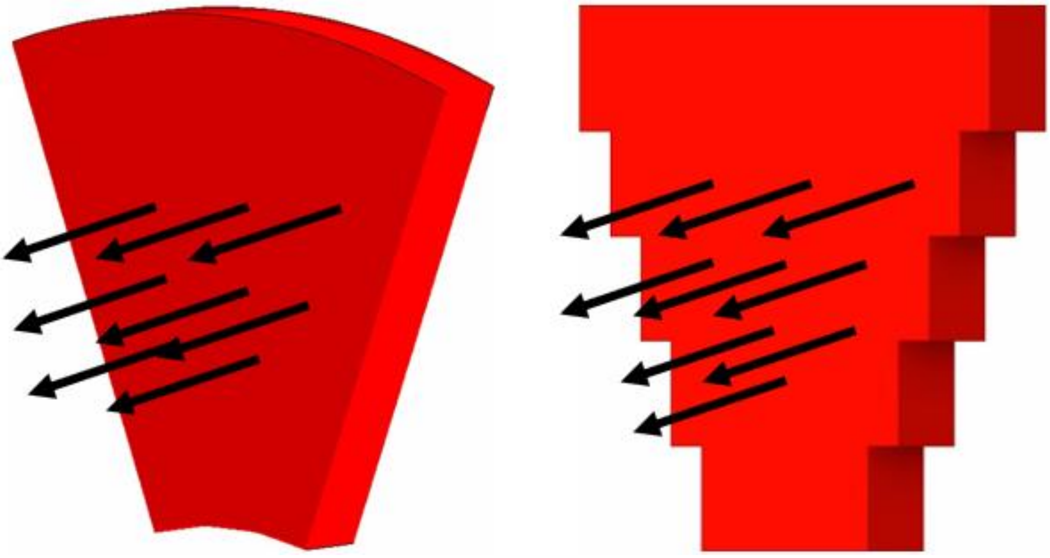

(a) (b)

Fig. 5.18 Shape of the axially magnetised PM. (a) FE, (b) practically.

5.3.2 Static torque measurements

The measurement of the static torque is undertaken using the same method mentioned in Fig. 5.15 and Fig. 5.16 with DC current supply connected to the both side of the machine winding input terminals (phase A, Phase B and phase C) as shown in Fig. 5.19 and Fig. 5.20.

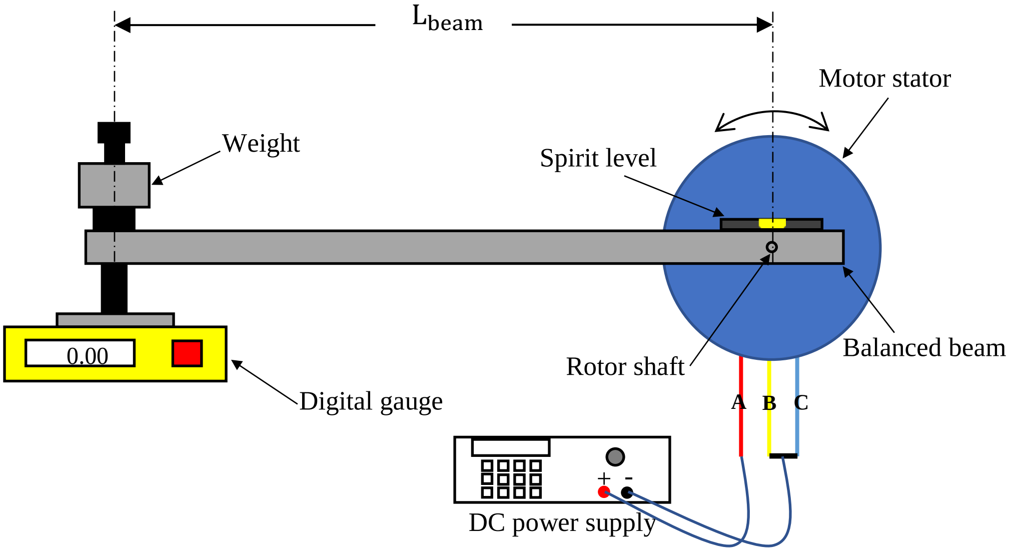

Fig. 5.19 Schematic diagram of static torque measurements.

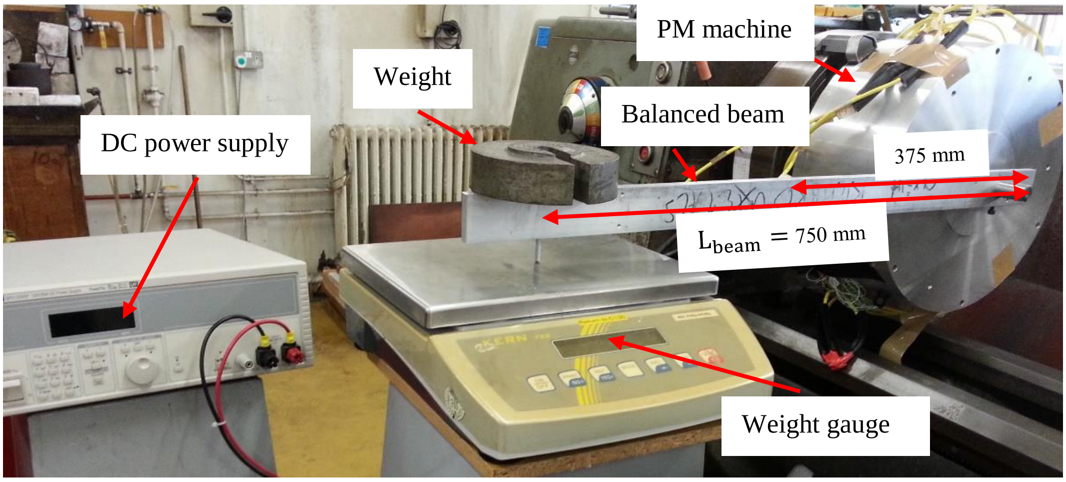

Fig. 5.20 Experimental set up for static torque measurements.

The output waveforms of the static torque which are calculated based on Eq. 5.10 – Eq. 5.13 at different value of injected DC current as shown in Fig. 5.21 & Fig. 5.22. The difference between the predicted and measured is coming from the rotor position which is difficult to fix as the same as in finite element simulation.

$$T_{static} = \left(\left(L_1\left(F_{reading} - F_{pre-load}\right)\right) - \left(L_2 F_{bar}\right)\right) - \left(T_{cogging}\right) \qquad 5.10$$

$$F_{reading} = w_{scale\ reading,with\ injected\ DC\ current}(\mathrm{kg}) \times g \qquad 5.11$$

$$F_{pre-load} = w_{pre-load}(\mathrm{kg}) \times g \qquad 5.12$$

$$F_{bar} = w_{bar}(\mathrm{kg}) \times g \qquad 5.13$$

Where:

$L_1 =$ The total length of the beam from the centre of the rotor shaft to the centre of the weight.

$L_2 =$ The length of the beam from the centre of the rotor shaft to the middle of the beam.

$g =$ gravity acceleration (9.8 m/s^2).

$T_{cogging}$ is shown in Eq. 5.5.

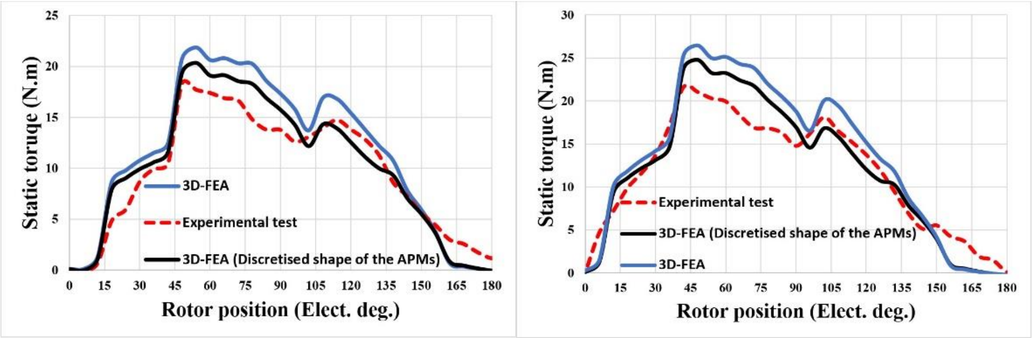

(a) $I_{max} = 18.3$ A, Airgap shear stress = 10 kPa (b) $I_{max} = 22$ A, Airgap shear stress = 12 kPa

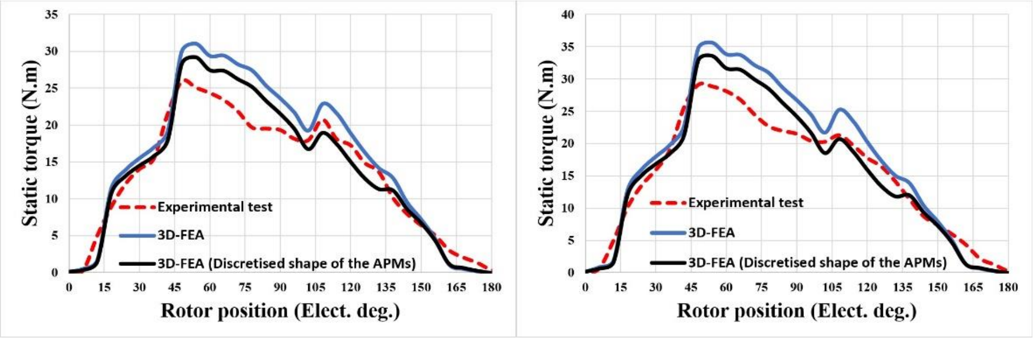

(c) $I_{max} = 25.67$ A, Airgap shear stress = 14 kPa (d) $I_{max} = 29.34$ A, Airgap shear stress = 16 kPa

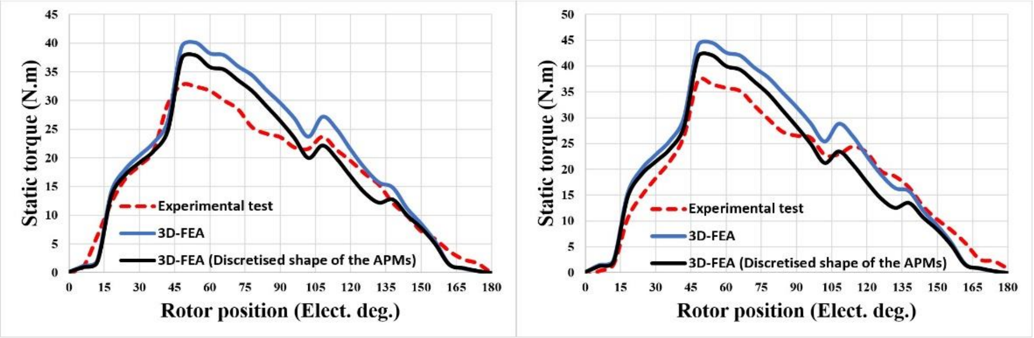

(e) $I_{max} = 33$ A, Airgap shear stress = 18 kPa (f) $I_{max} = 36.67$ A, Airgap shear stress = 20 kPa

Fig. 5.21 Static torque waveforms

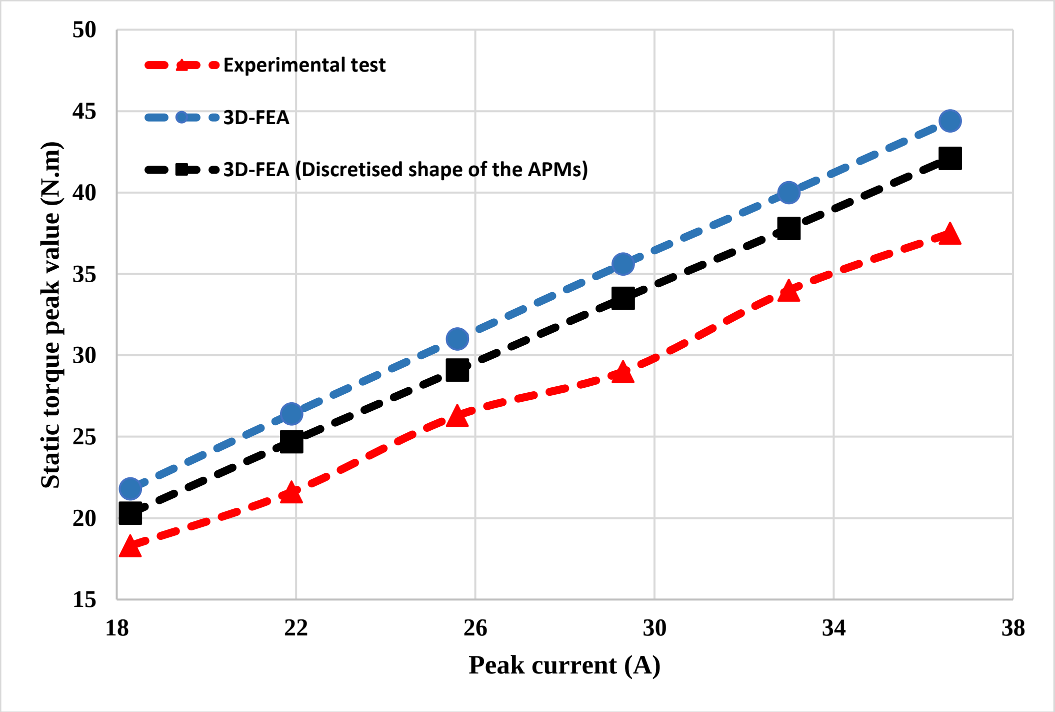

Fig. 5.22 Static torque peak value at different supply current.

5.3.3 Back EMF measurements

To measure back EMF waveforms, the new proposed machine is rotated at no load at different rotation speed as shown in Fig. 5.23. The waveforms of the phase and line voltage are measured by an oscilloscope across on the terminal of the three-phase windings. The waveform of the phase and line back EMFs are shown in Fig. 5.24, Fig. 5.25 and Fig. 5.26. It can be noticed that the emf waveforms are similar and relatively distorted.

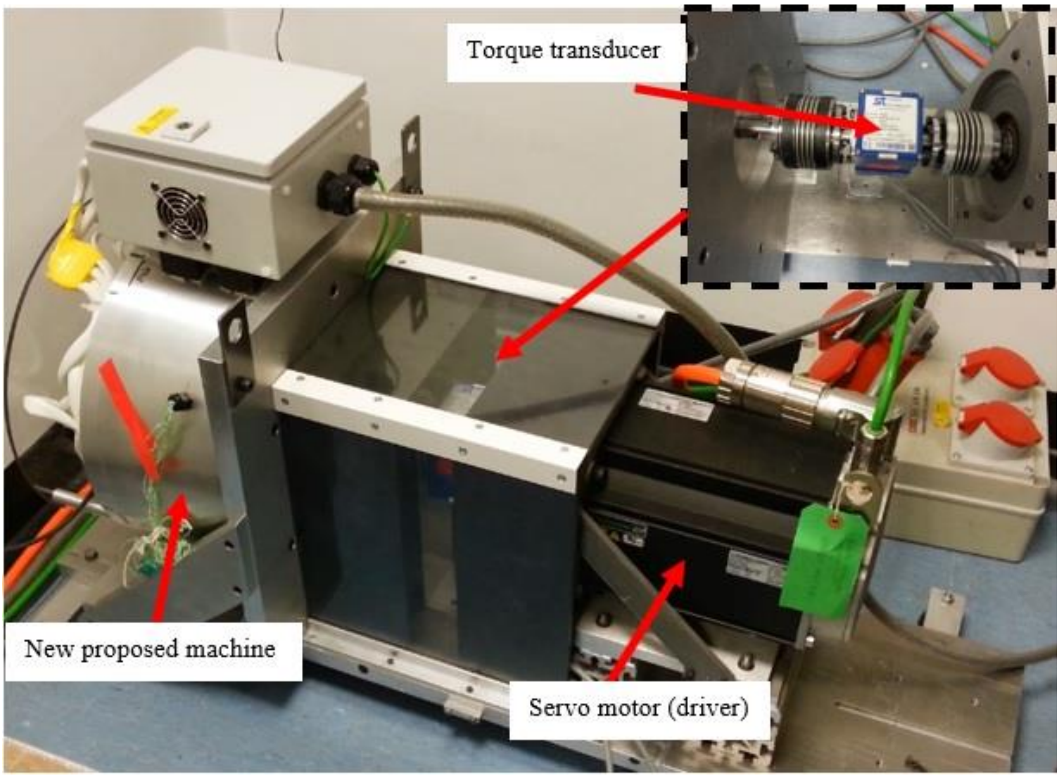

Fig. 5.23 Motor test rig.

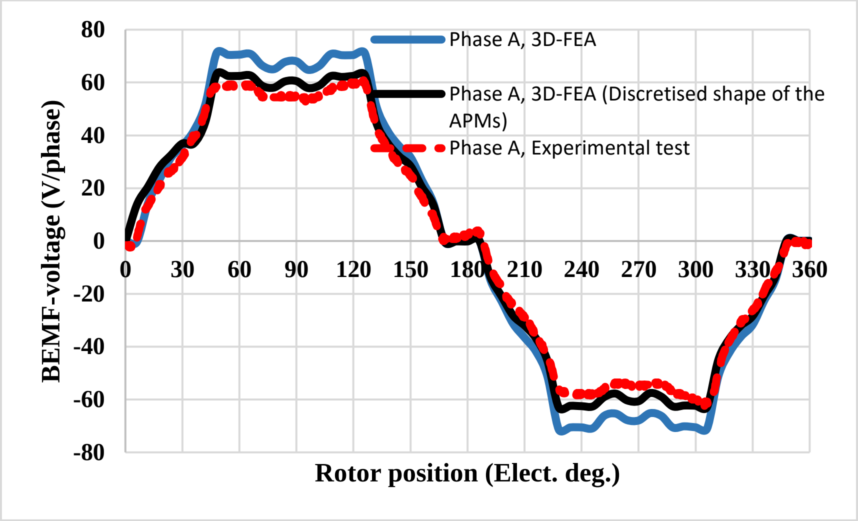

(i) BEMF waveform – phase A

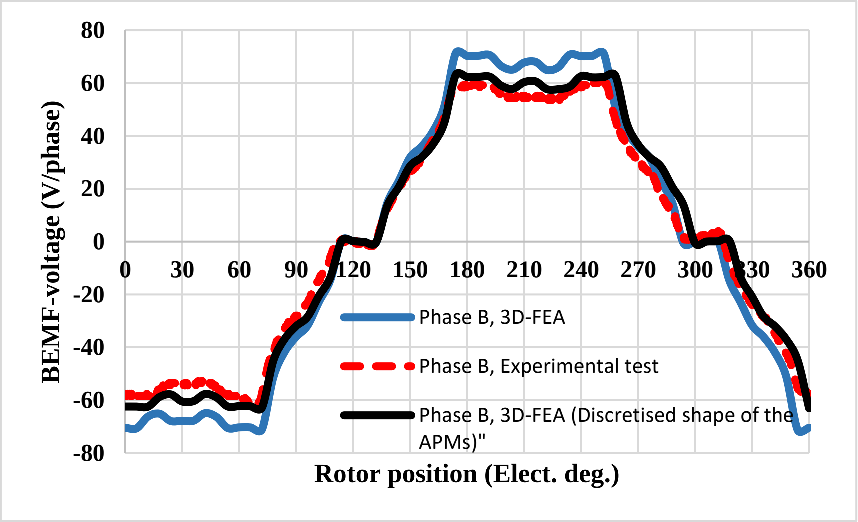

(ii) BEMF waveform – phase B

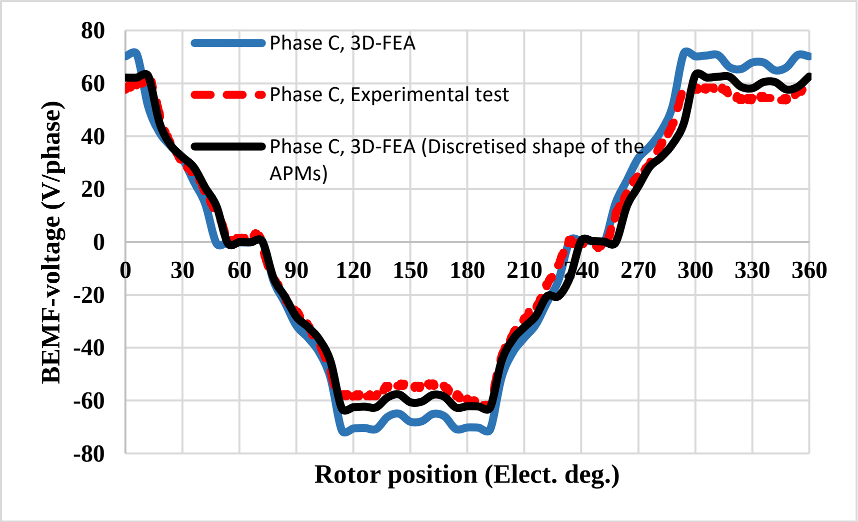

(iii) BEMF waveform – phase C

Fig. 5.24 BEMF wave forms – (phase voltages) at N_{speed} = 976.5 r/min.

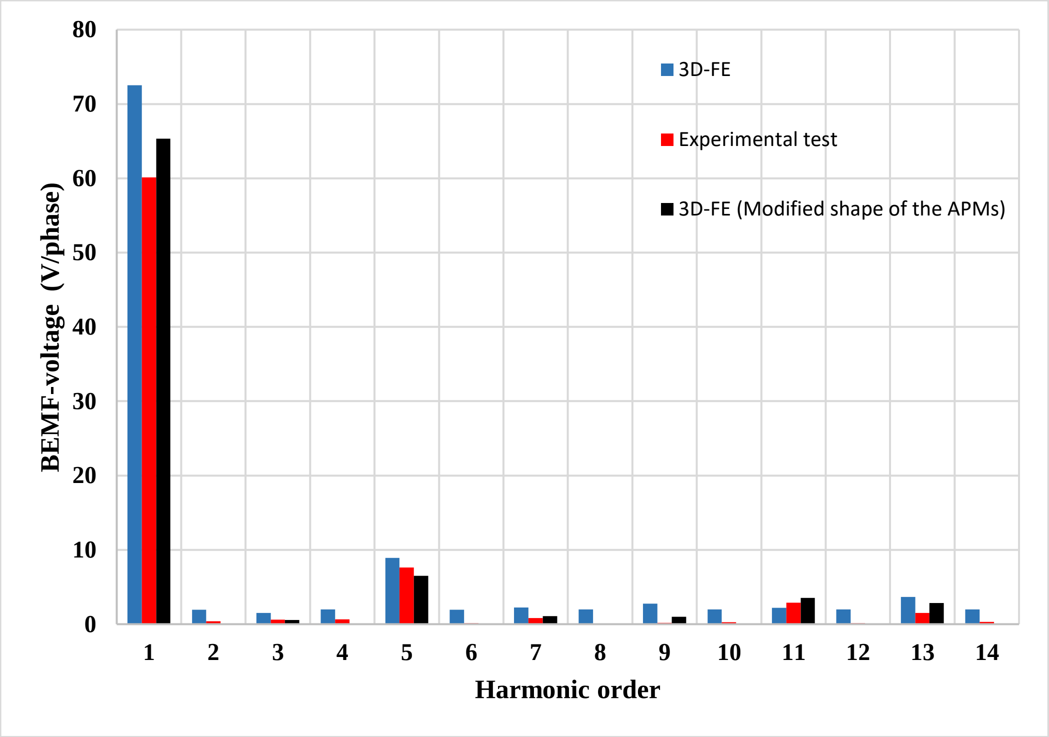

Fig. 5.25 Harmonic spectrum for BEMF- phase voltage at N_{speed} = 976.5 r/min.

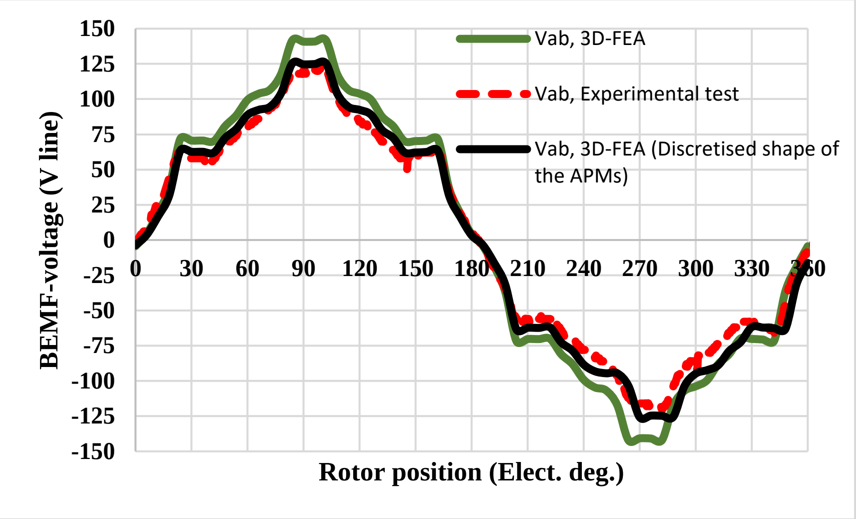

(i) BEMF waveform – Line voltage (Vab)

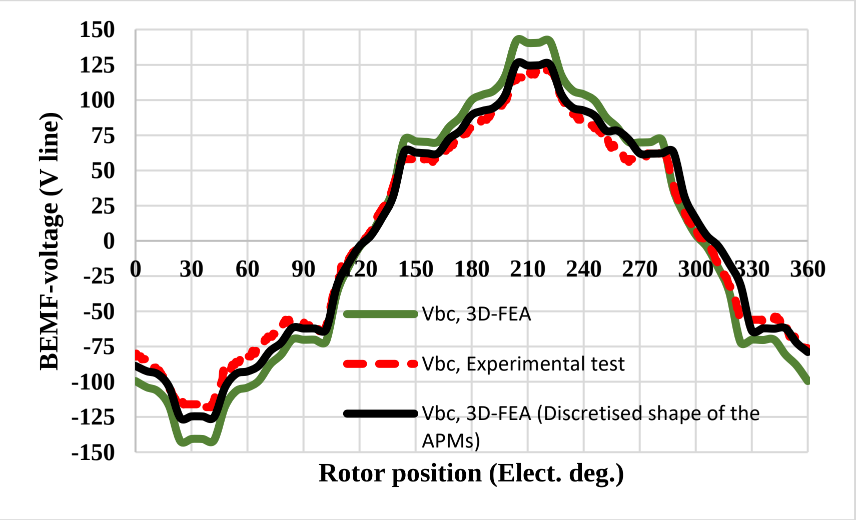

(ii) BEMF waveform – line voltage (Vbc)

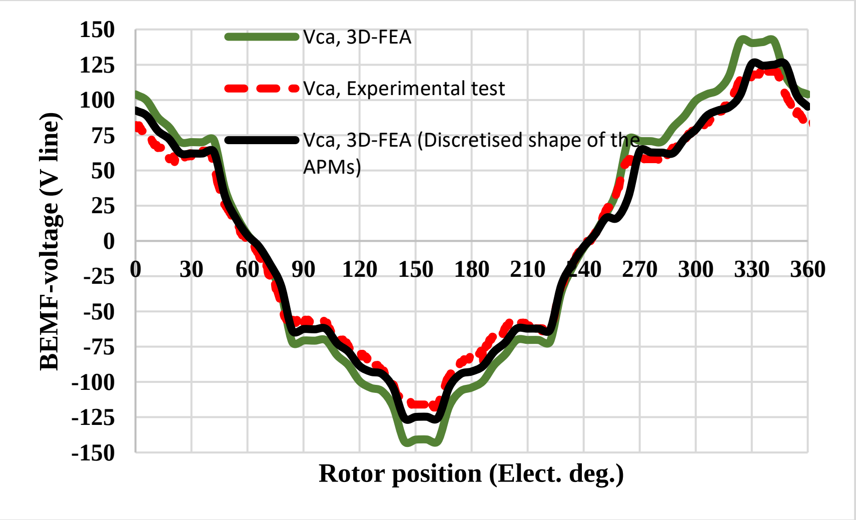

(iii) BEMF waveform – line voltage (Vca)

Fig. 5.26 BEMF waveforms- (line voltages) at N_{speed} = 976.5 r/min.

In summary, the new propose machine prototype is built and the different components such as stator, rotor and case are combined. For the realisation of the machines prototype, an experimental test such as cogging torque, static torque and BEMF measurements are undertaken to investigate the output characteristics. The output results are validated with 3D-FEA which shown a good and satisfy agreements.

According to the new modification in the manufacturing of the shape of the axially magnetized PM shown in Fig. 5.18, a new torque/power speed envelop and efficiency calculation are predicted as shown in Fig. 5.27 & Fig. 5.28. It can be noticed that the rated value of torque at base speed is reduced about 8% compared with the original value. The values of the calculated efficiency are not significantly affected.

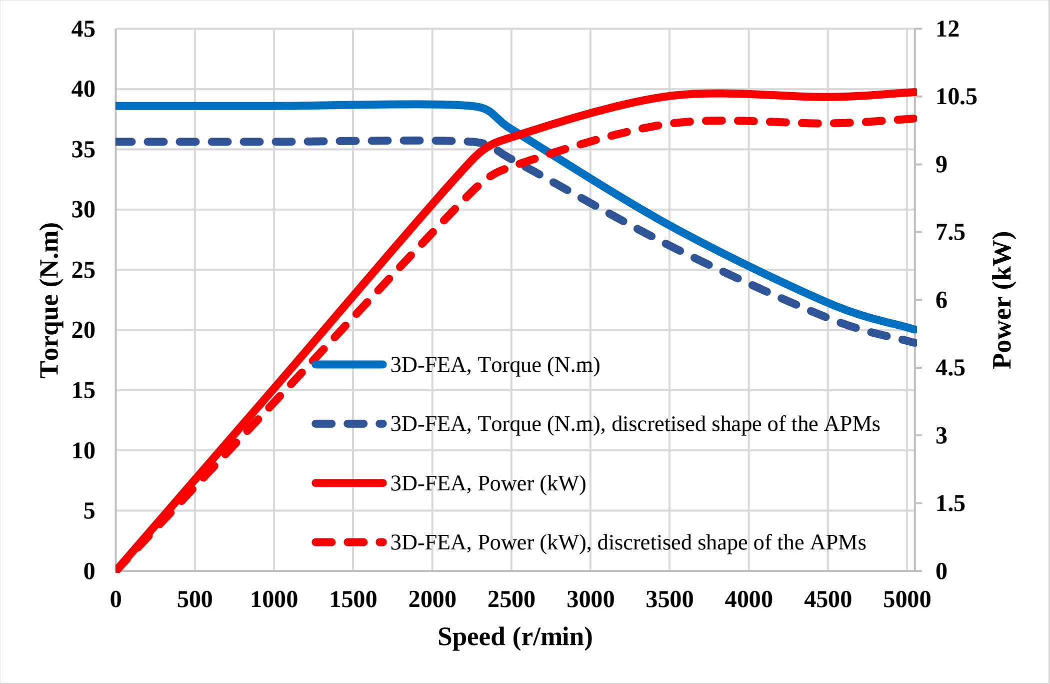

Fig. 5.27 Torque/power speed envelope of the new proposed machine.

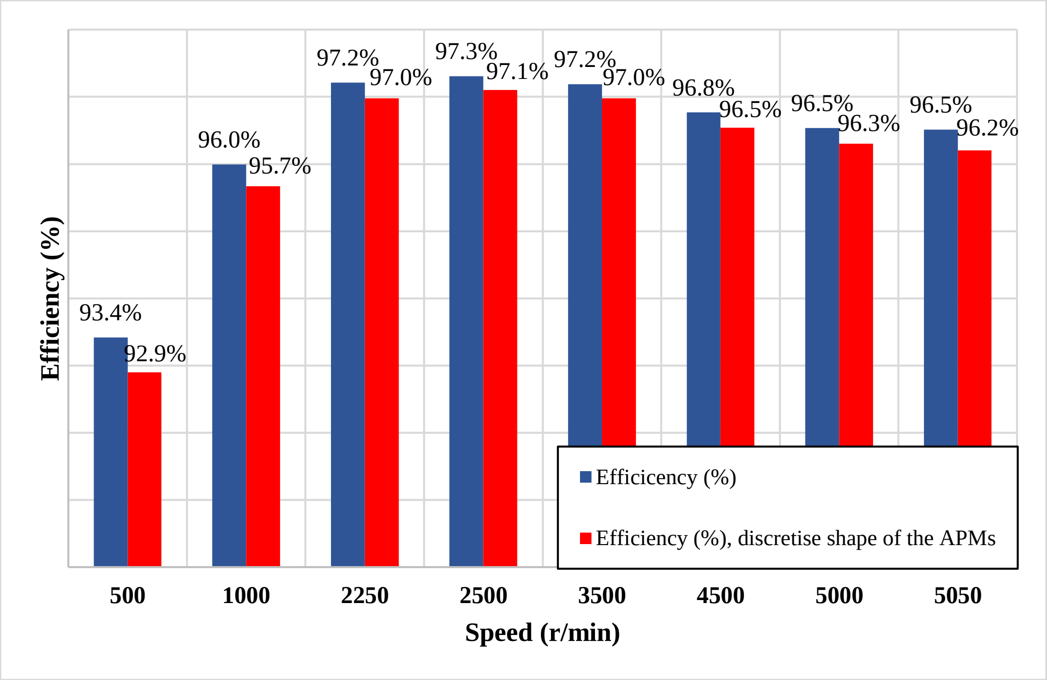

Fig. 5.28 Efficiency calculation of the new proposed machine.

5.4 Calculation of mechanical losses

In this section the mechanical losses which are due to bearing friction and windage losses are estimated. Bearing losses depend on bearing type, shaft rotation speed, force (applied to the shaft) and the properties of the lubricant [68]. According to SKF (a leading bearing and seal manufacturing company founded in Gothenburg, Sweden, in 1907), bearing losses have been calculated as shown in Eq. 5.14 [68].

$$P_{bearing} = 0.5\Omega C_f F_{bearing} D_{bearing} \qquad 5.14$$

Where:

Ω = Angular frequency of the shaft supported by a bearing (rad/s).

C_f = Friction coefficient, typically between 0.0010 and 0.0050. [68], page 460-461.

$F_{bearing}$ = The bearing loads (kN).

$D_{bearing}$ = Bearing inner diameter.

Windage losses are consequence of the friction between the rotating surface, in this case the rotor which can be modelled as a rotating cylinder and the surrounding air [68][69]. The significance of the windage losses becomes more and more important as the rotation speed increases as shown in Eq. 5.15.

$$P_{windage} = \pi C_d \rho R^4 \omega^3 L \qquad 5.15$$

C_d is skin friction coefficient and is evaluated as in Eq. 5.16.

$$\frac{1}{\sqrt{C_d}} = 2.04 + 1.768 \ln\left(R_e \sqrt{C_d}\right) \qquad 5.16$$

ρ = Density of air (1.225 kg/m^3).

R = Radius of the rotor.

Ω = angular velocity (rad/sec).

L = Length of the rotor part (m).

R_e = Reynolds number for the airgap. Eq. 5.17 [70].

$$R_e = \frac{\rho\Omega(D_{outer} - D_{inner})^2}{2\mu_{dyn}} \qquad 5.17$$

D_{outer} = Stator inner diameter.

D_{inner} = Rotor outer diameter.

μ_{dyn} = Dynamic viscosity of air (1.962E-5 $\mathrm{kg/m.s}$).

Due to rotor saliency of the new proposed machine, a correction factor (K) will be multiplied by the obtained windage losses [69]. The value of correction factor (K) has been calculated as shown in Eq. 5.18.

$$\mathrm{K} = 8.5(\mathrm{H/R}) + 2.2 \qquad 5.18$$

H = pole depth (mm)

R = Radius of the rotating cylinder (mm)

The effect of the shroud (end plates) of the new proposed rotor has been considered in the calculation of the windage losses by multiplied by (3/2) [69].

The total mechanical losses will be the summation of the bearing friction and windage losses Eq. 5.19 as shown in Fig. 5.29.

$$P_{mechanical} = P_{bearing} + (P_{windage} \times \mathrm{K} \times (3/2)) \qquad 5.19$$

The total losses which include the analytically calculated mechanical losses and the iron losses calculated using finite element, are shown in Fig. 5.30. The copper losses are (122.92 watt) at 20°.

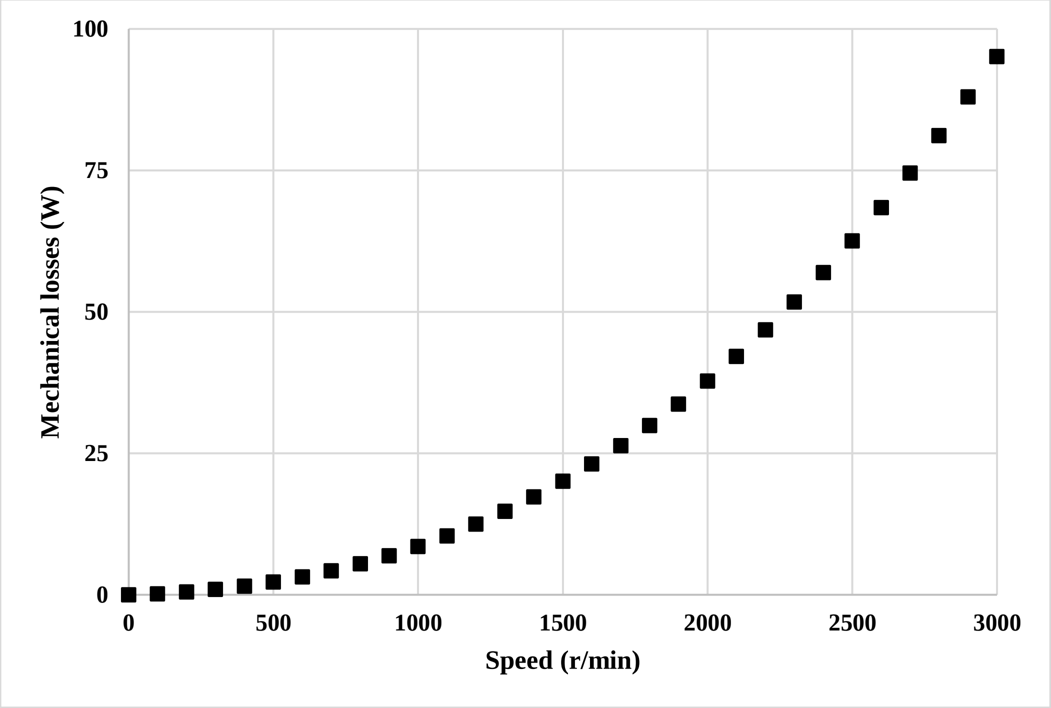

Fig. 5.29 Mechanical losses (theoretical calculation).

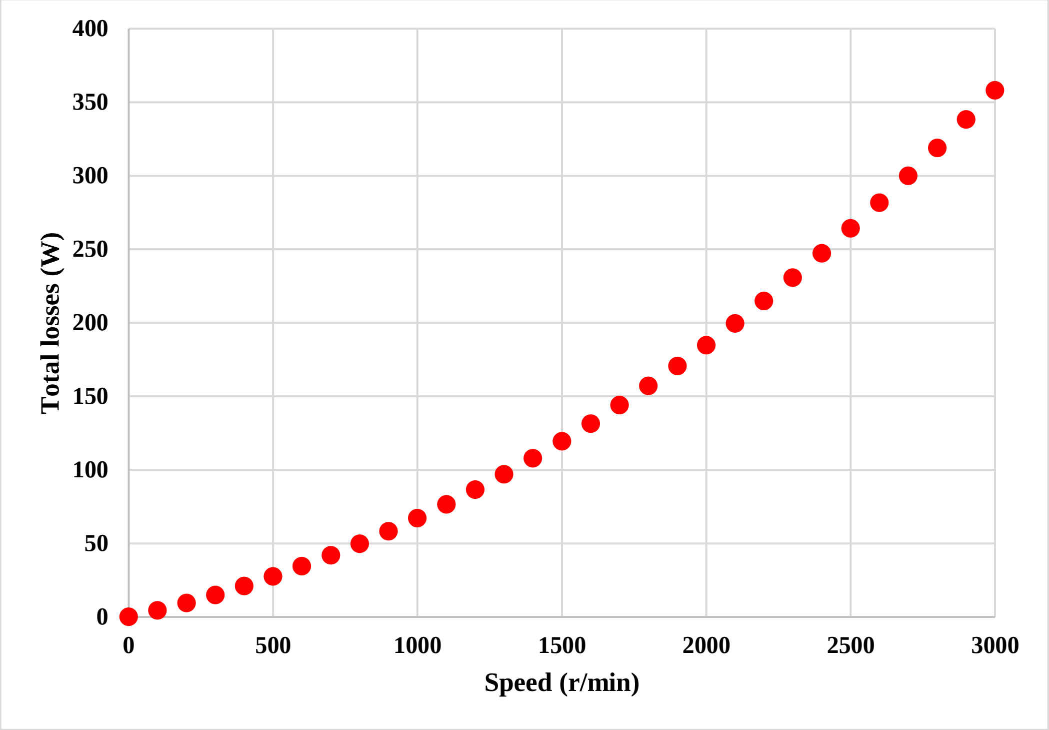

Fig. 5.30 Total losses (mechanical + iron losses).

5.5 Rotation test

During the NO-LOAD test of the new proposed machine at rotation speed = 3000 r/min, a fault occurred and caused change the position of the axially magnetized PM which damaged it and the windings of the stator as shown in Fig. 5.31 and Fig. 5.32. Therefore, the investigation of the no load losses (iron losses) has not been experimentally validated.

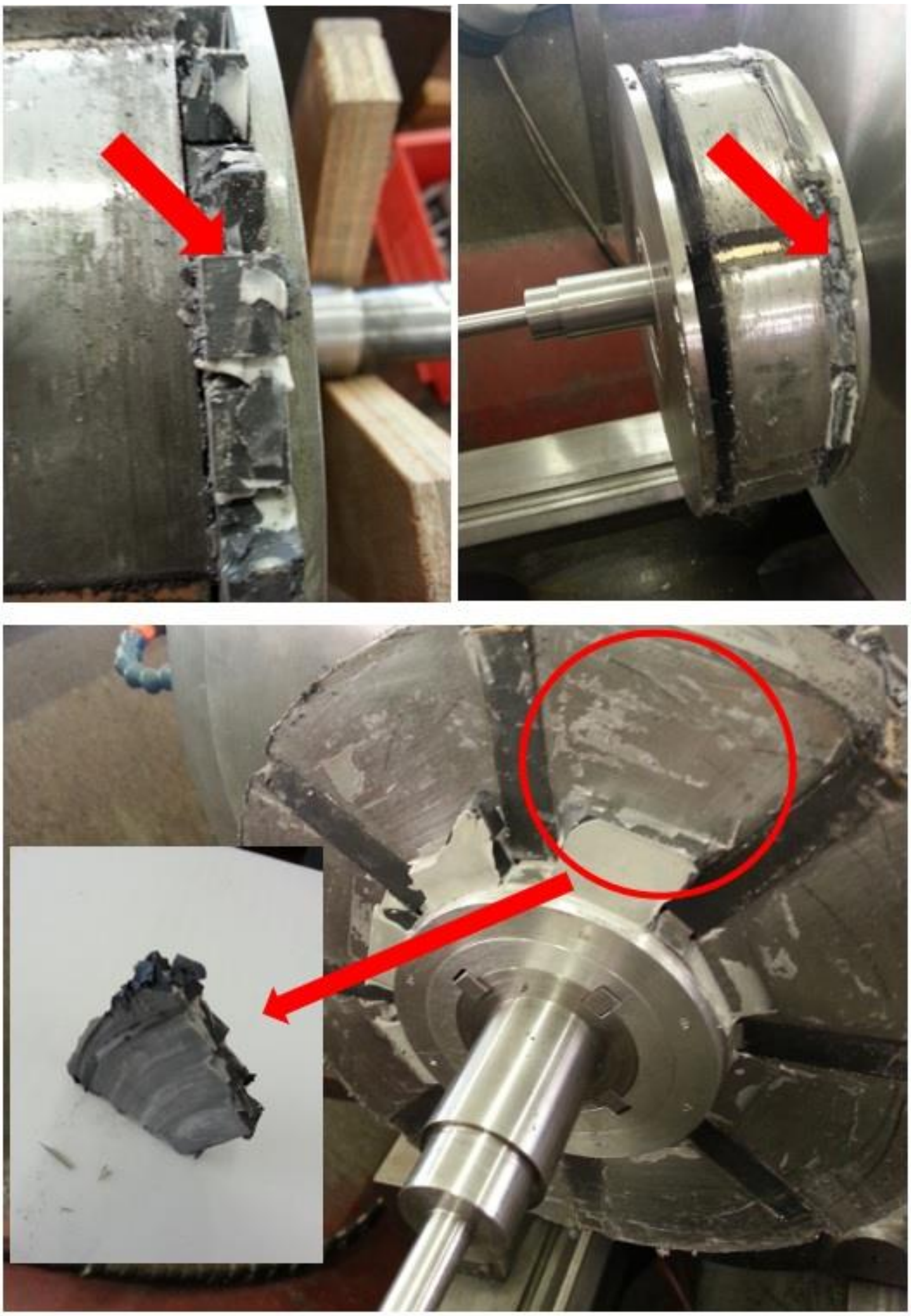

Fig. 5.31 Damages of the proposed rotor.

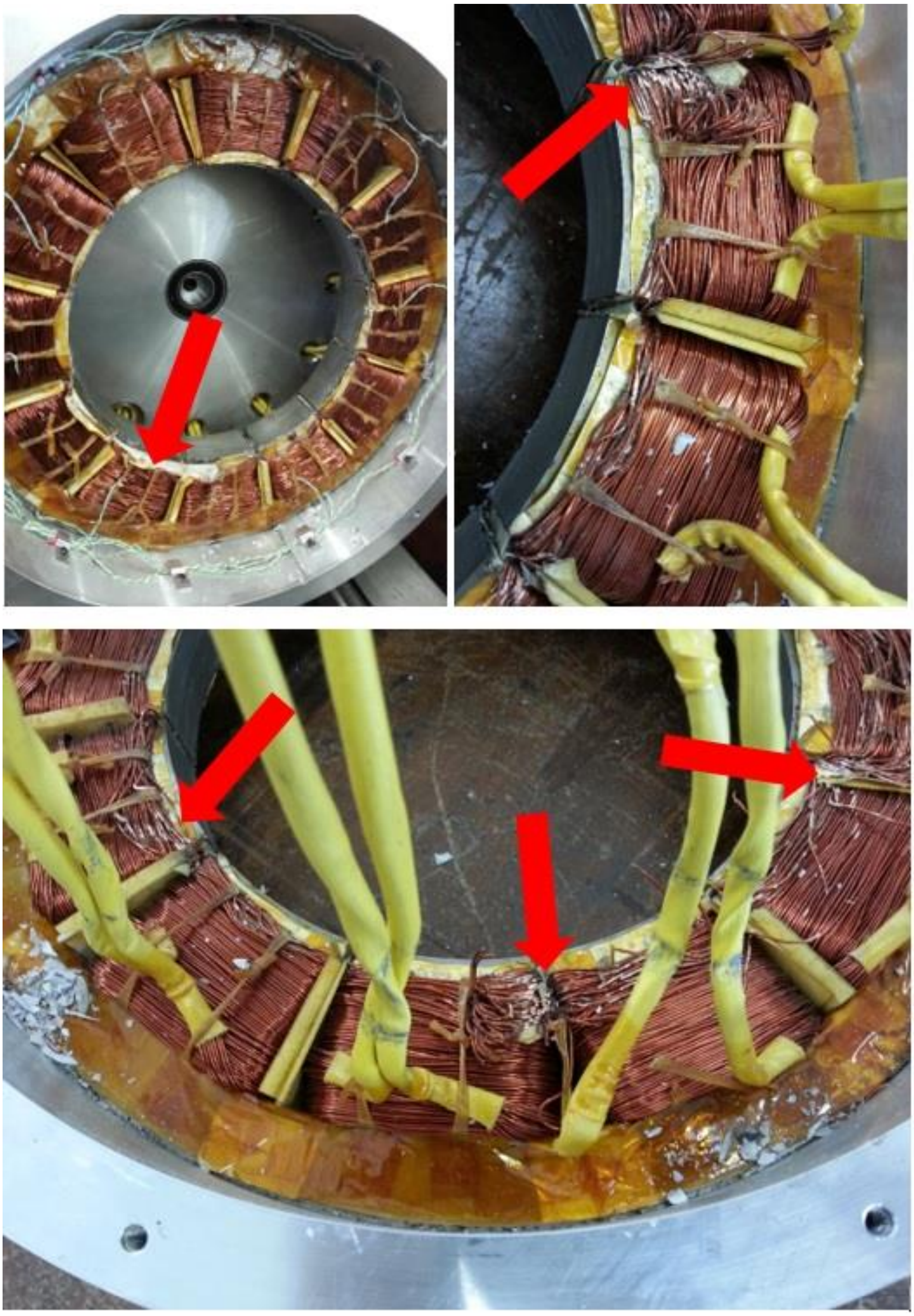

(i) Windings at the stator tooth edge

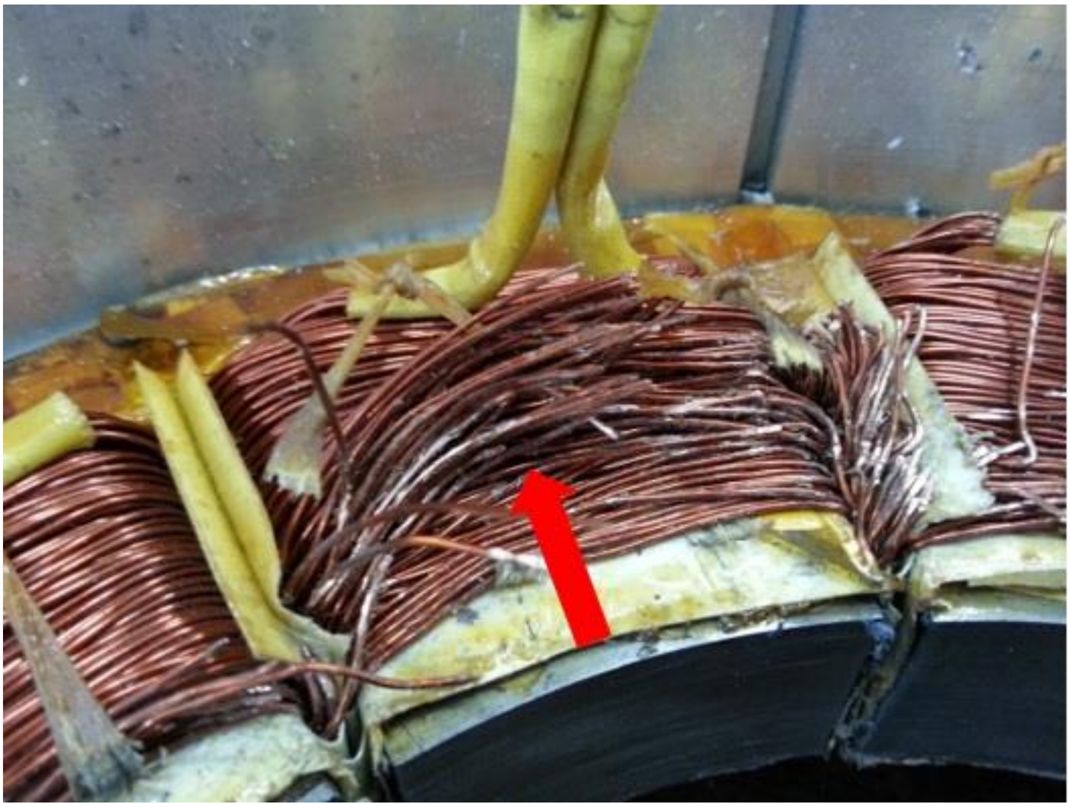

(ii) Windings in the middle of stator tooth

Fig. 5.32 Damages of the stator windings.

5.6 Conclusion

In this chapter a description for the manufacture of the parts such as: stator, rotor, shaft, bush and bush adapter, the axially and circumferentially magnetised PMs used of the new proposed machine is provided. After assembling these parts and for the realisation of the new proposed prototype, some important tests are undertaken to predict the output characteristics such as measurements of cogging torque, static torque and back EMF tests. The results are then validated with 3D-FEA. The comparison shows a good agreement between the measured and predicted results. Unfortunately, during no-load test at speed=3000 r/min, a fault happened suddenly which caused damage of the axially magnetised PM causing damage to the stator winding as well and full load tests haven’t been undertaken. The mechanical losses which include bearing and windage losses are then analytically calculated and the total losses which consists of the iron losses predicted from the 3D-FEA and the mechanical losses are represented as well.

Chapter 6
Conclusion and future work

6.1 Conclusion

In this thesis, the design and an analysis of a novel topology Ferrite machine is introduced. The main purpose of the proposed machine is to reduce/eliminate the use of high cost rare earth permanent magnets with cheaper alternative such as Ferrite permanent magnets. However, the energy of Ferrite permanent magnets is significantly smaller than rare earth counter parts. Therefore, new magnetic circuit topologies should be proposed and investigated in order to maximise the airgap flux density and achieve torque/power density and efficiency comparable with machine employing rare earth permanent magnets. Consequently, a spoke -type rotor equipped with axially magnetized permanent magnets in addition to the conventional circumferential permanent magnets is proposed in order to increase the flux focusing and the airgap flux density.

Firstly, the conventional spoke-type rotor machine is simulated using 2D-FEA and the important leading design parameters such as: number of poles, pole arc to pole pitch ratio, airgap length and the ratio of inner to outer diameter of the rotor are investigated to find the flux per pole and the fundamentals airgap flux density which are then compared with the one predicted from the new proposed rotor machine

A simple lumped parameter magnetic circuit which neglects the leakage flux and assumes a slotless stator is employed to model the rotor and investigate the generated flux per pole. The output results show there is a good agreement between 2D-FEA and lumped parameter magnetic circuit.

Due to the 3D nature of the rotor magnetic circuit, the proposed machine is simulated using (3D-FEA) and the investigation of leading parameters, such as airgap length, pole arc to pole pitch ratio and ratio of inner to outer diameter of the rotor are applied, which can be employed as initial design stage. The output results such as flux per pole and the fundamental airgap flux density are also compared with the one obtained from a simple lumped parameter magnetic circuit which neglects the leakage flux and assumes a slotless stator. It can be seen there is a good agreement between the predicted values using both methods,

Furthermore, 12 slots and 8 poles machine is designed to meet the specifications of a small personal mobility vehicle and the waveforms of flux linkage, airgap flux density and cogging torque are initially predicted at no-load condition. Then the waveforms of the electromagnetic torque and output power are predicted on load condition at different operating conditions. Furthermore, the iron losses in the stator iron and copper losses are computed and the torque / power speed envelopes and efficiency are predicted. The results show that the novel machine can achieve airgap shear stress in excess of 20KPa under natural air-cooling conditions with high efficiencies reaching 97% making it a strong contender for electric vehicle applications.

On the other hand. By using FLUX 3D software developed by CERDAT, the electromagnetic torque components of the new proposed rotor machine are modelled accurately by employed frozen permeability concept which allows separation of the components and taking into account the magnetic saturation of the material and the cross coupling effect.

A lumped parameter magnetic circuit model of the machine is developed, where the non-linear magnetic characteristic of the soft magnetic components is taken into account. Simulation results spanning a variety of load condition are compared with 3D-FEA, and relatively good agreement exists. Albeit, room for improvement of the lumped parameter magnetic circuit model still exists.

Last but not least, a prototype machine was built. Tests are undertaken and quantities such as the waveforms of the BEMFs, cogging torque and static torque were measured and compared with FEA. Good agreement between measured and predicted results exists, which confirms the advantages of the proposed topology. Unfortunately, during a no-load test at rotation speed = 3000 r/min, a fault occurred and one of the axially magnetized PMs lefts its position and was damaged together with the windings on the stator. Therefore, on-load tests have not been experimentally validated.

6.2 Proposed future work

Based on what is mentioned above, there are some points which could be proposed as follows:

(i) Investigate the proper method for fixing the axially magnetized permanent magnets, although it is fixed on the rotor pole pieces using a special type of glue which is also used at high temperature applications, it still did not fix them properly. Therefore, it is recommended that alternative techniques for building the rotor should be investigated in order to enable the machines to operate at required rotational speeds.

(ii) Undertake a thorough experimental investigation, subjecting the machine to different load conditions.

(iii) Investigate the possibility of realising a rotor using a number of stacked units, in order to reduce diameter, achieve higher speeds while keeping a rotor diameter to axial ratio sufficiently low to achieve large airgap flux density.

(iv) Further develop the LPCM in order to achieve improved accuracy. Furthermore, since the 3D flux is only in the rotor, investigate the possibility of combining 2D FEA with lumped parameter representation of the axially magnetised permanent magnets and soft magnetic rings.

(v) Validate the wave forms of the electromagnetic torque components which are predicted based on frozen permeability concept by comparison with the experimental measurements.

References

[1] S. Morimoto, “Trend of permanent magnet synchronous machines,” IEEJ Trans. Electr. Electron. Eng., vol. 2, no. 2, pp. 101–108, 2007.

[2] J. Ormerod, “Bonded Magnets: A Versatile Class of Permanent Magnets,” Magnetics Business & Technology Magazine, no. Summer 2015, Magnet Applications, Inc. A Bunting Magnetics Company, pp. 8–11, 2015.

[3] P. C. Dent and M. H. Walmer, “Supply chain sustainability - Rare earth materials,” 2010 IEEE Int. Vac. Electron. Conf. IVEC 2010, pp. 57–58, 2010.

[4] J. Ormerod, “Permanent Magnet Material Options : Why $ / kg And (BH) max Are Misleading Metrics”. The iInternational Forum on magnetic Application, Technologies & Materials.February 8-9, 2018.

[5] Z. Q. Zhu and W. Q. Chu, “Investigation on Torque in PM Machines - with particular reference to frozen permeability,” pp. 1–35, 2014.

[6] J. R. Hendershot and T. J. E. (Timothy J. E. Miller), “Design of brushless permanent-magnet motors,” Hillsboro OH ;Oxford: Magna Pysics Pub., 1994.

[7] Libert, F. “Design, optimization and comparison of permanent magnet motors for a low-speed direct-driven mixer,”. Licentiate Thesis, Royal Institute of Technology, TRITA-ETS-2004-12, ISSN-1650-674x, Stockholm. 2004.

[8] Z. Q. Zhu and D. Howe, “Electrical Machines and Drives for Electric, Hybrid, and Fuel Cell Vehicles,” Proc. IEEE, vol. 95, no. 4, pp. 746–765, 2007.

[9] T. Heikkila, “Permanent magnet synchronous motor for industrial inverter applications-analysis and design,” lappeenranta University of Technology, 2002.

[10] A. Parviainen, M. Niemela, J. Pyrhonen, and J. Mantere, “Performance comparison between low-speed axial-flux and radial-flux permanent-magnet machines including mechanical constraints,” IEEE Int. Conf. Electr. Mach. Drives, 2005., pp. 1695–1702, 2005.

[11] A. Mahmoudi, N. a. Rahim, and W. P. Hew, “Axial-flux permanent-magnet machine modeling, design, simulation and analysis,” Sci. Res. Essays, vol. 6, no. 12, pp. 2525–2549, 2011.

[12] K. Atallah and J. Wang, “A rotor with axially and circumferentially magnetized permanent magnets,” IEEE Trans. Magn., vol. 48, no. 11, pp. 3230–3233, 2012.

[13] J. D. Ede, K. Atallah, G. W. Jewell, J. B. Wang, and D. Howe, “Effect of axial segmentation of permanent magnets on rotor loss in modular permanent-magnet brushless machines,” IEEE Trans. Ind. Appl., vol. 43, no. 5, pp. 1207–1213, 2007.

[14] H. VuXuan, D. Lahaye, H. Polinder, and J. a. Ferreira, “Improved model for design of permanent magnet machines with concentrated windings,” 2011 IEEE Int. Electr. Mach. Drives Conf., pp. 948–954, 2011.

[15] Z. Q. Zhu, “Instantaneous magnetic field distribution in brushless permanent magnet dc motors. Part I: Open-circuit Field,” IEEE Trans. Magn., vol. 29, no. 1, 1993.

[16] T. Lubin, S. Mezani, and A. Rezzoug, “2-D exact analytical model for surface-mounted permanent-magnet motors with semi-closed slots,” IEEE Trans. Magn., vol. 47, no. 2 PART 2, pp. 479–492, 2011.

[17] Z. Q. Zhu and D. Howe, “Instantaneous magnetic field distribution in brushless permanent\nmagnet DC motors, Part II: Armature-Reaction Field,” IEEE Trans. Magn., vol. 29, no. 1, pp. 143–151, 1993.

[18] Z. Q. Zhu and D. Howe, “Instantaneous magnetic field distribution in brushless permanent magnet DC motors, Part III. Effect of stator slotting,” IEEE Trans. Magn., vol. 29, no. 1, pp. 143–151, 1993.

[19] M. F. Hsieh and Y. C. Hsu, “A generalized magnetic circuit modeling approach for design of surface permanent-magnet machines,” IEEE Trans. Ind. Electron., vol. 59, no. 2, pp. 779–792, 2012.

[20] A. Ebrahimi and N. Parspour, “Modified Analytical Modeling of Surface Mounted Permanent Magnet Synchronous Motor - Design and Prototype Tests,” no. May, pp. 13–17, 2013.

[21] Y. Kano, T. Kosaka, and N. Matsui, “Simple Non-Linear Magnetic Analysis for Permanent Magnet Motors,” vol. 41, no. 5, pp. 387–392, 2005.

[22] T. Gund and G. Komurgoz, “Design of Permanent Magnet Machines with Different Rotor Type,” vol. 4, no. 10, pp. 468–473, 2010.

[23] N. Bianchi, S. Bolognani, and P. Frare, “Design criteria for high-efficiency SPM synchronous motors,” IEEE Trans. Energy Convers., vol. 21, no. 2, pp. 396–404, 2006.

[24] K. Atallah, S. D. Calverley, and D. Howe, “A brushless permanent magnet motor with integrated torque-limiter,” IEEE Trans. Magn., vol. 43, no. 6, pp. 2498–2500, 2007.

[25] J. Wang, X. Yuan, and K. Atallah, “Design optimization of a surface-mounted permanent-magnet motor with concentrated windings for electric vehicle applications,” IEEE Trans. Veh. Technol., vol. 62, no. 3, pp. 1053–1064, 2013.

[26] D. C. Hanselman, “Brushless permanent magnet motor design,”. Magna Physics Publishing, 2006.

[27] C. Zhao, H. Qin, and Y. Yan, “FEM Analysis the Relation Between Pole Pairs and Air Gap Flux Density, Air Gap Flux Respectively in IPM Synchronous Machine,” pp. 1650–1655, 2005.

[28] Bing Xia, Weizhong Fei, and P. Luk, “Analysis and design of V-spoke ferrite interior permanent magnet machine for traction applications,” in 2015 6th International Conference on Power Electronics Systems and Applications (PESA), pp. 1–6, 2015.

[29] W. Kakihara, M. Takemoto, and S. Ogasawara, “Rotor structure in 50 kW spoke-type interior permanent magnet synchronous motor with ferrite permanent magnets for automotive applications,” 2013 IEEE Energy Convers. Congr. Expo. ECCE 2013, vol. 2, pp. 606–613, 2013.

[30] A. Wang, D. Ma, and H. Wang, “FEA-Based Calculation of Performances of IPM Machines with Five Topologies for Hybrid- Electric Vehicle Traction,” vol. 7, no. c, pp. 6–11, 2013.

[31] C. F. Wang, J. X. Shen, P. C. K. Luk, W. Z. Fei, and M. J. Jin, “Design issues of an IPM motor for EPS,” COMPEL Int. J. Comput. Math. Electr. Electron. Eng., vol. 31, no. 1, pp. 71–87, 2012.

[32] N. Bianchi and A. Canova, “FEM Analysis and Optimisation Design of an Ipm Synchronous Motor,” Power Electron. Mach. Drives, 2002. Int. Conf. (Conf. Publ. No. 487), pp. 49–54, 2002.

[33] Z. Q. Zhu and D. Howe, “Influence of design parameters on cogging torque in permanent magnet machines,” IEEE Trans. Energy Convers., vol. 15, no. 4, pp. 407–412, 2000.

[34] S. T. Lee, F. Hall, and L. M. Tolbert, “Analytical Method of Torque Calculation for Interior Permanent Magnet Synchronous Machines,” no. 3, pp. 173–177, 2009.

[35] K. Nakamura, K. Saito, and O. Ichinokura, “Dynamic analysis of interior permanent magnet motor based on a magnetic circuit model,” IEEE Trans. Magn., vol. 39, no. 5, pp. 3250–3252, 2003.

[36] C. Zhao and Y. Wang, “The Analysis of Air Gap Flux and Optimization of Rare Earth Magnet Thickness of IPM Synchronous Machine,” vol. 22, no. mm, pp. 1627–1632, 2005.

[37] C. Zhao, S. Li, and Y. Yan, “Influence factor analysis of PMSM air gap flux density,” Int. Conf. Electr. Mach. Syst., pp. 334–339, 2005.

[38] C. Mi, M. Filippa, W. Liu, and R. Ma, “Analytical Method for Predicting the Air-Gap Flux of Interior-Type Permanent-Magnet Machines,” IEEE Trans. Magn., vol. 40, no. 1 I, pp. 50–58, 2004.

[39] Chaohui Zhao, Deming Zhu, and Yangguang Yan, “The optimization of auxiliary poles of IPM synchronous machine,” in International Conference on Electrical Machines and Systems, p. 344–349 Vol. 1. 2005.

[40] L. J. Wu, Z. Q. Zhu, J. T. Chen, Z. P. Xia, and G. W. Jewell, “Optimal split ratio in fractional-slot interior permanent-magnet machines with non-overlapping windings,” IEEE Trans. Magn., vol. 46, no. 5, pp. 1235–1242, 2010.

[41] M. M. Rahman, K. T. Kim, and J. Hur, “Design and analysis of neodymium free SPOKE-type motor with segmented wing shape permanent-magnet for concentrating flux density,” 2013 IEEE Energy Convers. Congr. Expo. ECCE 2013, pp. 4991–4997, 2013.

[42] S. Hlioui, L. Vido, Y. Amara, M. Gabsi, A. Miraoui, and M. Lécrivain, “Magnetic equivalent circuit model of a hybrid excitation synchronous machine,” COMPEL - Int. J. Comput. Math. Electr. Electron. Eng., vol. 27, no. 5, pp. 1000–1015, Sep. 2008.

[43] J. K. Tangudu, T. M. Jahns, A. EL-Refaie, and Z. Q. Zhu, “Lumped parameter magnetic circuit model for fractional-slot concentrated-winding interior permanent magnet machines,” 2009 IEEE Energy Convers. Congr. Expo., pp. 2423–2430, 2009.

[44] S. H. Han, T. M. Jahns, and W. L. Soong, “A magnetic circuit model for an IPM synchronous machine incorporating moving airgap and cross-coupled saturation effects,” Proc. IEEE Int. Electr. Mach. Drives Conf. IEMDC 2007, vol. 1, pp. 21–26, 2007.

[45] I. M. Seo, H. K. Kim, and J. Hur, “Design and analysis of modified spoke type BLDC motor using a ferrite permanent-magnet,” 2014 17th Int. Conf. Electr. Mach. Syst. ICEMS 2014, vol. 1, no. c, pp. 1701–1705, 2015.

[46] S. Il Kim, S. Park, T. Park, J. Cho, W. Kim, and S. Lim, “Investigation and experimental verification of a novel spoke-type ferrite-magnet motor for electric-vehicle traction drive applications,” IEEE Trans. Ind. Electron., vol. 61, no. 10, pp. 5763–5770, 2014.

[47] K. Boughrara, R. Ibtiouen, and N. Takorabet, “Analytic calculation of magnetic field and electromagnetic performances of spoke type IPM topologies with auxiliary magnets,” Proc. - 2014 Int. Conf. Electr. Mach. ICEM 2014, vol. 7, pp. 51–57, 2014.

[48] W. Q. Chu and Z. Q. Zhu, “Average torque separation in permanent magnet synchronous machines using frozen permeability,” IEEE Trans. Magn., vol. 49, no. 3, pp. 1202–1210, 2013.

[49] X. Chen, J. Wang, V. I. Patel, P. Lazari, L. Chen, and P. Lombard, “Reluctance Torque Evaluation for Interior Permanent Magnet Machines Using Frozen Permeability,” Power Electron. Mach. Drives (PEMD 2014), 7th IET Int. Conf., no. 2, pp. 1–6, 2014.

[50] C. Liu, J. Zhu, Y. Wang, G. Lei, Y. Guo, and X. Liu, “A novel claw pole permanent magnet motor with SMC and ferrite PM,” 17th Int. Conf. Electr. Mach. Syst. ICEMS 2014, pp. 430–434, 2015.

[51] J.-M. S. J.-M. Seo, S.-H. R. S.-H. Rhyu, J.-H. K. J.-H. Kim, J.-H. C. J.-H. Choi, and I.-S. J. I.-S. Jung, “Design of axial flux permanent magnet brushless DC motor for robot joint module,” Power Electron. Conf. (IPEC), 2010 Int., pp. 1336–1340, 2010.

[52] A. Parviainen.“Design of axial flux permanent magnet low speed machines and performance comparison between radial-flux and axial-flux machines,” Lappeenranta University of Technology, 2005.

[53] M. Aydin, S. Huang, and T. A. Lipo, “axial flux permanent magnet disc machines: a review,”. University of Wisconsin Madison, college of engineering, wiscosin power electronic reseach center. January 2004.

[54] S. M. Mirimani, “Developing a 3D-FEM Model for Electromagnetic Analysis of an Axial Flux Permanent Magnet Machine,” J. Electromagn. Anal. Appl., vol. 02, no. 04, pp. 258–263, 2010.

[55] M. Aydin, S. Huang, and T. A. Lipo, “Optimum design and 3D finite element analysis of nonslotted and slotted internal rotor type axial flux PM disc machines,” Power Eng. Soc. Summer Meet. 2001, vol. 3, no. C, pp. 1409–1416 vol.3, 2001.

[56] S. Kahourzade, A. Mahmoudi, N. A. Rahim, and H. W. Ping, “Sizing equation and finite element analysis optimum design of axial-flux permanent-magnet motor for electric vehicle direct drive,” 2012 IEEE Int. Power Eng. Optim. Conf. PEOCO 2012 - Conf. Proc., no. June, pp. 1–6, 2012.

[57] X. Wang, Q. Wang, and Y. Wang, “Analysis of the Magnetic Field of the Six-phase Disc PMSM and Effect of Permanent Magnet Thickness on the Air Gap Magnetic Field,”. World Automation Congress, Hawaii, HI, pp. 1-4, 2008.

[58] C. Koechli and Y. Perriard, “Analytical model for slotless permanent magnet axial flux motors,” Proc. 2013 IEEE Int. Electr. Mach. Drives Conf. IEMDC 2013, pp. 788–792, 2013.

[59] S. M. Mirimani, A. Vahedi, and F. Marignetti, “Study the Influence of Air-gap Variation on Axial Forces in Axial Flux Permanent Magnet Motor Using 3D-FEM,” Cedrat, 2008.

[60] H. Tiegna, A. Bellara, Y. Amara, and G. Barakat, “Analytical modeling of the open-circuit magnetic field in axial flux permanent-magnet machines with semi-closed slots,” IEEE Trans. Magn., vol. 48, no. 3, pp. 1212–1226, 2012.

[61] T. A. Lipo, “Introduction to AC machine design,” 2nd ed. [Madison Wis.]: Wisconsin Power Electronics Research Center, University of Wisconsin, 2004.

[62] "Ferrite Magnets FB Series," TDK Product Center, https://product.tdk.com/en/search/magnet/magnet/ferrite/info?part_no=FB6H, accessed on 22/10/2018.

[63] I. Altair Engineering, “CAD package for electromagnetic and thermal analysis using finite elements. Brushless IPM motor tutorial 2D technical example,” 2018.

[64] Y. Kano, T. Kosaka, and N. Matsui, “Simple Non-Linear Magnetic Analysis for Permanent Magnet Motors2,” vol. 41, no. 5, pp. 387–392, 2003.

[65] M. Amrhein and P. T. Krein, “3-D Magnetic equivalent circuit framework for modeling electromechanical devices,” IEEE Trans. Energy Convers., vol. 24, no. 2, pp. 397–405, 2009.

[66] D. Singh, “Kruger Critical Speeds Shafts.”. Technical Bulletin TBN017.0/1998. https://www.academia.edu/20366355/Kruger_Critical_Speeds_Shafts.

[67] Z. Q. Zhu, “A simple method for measuring cogging torque in permanent magnet machines,” 2009 IEEE Power Energy Soc. Gen. Meet., pp. 3–6, 2009.

[68] J. Pyrhönen, T. Jokinen, and V. Hrabovcová, “Design of rotating electrical machines,”, Reprinted 2010. Chichester: Wiley, 2008.

[69] James E. Vkzncik, “Prediction of Windage power loss in alternators,”. National Aeronautics And Space Administration. October, 1968.

[70] J. F. Gieras, “Permanent magnet motor technology : design and applications,” 3rd ed. Boca Raton: CRC Press, 2010.

Appendix A

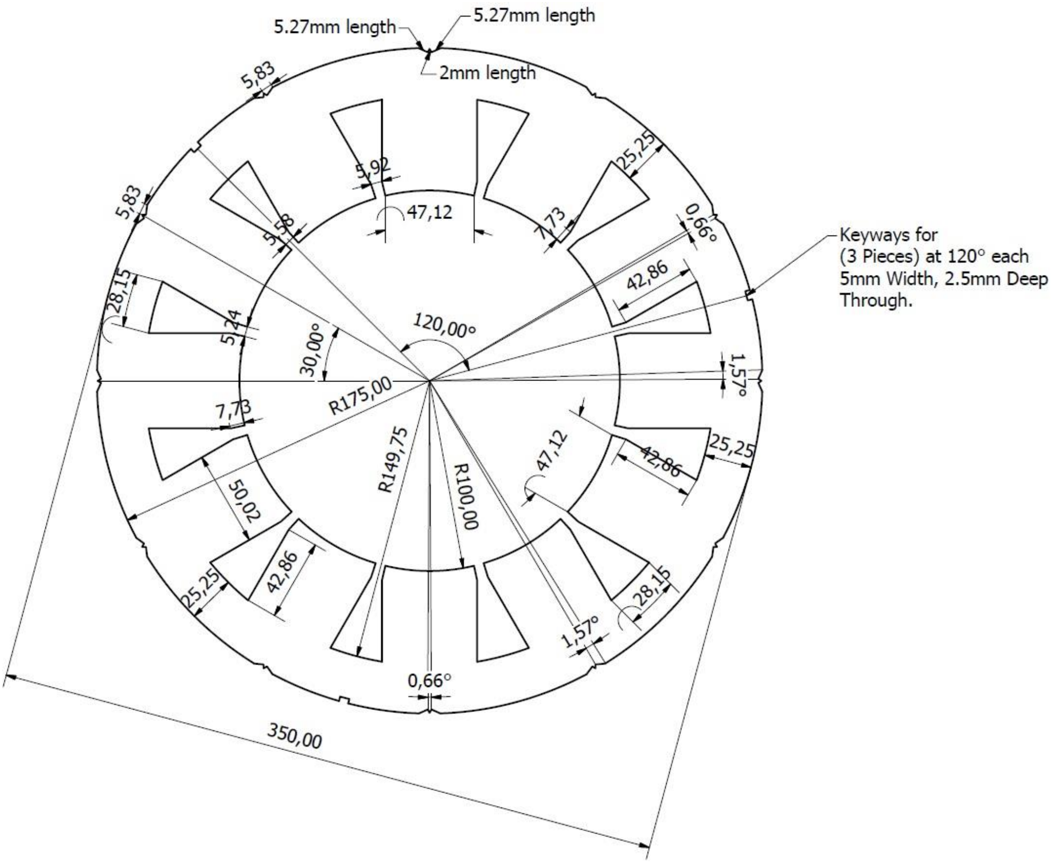

Appendix A1: Overall dimensions of the stator lamination

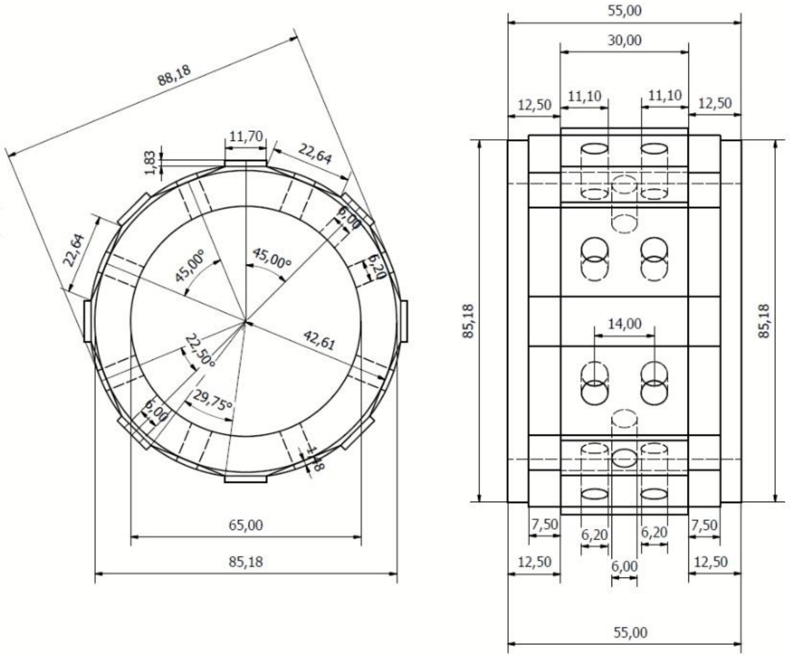

Appendix A2: Overall dimensions of the cylindrical bush

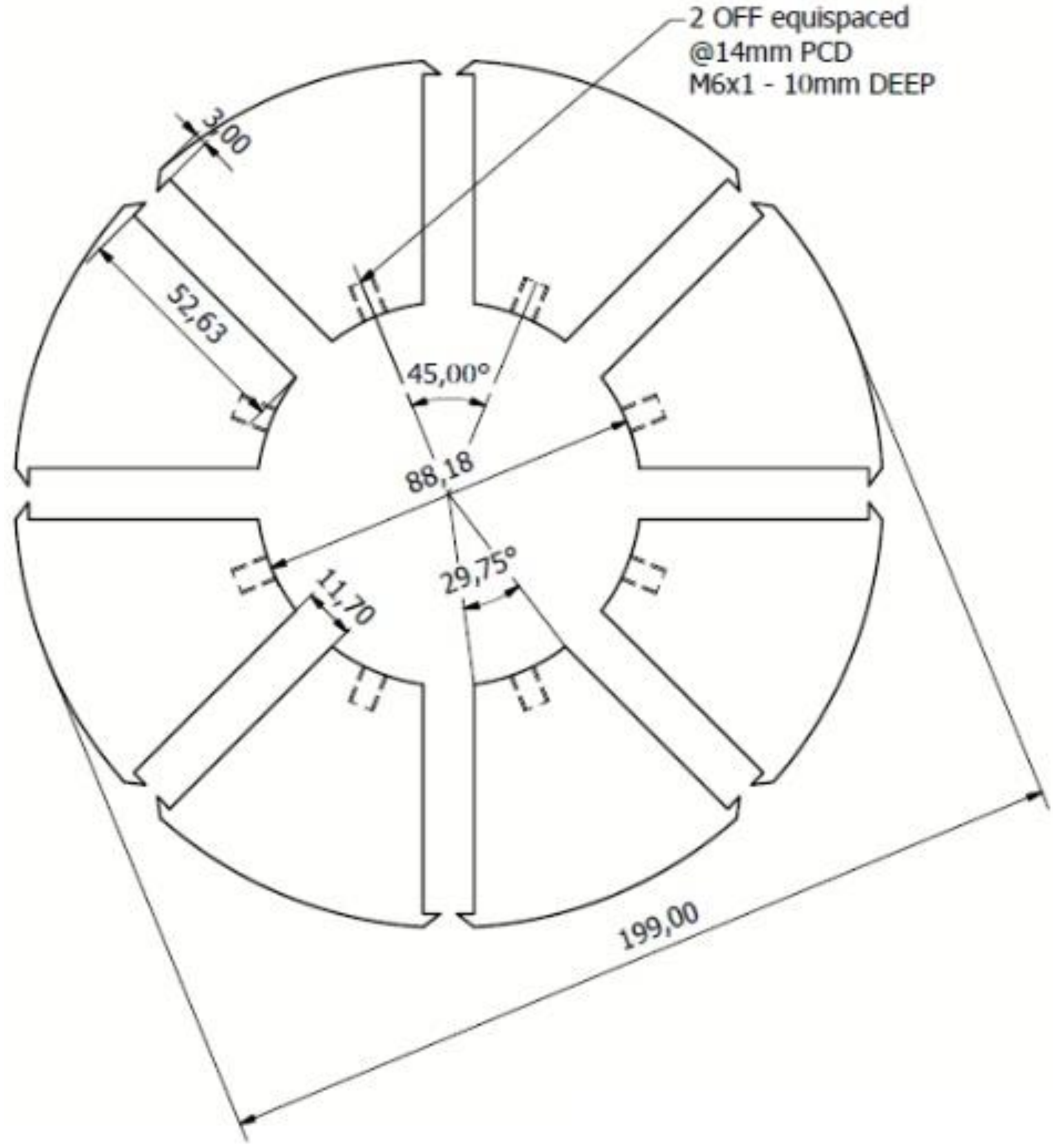

Appendix A3: Overall dimensions of the rotor pole pieces

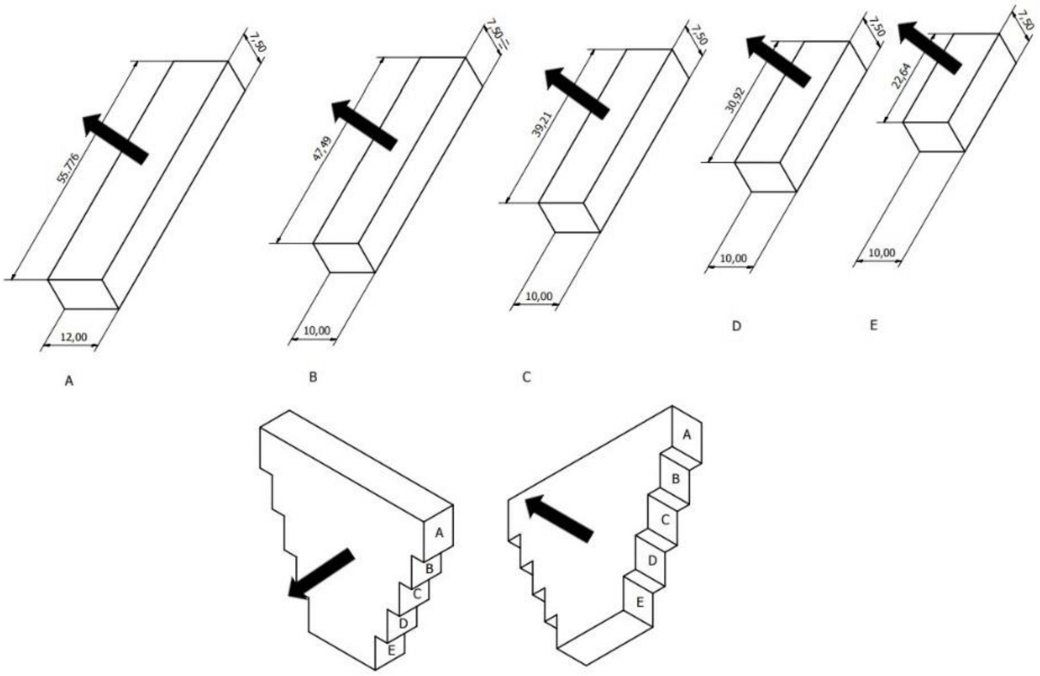

(a) Axially magnetised PM

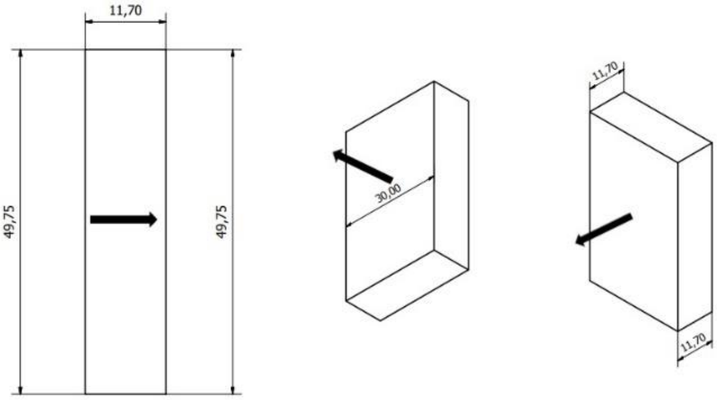

(b) Circumferentially magnetised PM

Appendix A4: Overall dimensions of the axially and circumferentially magnetised PMs